University of Southampton
Faculty of Engineering and the Environment
Institute of Sound and Vibration Research

A RANS-Based Jet Noise Prediction Method Using Ray Tracing Method

by
Balaji Jayanth Venkatesh

Thesis for the degree of
Doctor of Philosophy

April, 2019

UNIVERSITY OF SOUTHAMPTON

ABSTRACT

FACULTY OF ENGINEERING AND THE ENVIRONMENT
Institute of Sound and Vibration Research

A RANS-Based Jet Noise Prediction Method Using Ray Tracing Method

by Balaji Jayanth Venkatesh

Hybrid tools based on Reynolds Averaged Navier-Stokes (RANS) and Computational Aero-Acoustics (CAA) methods have been the current focus of industries to aid the design and development of quieter nozzles with novel configurations for future aircraft. In the current work, improvements to a RANS-based jet noise prediction method are proposed. The source model is based on Lighthill's acoustic analogy and ray theory (geometric acoustics) is used to compute the propagation effects. The method is named, Lighthill Ray Tracing, 'LRT'. In this thesis, improvements within the RANS informed source and propagation model are proposed. These improvements are applied to a wide range of nozzle geometries, both single stream and coaxial stream, with varying flow conditions. The LRT predictions are validated against experimental data.

All RANS-based jet noise methods include model coefficients associated with eddy length-scales and time-scales. Computation of these model coefficients are dependent on measured acoustic spectrum at the 90^o polar angle, thus making it difficult to predict noise from new conceptual nozzles. The current work focuses on arriving at a formalism to determine the RANS-associated length-scale and time-scale coefficients with reduced dependency on experimental data. This procedure is used to perform a parametric study on isothermal single stream and coaxial stream nozzles with varying geometry and flow parameters. Effect of velocity ratio, area ratio, bypass ratio and the effect of the primary nozzle in different noise producing regions of the nozzle are investigated. Along with the LRT method, the 4-source semi-empirical ESDU noise prediction program has been extensively used to perform a characterisation study of far-field noise from ultra high bypass ratio (UHBR) nozzles. The study showed that noise from nozzles with higher area ratios can be modelled using a single equivalent jet.

RANS-based prediction methods coupled with ray theory have been proven to be computationally fast and capable of providing good jet noise predictions. While the use of real rays to calculate propagation effects is not new, the calculation of so-called complex rays - that allow for the modelling of evanescent waves - is typically not accounted for in generic ray programmes. This presents serious shortcomings when dealing with high-speed jets, where high-frequency waves refract away from the downstream axis giving rise to a region exclusive to complex rays commonly referred to as the cone of silence (CoS). In the current work, two methods are proposed to model the field in the CoS. The first method is based on modelling the exponential decay using an approximate WKB solution for a parallel shear flow; the second method exploits the canonical nature of the cone of silence boundary to continue solutions inside the CoS via a complex ray embedded inside the Airy function and its derivative. To demonstrate both methods, the results are compared against Lilley's Green's function solution for a parallel shear flow using a variety of parametric studies. The first method is applied to an isothermal single stream jet and the noise predictions at the CoS angles are compared with experimental data.

Contents

List of Figures

List of Tables

Declaration Of Authorship

I, BALAJI JAYANTH VENKATESH, declare that this thesis and the work presented in it are my own and has been generated by me as the result of my own original research.

A RANS-Based Jet Noise Prediction Method
Using Ray Tracing Method

I confirm that:

1. This work was done wholly or mainly while in candidature for a research degree at this University;
2. Where any part of this thesis has previously been submitted for a degree or any other qualification at this University or any other institution, this has been clearly stated;
3. Where I have consulted the published work of others, this is always clearly attributed;
4. Where I have quoted from the work of others, the source is always given. With the exception of such quotations, this thesis is entirely my own work;
5. I have acknowledged all main sources of help;
6. Where the thesis is based on work done by myself jointly with others, I have made clear exactly what was done by others and what I have contributed myself;
7. Either none of this work has been published before submission, or parts of this work have been published as listed in Section (1.6).

Signed: .....

Date: .....

Acknowledgements

I would first like to thank my supervisor Professor Rod Self for all his support and guidance. Rod was always available to help me throughout my time at ISVR. I would also like to thank Professor Gary Page and Dr David Angland for serving on my PhD exam committee.

I would like to express my gratitude to Professor Jeremy Astley, the former Director of ISVR, who initially offered me this PhD position, and to Rod Self and Paul Strange for accepting me. I am grateful to my financial sponsors, Rolls-Royce plc and the Engineering and Physical Sciences Research Council (EPSRC), in the form of Rolls-Royce DHPA Postgraduate award.

I thank my colleagues at the Rolls-Royce Noise UTC and Acoustic Group for making my time a memorable one. In particular, I would like to thank Jonathan Stone and Jack Lawrence for all the technical discussions and for helping me out with various aspects of my work. I am also thankful to rest of "Team Jet Noise" for all the countless discussions on various matters and for all the memories. I would also like to thank our group secretary, Sue Brindle, for her patience and help. Thanks are also due to Erika Quaranta for helping me with some of the RANS CFD data used in this work. Special thanks to Anilkumar V J and Markus Zauner for their constant support during the course of this work.

I express my gratitude to my parents for always believing in me and for all their love, encouragement and endless support. I would not have been in this position without them. I thank them for everything they have given me - I dedicate this work to them.

Project Acknowledgements

I would like to thank Rolls-Royce Plc. and QinetiQ for providing experimental data from the following test campaigns: SYMPHONY project, which is part of the UK Technology Strategy Board contract TP11/HVM/6/I/AB201K, the Technology Strategy Board (TSB) and Rolls-Royce Plc. funded SILOET project (TP113013) and the EU-funded JERONIMO project (ACP2-GA-2012-314692-JERONIMO). I thank Rolls-Royce Plc. for permitting me to use the data, especially the UHBR data, for validation purposes.

Nomenclature

Roman Symbols

A - Ray-tube area, $[m^2]$

A_p - Primary nozzle area, $[m^2]$

A_s - Secondary nozzle area, $[m^2]$

c - Speed of sound, $[m/s]$

c_o - Ambient speed of sound, $[m/s]$

$c_{0,1}$ - Ray amplitude parameters

c_l - Turbulent length-scale coefficient

c_τ - Turbulent time scale coefficient

D_j - Jet diameter, $[m]$

D_m - Mixed diameter, $[m]$

D_s - Secondary/bypass diameter, $[m]$

e - Internal energy, $[J]$

f - Frequency, $[Hz]$

g_τ - Temporal part of the correlation function

${g_s}^2(r)$ - Shielding function

I - Sound intensity, $[dB]$

J - Jacobian

k - Turbulent kinetic energy, $[m^2/s^2]$

k_y - Radial wavenumber

L - Length scale, $(k^{3/2}/\epsilon)$, $[m]$

M - Mach number

M_s - Source Mach number

M_c - Convective Mach number

M_j - Nozzle exit Mach number

p' - Pressure fluctuation, $[Pa]$

p_{ff} - Far-field pressure, $[Pa]$

P_{ref} - Reference effective pressure amplitude, $[Pa]$

q - Heat flux, $[W/m^2]$

Q - Correlation function

r - Radial coordinate

r_s - Radial source location

r_σ - Turning point location

R - Distance between the source and the observer, [m]

$\boldsymbol{s}$ - Wave slowness vector (geometrical acoustics)

St - Strouhal number ($St = f\,D/U$)

T - Temperature, $[K]$

t - Time, $[s]$

T_{ij} - Lighthill stress tensor, $[Pa]$

u - Local flow velocity, $[m/s]$

u_t - Turbulent velocity, $[m/s]$

U - Mean flow velocity, $[m/s]$

U_c - Convection speed, $[m/s]$

u_x - Axial velocity component, $[m/s]$

u_y - Transverse velocity component, $[m/s]$

U_j - Jet exit velocity, $[m/s]$

U_p - Primary stream velocity, $[m/s]$

V - Volume, $[m^3]$

V_f - Flight stream velocity, $[m/s]$

V_{mix} - Mixed velocity, $[m/s]$

x_p - Coordinate of a moving point at time 't'

x_R - receiver/observer position

x_s - Source position

Greek Symbols

α_c - Empirical convection constant

α_T - Calibrating coefficient

β - Anisotropy level

Γ_p - Phase parameter

δ_{ij} - Knonecker's delta

δ_θ - Vorticity thickness, $[m]$

Δ - Length scale ratio

κ - Wave-number

Λ - Eddy size, $[m]$

μ - Fluid viscosity, $[Pa.s]$

ν - Kinematic viscosity, $[m^2/s]$

ϵ - Turbulence dissipation rate, $[m^2/s^3]$

θ - Observer angle

θ_c - Critical angle

ρ - Fluid density, $[kg/m^3]$

ρ_0 - Fluid density at rest, $[kg/m^3]$

ρ' - Density fluctuation, $[kg/m^3]$

τ - Retarded time, $[s]$

τ_d - Turbulent energy transfer time scale, (TET)

τ_d - Turbulent energy dissipation rate time scale

τ_p - Turbulent energy production rate time scale

τ_{ij} - Viscous stress tensor, $[Pa]$

$\Psi_{ij}(\boldsymbol{\xi})$ - Spatial part of the correlation function

$\boldsymbol{\xi}$ - Separation vector

ω - Observer radian frequency, $[Hz]$

Ω - Source radian frequency

Functions

Ai - Airy function

erfi - Imaginary error function

∇^2 - Laplacian $(\nabla.\nabla)$

sech - Hyperbolic secant function

Abbreviations

AR - Area Ratio

BPR - Bypass Ratio

BVP - Boundary Value Problem

CAA - Computational Aero-Acoustics

CoS - Cone of Silence

CFD - Computational Fluid Dynamics

CRT - Complex Ray Tracing

DNS - Direct Numerical Simulation

EPNL - Effective Perceived Noise Level

IVP - Initial Value Problem

LDV - Laser Doppler Velocimetry

LES - Large Eddy Simulation

LRT - Lighthill Ray Tracing

MGBK - Mani, Gliebe, Balsa and Khavaran

NTF - Noise Test Facility

OASPL - Overall Sound Pressure Level

PARC - Flow solver; product of NASA and AEDC

PIV - Particle Image Velocimetry

PWL - Sound Power Level

RANS - Reynolds-Averaged Navier-Stokes

SEJ - Single Equivalent Jet

SPL - Sound Pressure Level

TET - Turbulence energy transfer rate time scale

TKE - Turbulence Kinetic Energy

UHBR - Ultra High Bypass Ratio

VR - Velocity Ratio

WIND - Flow solver; product of NASA and AEDC

ನನ್ನ ವಿದ್ಯಾಭ್ಯಾಸಕ್ಕೆ ಸದಾ ತಮ್ಮ ಪ್ರೋತ್ಸಾಹ ಹಾಗು
ಉತ್ತೇಜನ ನೀಡಿದ ನನ್ನ ತಂದೆ, ಶ್ರೀ ವೆಂಕಟೇಶ್ ಹಾಗು
ತಾಯಿ ಶ್ರೀಮತಿ ಸುಲೋಚನ ಗೆ ನನ್ನ ಕೃತಜ್ಞತೆಗಳು.
ಈ ಮಹಾಪ್ರಬಂದ ನಿಮಗೆ ಸಮರ್ಪಣೆ.

To my parents

Chapter 1

Introduction

Jet noise still remains as one of the key contributors to the overall aircraft noise even after 60 years of research in the field. Further noise reductions are likely to demand radical improvements in the design of quieter engine nozzles for future aircraft and design activities should be complemented by state-of-the-art experiments and numerical predictions. This poses a challenge to the development of reliable and robust jet noise computational methods which are essential for the design of jet noise prediction tools. The prime aim of the current work is concerned towards improving an engineering jet noise prediction tool to aid novel nozzle design process.

1.1 Jet noise from turbofan engines

Aircraft noise is one of the objectionable impacts of aviation and an important environmental issue in the form of community noise, especially for those living close to airports. Although in general terms these effects are termed as "annoyance", this has got more serious health-related issues and has instigated considerable amount of research activities [4, 5]. Besides health issues, noise also causes flutter which can lead to structural damage to aircraft components. As a result, effective measures are required to mitigate the aircraft noise problem for attaining the sustainable development of the aviation industry. This vital issue has thus drawn the attention of the Government, various regulatory bodies, airline operators, engine manufacturers, the general public, health and occupational services to develop regulatory framework and policies concerning aviation environmental matters, including noise and emissions.

Regulatory bodies such as the Federal Aviation Administration (FAA) and the International Civil Aviation Organisation (ICAO) and other organisations over the course of many years have developed and have been amending the noise and emissions related regulations. These guidelines have evolved over time taking into consideration complex aspects of aircraft and airlines operations and also beyond noise itself. The FAA have issued a circular which provides noise level data for aircraft certificated under 14 CFR (Certificated and Foreign Aircraft) part 36 [6]. The ICAO have outlined stringent noise standards for new subsonic jet and heavy propeller-driven aeroplanes in Chapter 4 in AN-

NEX 16, and amendments were made from the Committee on Aviation Environmental Protection (CAEP) in Chapter 14 [7], issued in 2013.

While there has been progress in reducing aircraft noise over the past two decades, further noise reductions are harder to achieve. The ever-increasing aircraft operations however poses a challenge to abide by the enforced noise regulations. The FAA estimates a growth in business and general aviation at an average of 1.8% a year by 2025 [8]. One of the key strategies to tackle the aircraft noise problem while meeting the increasing demand for aircraft operations is to reduce the noise generation at the source level.

The modern day aircraft has two major noise contributors at approach and flyover reference noise measurement points: airframe noise and engine noise. The location of the certification points is shown in Figure (1.1). Noise generated by the airframe as a result of unsteady flow over high-lift devices (flaps and slats), the landing gear and the fuselage is the major contributor during approach. The engine generates fan and compressor noise which radiate from the intake of the engine. The fan, turbine and core noise radiates from the exhaust ducts and the bypass, and jet noise is generated by turbulent mixing of flow from the core with the bypass flow downstream of the exhaust nozzle. All these sources contributes towards the 'whole aircraft' noise signature for a given certification point with their combined source strength and inherent source directivities.

Contributions of the various aircraft noise sources to the radiated acoustic power is shown at takeoff and approach for a modern turbofan engine is illustrated in Figure (1.2). The contributions to overall sound power level (PWL) are plotted for each major source viz., fan, compressor, combustor, turbine, jet and airframe. Over the past decade, due to the advent of high bypass ratio turbofan engines, significant noise reductions from all sources can be perceived. While fan noise and airframe noise dominate at approach, jet noise remains the major source of noise during takeoff.

In the current work, we focus on methods to mitigate jet mixing noise by improving a semi-empirical prediction method to help design quieter engine nozzles. In the remainder of this chapter, prominent acoustic analogies which form the basis of several jet noise prediction methods are reviewed.

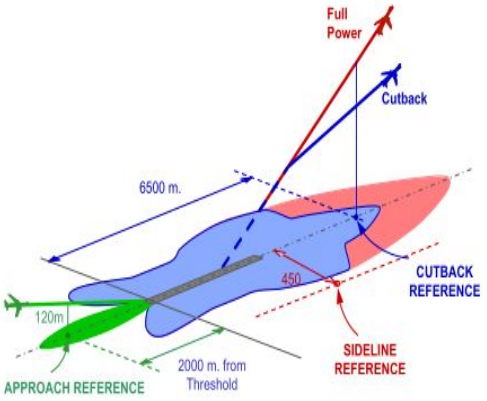

Figure 1.1 – Noise certification points for ICAO Annex 16 and FAA FAR36 [1].

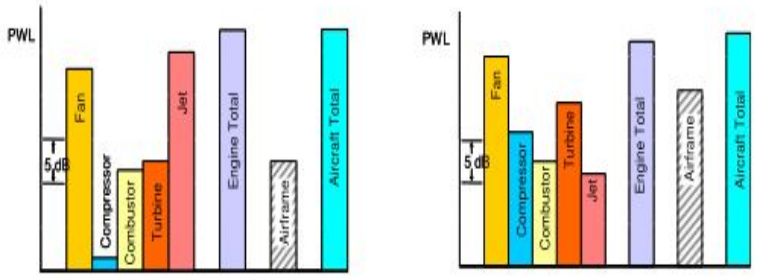

Figure 1.2 – Noise source breakdown for modern high bypass ratio engine [1].

1.2 Acoustic analogies

Jet noise comprises of three principal noise components: turbulent mixing noise and, in the case of imperfectly expanded jets, broadband shock-associated noise and screech tones [9, 10, 11]. In the current work, we focus only on turbulent mixing noise which arises due to the mixing of high velocity jet from the core nozzle with the bypass nozzle and its interaction with the flight stream. Theoretical and experimental investigations related to aerodynamic noise, applicable to engine exhaust noise have been carried since the late 1940s and early 1950s [12, 13]. However, Lighthill's work [14, 15] laid the foundation of aeroacoustic research which led to the understanding of the jet noise problem.

Lighthill's theory of aerodynamic noise is based on the exact rearrangement of Navier-Stokes equations. Lighthill showed that the kinetic energy in the flow responsible for the energy radiated outward as sound is such a small fraction that any approximation made in solving the flow equations for the fluctuating density could lead to an incorrect solution. To overcome these difficulties Lighthill formulated an analogy which is referred to as *Lighthill's acoustic analogy*. Before looking into Lighthill's equation, the main steps leading to the formulation of the analogy are presented for better understanding. Starting from the Navier-Stokes equation for a compressible viscous fluid (effect of solid surfaces are ignored):

$$\frac{\partial \rho}{\partial t} + \frac{\partial \rho \mathbf{u}_i}{\partial \mathbf{x}_j} = 0, \quad \text{(mass conservation equation)} \tag{1.1}$$

$$\frac{\partial \rho \mathbf{u}_i}{\partial t} + \frac{\partial}{\partial \mathbf{x}_i}(\rho \mathbf{u}_i \mathbf{u}_j + p\delta_{ij} - \tau_{ij}) = 0, \quad \text{(momentum conservation)} \tag{1.2}$$

where, δ_{ij} is the Kronecker delta function and τ_{ij}, the viscous stress tensor is given by:

$$\tau_{ij} = \mu \left(\frac{\partial \mathbf{u}_i}{\partial \mathbf{x}_j} + \frac{\partial \mathbf{u}_j}{\partial x_i} - \frac{2}{3} \frac{\partial \mathbf{u}_k}{\partial \mathbf{x}_k} \delta_{ij} \right). \tag{1.3}$$

Taking the time derivative of (1.1) and the divergence of (1.2), and subtracting the two equations, yields,

$$\frac{\partial^2 \rho}{\partial t^2} = \frac{\partial^2 T_{ij}}{\partial \mathbf{x}_i \, \partial \mathbf{x}_j} (\rho \mathbf{u}_i \mathbf{u}_j + p \, \delta_{ij} - \tau_{ij}). \tag{1.4}$$

Since $\partial^2\rho/\partial t^2 = \partial^2\rho'/\partial t^2$, where the density fluctuations $\rho' \equiv \rho - \rho_o$, and subtracting $c_o^2\,\nabla^2\rho'$ on either sides from equation (1.4), the following inhomogeneous equation is obtained:

$$\frac{\partial^2\rho'}{\partial t^2} - c_o^2\nabla^2\rho' = \frac{\partial^2 T_{ij}}{\partial \mathbf{x}_i \partial \mathbf{x}_j} \tag{1.5}$$

where, $T_{ij} = \rho \mathbf{u}_i \mathbf{u}_j + (p' - c_o^2\rho')\delta_{ij} - \tau_{ij}$.
The Lighthill tensor, T_{ij} represents a distribution of quadrupole and dipole sources (in the case of a heated jet) in a non-moving medium, $\rho\mathbf{u}_i\mathbf{u}_j$ is the Reynolds stress term and it represents non-linear effects, terms $(p' - c_o^2\rho')$ is the associated entropy term, and τ_{ij} denotes the viscous stress.

In the far-field, the fluctuations associated with the acoustic waves are such that $p' = c_o^2\rho'$. These acoustic disturbance propagate far away from the source region and they decay like $1/r$.

Using Green's function, the general solution for density fluctuation in the far field due to a volume of source can be given as [16]

$$\rho'(\mathbf{x}, t) = \frac{1}{4\pi c_o^4 \mathbf{x}} \frac{x_i x_j}{\mathbf{r}^2} \frac{\partial^2}{\partial t^2} \int_V T_{ij}[\mathbf{y}, t] d\mathbf{y}, \tag{1.6}$$

where $\mathbf{r} = \mathbf{x} - \mathbf{y}$ and the square brackets $[\mathbf{y}, t]$ is evaluated at the retarded time $t - r/c_o$.

Following Goldstein, the far field acoustic intensity spectrum can be obtained from Lighthill's equation as [16],

$$I_\omega(\mathbf{x}) = \frac{1}{32\pi^3\rho_o c_o^5} \frac{\omega^4}{x^2} \int\int \mathscr{S}(\mathbf{y}, \eta, \omega)\, e^{-i\omega\frac{\hat{\mathbf{x}}.\eta}{c_o}}\, d^3\eta\, d^3\mathbf{y}. \tag{1.7}$$

Here, η is the separation vector, ρ_o and c_o are the ambient pressure and speed of sound respectively and, using over-bars to denote time averages,

$$\mathscr{S}(\mathbf{y}, \eta, \omega) = \int_{-\infty}^{+\infty} \overline{T_{xx}(\mathbf{y}, t) T_{xx}(\mathbf{y} + \eta, t + \tau)}\, e^{-i\omega\tau} d\tau = \int_{-\infty}^{+\infty} \mathscr{R}(\mathbf{y}, \eta, \tau)\, e^{-i\omega\tau}\, d\tau, \tag{1.8}$$

is the Fourier transform of the two-point correlation of the Lighthill stress tensor components in the direction of the far-field observer.

The acoustic radiation field generated from a source of strength T_{ij} can be given by two-point pressure autocorrelation as a function of time as follows,

$$\Gamma(\mathbf{x}, \tau) = \frac{\rho_o}{16\pi^2 c_o^2} \frac{x_i x_j x_k x_l}{x^6} \frac{\partial^4}{\partial \tau^4} \int\int \mathscr{R}_{ijkl}\left(\mathbf{y}', \eta, \tau + \frac{\eta}{c_o}.\frac{\mathbf{x}}{x}\right) d\mathbf{y}\, d\eta \tag{1.9}$$

where $\mathscr{R}_{ijkl}$ is the fourth-order two-point correlation of the Lighthill stress tensor components in the sound field.

In this formalism, the unsteady fluid flow is replaced by a volume distribution of equivalent acoustic sources (right-hand side of equation (1.5)) throughout the entire flow field where density, ρ and entropy, s are taken to be constants, viscosity and heat conduction

are neglected. The theory also assumes a uniform medium at rest, but the embedded sources may move. Further, the source region is assumed to be acoustically compact, and is treated as point sources, meaning the spatial extent (length scale of eddies, L) over which the $\rho \mathbf{u}_i \mathbf{u}_j$ term is correlated to be small compared to the wavelength (λ) of the emitted sound. Lighthill points out that these are low Mach number theories. However, Freund [17] uses Direct Numerical Simulation results for a Mach 0.9 jet to show that higher frequency sources would be relatively less compact and that the source does not satisfy a $\lambda \gg L$ compactness condition. Lighthill's theory also assumes that the acoustic source field is known to some good approximation.

Lighthill's theory accounts for effects arising from the mean flow convection of the acoustic sources by a convective amplification factor comprising of the reciprocal of six powers of the Doppler factor. Ffowcs Williams [18] suggested that the convective amplification factor should comprise of five powers of Doppler factor due to the limited spatial extent of the jet. So far there has been numerous extensions and reformulations of Lighthill's theory confirming the features related to Mach number and consequent changes in directivity and spectra [19].

Despite its theoretical simplicity and applicability, Lighthill's theory is often criticised for not being able to deal with refraction of sound away from the jet axis due to flow-acoustic interaction and flow "shrouding" effects. The significance of refraction effects for high velocity jets for observer angles away from 90^o to the jet axis was demonstrated by Lush [20]. The notion of accounting for the effects of jet flow interaction was first considered by Phillips [21], and much more elaborately by Lilley [22]. Lilley reformulated the acoustic analogy to incorporate flow-acoustic interaction effects due to the mean-flow field of the jet. Lilley combined the flow equations to obtain a third order convected wave equation accounting for effects of a unidirectional sheared mean-flow on sound propagation. Lilley employed the Pridmore-Brown linear operator to describe sound propagation through a parallel flow.

The significant part of Lighthill's source term is quadratic in the total flow velocity, which can be decomposed into a mean and fluctuating component. The source term therefore contains terms that are both linear and quadratic in the fluctuating velocity components (equation (1.5)). Lilley [22, 23] argued that these linear terms, which are much larger than the quadratic quantities, do not actually radiate any sound and should, therefore, not be included in the source function as they tend to dominate over the smaller quadratic terms, which are the true sources of sound. Inclusion of these linear terms could induce errors in the actual computation of source terms leading to incorrect predictions of the sound field.

Lilley [24, 25] introduced a modification to the entropy source term in Lighthill's equation that separates this term into isentropic and non-isentropic components, which is important because the non-isentropic component is proportional to the heat flux vector q_i and the viscous work term $\tau_{ij} \mathbf{u}_j$ that are usually neglected at the high Reynolds numbers

where jet noise becomes important. So far, solutions to Lilley's equation are given in the form of a Green's function. This is beneficial to determine the mean-flow refraction effects independent of the source distribution and limits the empiricism inherent in the acoustic analogy to the source modelling problem. Despite the linear nature of Lilley's equation, obtaining accurate numerics of the associated Green's function is complicated and the focus has been shifted towards the use of high-frequency asymptotics [26]. Although solutions for a parallel shear flow are exact, it is hard to solve the Pridmore-Brown wave operator which contains instability wave modes which, when excited by the flow, can give rise to singularities in the physical solution. This restricts the application of Lilley's theory to practical engine nozzles.

The notion of interaction of sound and sources of sound with the fluctuating part of the flow was carried forward by Goldstein in the form a generalised acoustic theory [27]. Goldstein separated the flow variables into their mean and fluctuating components. The linear and inviscid terms were collected on one side of the equation and the remaining nonlinear and viscous terms on the other side, and the latter were treated as known source terms. With this, the propagation effects were removed from the source terms and the original problem of computing the sound field was converted into problem of estimating the source terms. The advantage is that the source terms, which are approximately quadratic in the fluctuating quantities, will be more localised than the linear terms and that the radiated sound field will relatively independent of the details of these nonlinear terms.

1.3 High bypass ratio nozzles and noise reduction

Ultimately, the three popular analogies that are reviewed, have been either simplified, extended or reformulated to adapt the theory to compute noise to reduce the jet noise issue. Of the three, Lighthill's theory has received considerable attention due to it's simplicity and the ease with which it could be used in a computational tool. Another main highlight of this theory is the eighth power law. According to Lighthill, if L denotes the length scale of the eddies, and u the velocity, the associated frequency will be proportional to (u/L). For a compact source (source is smaller than the acoustic wavelength, λ), the ratio (L/λ) will be proportional to (u/c_o).

The various source terms in equation (1.6) can then be estimated as,

$$\begin{aligned} T_{ij} &= \rho u_i u_j \sim \rho_o U_j^2 \\ \frac{U_j}{L} &= \frac{\partial}{\partial t} \sim \frac{c_o}{\lambda} \\ \int d\mathbf{y} &\sim L^3. \end{aligned}$$

Based on dimensional arguments, a scaling law for the acoustic density (as in equation 1.6) and the acoustic intensity, I, is proportional to the product of the flow area and the

eighth power of the jet velocity U_j, as given by equation (1.10),

$$I \sim \frac{\rho_o U_j^8 L^2}{c_o^5 r^2}. \tag{1.10}$$

This scaling law can be used to identify the parameters involved in the sound generation. Numerous theoretical and experimental work have been carried out based on Lighthill's framework, from the early 1950s till today. The eighth power law laid the basis for the advent of dual-stream or coaxial stream nozzles, which resulted in significant reduction of noise with gains in propulsive efficiency for a given thrust. Over the years the bypass ratio (BPR), i.e. the ratio of air passing through the engine bypass to the air flow through the engine core, has increased remarkably due to reduced noise levels and improved efficiency. The bypass ratio of the Rolls-Royce Trent 1000 engine is approximately 11:1, and is one of the highest bypass ratio engines in service today. The reduced noise levels of the modern day aircraft are mainly ascribable to these high bypass ratio engines. However, increased air traffic demands further reduction in the noise levels. Unfortunately, without a step change in technology, maximising the bypass ratio is constrained by several factors such as, the ground clearance (distance between nacelle lowest point and ground during landing), engine nacelle drag, rotor speed and the length of the fan blades. Another important aspect of increasing the bypass ratio is the reduced distance between the nozzle and the wing. This increases the noise due to interaction of the jet with the wing and control surfaces such as the slats, and also increases the weight penalty. Amidst these constraints, the current focus is on developing ultra high bypass ratio (UHBR) engine nozzles (BPR > 12) for the next-generation powerplants. Such technologies could be an alternative solution to move towards the specific fuel consumption (SFC) reduction goals with improved overall powerplant efficiency.

1.4 Other noise reduction techniques

So far, other techniques to lower the noise levels have been investigated in the past decades. Among these concepts, nozzles with mixing enhancements such as the lobed mixers, chevrons and tabs have proven to be effective. Greatrex [12] was amongst the first who conducted experiments with full-scale devices known as corrugated/lobed mixer nozzles, which have been fitted to numerous jet engines powering many types of civil aircraft. The lobed mixer efficiently evens out the velocity and temperature differences of the core flow and the bypass flow, which reduces the exhaust velocity and hence the generated sound. Chevrons and tabs are both devices added to the nozzle geometry that protrude into the flow and thereby enhance the mixing of the hot core, fan and ambient air streams. Bridges and Brown [3] conducted a parametric study to relate various chevron geometric parameters, flow characteristics and far field noise. They found that chevron nozzles can reduce jet noise particularly at low-frequencies but that strongly depends on the number of chevrons and their depth of penetration into the jet. Xia et al. [28] performed

hybrid large-eddy type simulations for two chevron nozzle configurations. The radiated far-field sound is predicted using the Ffowcs Williams and Hawkings (FW-H) surface integral method. They studied the effect of chevron penetration into the jet. As a result, an increase in high-frequency sound but reduction in low-frequency sound was predicted, and good agreement with experimental data was obtained.

Other noise reduction techniques such as the offset stream nozzles [29], bevel nozzles [30, 31] have been investigated. In the offset nozzle method, the core nozzle is displaced away from the centre-axis towards the bypass nozzle thereby increasing the flow path on one side of the nozzle and reducing in the other side. Such an arrangement offered noise benefits in the flyover microphone position due to reduced turbulence levels due to increased shear layer widths. However, increased noise levels were observed in the sideline position due to increased turbulence levels. Papamoschou [32] proposed methods to tilt the bypass stream by means of fixed or variable vanes installed near the exit of the exhaust nozzle which could reduce the convective Mach number of turbulent eddies. Reduction in the peak sound pressure levels have been reported but with a thrust penalty. Papamoschou also suggested an eccentric nozzle configuration for supersonic coaxial stream nozzles [33]. This was not a feasible engineering solution due to possible losses and imbalances caused by the new flow path. An eccentric arrangement would require new nacelle structures and radial design of propulsion systems such as the thrust reverser.

In order to develop new quieter nozzle concepts with minimal efficiency penalties, better understanding of the source and propagation mechanisms are essential. To evaluate the performance of these concepts, reliable predictions methods to model the source mechanisms must be available. Various theories described in the previous section to solve for the aeroacoustics problems have been well-complimented by development in the field of Computational Aero-Acoustics (CAA) method which are coupled with CFD numerics (Computational Fluid Dynamics) to obtain noise predictions and in turn gain understanding of the noise generation mechanisms involved.

1.5 Computational jet noise prediction methods

Computational methods of calculating flow generated sound can be classified into direct computations and indirect or hybrid computations. Direct computation involves solving for the noise sources along with unsteady fluid dynamic source field represented by the compressible flow equations. Methods like the Direct Numerical Simulation (DNS) involve the computation of the acoustic near field by solving the full compressible Navier-Stokes equations. This comprises of resolving all flow scales, including the small dissipative scales. The acoustic pressure is computed directly, without the use of any analogy. This enables to evaluate the acoustic theories and in assessing the modelling assumptions used by the theories [34, 35, 36]. Despite the advantages, the extreme cost of the simulation and its limitation to low Reynolds number flow restricts it for academic purposes only.

A Large Eddy Simulation (LES) also solves the time dependent Navier-Stokes equations; however it takes the approach of filtering out scales below a cut-off parameter which considerably reduces the computational cost of a simulation. LES computations have been extensively carried out by Freund, Bailly, Bodony, Lele [37, 38, 39] and others [40, 41]. But this method involves generation of sophisticated grids and there are concerns on the limitation on spectral bandwidth of the calculation while retaining the computational cost [42]. For these reasons, LES method has not been considered as an engineering tool. However, LES results can be used to gain a better understanding of the flow physics and for generating databases for evaluating RANS-based prediction tools. For example, higher-order statistics important for the understanding of noise generation, such as two-point space-time correlations, can be evaluated.

On the other hand, RANS-based jet noise prediction methods have become attractive due to their simplicity and reduced computational costs. These methods involve the usage of mean turbulent flow information to statistically represent the source with a turbulence closure, such as the k-ϵ transport equations, to predict the radiated acoustic far-field. Ribner's work [43] on separating the two-point space-time correlation function forms the basis of many statistical jet noise models. A combination of such a model with a CFD mean-flow field has been used by Mani et al. [44], Bechara [45], Bailly [46, 47], Khavaran [48, 49, 50, 51], Frendi [52] etc. Some of these works assumed isotropic flow where the use of a single characteristic length-scale and time-scale is justified to describe the spatial and temporal decay rate of the velocity correlation, respectively. While some [49, 53] have investigated the effect of anisotropic turbulence on the far-field noise.

All RANS-based methods involve determining the length-scale and time-scale coefficients, which are obtained as a best-fit to the experimental data at the 90^o polar angle, and are kept constant for the other polar angles. These coefficients account for various inadequacies associated with RANS modelling, such as the unsteadiness, anisotropy, temperature effect, large-scale structures etc. Tam [54] in his RANS-based semi-empirical method suggests that these coefficients includes the contributions from the large-scale structures. However, all RANS-based prediction methods are dependent on experimental data at the 90^o polar angle to determine the length-scale and time-scale coefficients. This poses a problem when predictions from a new nozzle geometry are required prior conducting experiments. Such predictions, even though preliminary, could assist in nozzle design process in the industry and significantly reduce the cost of experiments.

1.6 Thesis contribution and supporting work

To address the future requirements in noise reduction, especially in jet mixing noise, a step change in design of nozzles is essential. To support the design activities, along with model testing, robust noise prediction tools can play a vital role. The aim of this thesis is to improve an engineering jet noise prediction tool to predict jet noise with

acceptable agreement compared with experimental data, from realistic nozzle geometries. The prediction method is named 'Lighthill Ray Tracing', and will be referred to as 'LRT' in the rest of the thesis. The LRT method is aimed to be capable of predicting noise from non-axisymmetric nozzles and support optimisation studies of conceptual nozzle configurations with relatively low computational cost.

The LRT method uses Lighthill's acoustic analogy to define the sources and ray theory (Geometric Acoustics) to compute propagation effects through the mean flow field. The mean flow and turbulence properties of the flow such as mean turbulent kinetic energy (k) and turbulence dissipation rate (ϵ) are informed by Reynolds Averaged Navier-Stokes (RANS) two-equation turbulence model, such as the standard k-ϵ or SST k-ω turbulence model. These turbulence models are the most widely-used engineering turbulence models for industrial applications and it is known to provide robust and reasonably accurate flow solutions. To examine the effect of turbulence models on far-field noise predictions, Deparu Mohan et al. [55] used various turbulence models such as RNG and realizable k-ϵ, standard k-ϵ and SST k-ω, and Reynolds stress models for mean flow computations. Noise predictions using the mean flow data from these turbulence models were in good agreement with measured data (from Bridges and Brown [3]). The effect of turbulence models on far-field noise predictions was found to be less than 0.5 dB. This shows that the far-field noise prediction is almost insensitive to the turbulence model.

The LRT source code is written in Fortran and it uses a Matlab shell for preprocessing and post-processing of the ray tracing routine. On a Windows desktop computer with 12GB RAM and 2.67GHz processor speed, the LRT method requires about 20 minutes to calculate the far-field noise from 200Hz to 10kHz narrow-band frequency at the 90^o polar angle. For angles other than 90^o the ray tracing routine has to be run to account for the refraction effects. For approximately 2500 source points for a coaxial nozzle with a centre-body, LRT takes up to 72 hours to compute noise for 10 polar angles from 200Hz to 10kHz narrow-band frequency. The computational speed of LRT is beneficial to provide noise predictions for novel nozzle configurations and hence to aid the development of low-noise nozzle designs.

The key contributions of the thesis are as follows:

1. From the review, it has been highlighted that all RANS-based jet noise prediction methods rely on experimental data to compute the length-scale and time-scale coefficients. In this thesis, a novel procedure to determine the LRT length-scale and time-scale coefficients, with reduced dependencies on experimental data for a family of nozzle conditions has been proposed. The procedure has been implemented in the existing LRT source model in the form of a Fortran 90 code. See Chapter 3.

2. Using the improved procedure to determine the LRT coefficients, a parametric study has been performed on coplanar nozzles to study the effect of varying area ratio, velocity ratio and anisotropy on far-field noise.

3. A parametric study has been performed to gain insight into the eddy aspect ratio and its effect on noise generation from different noise producing regions of isothermal single stream and coaxial jets for vary flow conditions.

4. The LRT method along with the semi-empirical ESDU method have been used to characterise ultra high bypass ratio (UHBR) nozzles to investigate the effect of bypass ratio, area ratio, core nozzle and velocity ratio for varying and constant thrust conditions. It has been shown that noise from nozzles with higher area ratios can be modelled using a single equivalent jet. See Chapter 5.

5. Two new methods of modelling the acoustic field within the CoS, without recourse to complex ray tracing (CRT) have been proposed. See Chapter 6.

    - The first method (Patch method), is based on modelling the exponential decay using an approximate WKB solution developed by Mani et al. [44]. The Patch method is applied to an isothermal single stream jet and the LRT predictions are validated against experimental data. This method has been implemented in the form of a Matlab code.
    - The second method is a continuation from the work of Stone et al. [56], on uniform solutions and complex ray solutions in the cone of silence (CoS). In the current work, a novel a method that exploits the novel symmetry feature of the uniform solution given by the Airy function and its derivatives to continue the field computations into the complex space inside the CoS is presented. As a result of this, new method is computationally less expensive compared to explicit Complex ray tracing method and could be extended to compute the field within the CoS for realistic jets (e.g., mean flows derived from CFD computations).

Some of the work in this thesis has been presented by the author at the 21st AIAA/CEAS Aeroacoustics conference, Dallas, 2015, and at the 23rd International Congress on Sound and Vibration (ICSV), Athens, 2016.

1.7 Outline of the thesis

The structure of this thesis is as follows: review of various RANS-based jet noise prediction methods is given in Chapter 2. The review includes the source and propagation modelling methods employed by various other researchers. A literature review of some of the nozzle parametric study carried out is also included. In Chapter 3, an overview of the LRT method is presented. The source and propagation model of the LRT method is described. Chapter 4 concerns the improvements and the application of the LRT method. It includes the problem definition and the proposed solution. Results of the parametric study of single stream jets and coplanar nozzles are presented. The improved methodology is used

to perform a parametric study on ultra high bypass ratio (UHBR) nozzles for varying nozzle parameters. The effect of increased bypass ratio on far-field noise is described in Chapter 5. Finally, the procedure to model the attenuation in the Cone-of-Silence for an isothermal single stream jets is presented in Chapter 6. Conclusions are given in Chapter 7.

Chapter 2

RANS-based jet noise prediction

In this Chapter, a review of various RANS-based jet noise prediction methods available in the literature are presented. The source and propagation modelling procedure used in some of the popular prediction methods based on acoustic analogies are described.

2.1 Introduction

The long history of jet noise prediction began with Lighthill as the first application of his acoustic analogy. The U^8 scaling law, along with the work of Lush [20], who showed the applicability of scaling jet data on the one-third octave spectra, led to the introduction of coaxial stream jets. Compared to single stream jets, coaxial stream nozzles consists of additional flow (bypass and core flow, temperature ratio) and geometric parameters (area ratio), further increases the complexity to the problem of jet noise prediction. Fisher et al. [57, 58] introduced a prediction scheme to predict noise from coplanar coaxial nozzles, popularly known as the 'Four source method'. The four source method was based on the observation by Ko and Kwan [59] that the complex flow structure of coaxial jets can be simply related and described by "equivalent" single stream jet flows. This method involves constructing noise generated by the four main shear layers of a coaxial jet using single stream jet data with characteristic jet diameter and velocity. Although this empirical method formed the basic for prediction methods used in the industry [1], are effective in predicting noise levels for conventional nozzle configurations only. Such a method cannot resolve between subtle changes to the nozzle geometry or the turbulent structure in the jet. Therefore, there is a need for prediction methods which are capable of capturing the change in far-field noise levels due to changes in the nozzle geometry.

In the previous chapter, key advantages of high-fidelity computational methods such as the DNS and LES have been discussed. Also described are the inherent disadvantages of these methods which restrict their use in the industry. Methods based on 'Reynolds Averaged Navier-Stokes' (RANS) CFD modelling of the jet have been quite successful in computing noise from convectional and complex nozzle geometries. This method involves a steady RANS calculation of the jet flow field. Turbulence is modelled by using a turbulence closure model such as the k-ϵ, k-ω model or similar. Some information about the turbulent

unsteady motion in the mixing regions of the jet can be obtained from the computed turbulence parameters such as the turbulent kinetic energy, k, and turbulence dissipation rate, 'ϵ', in the case of the k-ϵ model.

The mean-flow and turbulence information obtained from these two-equation turbulence models are however not accurate. For example, problems while modelling unheated, incompressible, axisymmetric jets using k-ϵ model have been reported by Birch et al. [60], Béchara et al. [45] and Tam et al. [54, 61]. Capturing the initial jet growth region remains a difficulty for all of these RANS models with the calculated jet mixing rates generally being much slower than that exhibited by experimental data. For example, Koch et al. [62], investigated subsonic axisymmetric separate flow jets with three flow solvers using two-equation k-ϵ turbulence models where the mixing rate in each of the calculations was slower than that indicated by experimental results [63]. As a result, standard k-ϵ turbulence models are known to over-predict the potential core length. Although several turbulence model corrections have been proposed and discussed in the literature, we have used the standard k-ϵ model as it is widely available and used in an industrial context. There have been recent efforts to improve the accuracy of two-equation models as applied to jet flows. Some of these turbulence model corrections have been proposed by Thies and Tam [61], Kenzakowki [64], Pope [65]. Along with these shortcomings, some more anomalies associated with k-ϵ models in conjunction with our source modelling procedure are discussed later in Chapter 3 and 4.

Besides the RANS modelling inconsistencies, the computation time involved in a RANS computation is relatively less compared to a DNS and LES calculation. This aspect could play a significant role in providing preliminary data such as acoustic spectra and noise directivities from nozzles based on new concepts or for re-designed in-service nozzles with shorter design-lead times. In the next section, a review of popular RANS-based jet noise prediction methods has been presented. This includes the procedure followed in modelling the sources and propagation through the mean-flow field.

2.2 RANS-based acoustic analogies

2.2.1 Adjoint based acoustic analogy

The mixing noise of high speed jets consists of two distinct self-similarity components [66, 67]. The first component radiates predominantly in the downstream direction by the large-scale structures which are characterised by their low-frequencies. The other is the high-frequency component radiated by the fine-scale structures, that has a relatively uniform directivity is dominant in the sideline and upstream direction. Tam and Auriault [54], developed a theory to predict noise generated by fine-scale structures in hot, single and coaxial jets based on a analogy with the kinetic theory of gases. The propagation model is based on linearised Euler equations (LEE). The acoustic far-field is expressed using an integral formulation on the Green's function of the problem. In the adjoint

problem, the observer is located inside the jet at $\mathbf{x}_S$, and the source is in the far-field, at $\mathbf{x}_0$: in the adjoint problem the source and the observer are inverted. Using the adjoint Green's function, the pressure field is given by,

$$p(\mathbf{x}_0,t)=\iiiint_{-\infty}^{+\infty}\left[\int_{-\infty}^{+\infty}p_a\left(\mathbf{x}_S,\mathbf{x}_0,\omega\right).e^{-i\omega(t-t_S)}\mathrm{d}\omega\right]\frac{Dq_S\left(\mathbf{x}_S,t_S\right)}{Dt_S}\mathrm{d}t_S\,\mathrm{d}\mathbf{x}_S, \tag{2.1}$$

where, p_a is the adjoint pressure and $^{\mathrm{D}}/_{\mathrm{D}t_S}$ is the convective derivative following the mean flow. The source term in the integral formulation has to be modelled. The spectral density of the radiated sound is expressed by,

$$\begin{aligned}S\left(\mathbf{x}_0,\omega\right)=\iint_{-\infty}^{+\infty}\cdots\iint p_a\left(\mathbf{x}_{S1},\mathbf{x}_0,\omega_1\right)p_a\left(\mathbf{x}_{S2},\mathbf{x}_0,\omega_2\right)\left\langle\frac{\mathrm{D}q_S\left(\mathbf{x}_{S1},t_1\right)}{\mathrm{D}t_1}\frac{\mathrm{D}q_S\left(\mathbf{x}_{S2},t_2\right)}{\mathrm{D}t_2}\right\rangle\\ \times\exp^{-i(\omega_1+\omega_2)t+i\omega_1t_1+i\omega_2t_2}\,\delta\left(\omega-\omega_2\right)\mathrm{d}\omega_1\mathrm{d}\omega_2\mathrm{d}t_1\mathrm{d}t_2\mathrm{d}\mathbf{x}_{S1}\mathrm{d}\mathbf{x}_{S2},\end{aligned} \tag{2.2}$$

where, q_s is the fine-scale turbulence intensity, $\mathbf{x}_{S1}$ and $\mathbf{x}_{S2}$ refers to two source positions, t_1 and t_2 are the two source time, and, ω_1 and ω_2 are frequencies. In equation 2.2, $\langle\rangle$ is the ensemble average, and it represents the noise source space-time correlation function. Tam and Auriault use measured two-point space-time correlation function of axial velocity components to define the model source correlation function. They propose the following model space-time correlation function characterised by three parameters to fit the measured function of Davies et al. [2],

$$\left\langle\frac{\mathrm{D}q_S\left(\mathbf{x}_{S1},t_1\right)}{\mathrm{D}t_1}\frac{\mathrm{D}q_S\left(\mathbf{x}_{S2},t_2\right)}{\mathrm{D}t_2}\right\rangle=\frac{\hat{q}_S^2}{c^2\tau_S^2}e^{-\frac{|\xi|}{\bar{u}\tau_s}-\frac{\ln 2}{l_s^2}\left[(\xi-\bar{u}\tau)^2+\eta^2+\zeta^2\right]}, \tag{2.3}$$

where, the space vector, $\xi=x_1-x_2$, $\eta=y_1-y_2$, $\zeta=z_1-z_2$ and $\tau=t_1-t_2$. This model function has three parameters: the characteristic size of the fine-scale turbulence l_s, the characteristic decay time τ_s, and the RMS value of the fluctuating kinetic energy of the fine-scale turbulence $\bar{q}_S^2$. From the model function, the spectral density of the radiated sound is written as,

$$S\left(\mathbf{x}_0,\omega\right)=4\pi\left(\frac{\pi}{\ln 2}\right)\iiiint_{-\infty}^{+\infty}|p_a\left(\mathbf{x}_S,\mathbf{x}_0,\omega\right)|^2T_S\left(\mathbf{x}_S,\mathbf{x}_0,\omega\right)\mathrm{d}\mathbf{x}_S, \tag{2.4}$$

with the source term $T_S\left(\mathbf{x}_S,\mathbf{x}_0,\omega\right)$, defined as,

$$T_S\left(\mathbf{x}_S,\mathbf{x}_0,\omega\right)=\frac{\hat{q}_S^2}{c^2\tau_S^2}\times\frac{e^{-\frac{\omega^2l_s^2}{\bar{u}^2(4\ln 2)}}}{1+\omega^2\tau_s^2\left(1-\frac{\bar{u}}{c_o}\cos\theta\right)^2}, \tag{2.5}$$

where, c_o is the ambient speed of sound and θ is the polar observer angle. The parameters, l_s, τ_s and $\hat{q}_S^2$ were obtained from a modified k-ϵ turbulence model based on the work of Thies and Tam and they define the contribution from the fine-scale structures. The modified k-ϵ

model was used to overcome the drawbacks associated with standard k-ϵ model.

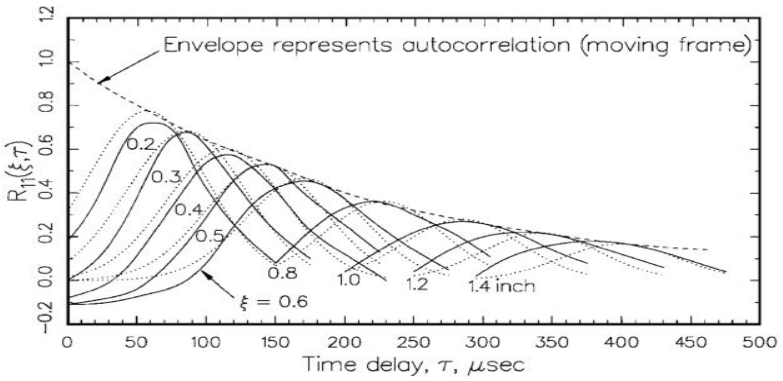

Figure 2.1 – Two-point space-time correlation of the axial velocity component in a jet: −, measured data [2], and ····, model function [54]

The k-ϵ turbulence model provides only two pieces of information about the turbulence of the jet flow. They are the averaged turbulence kinetic energy k, and the dissipation rate ϵ. But with k and ϵ known, it is possible to form a characteristic length scale l, and a decay time τ of the turbulence as follows:

$$l = \frac{k^{3/2}}{\epsilon}, \quad \tau = \frac{k}{\epsilon} \tag{2.6}$$

The parameters l and τ of equation (2.6) are directly relevant to the parameters l_s and τ_s of model two-point space-time correlation function (2.3). To establish their relationship, Tam et al. performed a k-ϵ model calculation for the jet flow of the Davies et al.[2] experiment. At the location of the measured correlation function shown in Figure (2.1), the value of l_s and τ_s obtained were used to match the correlation function (2.3) to the measurements. They believed that l_s and τ_s of their model function is directly related to l and τ of the k-ϵ model. Therefore, Tam et al. defined the model turbulence scales as follows,

$$l_s = C_l \frac{k^{3/2}}{\epsilon}, \quad \tau_s = C_\tau \frac{k}{\epsilon}, \quad \text{and,} \ \frac{\hat{q}_S^2}{c^2} = \frac{A^2}{q^2}, \ \text{with } q = \frac{2}{3}\bar{\rho}k, \tag{2.7}$$

where, A, C_l and C_τ are the model coefficients. These coefficients are determined on the basis of good-fit to the measured spectra.

2.2.2 Acoustic analogy based methods

Methods based on RANS CFD coupled with acoustic analogies have been widely prevalent as a design aid in the industry. The most popular and the earliest method was proposed by Mani, Gliebe and Balsa in the 1970's, called the MGB method [44, 68, 69]. This method uses RANS mean-flow information as an input to an acoustic analogy model based on Lighthill and Lilley's analogy to account for the flow-acoustic interaction. Khavaran improved the method by replacing the empirical basis of the flow prediction with a k-ϵ

turbulence model [48, 50]. This method is popularly referred to as the Mani-Gliebe-Balsa-Khavaran method (MGBK).

2.2.2.1 MGBK method

The governing equation describing the propagation as well as the source of sound in the MGBK method is Lilley's equation. This equation is linearised about a unidirectional transversely sheared base flow. The non-linear terms, second-order in turbulent fluctuations, are moved to the right-hand side of the equation and identified as the source. The sources considered in the following predictions are the so-called self- and shear-noise terms. Both sources are second-order in velocity fluctuations and are modelled using appropriate description of the statistical properties of turbulence.

This method considers only round jets, and replaces the actual jet velocity and temperature profiles by uniform or slug flow profiles for the purposes of estimating the acoustic field, and assumes that the quadrupole noise sources are convecting along the jet centreline. The method is similar to the work of Ribner [43], which deals with quadrupole corrections to Lighthill's acoustic analogy by modifying their directivity terms. Approximate mean-squared pressure from an eddy of isotropic turbulence was defined by Ribner as follows,

$$\overline{p^2}\left(\mathbf{x},\tau\right) \propto \int_y I_{1111}\left(\mathbf{y},\tau\right)\left(a_{xx}+4a_{xy}+2a_{yy}+2a_{yz}\right)\mathrm{d}\mathbf{y}, \tag{2.8}$$

where the directivity factors a_{xx}, a_{xy}, a_{yy} and a_{yz} are defined as,

$$\begin{aligned} a_{xx} &= \frac{\cos^4\theta}{\left(1-M_c\cos\theta\right)^4}, \\ a_{xy} &= \frac{g_s^2\cos^2\theta}{2\left(1-M_c\cos\theta\right)^2}, \\ a_{yy} &= \frac{3}{8}g_s^4, \\ a_{yz} &= \frac{1}{8}g_s^4. \end{aligned} \tag{2.9}$$

The directivity factors a_{xx}, a_{xy}, a_{yy} and a_{yz} describes the contribution to the noise field due to each of the quadrupoles contained within an eddy volume element. At the 90^o polar observer angle, their contribution to the noise field is insignificant.

The term g_s is the shielding function calculated at the source point. It is defined as follows,

$$g^2\left(r,\theta\right) = \frac{\left(1-M_s\,cos\theta\right)^2\left(c_s/c_o\right)^2 - cos^2\theta}{\left(1-M_c\,cos\theta\right)^2}, \tag{2.10}$$

where M_s and M_c are the source and convection Mach numbers respectively, c_s and c_o are the source and ambient sound speed, θ is the far-field observer angle.

Shielding function is used to locate the turning point in the flow. Along with quadrupole sources, the MGBK method also considers the effects of refraction on sound radiation from dipolar sources. Following the high frequency Green's function solution of Lilley's equation

and after few calculations (sequence of Fourier transforms and further simplifications), the solution to the Green's function for an acoustic field could be deduced as follows [70],

$$p_r + \left(k^2 g^2 \left(r; \sigma \right) - \frac{n^2 - 1/4}{r^2} \right) p_a = \frac{j}{k^2 \sqrt{2\pi}} \frac{c_s}{c_o^2} \frac{1}{\left(1 - N\sigma \right)^2} e^{jn\phi_s} \frac{\delta \left(r - r_s \right)}{\sqrt{r}} \tag{2.11}$$

From equations 2.10 and 2.11, relationship between source propagation and shielding characteristics of the mean-flow exists.

The dependence of behaviour of pressure p_a on the algebraic sign of g^2 is evident. The term p_a is oscillatory for $g^2 > 0$, and exponential for $g^2 < 0$. The location in the shear layer where g^2 changes sign is known as the 'turning point', r_σ (i.e., the radial location). When a negative region exists, fluid shielding of the source is possible and the amount of shielding depends on the proximity of the source with respect to the turning point as well as the number of turning points. In the current work, these shielding functions are used to determine the turning point for a source located in a shear layer. The location of the turning point is essential to determine the location in the flow where the mode splits into cut-on reflected part and a cut-off transmitted part [71]. At these turning points for the primary waves (also referred to as head waves, or refracted arrival rays) emanating from the source become parallel to the mixing layer, are used to locate a virtual source from which secondary waves (or rays) could be propagated into the far-field. A detailed description of this mechanism is presented in Chapter 6.

The MGB method has been used to predict noise from a wide variety of nozzle geometries and flow conditions. Several improvements to the MGB method were made by Khavaran. Due to the contributions from Khavaran, the MGB method was popularly known as the MGBK method. In the next section, some of the applications of the MGBK method are presented.

2.2.2.2 Applications of the MGBK method

The MGBK method uses a RANS two-equation solution, including mean flow-field and turbulence, to calculate the noise source strength, its spectral characteristics, and the propagation Green's function. The source strength was shown to scale as the 7/2 power of turbulence kinetic energy (TKE) [72]. Time- and length-scales of two-point correlation functions were calculated from the TKE and its dissipation rate. The Green's function governing the propagation of sound is a high-frequency asymptotic solution [73]. A detailed comparison of this solution with ray acoustics as well as exact Green's function was carried out by Wundrow and Khavaran for a parallel shear flow and showed that the solution remains accurate in the mid angle range (i.e., 60^o-120^o) and down to a Strouhal number of 0.5 [26].

The empirical based Reichardt's aerodynamic model in the MGBK method was replaced with a k-ϵ turbulence model to provide the mean-flow and turbulence information to calculate the source terms [48]. A separable two-point correlation was assumed and

the turbulence was considered isotropic. A Gaussian distribution for the time-delay of correlation was introduced. The effect of sound/flow interaction was incorporated using the high frequency asymptotic solution to Lilley's equation for axisymmetric geometries. This method was extended to compute noise from supersonic elliptic nozzles [74].

Engblom et al. [72] used the MGBK method to study the flow performance and far-field noise from single stream chevron nozzles. Reynolds Averaged Navier-Stokes (RANS) solutions, were produced via the WIND flow solver, which is a multi-block structured-grid finite volume solver that offers multi-physics flow simulation capabilities. The mean-flow from the WIND solver was used as an input to the MGBK code for prediction of far-field noise distributions. This methodology was applied to a set of chevron nozzle configurations involving varying degrees of chevron inward bend angle relative to the core flow, for both cold and hot exhaust conditions to evaluate the effect of chevron configurations on far-field noise. Direct comparisons with experimental data, including stagnation pressure and temperature rake data, PIV turbulent kinetic energy fields, and far-field noise computations were presented. Over-predictions up to 3dB was obtained at the peak and high frequencies for cold exhaust cases, under-prediction up to 4dB was observed for the hot exhaust cases at the 90^o polar angle for the round jet and various chevron configurations.

Hamed et al. used the method to solve for high bypass ratio (bypass ratio 5.2) coplanar axisymmetric nozzle with an internal plug [75]. Aerodynamic computations were performed using the PARC CFD code with a k-ϵ turbulence model. Khavaran and Krejsa improved the source model to investigate the role of anisotropic parameters from a splitter nozzle geometry [49]. The source model used by Khavaran forms the basis of the LRT source model. A detailed description of the LRT source model is presented in Section (3.3).

Frendi et al. used the MGBK method with a dual time-scale model to investigate mixing noise from axisymmetric and non-axisymmetric engine nozzles [76]. In their work, three different time scales proportional to $(\partial U/\partial n)^{-1}$, k/ϵ and k/Pr were tested. The term Pr is the production of the kinetic energy term and $(\partial U/\partial n)$ is a measure of the local strain rate in the jet. Later, Frendi et al. [52] applied this method together with an innovative jet engine noise measurement technique. The method involved using previously optimised model length-scale and time-scale empirical coefficients to adjust the predicted noise level in real time (i.e., during a test).

Khavaran et al. [51] investigated the effect of source compactness between the Gaussian and exponential model functions. This argument was used to improve the spectral fall-off at high frequencies in the MGBK prediction method. It was shown that a non-compact source with an exponential model function results in a broader spectrum and better agreement with data. Comparison with Tam and Auriault's fine-scale turbulence noise model were presented. Khavaran et al. [77] applied ray theory to study the propagation of high frequency jet noise using velocity profiles for a spreading jet. They investigated the factors influencing the cone-of-silence. They also suggested the application of ray theory to

compute noise directivities from non-axisymmetric jets. This method was extended to study refraction effects due to mean-flow gradients from 3D nozzle geometries [78]. The LRT method employs ray theory to compute the mean-flow propagation effects from 3D nozzle geometries. Solutions are proposed in Chapter (**??**) to model the attenuation in the cone-of-silence from single stream nozzles for varying Mach numbers.

2.2.2.3 Contributions from Morris et al.

Morris and Farrasat [79], developed a model based on Lighthill's acoustic analogy. The noise sources are modelled using the turbulence statistics from a k-ϵ turbulence model. The method was applied to an isothermal single stream jet operating at a jet Mach number of 0.9. They compared Tam's method with acoustic analogy and showed that, at 90^o to the jet axis, both the methods are similar if the statistical description of the turbulent noise sources were the same. The predictions obtained from this model were in good agreement with the measured data at the low and peak frequencies at the 90^o polar angle. However, under-predictions for polar angles, $\theta \leq 60^o$ were obtained due to the refraction effects in the cone-of-silence. From the comparison study it was shown that Tam's model is computationally expensive compared to Morris and Farrasat's model.

Morris and Boluriaan [80] presented a theory for the prediction of jet noise based on data from a RANS two-equation turbulence model. The noise model was based on an acoustic analogy based on linearised Euler equations. The mean flow acoustic interaction effects were based on high and low frequency solutions to Lilley's equation as well as linearised Euler equations. Comparisons were made between predictions and measurements for a high subsonic (Mach no., M_j=0.9) unheated jet. Reasonable predictions within $\pm$2dB at low and peak frequencies were obtained at polar angles greater than 55^o. At high frequencies (at 40kHz), an under-prediction up to 4dB difference with experimental data at all observer angles was reported. The reason for the under-prediction at the high frequencies were owed due to the modelling of the source statistics. They suggested the use of a Gaussian form of source autocorrelation function and incorporating a frequency dependent model for length scales. In the LRT method, the turbulence length scales and time scales are modelled using Gaussian formulations. The LRT time scale is modelled using an expression which addresses the frequency dependence characteristics of turbulent flows.

Raizada and Morris [81], used a RANS based two-equation k-ϵ turbulence model to estimate the mean flow. The source model was based on the high and low frequency asymptotic solutions to the Lilley's equation. The acoustic analogy used for the noise prediction was based on the linearised Euler equations, so the Green's function to Lilley's equation was transformed to obtain the Green's functions to the linearised Euler equations. This transformation was performed numerically for the adjoint solutions and analytically for the asymptotic solutions. Comparisons of predictions obtained using the high and low frequency solutions, and the adjoint solution for the Green's function to Lilley's equations

against the experimental data for an unheated single stream jet (Mach no. = 0.9) were presented. It was shown that the high and low frequency solution agree well with the experiments at large polar angles but fails at polar angles closer to the jet axis. As noted by Thies & Tam [61], the reason for the under-prediction at high frequencies could be due to the locally parallel assumption used in making approximations of the Green's function to Lilley's equation. For a truly parallel flow the sound radiation would propagate over a longer distance in a higher speed mean flow before radiating to the far-field than it would in a real spreading mean flow. This is likely to be more of an issue for high frequency radiation as it suffers the greatest propagation decay.

Jet noise prediction methods which are based on acoustic analogies and RANS data prediction methods have been successful in computing noise from convectional and complex nozzle geometries such as nozzles with chevrons. Some of the popular semi-empirical methods such as the MGBK has been reported to have issues when applied to complex nozzle geometries. The MGBK fails at angles close to the jet axis and does not capture the effect of geometry change. Propagation methods which solves the adjoint formulation of the linearised Euler equations uses a finite difference method (FDM) or a finite element method (FEM). Using numerical methods such as the FEM and FDM increases the computational cost of the overall prediction method as these methods require a finer and structured mesh compared to the RANS mesh [82]. Therefore, there is a need for a computationally fast and robust jet noise prediction method which is capable of computing noise from complex nozzle geometries.

2.2.2.4 Development of the LRT method

In this section, the development of a computational aeroacoustics prediction tool based on the application of Lighthill's theory being developed at the ISVR, University of Southampton, is described. The method is called 'Lighthill Ray Tracing', and will be referred as LRT in the rest of the thesis. The main goal of the LRT method is to assist novel nozzle designs with lower computational costs.

The LRT source model is based on Lighthill's acoustic analogy and uses geometric acoustics to model the propagation. Self [83] proposed a noise prediction model based on Lighthill's acoustic analogy with an improved description of the relevant turbulence statistics based on empirical evidence by Harper-Bourne [84]. The main improvement was the consideration of frequency dependence of length-scale and time-scale used in the two-point correlation function in the source model. Self and Bassetti [85] applied this feature to isothermal single stream jets coupled with flow-factors derived from Lilley's equation to calculate the directives. Page et al. [86] extended this method to predict noise from coplanar nozzle with varying area ratios and also to serrated nozzle geometries.

Azarpeyvand and Self [87, 88] continued the work of addressing the frequency dependence by introducing a time-scale based on the energy transfer in the turbulence cascade. The new time-scale was referred to as the TET time-scale. They investigated the effect

of the TET time-scale on far-field noise from heated jets by applying it to the MGBK method. The TET time-scale was applied to a a range of nozzle geometries and flow conditions and the predictions were compared with the experimental data.

Il*á*rio [89, 90] coupled the TET time-scale with Khavaran's source definitions [49] to calculate far-field noise from single stream and coaxial stream nozzles. Ray theory was used to compute the mean-flow propagation effects in the far-field. Both the source and propagation models used the flow information from a RANS calculation with a standard k-ϵ turbulence model. By adopting the ray tracing method to compute the refraction effects a high-frequency approximation was implied, while no assumption about the mean flow was needed, which enabled the application of the method to jet noise problems with inherently three-dimensional propagation effects.

To model the source cross-correlations, the LRT method assumes that the turbulence is isotropic and locally homogeneous. This assumption is valid in regions of the jet where the turbulence kinetic energy is high (e.g. nozzle lipline) and as per the acoustic analogy, the sources are located in this region. However, it is known that such assumption is not broadly real for jet flows. The importance of the jet flow anisotropy and its effects on radiated noise have been emphasized by many authors [49, 91, 92]. The impact of anisotropy on jet noise predictions has been largely neglected by most engineering models. Lilley [93] pointed out that the assumption of isotropic turbulence neglects important anisotropic effects such as vorticity stretching. It also neglects the effects of the marked reduction in the lateral integral scale of the turbulence pointed out by Townsend [94]. According to Ribner [43] the non-isotropic structure of turbulence can have an important effect on the directivity pattern of the narrow-band noise at sufficiently low frequencies. These local variations in the flow field, which are translated to anisotropy effects, are extremely difficult to investigate experimentally and only few sets of incomplete data are available. Therefore, it is important at least to consider the effect of anisotropy within the jet noise modelling framework. In the LRT method, the source definitions proposed by Khavaran and Krejsa [49] allow the modelling of anisotropic parameters.

The temporal and the spatial correlation functions are assumed to take a Gaussian distribution. A detailed description of the LRT source and propagation model is presented in the next chapter. The LRT length-scale and time-scale are calculated using the parameters obtained from the RANS solution. Like the other RANS-acoustic analogy based jet noise prediction methods [44, 49, 54, 79], the LRT method too requires the calculation of LRT time-scale and length-scale coefficients which relies upon the availability of the experimental data. This imposes a dependence on measured acoustic data thus rendering the application of RANS-based methods to make rapid calculation of noise from conceptual nozzles difficult. In the current thesis, this limitation of dependence of the LRT coefficients on experimental data is addressed.

The LRT method uses the ray tracing method to calculate the propagation effects. Il*á*rio et al. [90] claimed that it the first time that a method which couples ray tracing with

a source model based on Lighthill's acoustic analogy has been proposed. The predictions from the LRT method were compared with experimental data for isothermal and hot jets with acoustic Mach number ranging from 0.5 to 1.0. Predictions showed good agreement with the measured data for polar angles between 60^o and 110^o. For angles closer to the jet axis, the ray theory fails due to a phenomena called the Cone of Silence (CoS). It is essential to obtain good predictions at all observer angles, especially at the angles closer to the jet axis to calculate the Effective Perceived Noise Levels (EPNL). The background theory and methods to compute noise in the CoS is presented in Chapter 6. In this thesis, further developments of the LRT method are presented in Chapters 4, 5 and 6. A summary of the improvements are presented in Section (2.3). Before discussing the improvements, the theory and procedure used in the LRT method is presented in the next chapter.

2.3 Thesis Contribution

In the current thesis, some of the limitations in the RANS-based jet noise prediction methods which were discussed so far will be addressed.

Improved procedure to determine the LRT coefficients

From the literature review, it is clear that all RANS-based prediction methods rely on experimental data to compute the length-scale and time-scale coefficients. Most of these methods assume isotropic turbulence which is not physical. In this thesis, a simple procedure to determine these coefficients with reduced dependencies on measured spectra has been proposed. RANS CFD solutions do not have the ability to provide anisotropic information. The mean-flow data cannot be used to model the variation of length-scales and time-scales in the radial and azimuthal direction. Availability of experimentally determined anisotropic parameters are scarce. Therefore, the advantage of the modelling flexibility available within the LRT method has been made use to model and study the effect of anisotropy for varying the jet parameters.

Parametric study of UHBR nozzles using the LRT method

In this chapter, a characterisation study of coaxial jet noise from ultra high bypass ratio (UHBR) nozzles for varying velocity ratio, area ratio, flight velocity and bypass ratio using both the LRT method and the semi-empirical ESDU method are presented. The parametric study of the noise from UHBR nozzles has been carried out to assess the importance of the noise generated by the primary and secondary shear layers and their directivities under different operating conditions. The LRT and ESDU predictions are validated against experimental data. From the parametric study, the effect of the core nozzle and the variation of anisotropy parameters for UHBR nozzles are investigated.

Preliminary cone of silence prediction method

Jet noise prediction method coupled with ray theory suffers attenuation at polar angles close to the jet axis due to the cone of silence effect. Experiments show increased levels of sound intensity at these shallow angles, and that they contribute towards the effective perceived noise levels (EPNL). Hence, predicting noise in the cone of silence is important. Obtaining ray solutions for stratified flows are computationally difficult as the wave-number in the cone of silence migrates to the complex plane. Instead of computing ray solutions in the complex plane, two methods are presented to model the attenuation in the CoS. The first method is based on modelling the exponential decay using an approximate WKB solution for a parallel shear flow; the second exploits the canonical nature of the cone of silence boundary to continue solutions inside the CoS via a complex ray embedded inside the Airy function and its derivative. To demonstrate both methods, the results are compared against Lilley's Green's function solution for a parallel shear flow using a variety of parametric studies. The MGB solution is applied to an isothermal single stream jet and the noise predictions at the CoS angles are compared with experimental data.

2.4 Chapter summary

- Developments in the field of CFD-CAA coupled methods have made remarkable progress in the past decade. RANS-based prediction methods have the potential to provide assistance in the preliminary nozzle design phase.

- Acoustic analogies proposed by Lighthill and Lilley have been optimally used by exploiting its strengths and weakness. Source definitions based on Lighthill's analogy are coupled with ray theory to compute far field directivities, thus accounting for the flow-acoustics interaction. This routine is relatively faster compared to propagation models used by Tam and Auriault. This is also useful in assessing the amplification/attenuation characteristics of the source based on its location in the jet.

- All RANS-based methods described so far, use length-scale and time-scale coefficients which are determined on the basis of best fit to the measured acoustic spectra at the 90^{o} polar angle. This imposes a constant need for experiments, which is expensive and time consuming. Thus there is a need for a procedure to determine the coefficients with limited dependencies on experimental data.

- All prediction methods, except Khavaran [49], assumed isotropic turbulence. It has been shown by experiments that jet turbulence is anisotropic [95, 96]. Khavaran uses axisymmetric turbulence model and highlighted the role of anisotropic parameters in noise generation. It was demonstrated that anisotropic parameters can vary the amplitude of the sound pressure level.

Chapter 3

LRT source and propagation model

In this current chapter, a hybrid CAA method, named LRT, capable of predicting jet mixing noise using the Reynolds Averaged Navier-Stokes mean flow data is described. The chapter includes the theory behind the source and propagation modelling used in the LRT method. The noise sources are defined based on Lighthill's formalism and a ray tracing technique is used to determine the mean flow propagation effects.

3.1 Background

Lighthill's acoustic analogy has been, convincingly, the dominant jet noise theory. Although, over the years, Lighthill's analogy has influenced many variants of the basic theory; e.g. Proudman [97], Lilley [22], Goldstein [27], to name just a few, the source terms of these theories are not the same. However, there is a universal agreement that jet mixing noise is generated by the turbulence of the jet flow. Brown & Roshko [98] were the first to report the observation of large coherent structures in turbulent jets and free shear layers. This was in addition to classical small-scale turbulence. Since their work, there has been an abundance of papers in the literature devoted to the measurement, study, analysis and numerical simulation of these structures (see Tam [99] and Viswanathan [67]).

Figure (3.1) presents a schematic of a jet flow with two main scales of turbulence generated noise. However, turbulence motions have a number of scales associated with them. In the turbulence cascade, energy enters through a mechanism at the largest scale and is transferred by a cascade process to smaller scales; at the smallest scale it is dissipated. Large scales break up into smaller ones and this happens on a characteristic time scale. With the smallest eddies, viscosity dominates and the energy dissipates as heat. Moving further through the cascade, the length scale associated with eddies increases and it is useful to identify different regions. The largest scales are produced by transferring energy from the mean flow and are produced at a length scale characteristic of the macroscopic problem. The largest eddies form what is known as the energy containing region and, as the name suggests, they contain the bulk of the turbulent energy. The energy containing range is bounded below by length l_E where the inertial subrange begins. As the length scale decreases the viscous forces become more important and at l_D the inertial subrange

gives way to the dissipation range where viscosity dominates and the energy is dissipated [87].

Each of the two different processes, production of turbulent energy and dissipation of turbulent energy can be associated with a region of the turbulent jet where they are the dominant physical process [52, 76]. This is illustrated schematically in Figure (3.2) (although it should be borne in mind that in reality both two physical processes are present everywhere in the jet flow). It has been shown that the inertial subrange plays a central role in the noise production mechanism [100, 101], and the energy transfer, or the so-called cascade process, is the most important feature of the inertial subrange. The inertial subrange transfers turbulent energy from the energetic region (energy-containing range), to the dissipation subrange (low-energy).

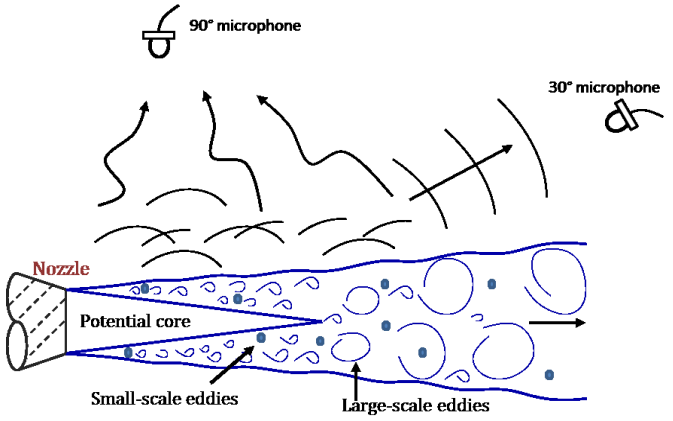

Figure 3.1 – Schematic diagram showing the key turbulence structures of a jet and noise radiation to the sideline and the downstream directions [99].

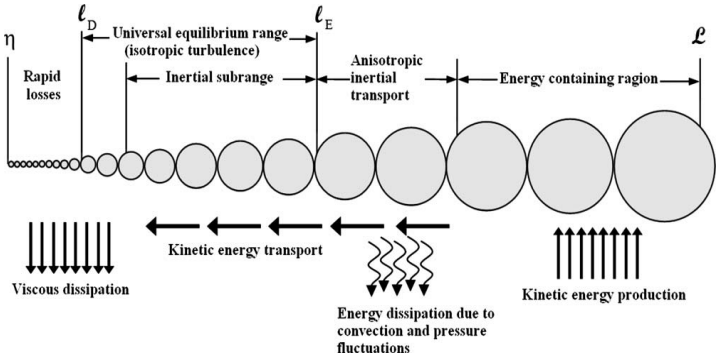

Figure 3.2 – A schematic diagram of the energy cascade and eddy sizes, showing the various length-scales and the ranges [87].

3.2 Turbulence and Noise Generation

There is a universal agreement that jet mixing noise is generated by the turbulence of the jet flow. To estimate the amount of noise generated by turbulent flows, definite information is required concerning the characteristics of turbulent flows. Before the nineteen seventies,

jet turbulence was conceived as consisting of numerous small eddies distributed throughout the jet as shown in Figure (3.3). Figure (3.3) is a spark schlieren photograph of a Mach 1.4 jet taken by Thurow et al. [102]. Crow and Champagne [103] and Brown & Roshko [98] were amongst the first to report the observation of large coherent structures in turbulent jets and free shear layers. This was in addition to classical small-scale turbulence. Since their work, there have been an abundance of papers in the literature devoted to the measurement, study, analysis and numerical simulation of these structures [99].

Figure 3.3 – Spark schlieren photograph of a Mach 1.4 jet [99].

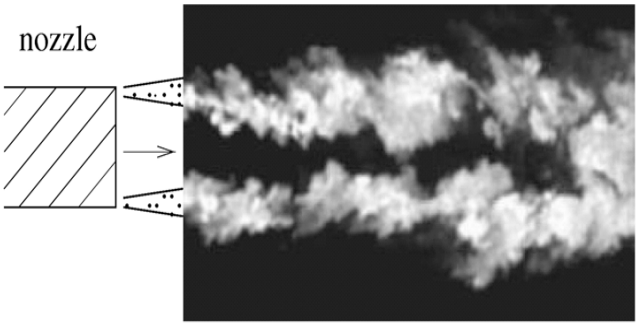

Figure 3.4 – Pulsed laser picture of the large turbulence structures in the mixing layer of a Mach 1.3 jet taken by Thurow et al. [102].

In the model shown in Figure (3.1) (as proposed by Tam and Auriault [99, 104]), the two noise sources are the fine-scale turbulence and the large turbulence structures of the jet flow. Fine-scale turbulence is distributed throughout the mixing layer of the jet. According to Tam and Auriault [104], fine-scale turbulence exerts an effective turbulence pressure on its surroundings. The intensity of the turbulence pressure is equal to 2/3 of the turbulence kinetic energy. Noise is generated when there are fluctuations in the turbulence pressure arising from fluctuations in turbulence kinetic energy. However, because the fine-scale turbulence is being transported downstream by the mean flow, this convection effect leads to a slight preference to downstream noise propagation. In addition, the radiated sound from a volume of fine-scale turbulence has to traverse the shear layer of the jet to reach the far-field. Therefore, the radiated sound will undergo refraction due to velocity

and density gradients in the jet mixing layer. Hence, one would expect the noise from the fine-scale turbulence of the jet to be nearly omni-directional. It is slightly stronger in the downstream direction except in the cone of relative silence (see Atvars et al. [105] for an experimental demonstration of the existence of a cone of silence). The cone of relative silence is created due to the bending of acoustic waves away from the jet flow direction by refraction [99]. This effect is especially strong for high-speed hot jets. More about the cone of silence is discussed in Chapter (6).

Figure (3.4) shows a pulsed laser image of the large turbulence structures in the mixing layer of a Mach 1.3 jet taken by Thurow et al. [102]. This picture is typical of most optical observations of large turbulence structures in a turbulent jet flow. These structures are generated near the nozzle exit. They grow quickly as they are convected or propagated downstream. They are coherent over distances comparable to and often longer than the jet diameter in the axial direction. Optical observations such as that shown in Figure (3.4) indicate that the large turbulence structures are the dominant dynamical entities in the mixing layer of a jet in the region starting from the nozzle exit extending to some distance downstream of the end of the potential core. In these mixing layers, especially where the shear layer is thinner (usually between the nozzle tip and end of the potential core), most of the high frequency noise sources are located.

It is important to recognise that the most turbulent and dynamically most energetic region of a jet lies in the first two potential core lengths of the jet. Within this region, there is a distinct separation of turbulence scales. The principal scales are those of the small turbulent eddies with dimensions much smaller than the jet diameter and the large turbulence structures with dimensions longer than or comparable to the jet diameter [99]. Further downstream of the potential core, the large turbulence structures decay through merging and cascading to smaller and smaller scale turbulence. The low frequency sources are associated with larger eddies which are mostly formed in the fully developed region and close to the jet axis. One of the earliest works on this subject was published by Ribner [91] in 1958. This work was very short and it's most important result was that the overwhelming bulk of the jet noise is emitted from first eight to ten diameters, which is regarded as the mixing region. It was found that the sound power distribution in the mixing region is constant, while it is proportional to the reciprocal seventh power of axial distance for the fully developed region [87].

In a series of two-point space-time correlation experiments, Panda et al. [106, 107] used a technique based on Rayleigh scattering to measure the turbulent velocity and density fluctuations in a very localized volume (almost point-like measurements) inside a jet. They correlated this signal with the acoustic pressure measured by a far-field microphone to determine the source of noise. They found significant normalised correlations for point-like measurements at the end of the potential core of the jet and far field microphone at 30^{o} to the jet axis. A good fraction of the noise received by the far-field microphone at shallow angles to the jet comes from the large coherent source. The experimental results of

Panda et al. are consistent with the earlier observations of Hurdle, Meecham and Hodder [108] and Shaffar [109]. Similar conclusions were obtained by Bogey and Bailly [110] using numerical simulation data computed by LES methodology. The pressure signal, measured by a far field microphone at, say, 90°, however, comes from the numerous volumes of turbulence of the entire jet (see Figure (3.1)).

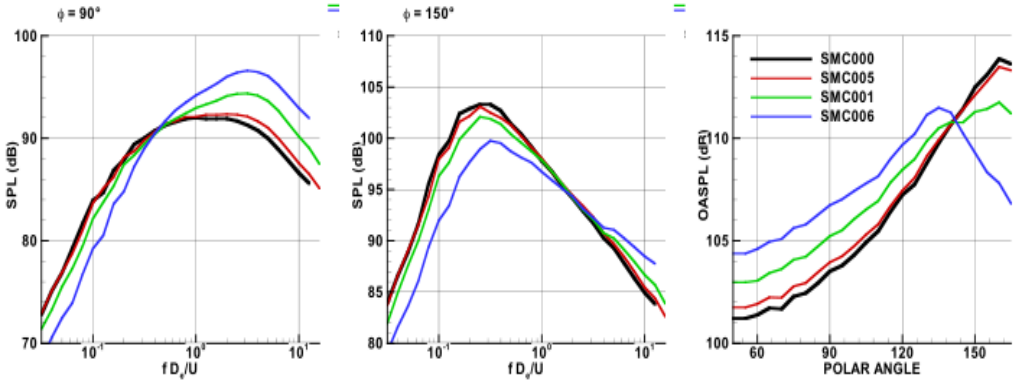

Figure 3.5 – Comparison of acoustic data for 6-chevon nozzles with different penetration lengths with a baseline round jet (SMC000) [3].

To adhere to the demanding noise regulations, noise suppressor devices such as tabs and chevrons were introduced. Bridges et al. have conducted numerous experimental and numerical simulations of the flow and far-field acoustics of various noise suppressor devices such as the chevrons. Figure (3.5) shows the spectra and the OASPL for single streams nozzles for 6-chevron nozzles with different penetrations [3]. Chevron nozzles have been shown to exhibit a reduction in low frequency noise at the cost of an increase in high frequency noise due to enhanced mixing. The predictions are also compared with a baseline round jet. Studies show that chevron nozzles produce asymmetric flows. Many of the current methods are limited to assumptions of symmetry or through computational demand. Therefore, an accurate and robust solver is required that can be used in the design of more efficient noise-suppression devices.

The current day aeroengine nozzles are predominantly coaxial flows, where a large cold flow bypasses the engine core that mixes with a hot core flow in the jet exhaust, giving rise to jet mixing noise. These engine nozzles have higher bypass ratios which slow the jet velocity and reduce the turbulence intensity, and thereby the noise emissions. More about noise from high bypass ratio nozzles will be discussed later.

For nozzles with noise suppressor devices the main idea is to break the large energy bearing eddies to fine scale structures which in turn increases the high frequency noise in the far field. Moreover, the flow from a modern high bypass ratio nozzles are issued at higher Mach numbers. For such flows with high Mach numbers, the speed of sound is of the same order as the characteristic velocity, so the acoustic wavelengths of the small-scale disturbances would also be small compared to the shear-layer thickness. Therefore, high frequency approximations can be used to simplify the governing equations. It is

thus possible that geometric acoustics, and the related ray theory, could be a reasonable approximation for studying sound propagation in a compressible shear layer, at least for obtaining qualitative trends. The approximation improves as the acoustic wavelength becomes much smaller than the shear-layer thickness. Hence, it is justifiable to employ ray theory to model the propagation from high speed jets.

In the next section, theory behind the source and propagation modelling used in the LRT method is described. It is followed by the procedure to calculate far-field noise using the LRT method.

3.3 Source Modelling

A Reynolds averaged Navier-Stokes solution with a Standard k-ϵ turbulence model has been used to obtain the mean flow and statistical representation of the turbulence in the form of turbulent kinetic energy and a local length scale. These mean flow quantities are used to model the fourth-order auto-correlation function, which is a function of the turbulence time-scale and length-scale. There are various methods proposed in the literature to model these turbulence parameters. Starting from the simple isotropic turbulence modelling approach proposed by Ribner [43], better models based on axisymmetric turbulence and anisotropic models will be discussed.
Following Ribner [43], the acoustic field generated by a round jet can be expressed in a simplified form as,

$$\overline{p^2}(\mathbf{R},\theta) = A\, I_{ijkl}\ \mathrm{dir}(ijkl), \tag{3.1}$$

where,

$$A = \frac{\rho_o}{16\pi^2 c_o^5 R^2 (1 - M_c\cos\theta)^5}, \tag{3.2}$$

ρ_0 is the ambient air density, c_o the speed of sound, and $(1 - M_c\cos\theta)$ the convective amplification factor.

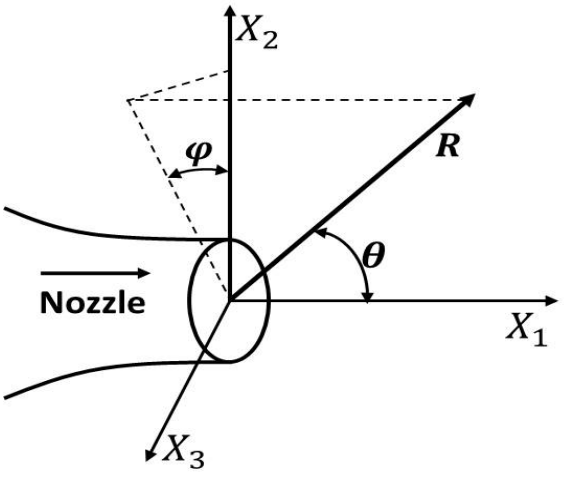

Figure 3.6 – Co-ordinate system used within the LRT method

The fourth-order autocorrelation function for a unit volume of turbulence is given by,

$$I_{ijkl}(\tau) = \int \frac{\partial^4}{\partial \tau^4} \overline{u_i u_j u'_k u'_l}\, d^3\mathbf{r}, \tag{3.3}$$

where $\overline{u_i u_j}$ is the velocity correlation between two points in an eddy, and the source polar directivity patterns can be calculated by

$$dir(ijkl) = \frac{1}{2\pi} \int_0^{2\pi} \left(\frac{x_i x_j x_k x_l}{x^4} \right) d\varphi. \tag{3.4}$$

From Figure (3.6), we can write the following mathematical relations:

$$x_1 = R\,\cos\theta$$

$$x_2 = R\,\cos\varphi\,\sin\theta$$

$$x_3 = R\,\sin\theta\,\sin\varphi$$

Of the 36 possible quadrupole correlations only 9 yield distinct non-zero contributions. The components of the velocity correlation tensor which contribute to the sound field are:

$$\mathrm{dir}(1111) = \cos^4\theta,$$

$$\mathrm{dir}(1212) = \mathrm{dir}(1122) = \mathrm{dir}(1313) = \mathrm{dir}1133 = \frac{1}{2}\cos^2\theta \sin^2\theta,$$

$$\begin{aligned} \mathrm{dir}(2222) = \mathrm{dir}(3333) &= \frac{3}{8}\sin^4\theta, \\ \mathrm{dir}(2323) = \mathrm{dir}(2233) &= \frac{1}{8}\sin^4\theta. \end{aligned} \tag{3.5}$$

Following the acoustic analogies, the sound power radiated from a jet consisting of randomly distributed, compact, convected acoustic sources can be related to the fourth order, space-time velocity correlation tensor. By means of a Reynolds decomposition of the velocity field, it has been shown to comprise of second, third and fourth order terms. The third order terms are generally neglected as they integrate to zero when homogenous, isotropic turbulence is assumed. With an assumption of quasi-normal joint probability (Gaussian probability) of turbulence statistics, the fourth order can be expressed in terms of the second order velocity correlation tensor. This assumption has been experimentally justified by Seiner et al. [111], and numerically by Freund [112] using DNS.

From the fourth-order space-time correlation, and assuming that it can be expressed in second order correlation as, [49],

$$\overline{u_i u_j u'_k u'_l} = \overline{(u_i u_j)(u'_k u'_l)} + \overline{(u_i u'_k)}\,\overline{(u_j u'_l)} + \overline{(u_i u'_l)}\,\overline{(u_j u'_k)}. \tag{3.6}$$

Substituting equation (3.6) in equation (3.3), we obtain

$$I_{ijkl}(\tau) = \frac{\partial^4}{\partial\tau^4} \int [\overline{(u_i u_j)}\,\overline{(u'_k u'_l)} + \overline{(u_i u'_k)}\,\overline{(u_j u'_l)} + \overline{(u_i u'_l)}\,\overline{(u_j u'_k)}]\, d^3\mathbf{r}. \tag{3.7}$$

The Fourier transform of the autocorrelation function gives the noise spectra for a source of frequency, Ω

$$I_{ijkl}(\Omega) = \frac{1}{2\pi} \int_{-\infty}^{\infty} I_{ijkl}(\tau)\, e^{i\Omega\tau}\, d\tau. \tag{3.8}$$

3.3.1 Isotropic Turbulence

Here the turbulence is assumed to be homogenous and isotropic. For convenience, separate space and time correlation is assumed for the integration of equation (3.7) and (3.8) as suggested by Ribner [43], and the two point velocity correlation is expressed as;

$$\overline{u_i u'_j} = \Psi_{ij}(\boldsymbol{\xi}) g(\tau), \tag{3.9}$$

where $\overline{u_i u'_j}$ is the velocity correlation between two points $\mathbf{y}$ and $\mathbf{y}'$ separated by a vector $\boldsymbol{\xi}$, i.e., $\boldsymbol{\xi} = \mathbf{y} - \mathbf{y}'$, and a time delay τ.
For homogenous isotropic turbulence, the spatial term Ψ_{ij} can be expressed as (after Batchelor [92] and Khavaran [49])

$$\Psi_{ij}(\boldsymbol{\xi}) = k[(f + 1/2\,\xi\, f')\,\delta_{ij} - 1/2\, f'\,\xi_i \xi_j/\xi], \tag{3.10}$$

where, the local turbulent kinetic energy term, $k = \frac{1}{2}(\overline{u_1^2} + \overline{u_2^2} + \overline{u_3^2})$, and u_1, $u_{2,3}$ are the stream-wise and span-wise turbulent velocities respectively, and $f' = \partial f/\partial\xi$, where f is a function of the separation vector ξ. The three components of the separation vector are represented as ξ_i for $i = 1, 2, 3$. Function $f(\xi)$ is assumed to be Gaussian and may be expressed as $f(\xi) = \exp(-\pi\xi^2/L_1^2)$, where L_1 is the longitudinal integral length scale in the axial direction. For the longitudinal correlation term, substitution of equation (3.9) and equation (3.10) in equation (3.7) gives various correlation coefficients,

$$\begin{aligned}
I_{1111}(\tau) &= \rho^2 \frac{\partial^4}{\partial\tau^4} g^2(\tau) \frac{(\overline{u_1^2})^2\, L^3}{2\sqrt{2}}, \\
I_{2222} &= I_{3333} = I_{1111}, \\
I_{1122} &= I_{1133} = I_{2233} = \frac{1}{8}\, I_{1111}, \\
I_{1212} &= I_{1313} = I_{2323} = \frac{7}{16}\, I_{1111}.
\end{aligned} \tag{3.11}$$

These relations hold with either Gaussian or exponential spatial functions and apply to compact as well as non-compact source models [51].

3.3.2 Axisymmetric Turbulence

The isotropic turbulence model is based on decaying isotropic turbulence which neglects the anisotropic effects such as vortex stretching, and also neglects the reduction in the lateral length scales of turbulence [92]. These effects can have an influence on the directivity pattern of low frequency noise. Therefore, an axisymmetric turbulence model would be a better approximation compared to an isotropic model. The theory of axisymmetric turbulence was first proposed by Batchelor [113], and was developed by Chandrasekar [114]. According to Chandrasekar, the concept of axisymmetry which will require the mean value of any function of the velocities and their derivatives to be invariant, not for the full rotation group, but only for rotations about the preferred direction, $\boldsymbol{\lambda}$ (say), and for reflections in planes containing $\boldsymbol{\lambda}$ and perpendicular to $\boldsymbol{\lambda}$.

For an axisymmetric turbulence, the span-wise velocity components can be related as

$$\overline{u_2^2} = \overline{u_3^2}. \tag{3.12}$$

Let $\beta = (1 - \overline{u_2^2}/\overline{u_1^2})$ and then the turbulence kinetic energy can be expressed as,

$$k = \frac{1}{2}(\overline{u_1^2} + \overline{u_2^2} + \overline{u_3^2}) = \frac{3}{2}\,\overline{u_1^2}(1 - \frac{2}{3}\beta). \tag{3.13}$$

The two-point velocity correlations are given as [114, 49],

$$\overline{u_i u_j'} = \epsilon_{jlm}\frac{\partial q_{im}}{\partial \xi_l}, \tag{3.14}$$

where the axisymmetric skew tensor q_{im} is

$$q_{im} = Q_1\epsilon_{imk}\xi k + (Q_2\lambda_m + Q_3\xi_m)\xi_{jlk}\lambda_l\xi_k, \tag{3.15}$$

and scalar functions Q_1, Q_2 and Q_3 are functions of $|\boldsymbol{\xi}|$, ξ_1, τ and source location $\mathbf{y}$. The unit vector $\boldsymbol{\lambda}$ is in the direction of turbulence symmetry and ϵ_{jlm} is the alternating tensor. With $\boldsymbol{\lambda} = (1, 0, 0)$, equation (3.15) can be written as

$$q_{im} = \epsilon_k[\epsilon_{imk}Q_1 + \epsilon_{ilk}(\delta_{1m}Q_2 + \epsilon_m Q_3)]. \tag{3.16}$$

Interchangeability requires $\overline{u_i u_j'} = \overline{u_j u_i'}$ and when we use equations (3.14) and (3.16), it leads to the following relations between scalar functions Q_1, Q_2 and Q_3,

$$(\xi_3\frac{\partial}{\partial \xi_2} - \xi_2\frac{\partial}{\partial_3})Q_i = 0, \quad (i = 1, 2) \tag{3.17a}$$

$$Q_3 = (\frac{\partial}{\partial \xi_1} - \frac{\xi_1}{\xi_3}\frac{\partial}{\partial \xi_3})\,Q_1. \tag{3.17b}$$

Khavaran et al. [49], proposed a set of scalar functions Q_1 and Q_2 which are kinematically

compatible with conditions (3.17a)

$$Q_1 = -(\frac{\overline{u_1^2}}{2})g(\tau)\, e^{-\pi(\xi_1^2/L_1^2+\xi_{23}^2/L_2^2)}, \tag{3.18a}$$

$$Q_2 = -(\overline{u_2^2} - \overline{u_1^2})g(\tau)\, e^{-\pi(\xi_1^2/L_1^2+\xi_{23}^2/L_2^2)}. \tag{3.18b}$$

Function Q_3 is derived from equation (3.17b). In equation (3.18b), $\xi_{23}^2 = \xi_2^2 + \xi_3^2$, and L_1 and L_2 denote stream-wise and span-wise correlation length-scales, respectively. It is implicit that $g(\tau)$ be a function of source coordinate $\mathbf{y}$. Substitution of equation(3.18b) into (3.16) and (3.14) leads to the general expressions for quadrupole sources of an axisymmetric turbulence,

$$\begin{aligned}
I_{1111}(\tau) &= \rho^2 \frac{\partial^4}{\partial\tau^4} g^2(\tau) \frac{(\overline{u_1^2})^2 L_1^3 \Delta^2}{2\sqrt{2}}, \\
I_{2222}(\tau) &= I_{3333} = C_1 I_{1111}, \\
I_{1122}(\tau) &= I_{1133} = C_2 I_{1111}, \\
I_{2233}(\tau) &= C_3 I_{1111}, \\
I_{1212}(\tau) &= I_{1313} = C_4 I_{1111}, \\
I_{2323}(\tau) &= C_5 I_{1111},
\end{aligned} \tag{3.19}$$

where the weight coefficients, C_i $(i = 1, ...5)$ are given by:

$$\begin{aligned}
C_1 &= \frac{3}{2}\beta^2 + \frac{1}{32}[9\left(\Delta + \Delta^{-1}\right)^4 - 48\left(\Delta + \Delta^{-1}\right)^2 + 80] - \frac{\beta}{4}\left(6 - \Delta^2 + 3\Delta^{-2}\right), \\
C_2 &= \frac{1}{8}, \\
C_3 &= \frac{1}{8}\left[\frac{3}{4}\left(\Delta + \Delta^{-1}\right)^4 - 4\left(\Delta + \Delta^{-1}\right)^2 + 7 + 2\Delta^2 + 4\beta^2 + 2\beta\left(\Delta^2 - 2 - \Delta^{-2}\right)\right], \\
C_4 &= \frac{1}{16}\left(5 + 2\Delta^{-2} - 8\beta\right), \\
C_5 &= \frac{1}{2}\left(C_1 - C3\right),
\end{aligned} \tag{3.20}$$

here $\Delta = L_2/L_1$ is the length-scale ratio and $\beta = (1 - \overline{u_2^2}/\overline{u_1^2})$ is the flow anisotropy parameter. These two parameters are provided as inputs to the noise prediction method. Subscripts 1 and 2 denote the axial and lateral directions respectively. Values of $\Delta = 1$ and $\beta = 0$ represents the case of isotropic turbulence.

Khavaran et al. [48] used this formulation to define source strength using mean flow data from the PARC code with a k-ϵ turbulence model. Lighthill's acoustic analogy was adopted along with the high frequency asymptotic solution to Lilley's equation to model the acoustic/flow interaction. The solution technique is essentially based upon the methodology followed by Mani et al. [44] in the MGB code. Noise predictions from an axisymmetric convergent-divergent nozzle were compared with measured data.

3.3.3 Turbulence length-scales and time-scales

A list of various forms of function $f(r)$ as correlated in equation (3.10), used to define the turbulence length scales are given below:

$$f(r) = e^{-\frac{\pi^2\xi^2}{L^2}}, \qquad [43,\ 49] \tag{3.21a}$$

$$f(r) = e^{-\pi(\frac{\xi_1^2}{L_1^2}+\frac{\xi_2^2}{L_2^2}+\frac{\xi_3^2}{L_3^2})}, \quad [51,\ 115] \tag{3.21b}$$

$$f(r) = e^{-\pi(\frac{\xi_1}{L_1}+\frac{\xi_2}{L_2}+\frac{\xi_3}{L_3})}, \quad [51,\ 115] \tag{3.21c}$$

$$f(r) = e^{-(\frac{\xi_1}{L_1}+\frac{\xi_2^2}{L_2^2}+\frac{\xi_3^2}{L_3^2})}, \qquad [116] \tag{3.21d}$$

$$f(r) = e^{-\sqrt{\left(\frac{\xi_1}{L_1}\right)^2+\left(\frac{\xi_2^2}{L_2^2}+\frac{\xi_3^2}{L_3^2}\right)^2}}, \ [116] \tag{3.21e}$$

$$f(r) = e^{-\frac{\xi^2}{L^2}}, \qquad [117] \tag{3.21f}$$

where L_1, L_2 and L_3 are length scales in the axial, radial and azimuthal directions respectively. The LRT method uses the Gaussian formulation presented in equation (3.21a), for the function f, when isotropic turbulence is considered. However, measurements of Bridges and Wernet [118] suggest that an exponential spatial function provides a better fit to data relative to the Gaussian function. Similarly, from the literature, the temporal factor, $g(\tau)$, which gives the temporal decay of the correlation has been modelled as:

$$g(\tau) = e^{-(\omega_f/f)}, \qquad [43] \tag{3.22a}$$

$$g(\tau) = e^{-(\frac{\tau}{\tau_o})^2}, \qquad [48,\ 49] \tag{3.22b}$$

$$g(\tau) = e^{-|\frac{\tau}{\tau_o}|}, \qquad [95] \tag{3.22c}$$

$$g(\tau) = e^{-\sqrt{(\sigma/2)^2+(\tau/\tau_o)^2}}, \qquad [49] \tag{3.22d}$$

$$g(\tau) = e^{-c_1(\tau/\tau_o)^2-c_2\sqrt{c_3+(\tau/\tau_o)^2}}, \quad [119] \tag{3.22e}$$

where τ_o is the characteristic time scale of the turbulence, and c_1 c_2 and c_3 and σ are the empirical constants.

In the LRT source model, equation (3.22b), a Gaussian decay function has been chosen. The integral length scale used in the current LRT source model is associated with turbulence kinetic energy and its dissipation rate, ϵ [48],

$$L_1 = C_l\frac{(\overline{u_1^2})^{3/2}}{\epsilon}, \tag{3.23}$$

where L_1 is the integral length scale of the eddy, ϵ is the eddy dissipation rate (m^2/s^3) and u_1^2 is the turbulence kinetic energy, C_l is an empirical constant. The time-delay, also called as decay rate is given by,

$$\tau_d = C_\tau\frac{k}{\epsilon} = \frac{1}{\Omega_o}, \tag{3.24}$$

where C_τ is a proportionality constant, and Ω_o is the characteristic source frequency. From equations (3.23) and (3.24), the longitudinal time scale L_1 can be expressed as inversely proportional to the characteristic source frequency,

$$L_1 = \left(\frac{C_l}{C_\tau}\right) \frac{\sqrt{k}}{\Omega_o} \left(\frac{3}{2} - \beta\right)^{-3/2}. \tag{3.25}$$

The transverse integral length scale L_2 can be written as $L_2 = (\overline{u_2^2})^{3/2}/\epsilon$, or can be expressed in terms of the anisotropic parameter, $\Delta = L_2/L_1$. From equations (3.13), (3.25) in (3.19), we can write,

$$I_{1111}(\tau) = \left(\frac{C_l}{C_\tau}\right)^3 \frac{\sqrt{2}}{4} \rho^2 \frac{\partial^4}{\partial \tau^4} g^2(\tau)\, k^{7/2}\, \tau_d^3\, \Delta^2 \left(\frac{3}{2} - \beta\right)^{-13/2}. \tag{3.26}$$

3.3.4 Incorporating the Turbulence Energy Transfer (TET) time scale

As mentioned in Section 2.2, three time-scale expressions have been used in the literature related to RANS based jet noise prediction methods. They are as given below,

$$\tau_P = \alpha_P \frac{k}{Pr}, \quad \tau_s = \alpha_s \left|\frac{\partial U}{\partial r}\right|^{-1}, \quad \tau_d = \alpha_d \frac{k}{\epsilon}, \tag{3.27}$$

where, Pr is the production rate of turbulent kinetic energy [76], $|\partial U/\partial r|^{-1}$ is the local strain rate in the jet, k/ϵ is the turbulent energy decay rate, and α_p, α_s, and α_d are the three empirical coefficients. Each of the three time-scales account for three different physical processes that takes place in a typical turbulence cascade, such as the energy production, dissipation and local straining, which is dominant in the initial subrange. In reality, noise generation in a jet is a consequence of all physical processes (energy production rate, energy transfer rate (TET) and energy dissipation rate). In order to account for turbulent energy transfer, Azarpeyvand and Self [88, 87], integrated Pao's energy spectrum model [120] within the turbulence energy spectrum, between mid and higher limits of the wave number, κ. Pao's energy spectrum model is given as [120],

$$E(\kappa) = \alpha \epsilon^{2/3} \kappa^{-5/3} e^{-\frac{3}{2}\alpha(\kappa\eta)^{(4/3)}}. \tag{3.28}$$

The time scale was obtained by integrating Pao's model in the turbulent energy cascade equation,

$$\tau \propto \int \frac{E(\kappa)}{\epsilon}\, \mathrm{d}\kappa. \tag{3.29}$$

The turbulent energy transfer time scale, τ_t is given by, [88, 87],

$$\tau_t = \alpha_T\, \tau_d \left(\frac{L}{\Lambda}\right)^{2/3} .e^{\frac{3}{2}C(2\pi\frac{\eta}{l})^{4/3}} - \beta^T \tau_\eta \mathrm{Erfi}\left(\frac{3}{2}\alpha\left(2\pi\frac{\eta}{l}\right)^{2/3}\right). \tag{3.30}$$

Here, α_T is a calibrating parameter, Λ denotes the size of the eddy which can be estimated from the local width of the shear layer, L is the length scale given by equation (3.23), C

is set to 1.5 [88, 87], $\tau_\eta = \sqrt{\nu/\epsilon}$ is the Kolmogorov time scale, Erfi is the imaginary error function, defined by,

$$\mathrm{Erfi}(z) = \frac{2}{i\sqrt{\pi}} \int_0^{iz} e^{-t^2} \mathrm{d}t. \tag{3.31}$$

The exponential factors in the first and second terms of equation (3.30), which depend on the Kolmogorov scales, can be neglected in comparison with the other terms. This is because the eddy scales closer to the Kolmogorov scales are not significant contributors to the noise generation and propagation mechanism. Therefore, equation (3.30) can be simplified to,

$$\tau_t \approx \alpha_T \, \tau_d \left(\frac{\Lambda}{L}\right)^{2/3}. \tag{3.32}$$

The TET time-scale addresses the frequency dependency, and has been shown that it provides good predictions compared the other time scales given by equation (3.27) [70]. Incorporating the new time scale equation (3.32) into equation (3.26) and taking the Fourier transform, gives,

$$I_{1111}(\Omega)_{=}\rho^2 \frac{\sqrt{\pi}}{4} \left(\frac{C_l}{C_\tau}\right)^3 \Delta^2 \left(\frac{3}{2} - \beta\right)^{-\frac{13}{2}} \tau_t^4 \, \Omega^4 \, \kappa^{7/2} e^{\left(-\frac{\tau_t^2 \Omega^2}{8}\right)}, \tag{3.33}$$

here, $\Omega = \omega \sqrt{(1 - M_c \cos\theta)^2 + (\alpha_c \sqrt{\kappa}/c_o)^2}$ is the modified convection frequency, α_c is an empirical convection constant and is fixed at 0.55 (based on experimental data) [45]. Coefficients C_l, C_τ and α_τ are transformed to only two calibrating constants,

$$\alpha_\tau = C_\tau \, C_l^{2/3}, \qquad C_\tau = \frac{\alpha_\tau}{C_l^{2/3}}. \tag{3.34}$$

After implementing this change, the first component of source/spectrum correlation tensor is given as,

$$I_{1111}(\Omega) = \rho^2 \frac{\sqrt{\pi}}{4} \left(\frac{C_l^5}{\alpha_\tau^3}\right) \Delta^2 \left(\frac{3}{2} - \beta\right)^{-\frac{13}{2}} \tau_t^4 \, \Omega^4 \, \kappa^{7/2} e^{\left(-\frac{\tau_t^2 \Omega^2}{8}\right)}. \tag{3.35}$$

The remaining components are expressed similarly as defined in equation (3.19). To account for the refraction of sound due to the mean flow, each correlation tensor will be multiplied by the corresponding directivity factor.

3.3.5 Role of LRT length-scale and time-scale coefficients

RANS-based solutions provide steady, average mean-flow quantities, and are not capable of resolving the turbulence velocity fluctuations to define the acoustic sources [45]. RANS data do not account for flow unsteadiness, flow anisotropy, temperature effects and also the effect of large-scale structures. Therefore, when a RANS-based mean flow field is used, the usual procedure is to model the turbulence length-scales and time-scales with the help of model coefficients which are part of the LRT source model. In the LRT source model, coefficients C_L and α_T are the length-scale and time-scale coefficients, respectively.

In the LRT method, a set of four model coefficients are used to model the noise from

the turbulence as informed by the RANS.

$$\Delta = L_2/L_1, \tag{3.36}$$

where, L_1 and L_2 are the stream-wise and span-wise length scales.

$$\beta = \left(1 - \overline{\mathbf{u}_2^2}/\overline{\mathbf{u}_1^2}\right), \tag{3.37}$$

$\mathbf{u}_1$ represents the stream-wise velocity component and $\mathbf{u}_2 = \mathbf{u}_3$ represents the span-wise velocity components.

$$L_1 = C_l \frac{(k)^{3/2}}{\epsilon}, \tag{3.38}$$

here, C_l is the LRT length-scale coefficient, L_1 is a length scale of the eddy, ϵ is the eddy dissipation rate (m^2/s^3) and $\mathbf{u}_1^2$ is the axial velocity fluctuation.

$$\tau_t = \alpha_T \, \tau_d \left(\frac{L}{\Lambda}\right)^{2/3}, \tag{3.39}$$

here, α_T is the LRT time-scale coefficient, L is the integral length-scale, Λ is the local size of an eddy, τ_o is the characteristic time-delay of the eddy (s).
If assuming isotropic turbulence, $\overline{\mathbf{u}_1^2} = \overline{\mathbf{u}_2^2} = \overline{\mathbf{u}_3^2}$, so $\beta = 0$; and $L_1 = L_2$, $\Delta = 1$.

The constants C_l and α_T are determined on the basis of best fit to the noise measurements at the 90^o polar observer angle where the convection and refraction effects due to the mean-flow are negligible. These coefficients are then fixed when computing the spectra for other polar angles. In the LRT method, α_T is responsible for modelling the spectral shape whereas C_l affects the amplitude.

3.4 Mean flow refraction effects on noise propagation

The estimation by Lighthill that $(\rho \mathbf{u_i} \mathbf{u_j})$ is the most important part of the tensor $\mathrm{T_{ij}}$ has been valuable in provided key insights into the jet noise problem. However, this approximation suppress all effects associated with the influence of mean-flow velocity and temperature of the jet, i.e., convection, refraction, and shielding of the radiation from the moving eddies. This neglect of mean-flow effects in Lighthill's theory was pointed out by the works of Ribner [43], Phillips [21] and Csanady [121]. The concept of systematically accounting for the effect of mean-flow effects was first pursued by Phillips [21] and subsequently and somewhat more completely by Lilley [122].

Acoustic/mean-flow interactions affect jet noise radiation in several ways. First, the mean flow velocity and temperature cause the radiated sound to refract, resulting in the reduction of sound pressure levels close to the jet axis. Second, the mean-flow structure around the radiating eddies provides an acoustics impedance environment, in other words 'shielding', that fundamentally alters the radiation efficiency with which the eddies radiate from compared to a conditions where the eddies radiated into a stationary homo-

geneous medium, as assumed by Lighthill. The acoustic/mean-flow interaction is strongly frequency dependent [44].

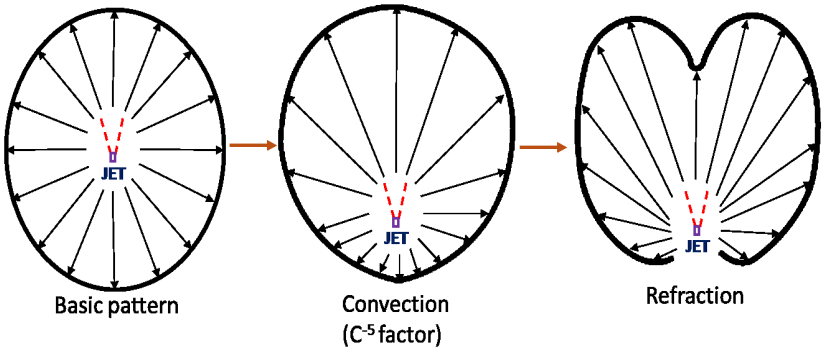

Figure 3.7 – Basic pattern of jet noise modified by source convection and refraction of sound waves by the mean flow [43].

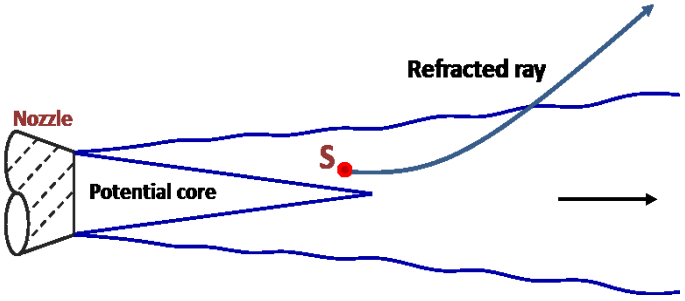

Figure 3.8 – Schematic diagram showing the refraction of a ray of sound emitted by a point source at S in a jet.

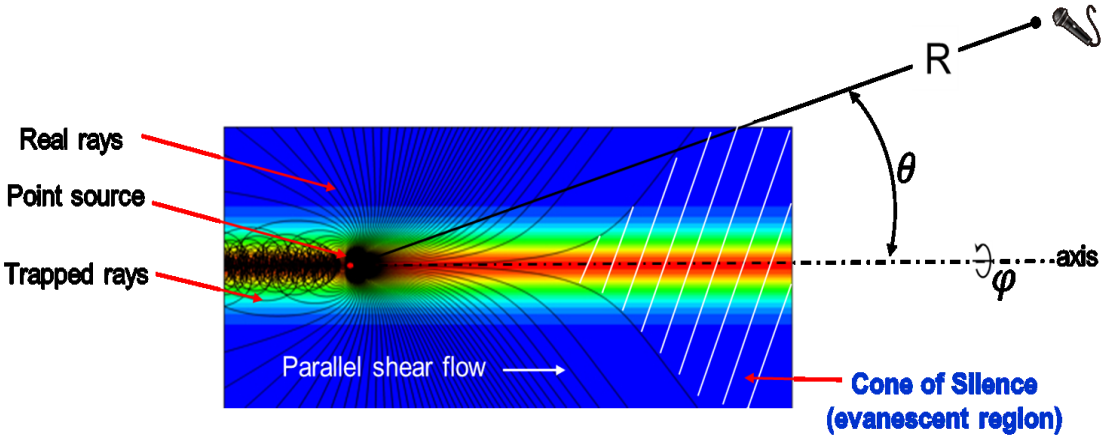

Figure 3.9 – Schematic showing the refraction of rays due to the mean flow creating a cone of silence.

Propagation and refraction of sound emitted from convecting acoustic sources embedded in a shear flow has its application in jet noise studies. The effects of convection and refraction on sound waves propagating from a jet are shown schematically in Figure (3.7).

The effect of convection is to stretch the inherent source directivity pattern in the downstream direction, while the effect of refraction causes the deflection of sound waves away from the jet flow direction. Figure (3.8) illustrates the refraction of a ray of sound emitted by a point source S located in the mixing layer of a jet. The final direction pattern is the result of these two effects. The bending of the sound waves away from the jet axis direction creates an attenuated region called as the 'cone-of-silence' (CoS) as shown in Figure (3.9).

There has been numerous investigations on the effects of mean-flow refraction on the radiation of sound from localised sources in jets. Due to entrainment, the mean flow spreads in the axial direction by transferring the momentum in the radial direction as well. Thus, there are axial as well as radial gradients to be considered, although the former is much smaller than the latter. Because of this complexity in the mean flow profile, so far only approximate solutions are available. In order to provide a viable analytical solution, Mani [123, 124] simplified the problem by replacing the jet with a plug flow. Lilley's equation was used to obtain closed-form solutions for a parallel shear flow. In his work, Mani points out that Lighthill's expression for directivity $(1 - \mathrm{M_c}\cos\theta)^{-5}$, underestimates the variation of OASPL at low-frequencies while it overestimates this for the high frequency sound.

Tester & Morfey [125] used a parallel flow model to construct approximate point source solutions of the flow equations in both the low- and high-frequency limits. It also introduces the ring source model that has proved extremely popular in aero-acoustics due to both the analytic simplifications it engenders and the turbulence physics it reflects. Balsa [69] highlights the variation of the convective amplification factor at low and high frequencies due to the effect of mean flow shrouding from theories proposed by Lighthill and Lilley for a parallel shear flow. Tam & Auriault [104] used adjoint Green's function to determine mean flow refraction effect on sound by sources for realistic jet profiles. Tam compares refraction effects from locally parallel and non-parallel flow profiles. RANS k-ϵ model was used to calculate the mean flow. For both type of flow profiles, good estimates of sound radiation was obtained but only for angles outside the cone-of-silence.

Khavaran & Krejsa [49, 77, 78] and Khavaran [50, 119] used geometric acoustics to non-parallel non-axisymmetric jets. The method employed a high frequency approximate solution which is generally useful within the intended range of validity. The LRT method employs ray theory to model refraction effects from nozzles. In the next section ray theory is described in detail followed by its application in the LRT method.

3.5 LRT Propagation Modelling

As described in the previous section, the LRT source model is based on Lighthill's analogy which does not account for the effect of mean-flow refraction in its formalism. Many corrections incorporating the fluid-acoustic interaction have been proposed. Consequently,

several RANS/CAA based methods to model the mean-flow propagation effects were described in Section (2.2). For practical jet Mach numbers, which are higher subsonic, the speed of sound is of the order as the characteristics velocity, so the acoustic wavelengths of the fine-scale disturbances would be small compared to the shear-layer thickness. When the acoustic wavelength is much less than the shear layer thickness, the sound radiation can be described using "Geometric Acoustics" (G.A.). Geometric acoustics is a high frequency concept, where sound propagation is analogous to light in optics, where a ray is a representative of a narrow beam of light. On the same lines, a sound wave can be idealised as a narrow beam of sound, also called rays.

3.5.1 Background to Ray Theory

Ray theory is an approach in which a point on the wavefront is tracked rather than the complete wavefield. This makes the method computationally faster and simple to be extensively applicable to a wide range problems such as in the field of optics, underwater acoustics, Seismology, atmospheric science etc. Ray theory is an high frequency approximation which makes it strictly valid for media whose characteristic length scale λ is much larger than the acoustic wavelength, ω. Therefore, ray theory is ideal to study noise emitted by jets which is essentially high frequency. At low frequencies, diffraction and scattering can be significant, and ray theory is not generally valid.

Ray theory dates back to the 17^{th} century when Fermat (1662) proposed the principle of least time, where the path taken between two points by a ray of light in an inhomogeneous media is the path traversed in the least time. The application of ray theory provides a particularly useful approximation when considering a moving inhomogeneous medium, i.e. when solutions of the full wave equation become difficult. This case was first addressed by Lord Rayleigh [126] who presented the basic principles governing sound propagation in wind shear and used simple arguments to expand Snell's law to include velocity gradients.

The fundamental wave and energy equations were formally established by Blockhintzev [127] whose "energy invariance" law allows the calculation of acoustic intensity once the ray paths are determined. Hayes [128] developed concise equations for ray geometry and acoustic energy using the energy conservation concepts from Rayleigh and Blokhintzev in a three-dimensional environment and showed that these equations hold even when the moving medium is unsteady, in the linearised sense. Seckler & Keller [129, 130] contributed significantly to the field of ray theory with a series of papers which greatly improved the application of ray methods.

The effect of Mach number on the sound field created by a source was shown by Papamoschou [131] by using GA inside a two-dimensional shear layer. The application of GA to jet noise problems for high and peak Strouhal numbers have been shown to provide good agreement with experiment data by Csanady [121], while Tester and Morfey [125], compared GA results with solutions of Lilley equation for low Mach numbers and Strouhal numbers as low as St=0.2. It is thus justifiable that geometric acoustics (GA), and the

related ray theory, could be a reasonable approximation for studying sound propagation in a compressible shear layer over a wide frequency interest, at least for obtaining qualitative trends. The approximation improves as the acoustic wavelength becomes much smaller than the shear-layer thickness.

In the LRT method, mean-flow propagation is modelled using ray theory. The use of GA for jet noise applications is not new. The advantages of geometric acoustics theory is its relative simplicity and capability to produce a physical interpretation of the sound field via ray tracing. It enables the modelling of reflections and its visualisation in a qualitative way and it provides the possibility of including all kinds of inhomogeneities in the medium, like the local speed of sound and velocity. These advantages associated with ray tracing makes it an effective method to calculate far field propagation effects from a jet. The ray equations used in acoustic propagation models available in the literature vary by certain degree. We use ray tracing equations formulated by Pierce [132]. In the following sections, the theoretical model and its implementation within the LRT method is presented.

3.5.2 Ray expansions

In this section a mathematical approach to the derivation of the basic ray equations is presented. Consider the wave equation for pressure disturbances in a non-moving medium,

$$\nabla^2 p = \frac{1}{c^2}\frac{\partial^2 p}{\partial t^2}. \tag{3.40}$$

For a wave propagating through a region with a slowly varying sound speed will have slightly curved wavefront, and its direction of propagation and amplitudes will vary gradually from point to point. For such waves propagating with constant frequency, where frequency is large ($\mathrm{L} \gg \omega$), a time harmonic solution can be given as,

$$p\left(x, y, t\right) = P\left(x, y; \omega\right) \mathrm{e}^{i\omega(t-\tau(x,y))}. \tag{3.41}$$

Here, P, the amplitude term, varies because of gradual changes in the sound speed, and therefore an appreciable variation of P only occurs over L, the length scale over which the sound speed varies. The phase, τ, is a function of position and accounts for the variation of p over the scale of wavelength. For a disturbance of constant frequency where the frequency is large such that the wavelength $\lambda \gg \mathrm{L}$, where, $\lambda = 2\pi c/\omega$, then P is slowly varying compared with τ, the moving surfaces $t - \tau\left(x, y\right) =$ constant to the wavefronts. Rays are defined to be curves which are always normals to the wavefronts.

If we take the gradient of the scalar potential, then, we get,

$$\nabla p = \nabla P \exp^{i\omega(t-\tau)} - i\omega P \nabla\tau \exp^{i\omega(t-\tau)}. \tag{3.42}$$

The divergence of the gradient of the scalar potential is,

$$\begin{aligned}\nabla^2 p = \nabla^2 P \exp^{i\omega(t-\tau)} &- i\omega\nabla\tau.\nabla P \exp^{i\omega(t-\tau)} \\ &- i\omega\nabla P.\nabla\tau \exp^{i\omega(t-\tau)} \\ &- i\omega P\nabla^2\tau \exp^{i\omega(t-\tau)} \\ &- \omega^2 P\nabla\tau \exp^{i\omega(t-\tau)}\,.\end{aligned} \tag{3.43}$$

The second derivative of p with respect to time is,

$$\frac{\partial^2 p}{\partial t^2} = -\omega^2 P \exp^{i\omega(t-\tau)}\,. \tag{3.44}$$

Substituting the above terms in the wave equation, and rearranging the terms according to frequency, ω we get,

$$-\omega^2 P\left[(\nabla\tau)^2 - 1/c^2\right] + i\omega\left[2\nabla P + P\nabla^2\tau\right] + \nabla^2 P = 0. \tag{3.45}$$

At this point, we can assume an asymptotic expansion of P:

$$P(x,y;\omega) = P_0(x,y) + \frac{1}{\omega}P_1(x) + \frac{1}{\omega^2}P_2(x) + ... \tag{3.46}$$

But we are only interested in the dominant term; which gives, $\mathrm{P} = \mathrm{P}_0$. Another important parameter in the ray solution (equation 3.41) is the phase term, τ. If the phase is positive, it keeps increasing monotonically along the ray. If we assume a complex ray (an evanescent or decaying ray), then equation (3.41), can be written as,

$$p(x,y,t) = P(x,y;\omega)\,\mathrm{e}^{i\omega(t-\mathrm{Re}(\tau(x,y))\pm\mathrm{iIm}(\tau(x,y)))}, \tag{3.47}$$

here, the $\pm$ sign indicates that there are two complex ray solutions. From equations (3.46) and (3.47), it is clear that the negative solution will give us a physical decaying solution as ω gets larger. This is exactly the kind of solutions we need in flows where there is an exponential decay. Such a zone is called a Cone of Silence (CoS). The CoS phenomena, its implications and methods to model it will be discussed in Chapter 6.

If equation (3.45) is to be satisfied for any frequency ω, the expressions with ω^2, ω^1 and ω^0 must vanish. Of the three expressions, the two unknowns τ and P does not depend on ω. Thus equation (3.45) cannot be satisfied exactly. For high frequencies ω, the most important terms will be the first (with ω^2) and the second (with ω). Since we are interested in the high frequency solutions of equation (3.45), the coefficients of the highest power of ω^2 and ω is set to zero. We then arrive at the *eikonal equation*,

$$(\nabla\tau)^2 = 1/c^2, \tag{3.48}$$

and the *transport equation*,

$$2\nabla P.\nabla\tau + P\nabla^2\tau = 0 \quad or, \tag{3.49}$$

can be written in divergence form, as

$$\nabla.\left(P^2\nabla\tau\right) = 0. \tag{3.50}$$

Both, the eikonal and transport equations play a fundamental role in the ray method. The eikonal equation represents a nonlinear partial differential equation of the first order for travel time $\tau\,(x, y)$. It describes the kinematic propagation of the sound waves. The transport equation can be used to compute the amplitude of propagating waves. It represents a linear partial differential equation of the first order in $P\,(x, y)$. It simplifies further if it is solved along the rays. It then reduces to an ordinary differential equation of the first order for $P\,(x, y)$ and can be solved analytically in terms of the ray Jacobian. We can generalise this to more complicated flows. This means generalising equations (3.48) and (3.50).

3.5.3 Ray equations

In the previous section, ray solutions for a simple flow has been derived. However, the ray ansatz in equation (3.41) still holds good for complex flow solutions such as Lilley's equation or linearised Euler equations (LEE). Rather than applying it to a wave equation or to LEE, we develop a geometric approach as given by Pierce [132].

The theory of plane-wave propagation predicts that wave-fronts move with speed $\mathbf{c}$ when viewed in a coordinate system in which the ambient medium appears at rest. If the ambient medium is moving with velocity $\mathbf{u}$, the wave velocity $\mathbf{n}c$ seen by an observer moving with the fluid becomes $\mathbf{u} + \mathbf{nc}$ in a coordinate system at rest, where $\mathbf{n}$ is the unit vector normal to the wave-front.

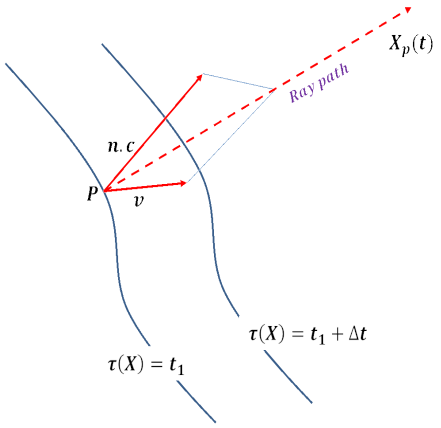

Figure 3.10 – Schematic of a wavefont and a ray trajectory.

If $\mathbf{x}_p$ is the co-ordinate of a moving point on a wave-front $t = \tau(\mathbf{x})$ at an initial time,

this point will always lie on the moving wave-front with its velocity $\mathbf{u}_{ray}$ and obey the equation:

$$\frac{\mathrm{d}\mathbf{x}_p}{\mathrm{d}t} = \mathbf{u}(\mathbf{x}_p, t) + \mathbf{n}(\mathbf{x}_p, t)\mathbf{c}(\mathbf{x}_p, t) = \mathbf{u}_{ray}. \tag{3.51}$$

As rays propagate through a moving media, the velocity $\mathbf{u}$, and sound speed c, varies with space and time, and it is accounted in equation (3.51). The path described by $\mathbf{x}_p$ in space and time is the ray path and the function $\mathbf{x}_p(t)$ is the ray trajectory. The wave-slowness vector $\mathbf{s}$, is another alternative to account for the time rate of change of normal vector $\mathbf{n}$, defined as:

$$\mathbf{s}(\mathbf{x}) = \nabla\tau(\mathbf{x}) \tag{3.52}$$

$$\mathbf{s}.\big(c\mathbf{n} + \mathbf{u}\big) = 1 - \mathbf{u}.\mathbf{s} \tag{3.53}$$

$$c\mathbf{s}.\mathbf{n} = 1 - \mathbf{u}.\mathbf{s} \tag{3.54}$$

$$\mathbf{n} = \frac{c\mathbf{s}}{\chi} \tag{3.55}$$

where, $\chi = 1 - \mathbf{u}.\mathbf{s}$.

From above relations, we can deduce the following *eikonal* equation,

$$\mathbf{s}^2 = \frac{\chi^2}{c^2}, \quad (\nabla\tau)^2 = \frac{\chi^2}{c^2}. \tag{3.56}$$

An equation for the time rate of change of $\mathbf{s}$ along a ray trajectory can be derived from equation (3.56);

$$\frac{\mathrm{d}\mathbf{s}(\mathbf{x}_p)}{\mathrm{d}t} = \Big(\dot{\mathbf{x}_p}.\nabla\Big)\mathbf{s} = c(\mathbf{n}.\nabla)\mathbf{s} + (\mathbf{u}.\nabla)\mathbf{s} \tag{3.57}$$

where all the quantities are evaluated at $\mathbf{x}_p(t)$.

After few simplifications, the ray tracing equations can be written as follows (in Cartesian co-ordinates),

$$\frac{\mathrm{d}\mathbf{x}_i}{\mathrm{d}t} = \mathbf{u}_i + \frac{c^2\mathbf{s}_i}{\chi}, \tag{3.58}$$

$$\frac{\mathrm{d}\mathbf{s}_i}{\mathrm{d}t} = -\frac{\chi}{c}\frac{\partial c}{\partial x_i} - \sum_{j=1}^{3}\mathbf{s}_j\frac{\partial}{\partial x_i}\mathbf{u}_j. \tag{3.59}$$

Equations (3.58) and (3.59) form the ray tracing equations which determine position along a ray and the direction in which it travels. These equations do not depend on the spatial derivatives of $\mathbf{s}$; so if $c\,(\mathbf{x}, t)$ and $\mathbf{u}\,(\mathbf{x}, t)$ are specified, and if a ray position $\mathbf{x}$ and wave-slowness vectors $\mathbf{s}$ are specified at time, t_0, Equations (3.58) and (3.59) can be integrated in time to determine $\mathbf{x}$ and $\mathbf{s}$ at any subsequent instant; no information concerning neighbouring rays are required. These nonlinear, first order ordinary differential equations can be solved using standard numerical methods. These equations can be solved as an initial value problem using a finite difference method. A second-order forward difference method was used to march in space and a fourth-order Runge-Kutta method was employed to integrate the solutions in time. A fourth order Runge-Kutta method can easily

be implemented using mathematical software such as Matlab.

3.5.4 Ray tracing method

In this section, the sound field generated by a source in a shear layer will be examined. The effect of Mach number on ray distortion and the resulting acoustic intensity distribution. We consider a parallel shear layer with velocity dependent only on the transverse coordinate r, to infer the influence of the surrounding flow field on the acoustic source inside the shear layer. To simplify the analysis, we place ourselves in the frame of reference moving with the local flow velocity (see Figure (3.11)). Let r = 0 be the observer plane. From this plane, we see a velocity distribution $\mathbf{u}_0(r)$, and consequently Mach number distribution $\mathrm{M}(r)$. Acoustic sources are located on the plane $r = r_1$ where the velocity is u_1 and the Mach number is M_1. For simplicity purposes, the problem is consider two-dimensional where all interactions occur on the x-r plane.

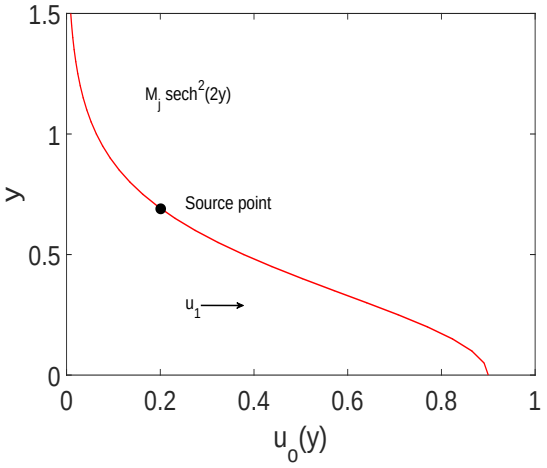

Figure 3.11 – Velocity profile, $u_0(r) = M_j\, sech^2(2r)$.

The relation between wave velocity, u, speed of sound, c and the wave-normal angle θ can be given as:

$$\sin\theta = \frac{c}{u + C}, \tag{3.60}$$

where, C is the Rayleigh's constant which assumes the velocity of an acoustic wave on an interference between gases of slightly different velocities is constant. The constant, C can be related to conditions u_1, c_1 and θ_1 at the source plane. Relating the constant C in equation (3.60), we obtain the following:

$$\sin\theta = \sin\theta_1 \left(\frac{c}{c_1 + (u - u_1 \sin\theta_1)} \right), \tag{3.61}$$

which can be viewed as Snell's law of refraction generalized to a moving medium. For

constant speed of sound, equation (3.61) reduces to,

$$\sin\theta = \frac{\sin\theta_1}{1 + (M - M_1)\sin\theta_1}. \tag{3.62}$$

Given the conditions at the source point $(u_1, \mathrm{M}_1, \theta_1)$ and the velocity distribution, rays can be traced through shear flow profiles by calculating θ from equation (3.62). Parallel shear flows have mean flow $\boldsymbol{u}_0(\boldsymbol{x}) = \delta_{i1} u_0(r)$ and sound speed profile c(r) = 1. For this study we will use the velocity profile $\mathrm{M}(r) = \mathrm{M_j}\,\mathrm{sech}^2(2r)$, where $\mathrm{M_j}$ is the Mach number. Rays are traced from the source location, $r_s = (0, 0.5)$.

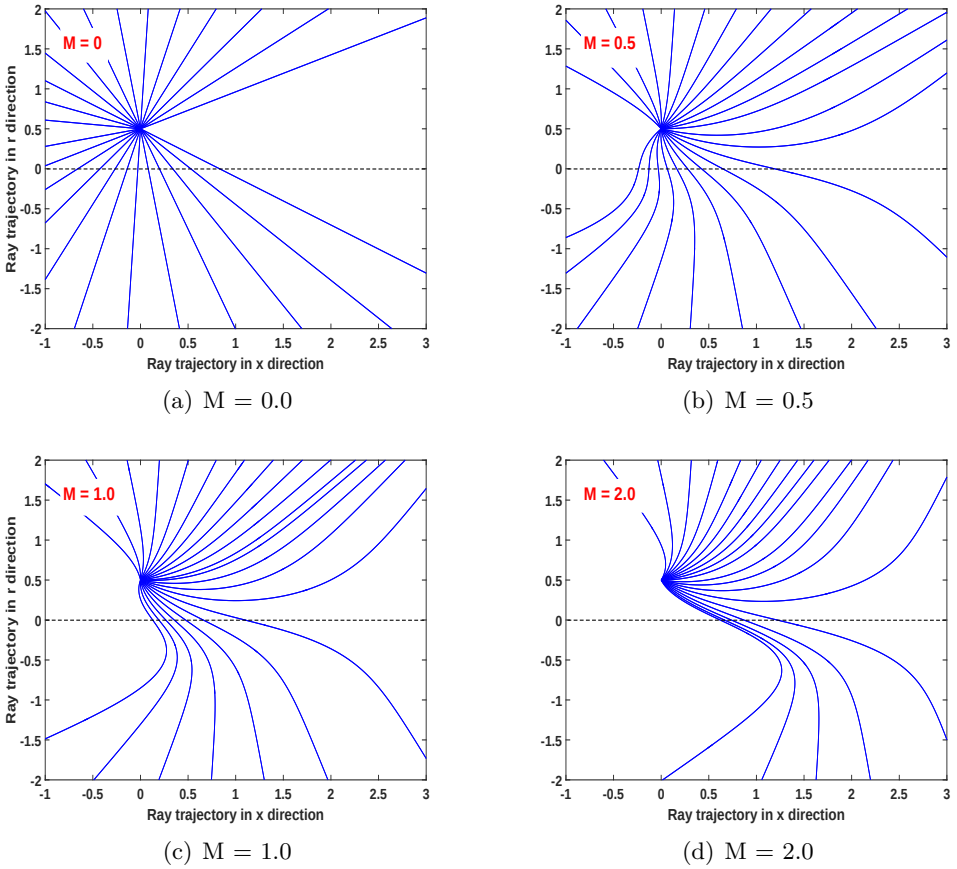

(a) M = 0.0 (b) M = 0.5

(c) M = 1.0 (d) M = 2.0

Figure 3.12 – Ray paths from a point source, $r_s = 0.5$ in a shear layer profile for varying Mach numbers = 0, 0.5, 1.0, 2.0

Figure (3.12) shows the ray paths for M = 0, 0.5, 1.0, and 2.0. Rays were launched from the source point with θ_1 ranging from 0° to 360° in 12° increments. For $\mathrm{M}_1 = 0$, the rays are straight, as there are no flow gradients. As M_1 increases, the rays get progressively more distorted. Rays propagating upwards move into regions where velocity gradients decreases and are refracted upwards. In real jets, besides velocity gradients, refraction is affected by gradients created by the speed of sound and temperature (variations in density). Similarly rays propagating downwards are refracted downwards more steeply. The downward bending of the rays increases with the increase in Mach number.

For jet flows, one of the important consequences of mean flow refraction is that less

sound is radiated in the direction of the jet flow. This gives rise to a relatively quiet region around the jet axis commonly known as the 'Cone of Silence' (CoS), where there is a significant reduction in the radiated sound intensity. The CoS is one of the drawbacks associated with the use of ray theory. It is essential for prediction tools to be able to compute noise at all observer angles of interest, including in the CoS region. It is therefore important to understand the reason for the reduction in sound intensities and to find solutions inside the CoS. Before we look into reduced amplitudes in the CoS, it is important to discuss ways to compute ray amplitudes. In the next section, three popular methods used to calculate ray amplitudes are described.

3.5.5 Determination of ray amplitudes

Rays are very useful trajectories for calculating not only travel time but also amplitude variations. The amplitude variations give an account of the sound level. In the following section, 3 methods to determine ray amplitudes are described. The ray bin and ray tube methods are approximate methods and the third method, which involves solving the transport equation is an exact method.

3.5.5.1 Ray tube method

The concept of ray tube is the simplest method to determine amplitude along the ray path. The sound intensity is commonly defined as $P = p^2/(\rho c)$, where p is the acoustic pressure fluctuation and ρ the density of the medium. A fundamental energy-conservation law in stationary-medium acoustics is that the product of intensity and ray-tube area remains constant. For the moving-medium case, the conservation law for intensity, P, as given by Blockhintzev [127] and by Hayes [128], is of the form

$$\frac{p^2\,\mathbf{u_{ray}}\,A}{(1-\mathbf{u}.\nabla\tau)\,\rho c^2} = \text{constant} \tag{3.63}$$

where, $\mathbf{u_{ray}} = \mathbf{u} + c\mathbf{n}$, and A is the area of the ray-tube. A ray tube is defined by two adjacent rays originating from the source as shown in Figure (3.13). It is worth noting that equation (3.63) cannot be evaluated at the source. Instead, an assumption must be made that the acoustic energy defined in equation (3.63) is conserved within each ray tube. Considering that the acoustic energy is conserved within a ray tube and then using the Blockhintzev invariant concept, the change in pressure along a ray tube between two positions $\mathbf{x}_1$ and $\mathbf{x}_2$ can be given as,

$$\frac{p\,(\mathbf{x}_2)^2}{p\,(\mathbf{x}_1)^2} \propto \frac{A\,(\mathbf{x}_1)}{A\,(\mathbf{x}_2)}. \tag{3.64}$$

The ray tube area is generated by a family of rays neighbouring rays and its normal along the ray. If the ray tube area A, decreases the pressure tends to increase as the rays

focus the sound. Conversely, as the rays path diverge, the acoustic energy is spread out over a larger area, and the amplitude of the pressure disturbance is decreased.

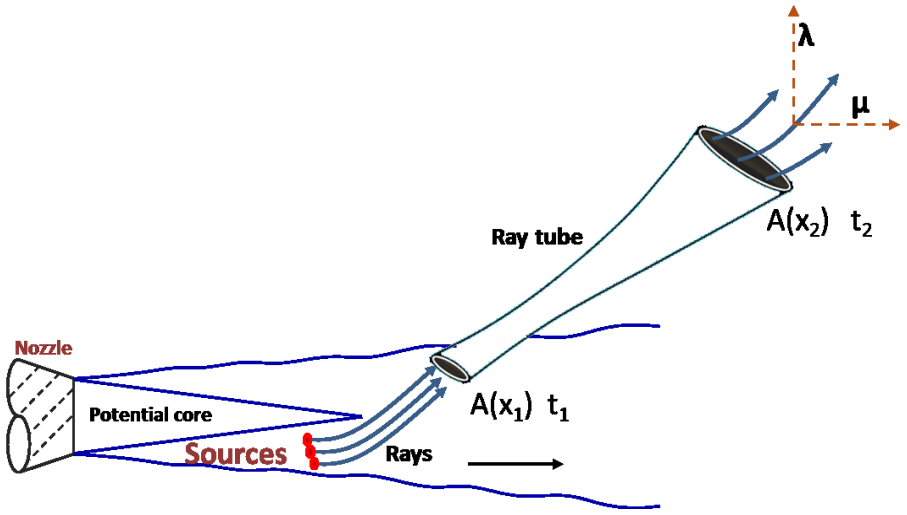

Figure 3.13 – Schematic showing the concept of a ray tube to determine the amplitude of rays propagating from a jet; 'A' is the area of the ray tube, λ and μ represent the ray position, subscripts 1 and 2 represent the ray tube entry and exit quantities, respectively

3.5.5.2 Ray bin method

The effect of flow gradients when tracing rays through inhomogeneous moving media, causes ray paths to cross at points in their trajectories. This results in more than one ray arriving at the desired observer location. This is called the multiplicity problem. In Figure (3.14) there exists a multiplicity of real solutions as both rays that propagate directly towards the receiver and rays that are refracted indirectly, i.e. rays bent towards the receiver by the flow, reach the same points. The pressure seen at this location is a combination (incoherent sum) of individual ray tube pressures. The point where the ray paths cross is called a caustic. At these caustics, the high-frequency approximation for amplitude, which can be obtained from the next highest terms in ω, fails because the wave fronts develop cusps, a feature that is always small with respect to a wavelength of the sound [133]. The multiplicity problem can be solved using a simple but effective method by dividing the far-field into an evenly distributed, equally sized regions called 'ray bins'.

To estimate the effect of refraction, the number of rays launched from the sources can be counted at different regions (ray bins) in the far-field sphere located at the distance, R from the source. A schematic of the ray bin method is shown in Figure (3.14). The resulting ray number density, can be shown to be inversely related to the ray tube area, A, and thus proportional to the tube intensity, I. This method is valid at regions where there are no caustics. Ray tracing using ray bins was used by Freund and Fleischman [134] for unsteady flows computed using DNS.

McLaughlin et al. [135, 136] adopted the method of ray bins to study jet propagation effects from aircraft wings by tracing rays in three-dimensions. McLaughlin et al. de-

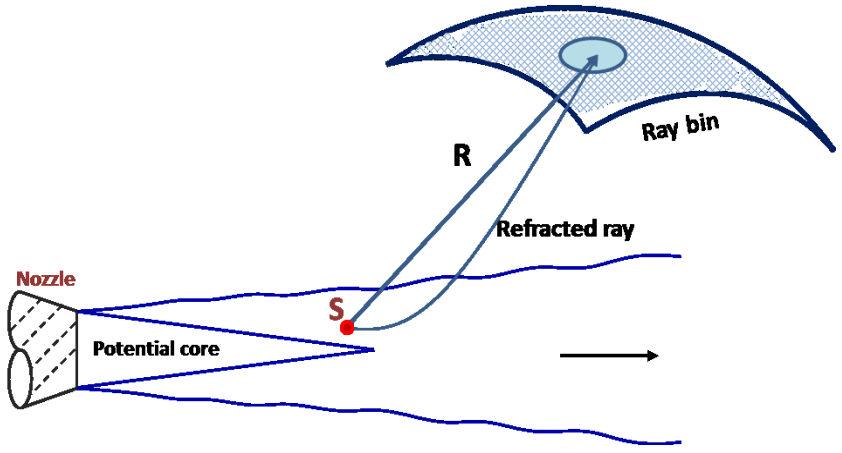

Figure 3.14 – Schematic showing the concept of a ray bin to determine the amplitude of rays propagating from a jet; 'R' is the distance between the source, S and the observer.

veloped 2D and 3D ray tracing codes and benchmarked them using solutions to Lilley's equation for a parallel sheared flow. In their work, the significance of the parallel jet assumption was investigated by tracing rays through a spreading jet and compared the solution with an equivalent parallel jet. The 3D jet propagation ray was integrated with a number of CFD profiles, using realistic jet nozzles, and benchmarked using data from the Andante external loud speaker experiment. It was found that the spreading jet had a significant effect on the cone of silence angle. Ilário da Silva [89] used 3D ray tracing coupled with ray bins to compute noise from jet nozzles with varying geometry and flow conditions.

3.5.5.3 Solving the transport equation

The eikonal and transport equations are fundamental ingredients of ray theory and highlight required properties such as wave-front smooth spatial continuity as well as amplitude conservation along ray tubes. From the transport equation (3.49), the amplitude estimation can be linked to the travel-time field. Rays are defined as being perpendicular to the wavefront, so

$$\frac{2}{c}\frac{dx}{ds}.\nabla P + \left(\nabla^2\tau\right) P = 0. \tag{3.65}$$

The first term represents the directional derivative along the ray path, so

$$\frac{2}{c}\frac{d\nabla P}{ds} + \left(\nabla^2\tau\right) P = 0. \tag{3.66}$$

In the above equation, the term $\nabla^2\tau$ can be calculated using the Jacobian

$$\nabla^2\tau = \frac{1}{J}\frac{d}{ds}\left(\frac{J}{c}\right). \tag{3.67}$$

The Jacobian J, is obtained by looking at the wave-front evolving inside a ray tube defined by neighbouring rays with slightly different initial conditions. By noting two variables μ

and λ related to the ray position at time t_1 parametrising the wavefront and orthogonal to the wavefront normal (Figure (3.13)), the geometrical spreading can be defined as the Jacobian J,

$$J = \left|\frac{\partial\,(x,y,z)}{\partial\,(t,\mu,\lambda)}\right| = \begin{vmatrix} \frac{\partial(x)}{\partial(t)} & \frac{\partial(x)}{\partial(\mu)} & \frac{\partial(x)}{\partial(\lambda)} \\ \frac{\partial(y)}{\partial(t)} & \frac{\partial(y)}{\partial(\mu)} & \frac{\partial(y)}{\partial(\lambda)} \\ \frac{\partial(z)}{\partial(t)} & \frac{\partial(z)}{\partial(\mu)} & \frac{\partial(z)}{\partial(\lambda)} \end{vmatrix} \tag{3.68}$$

The procedure of computing ray Jacobian requires the calculation of at least three near rays in 3D media, or two near rays in 2D media. The ray Jacobian, however, can be computed along one ray only using the procedure called dynamic ray tracing [137]. It involves solving an additional system of linear ordinary differential equations of the first or second order. In the system, $\partial x_i/\partial\mu$ and $\partial x_i/\partial\lambda$ are calculated (i = 1, 2, 3). The additional system of ordinary differential equations can be solved simultaneously with the ray tracing system or after it, along a known ray. The results of ray tracing, allow us to compute the ray Jacobian and the geometrical spreading analytically. This method of calculating the Jacobian will be used to compute the amplitude of rays in Chapter 6.

3.5.5.4 Comparison of far-field amplitudes using ray bins and ray tubes

Two popular methods to calculate the far-field amplitude are described. In this section, a comparison between the two methods are presented for a parallel shear flow profile. The velocity profile is shown in Figure (6.7). The expression for the velocity profile is $\mathrm{M}\,(\mathrm{r}) = \mathrm{M}\,\mathrm{sech}^2(2\mathrm{r})$, where the Mach number M = 0.9. A total of 1000 rays are 'fired' in two-dimensions from varying source point locations in the shear layer. From both methods, the ray equations are solved to compute the ray paths and ray amplitudes at various polar angle positions in the far-field.

The attenuation or amplification of the source in the far-field is quantified in terms of flow factors, or in other words as a ΔSPL. This equation does not include the phase term. The ΔSPL from each source is calculated using equation (3.69) and are as shown in Figure (3.15),

$$\Delta SPL = 10\log_{10}\left(\frac{p^2_{\mathrm{jet}}}{p^2_{ff}}\right), \tag{3.69}$$

where, p^2_{jet} is the far-field pressure due to the source due to the flow, and p^2_{ff} is the pressure measured in the far-field from the same source but with no propagation effects.

For convenience, for this plot only, the polar angle, θ is extended up to 360^o to show the contribution of the rays. From Figure (3.15), it can be seen that both methods model the acoustic field for varying source positions for most for the polar angles. Both these methods are computationally fast. Despite the numerous advantages that ray theory offers, there are several fundamental deficiencies suffered ray ansatz. The most common of these can be summarised as follows: the multiplicity problem which involves the arrival of multiple ray trajectories at a given observer location, the determination and tracking of complex

ray solutions, and the divergence of ray amplitudes at caustics. Recent developments by Stone et al. [138] have seen these deficiencies accounted for, creating a global complex ray tracing (CRT) routine. These deficiencies will be addressed in detail in Chapter 6.

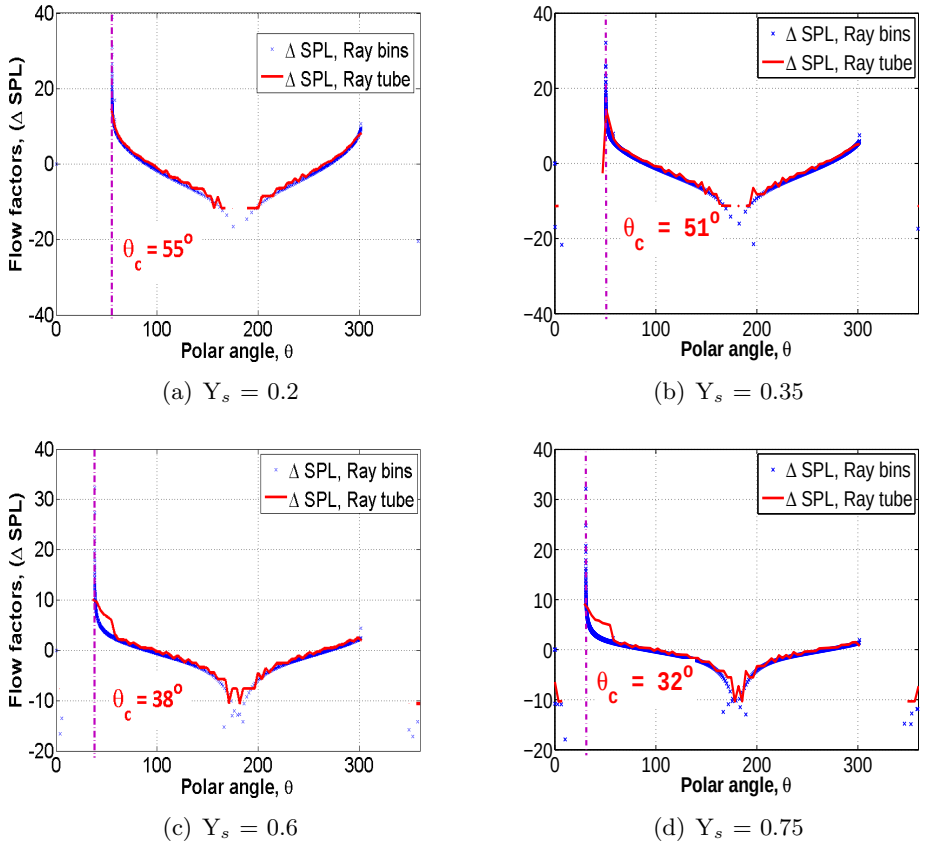

(a) $Y_s = 0.2$ (b) $Y_s = 0.35$

(c) $Y_s = 0.6$ (d) $Y_s = 0.75$

Figure 3.15 – Comparison of ray amplitudes calculated using the ray bins and ray tube concept for varying source position, Y_s and varying polar angle, θ; azimuthal angle, φ=0^o.

At this point, some of the deficiencies of ray theory can be described using the results presented in Figure (3.15). At all source positions, the ray amplitudes peaks at polar angles closer to the axis of the shear layer. After a particular polar angle, a shadow zone exists for all source locations, where no rays have been able to propagate through. The creation of such shadow zones also called as the cone of silence (CoS) is due to the effect of refraction. For sources closer to the jet axis (eg. $Y_s = 0.75$), the critical CoS angle, θ_c is larger compared to sources located near to the edge of the shear layer (eg. $Y_s = 0.2$). The rays from sources located deep in the shear layer (closer to the axis) have to propagate through a thick shear layer and undergoes huge refraction. Due to the bending of rays, a larger CoS angle is formed for sources embedded deep within the shear layer.

Ray theory fails in the vicinity of the critical CoS angle, θ_c. This point is also called the caustic point. At the caustic, the Jacobian is equal to zero and thus the ray amplitude is infinite. Since the Jacobian is equal to the area of the cross-sectional surface element of the elementary ray tube, it is clear that at the caustic point the rays forming the tube cross each other so that the tube shrinks to zero. This may happen provided the medium

is complex enough for the ray field to develop multipathing of rays. Ray multipathing or ray multiplicity is another deficiency of ray theory, where more than one ray arrives at a point in the far-field. Further, when 2 or 3 ray paths tangent in space they generate caustics. A caustic can be defined as an envelope of a family of rays. Caustics are another deficiency of ray theory where rays predict erroneously singular amplitudes. More details regarding these caustics and methods to tackle them are described in Chapter 6.

3.5.5.5 The need for complex rays

It is clear that the real ray solutions does not cover the complete angular range. These are the polar angular regions where real rays cannot propagate. Even though the above example is for a 2D jet, this still holds true for the 3D case. The CoS region lies at angles close to the jet axis and is well known to be due to refractive effects, where the real rays bend away from the axis. The CoS is somewhat a misnomer as it is actually an asymmetric region.

The absence of solution in the CoS is not a fault of the ray solution, but is just a limitation of using only real rays. It is well known that the CoS is a shadow zone where evanescent waves are found. These cannot be modelled by real ray trajectories. Therefore, it is important to account for the contributions from the complex rays.
In the next section, the steps followed in the LRT method are described.

3.6 LRT procedure

This section describes the various steps involved in the LRT method. The computation procedure involved in each step starting from obtaining the mean flow data, generating acoustic grids, computational routines used to perform the propagation and source strength computations. The various process of the LRT method is shown in Figure (3.16).

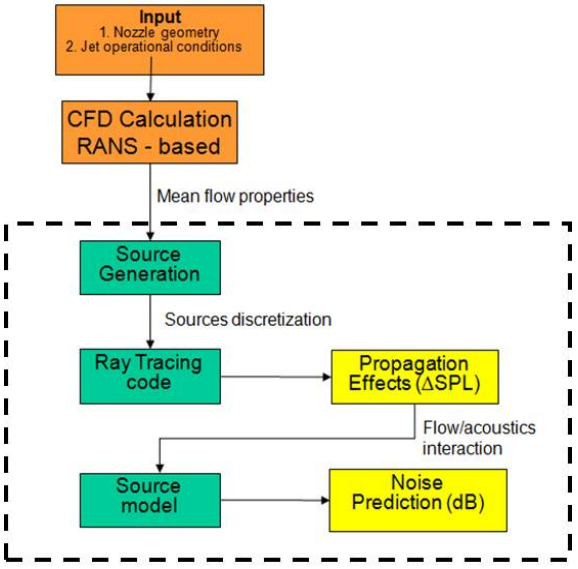

Figure 3.16 – Schematic showing the steps involved in the LRT method

The LRT method can be divided basically into two main parts: in the first part, the inherent source strength are calculated, and in the second part, ray tracing is used to calculate refraction effects. The steps involved are listed below:

- Source modelling: Using the mean flow data from CFD, inherent source definitions are calculated using equation (3.35) to compute the noise spectrum at the 90^o polar angle. At this point, LRT model coefficients are determined using the procedure described in Section (4.5.1). The source equations are solved using a FORTRAN code.
- Propagation modelling: Effect of refraction on mean flow propagation is calculated using ray tracing method. Source coordinates for tracing rays are generated in the acoustic grid where the flow gradients are high (e.g. in the jet shear layer). See Section (3.6.2). From each source point, 655,000 rays are launched in to the far-field. Eikonal equations (3.58) and (3.59) are solved using an iterative scheme (see Section (3.5.3)) to compute ray trajectories in 3 dimensions. Ray amplitudes in the form of a delta SPL (as referred to as flow factors) are computed using ray tubes and ray bins approach (see Section (3.5.5.4)) in the far-field.
- The Eikonal equations for ray tracing are solved using a separate FORTRAN code within a MATLAB shell.
- The source definitions for observer angles and frequencies of interest are integrated with flow factors from ray tracing over the entire volume of the jet to obtain the noise spectra and OASPL using equation (3.70).

3.6.1 Acoustic grid

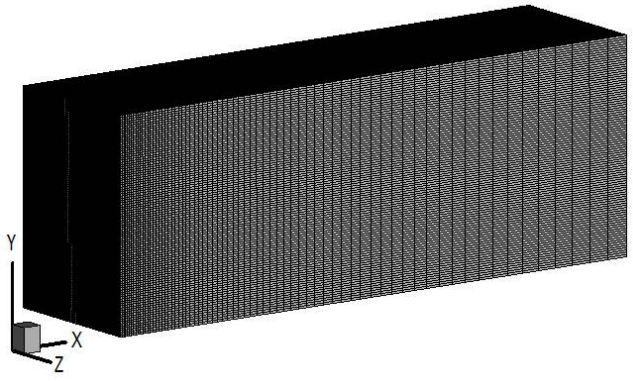

Figure 3.17 – Acoustic grid used in the LRT method.

The first step in the LRT method is to obtain the mean flow data through CFD. The RANS CFD data used in the current work were available in the ISVR database. The RANS CFD procedure followed to obtain the mean-flow is outlined in the Appendix (B). The grid size of

a 2D axisymmetric RANS CFD grid used (see Figure (3.18)) was approximately 60,000 and for the 3D axisymmetric CFD grid was approximately 14 million. Grids with such a grid size when used within the LRT method will require huge computational time. Therefore, a cartesian box-type grid with relatively less number of grid points (approximately 1 million grid points) was generated, into which the CFD flow quantities such as density, axial velocity, turbulence kinetic energy, turbulence dissipation rate and sound speed were interpolated between the acoustic grid and CFD grid.

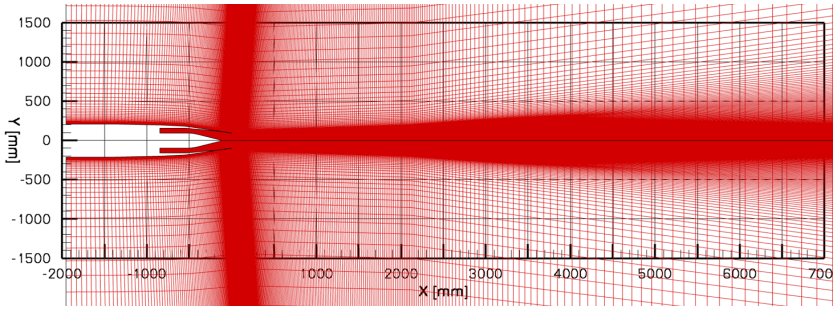

Figure 3.18 – Schematic of a 2D RANS CFD mesh with approximately 60,000 cells for a single stream nozzle. Mesh generated at the Institute of Acoustics (IoA), Warsaw, contracted through Rolls-Royce plc.

The dimension of the acoustic grid depended on the flow field of each jet that was to be computed. The axial length of the grid extended up to 30 jet diameters and the radial and azimuthal dimensions depended on the spreading of the jet. It was ensured that the jet shear layers were well captured. The resolution of the grid in the radial and azimuthal direction were generally high. For the acoustic grid, 10 grid points per wavelength was used. Almeida [139] calculated the minimum number of points required in the acoustic grid that provide good noise prediction. For a frequency of 20 kHz, the minimum mesh size was of the order of 0.002 m, when 10 points per wavelength was considered. This facilitated better interpolation of flow variables in the shear layer where the source densities are high (see Figure (3.17)).

3.6.2 Source points for ray tracing

Once the RANS data has been interpolated onto the acoustic grid, the mean flow variables are used to spatially distribute the source points within the grid. The distribution of the source points are based on the local Mach number of the flow. The density of the source points are higher at regions where the gradients are high, such as in the shear layer, and coarsens with the spreading of the jet. Source point distribution for an isothermal single stream nozzle is as shown in Figure (3.19). The jet is discretised into approximately 2000 source points.

From each source point, 655,000 rays are launched evenly in all directions and their paths are traced with the help of a 4^{th}-order Runge-Kutta scheme. In the far-field, flow

factors are calculated as ΔSPL. For a given source point and a given polar and azimuthal observer location, a negative ΔSPL refers to attenuation and a positive ΔSPL refers to sound amplification. The path followed by a ray is a function of gradients of velocity, sound speed and temperature and the location of the source in the jet. For example, a source located in the midst of the shear layer refracts (or bends) more from its initial trajectory due to the strong flow gradients in the shear layer compared to a source placed along the jet axis. This can also influence the amplitude of the ray in the far-field.

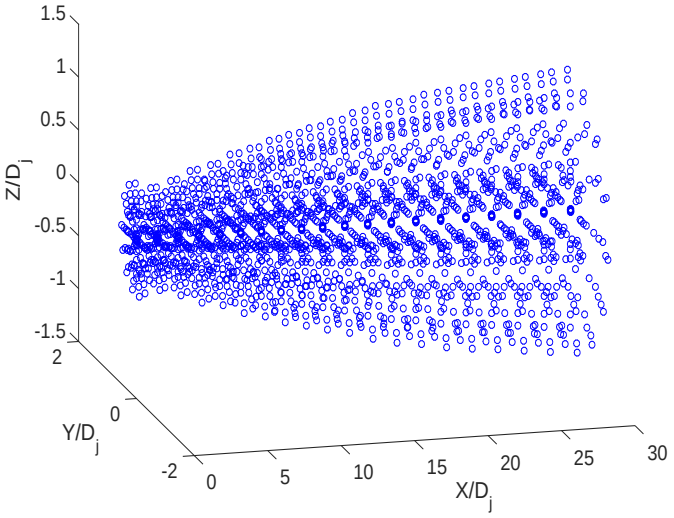

Figure 3.19 – Discretisation of the jet with 2060 source points.

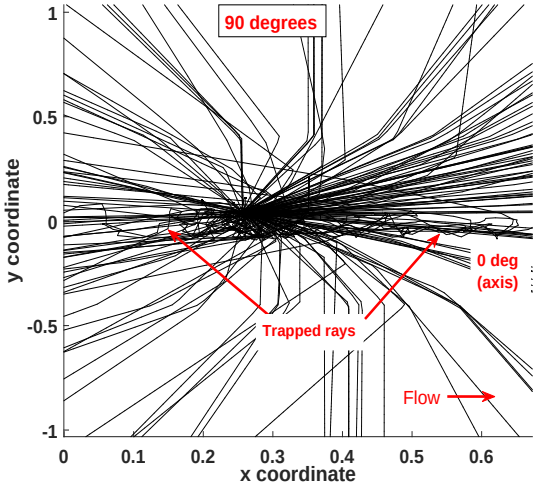

Figure 3.20 – Ray trajectories calculated at the θ=90^{o} polar angles for a source located in midst of the shear layer.

Figure (3.20) shows ray trajectories from a source placed in the shear layer of a single stream jet. The plot shows refracted rays and also trapped rays which are formed due to total internal reflection (TIR). Such trapped rays were also observed by Fruend et al.

[134], where rays were traced in an unsteady medium computed using the DNS. These trapped rays spend longer time in the jet before it reaches the desired far-field ray bin location. In the LRT method, to reduce the computational time, the number of time steps is limited to 400. Therefore, rays which do not reach the end of the jet boundary (0.8 times less than the polar radius of the jet domain), are considered as 'trapped rays'. For these trapped rays, a default flow factor value of -200 dB is assigned.

3.6.3 Coupling source and refraction results

Once the ray tracing results are calculated for the desired polar and azimuthal angles, the ΔSPL results are coupled with source strength and directivities to calculate the far-field intensity using equation (3.70),

$$I(\mathbf{r},\theta) = \int \overline{p^2}(\mathbf{y},\theta).10^{(0.1\Delta SPL_{(RT)})}\mathrm{d}\mathbf{y}. \tag{3.70}$$

In the next section, the application of the LRT method to a single stream jet to compute the far-field noise spectra is presented.

3.7 Applications of the LRT method

The LRT method has so far been used to calculate far-field noise from different types of nozzle geometries and flow conditions [89]. Some of the results were stored in the ISVR database. The LRT method was also applied to compute noise from axisymmetric short-cowl nozzles and 3D installed nozzle (pylon with centre-body) configurations as part of the HARMONY [wHole AiRcraft Multidisciplinary nOise desigN sYstem] programme [140]. In this section, LRT predictions for an isothermal single stream nozzle are compared against experimental data are presented. The nozzle design and the experiments were part of the SYMPHONY test programme. The noise measurements were conducted at the large-scale noise testing facility at QinetiQ, in Farnborough, UK.

The comparison of predicted spectra and OASPL directivities against experimental data at various polar angles are presented in Figure (3.21) and (3.22). From the plots it is clear that the LRT predictions compare well with the experimental data with ±1dB difference at the 90^o and 110^o polar angle throughout the spectrum, and an over-prediction of up to 2dB at 10 kHz at the 60^o polar angle. At the 30^o, a significant under-prediction in the entire frequency range can be observed. The under-prediction is more severe at the high frequencies. From the directivity plot (see Figure (3.22)), it can be observed that the under-prediction is observed up to θ_c= 55^o. Such an attenuation in the noise at the shallow angles to the jet axis is due to the exponential decay in the CoS region. The critical CoS angle, θ_c depends on the flow condition. This means that the LRT method fails at the angles near to the jet axis. Therefore, there is a need to develop solutions to model the attenuation within the CoS.

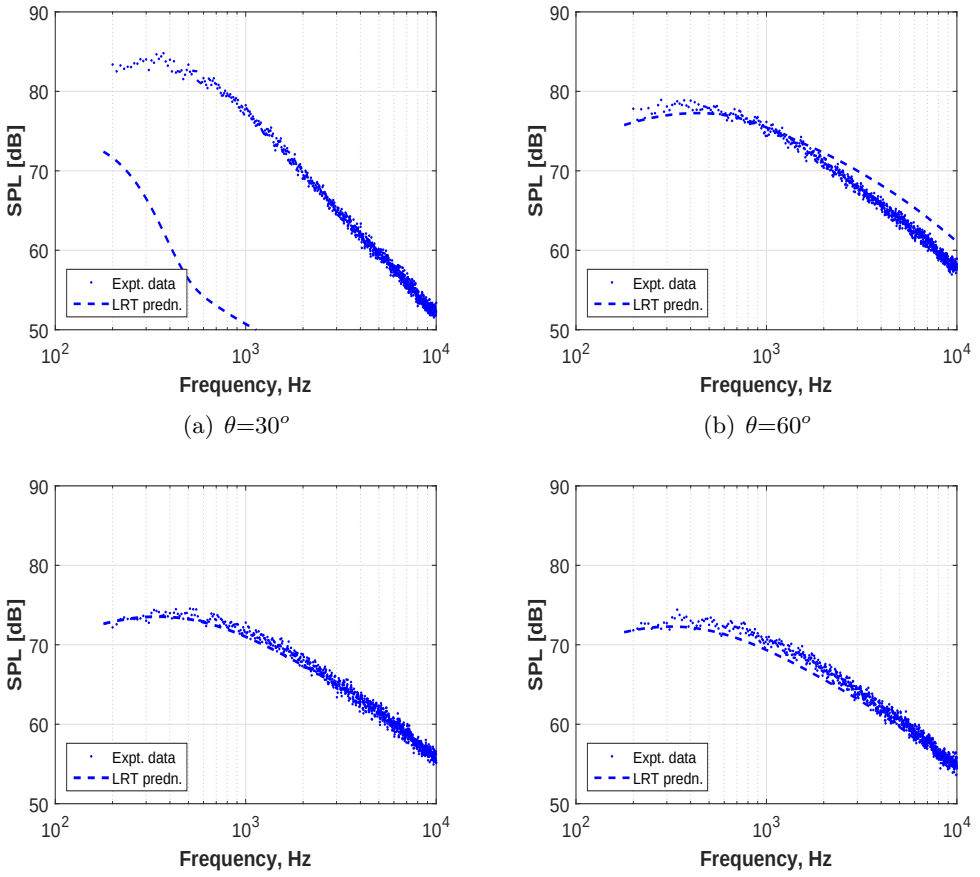

(a) θ=30^o (b) θ=60^o

(c) θ=90^o (d) θ=110^o

Figure 3.21 – Comparison of spectral predictions against expt. data for an isothermal single stream jet at various polar angles, θ and at azimuthal angle, φ=0^o; [D$_j$= 0.1016m, Mach no., M = 0.5].

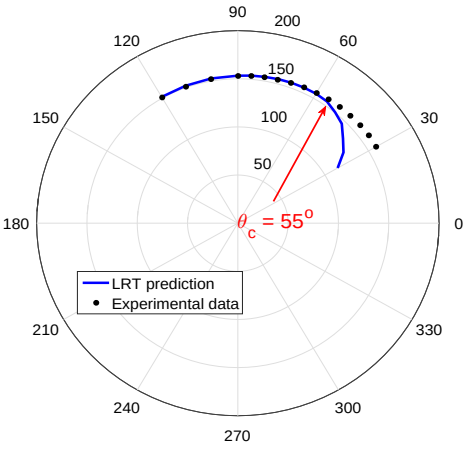

Figure 3.22 – Comparison of OASPL directivity predictions against expt. data for an isothermal single stream jet at various polar angles, θ and at azimuthal angle, φ=0^o; [D$_j$= 0.1016m, Mach no., M = 0.5].

3.8 Chapter summary

The LRT source model is based on Lighthill's acoustic analogy with the acoustic solution based on the methodology followed by Khavaran and Krejsa [49]. The source correlation function is expressed as a linear combination of second-order velocity correlation tensors. Based on Ribner's assumption, a separable spatial and temporal functions are used to model the turbulence kinetic energy. A Gaussian function is used to model the time-delay of correlation. A RANS solution with a k-ϵ turbulence model is used to obtain the source strength and the characteristic time-delay of correlation. The expression for the source strength (see equation (3.35)) is a function of the turbulence kinetic energy, k, source frequency, Ω, fluid density, ρ, eddy length-scale, L_s, eddy time-scale, τ_t, model length-scale and time-scale coefficients, C_L and α_τ, respectively. The length-scale and time-scale coefficients are determined using measured spectral data at the 90^o polar observer angle. The LRT source definition models the impact of source anisotropic on aerodynamic noise using anisotropic parameters Δ and β, which are defined in equations (3.36) and (3.37), respectively.

Ray tracing equations (3.58 and 3.59) are solved using an iterative scheme to calculate the ΔSPL from each source point in the jet. The ΔSPL for all sources are summed up and coupled with the source strength using equation (3.70) to obtain the far field intensity.

Chapter 4

Improvements and application of the LRT method

From the literature review (Section (2.2)), and the current status of the LRT method presented in Section (3.6), the computation of eddy length-scale and time-scale coefficients requires measured acoustic data as a prerequisite. Such a dependence on experimental data hinders the applicability of RANS-based jet noise prediction methods, such as the LRT method, for quieter nozzle designs. Also, the current LRT method does not account for the contribution of anisotropic parameters towards the noise generation. In this chapter, these two aspects are addressed with the help of a parametric study on isothermal single stream and coplanar nozzles for varying flow conditions.

4.1 Background

The governing equations used in the LRT source model are described in Section (3.3.3). The expression for the LRT length-scale, L_s, and time-scale, τ_t, are defined in equations (3.23) and (3.32), respectively. The LRT length-scale coefficient C_l, and time-scale coefficient α_T, and the anisotropic parameters, Δ and β, are an integral part of the LRT source function defined in equation (3.35). From the source equation, it is clear that the LRT coefficients and anisotropic parameters play an important role in coupling the RANS turbulence statistics to the far field noise generation. The LRT coefficients and anisotropic parameters are functions of nozzle flow conditions. The turbulence length-scale and time-scales vary throughout the jet depending on the turbulence decay rate.

Variation of eddy length-scales and time-scales in cold and hot single stream jets were measured by Bridges [141], at the AeroAcoustics Propulsion Lab at NASA Glenn Research Center. Two-point space-time PIV measurements of space-time correlations of velocity for jets for acoustic Mach numbers 0.5 to 1.5, and static temperature ratios up to 2.7 were conducted and analysed. Length-scales and time-scales of cold and hot jets derived from the envelope of cross-correlation peaks in space-time are presented in Figures (4.1) and (4.2), respectively. The measurement shows that the length-scales vary axially (measured at the jet lipline, $\mathrm{y/D_j} = 0.5$) and radially from exit of the nozzle up to 25 jet diameters

downstream of the nozzle. The eddy length-scales closer to the nozzle exit are smaller relative to the jet diameter. These small-scale structures convect with faster decay rate (shorter time-scales) and contribute towards the high frequency part of the noise spectrum. Downstream of the jet axis, large energy bearing structures with higher time-scales produces low frequency noise.

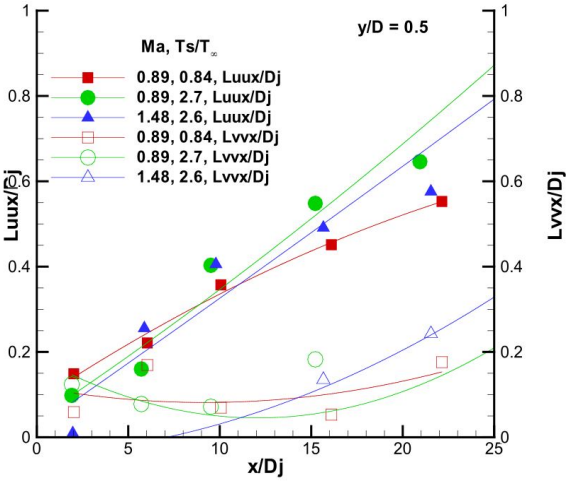

Figure 4.1 – Measured axial (L_{uux}) and radial (L_{vvx}) variation of eddy length-scales for cold and hot single stream jets; $y/D_j = 0.5$, M_a = Acoustic Mach number, T_s/T_∞ = static temperature ratio, $D_j = 0.051$m; Bridges, 2006 [141].

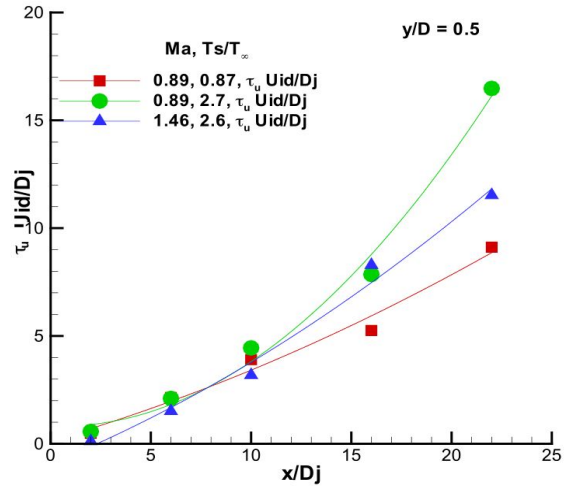

Figure 4.2 – Measured axial and radial variation of eddy time-scales for cold and hot single stream jets; $y/D_j = 0.5$, M_a = Acoustic Mach number, T_s/T_∞ = static temperature ratio, $D_j = 0.051$m; Bridges, 2006 [141].

From Figure (4.1), it can be observed that the axial length-scales are not equal to the radial length-scales, which suggests that turbulence is not isotropic. The time-scales are also observed to increase axially downstream the jet. These measurements also suggests that time-scales are dependent on the shear layer thickness, which complements some of the theoretical [87, 88], and other experimental observations [95, 142], made by other

researchers.

The exponential function, $g(\tau) = e^{-(\frac{\tau}{\tau_o})^2}$, has been used to fit the temporal correlation function. It is worth noting that the LRT source model uses the same function to model the time-scale function (see equation (3.22b)).

From figures (4.1) and (4.2), it is clear that length-scales, ratio of length-scales and time-scales are best modelled as a function of local flow conditions within the jet. The LRT length-scales and time-scales are functions of the mean turbulence kinetic energy, turbulence dissipation rate, and width of the shear layer. The mean turbulence information for the LRT is obtained from a RANS solution with a Standard k-ϵ turbulence model. Therefore it is essential to discuss the RANS modelling procedure used to obtain the mean flow quantities.

4.2 Turbulence statistics from RANS

The first step in the LRT method is to obtain the mean turbulence flow quantities from RANS numerical solution associated with a k-ϵ model. The parameter k designates the turbulent kinetic energy of the flow while ϵ is the turbulent dissipation:

$$\epsilon = \nu \overline{\frac{\partial u_i}{\partial x_j}\left(\frac{\partial u_i}{\partial x_j} + \frac{\partial u_j}{\partial x_i}\right)}, \tag{4.1}$$

where, ν is the kinematic viscosity.

When RANS numerics are used for jet noise calculations, it is important to recall that an average flow field is not sufficient to model the far field noise. For example, the Standard k-ϵ turbulence model is shown to over-predicts the length of the potential core and thereby under-predicts the spreading rate of the shear layer. The average mean flow is computed by assuming isotropic turbulence [64]. The time-averaged solutions are provided based on eddy viscosity models using Boussinesq hypothesis. The Boussinesq hypothesis ignores the small-scale vortices but considers the large-scale energy bearing eddies to calculate the length scales.

The integral scales however should be in principle determined from turbulence spectral correlations. However, from RANS, longitudinal and transverse integral length scales of turbulence may be specified in terms of k and ϵ as,

$$L_1 = \frac{\left(\overline{u_{t1}^2}\right)^{3/2}}{\epsilon} \qquad \text{and} \qquad L_2 = \frac{\left(\overline{u_{t2}^2}\right)^{3/2}}{\epsilon}. \tag{4.2}$$

The RANS model considers $\overline{u_{t1}^2} \approx \overline{u_{t2}^2} \approx {}^2/_3 k$ and as a consequence, the scale L_2 becomes identical to L_1. This is because the concept of turbulent viscosity is unable to correctly represent the parting of the kinetic energy between the longitudinal and transverse directions [45]. In a jet, the eddies in the shear layer are stretched as it convects downstream of the jet. The stretching of the eddies brings in a variation in the eddy aspect

ratio, which is very important in the noise generation process. The k-ϵ type turbulence models cannot model such flow effects. To account for this, the LRT source model uses the parameter, $\Delta = L_2/L_1$ to model the length scale ratio, and $\beta = \overline{u_{t2}^2}/\overline{u_{t1}^2}$ to model the ratio of turbulence intensities. In the literature on jet noise modelling [45, 83], the parameter Δ has been assumed to be equal to 1/3 throughout the jet. Some of the early experiments suggests this, but this was measured at the end of the potential core, for low subsonic Mach numbers [2, 84]. Recent experiments suggests that the ratio of length scales in the shear layer vary as a function of jet parameters along the jet flow direction [96, 118]. Therefore, in the current work, to account for the variation in the anisotropy, Δ and β are added as an input to the source model.

4.3 Problem definition

This section presents the improvements incorporated within the LRT method. The improvements proposed are listed below:

- In the current equation for the LRT time-scale, along with mean turbulence kinetic energy and dissipation rate, the jet diameter is used to define the width of the shear layer, which is not physical. Therefore, the LRT time-scale has been amended to depend on the local flow parameters in the jet.
- A procedure to determine the LRT coefficients has been proposed for single stream and coplanar nozzles.
- Using this procedure, a parametric study has been carried out to study the effect of various jet parameters.
- Effect of anisotropy on varying jet parameters has also been investigated.

4.4 Amendment expression of the LRT time-scale

The LRT time-scale (equation 4.3) addresses the frequency dependence and has been shown to provide better predictions compared to the traditional dissipation rate time scale. In this expression, the parameter, Λ, denotes the size of an eddy.

$$\tau_t = \alpha_T \, \tau_d \left(\frac{L}{\Lambda} \right)^{2/3} \tag{4.3}$$

Previously, it was assumed that Λ scaled with the jet diameter [88]. Such an approach focuses only on the high-frequencies. The size of an eddy in the jet shear layer varies with the convective Mach number along the jet. In coaxial jets, the spreading of the shear layer depends on the area ratio and velocity ratio which affects the mixing characteristics and in turn varies the size of eddies. In the current work, Λ is related to the local vorticity

thickness, δ_θ. The vorticity thickness is defined as,

$$\delta_\theta = \frac{\Delta U}{|\partial U/\partial r|_{max}}, \tag{4.4}$$

where, the difference in mean velocity, ΔU = $r_{5\%}$ - $r_{95\%}$, where $r_{5\%}$ and $r_{95\%}$ are the radial distances at which the mean velocity has fallen by 5% and 95% respectively. The variation of vorticity thickness for single stream jets with varying Mach number is shown in Figure (4.3). This variation in the vorticity thickness in the LRT time-scale comple ments the frequency dependence aspect.

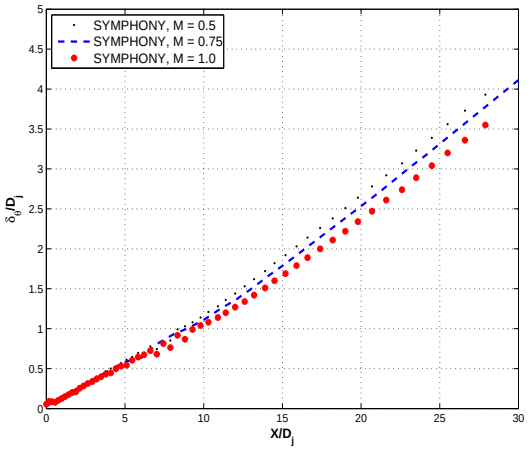

Figure 4.3 – Axial variation of vorticity thickness computed using RANS mean-flow for single stream jets for varying Mach number [SYMPHONY test nozzle, nozzle diameter, D_j = 0.1016m].

With the amended LRT time-scale, the task of making the LRT parameters depend on the local flow conditions is partially achieved. The role of LRT coefficients are described in Section (3.3.5). The next step is to arrive at a method to determine the LRT length-scale and time-scale coefficients with minimal dependence on measured acoustic data. This is achieved by carrying out a parametric study on isothermal single stream jets. Later, the parametric study will be extended to isothermal coplanar nozzles.

4.5 Parametric study using single stream jets

This parametric study is initially focused on isothermal single stream nozzles with varying jet diameter and Mach number. Single stream nozzles pose a simple case with fewer jet parameters compared to coaxial jets. The LRT coefficients C_l, α_T, including Δ and β (the anisotropic parameters), are part of the parametric study. The procedure to determine these coefficients are first addressed in the following section. The improved procedure is focused on the main noise producing regions in a jet, individually.

Fisher et al. [57, 58] and, Ko and Kwan [59] proposed the concept of a 4-source method, where the 4 main noise producing regions in a coaxial nozzles were identified. This concept is adopted in the current work to distinguish between the different noise

producing regions in a single stream jet. With the lack of measured turbulence data at various location in the jet, such an approach, can give an insight at the source mechanism at the main noise producing regions. The aim here is also to understand the variation of anisotropic parameters in the major noise producing regions and their effect on varying flow conditions.

In the next section, the description of a 4-source model is presented. Further, this concept is used to compute the LRT length-scale and time-scale coefficients for single stream jets.

4.5.1 Improved procedure to determine the LRT coefficients

Following the concept of a 4-source method [57, 58, 59], the jet is split into 3 main noise producing regions: secondary jet, effective jet and mixed jet. The interaction between the primary and secondary shear layers are of little significance for velocity ratios less than 0.6. The noise source strength in this region is a function of the relative velocities between the primary and the secondary nozzles. Since the velocity ratio of modern aero-engines typically ranges from 0.6 to 1.0, this source region has been shown by Fisher et al. [57, 58], to be of little importance in the overall noise produced by coaxial nozzles. The schematic of the concept is shown in Figure (4.4).

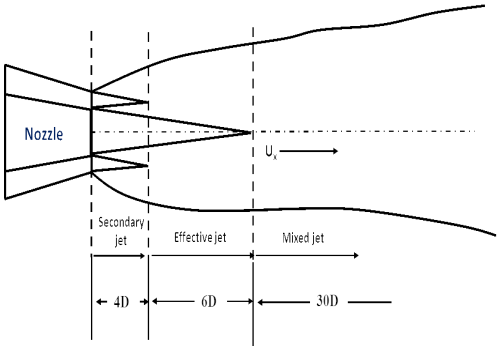

Figure 4.4 – Main noise producing regions for a coaxial jet.

Each of the 3 main noise producing regions are described as follows:

Secondary region:

This region comprises of potential cores of both primary and secondary jets and axially extends up to the end of the potential core of the secondary jet, i.e., equivalent of a single stream jet. This region is characterised by the secondary jet velocity, temperature and nozzle diameter. This region mainly comprises of small-scale turbulence and contributes towards the high frequency part of the spectrum.

Effective region:

In this region the shear layers of both the primary and secondary merge giving rise to peak turbulence levels up to 10% of the primary velocity for a coaxial jet (up to 15% for a single stream isolated, isothermal jet). The velocity in this region is characterised by

primary velocity and by effective diameter, D_e defined as,

$$D_e = D_p \sqrt{(1 + AR \times VR^2)}, \tag{4.5}$$

where, area ratio, AR is the ratio of area of secondary diameter to primary/core diameter ($AR = A_s/A_p$), and velocity ratio, VR is the ratio of secondary/bypass velocity to primary/core velocity, ($VR = U_s/U_p$).

Mixed region:

Far downstream of the jet, noise is characterised by mixed-flow jet velocity (primary, secondary and ambient flow), mixed diameter, and mixed temperature. This region mainly comprises of large-scale turbulence and contributes towards the low frequency part of the spectrum. Expressions for mixed velocity U_m, and mixed diameter, D_m is defined as,

$$V_{mix} = U_p \frac{(1 + AR \times VR^2)}{(1 + AR \times VR)}, \qquad \text{and} \qquad D_m = D_p \frac{(1 + AR \times VR)^2}{\sqrt{(1 + AR \times VR^2)}} \tag{4.6}$$

4.5.1.1 Process to determine LRT coefficients

The LRT methods has 2 coefficients , C_l & α_T, and 2 anisotropy parameters Δ & β.

- Using the concept of the 4-source method, divide the jet domain into secondary, effective and mixed jet.
- From the literature it has been shown that the ratio of length scales Δ can be assumed as 1.0, and β as 0.5 in the mixed jet region. Using these values, determine coefficients C_l and α_T as best fits to the mixed jet spectrum compared with measured data at the 90^o polar angle.
- Fix the values of C_l and α_T for rest of the calculations. From Almeida et al. it has been shown that the value of β=0.5 in the effective and secondary jet region. Determine anisotropy parameter Δ as best fits to the effective and secondary jet spectra compared with measured data at the 90^o polar angle.
- Add the individual spectrum for secondary, effective and mixed jet to obtain the total spectrum at the 90^o polar angle.
- The LRT coefficients and anisotropy parameters remain fixed while computing spectra for other polar angles.

4.5.2 Computation of LRT length-scale and time-scale coefficients

Experiments [96, 143, 144] have shown that turbulence in the mixed region tends to be isotropically moving axially downstream of the jet. These experiments were conducted using single stream jets for high subsonic Mach numbers. Morris and Zaman have conducted hot-wire measurements on a 50.8mm diameter nozzle for a nominal jet velocity of

87m/s. Variation of axial, radial and azimuthal length scales in the mid-shear layer at two axial locations, $5D_j$ and $9D_j$. Measurements near the end of the potential core (see Figure (4.5(a))) suggests that the decay of the spatial cross-correlation is dominated by the high frequency. Also compared are the second and fourth-order correlations. Downstream of the jet (Figure 4.5(b)), the axial length scales at the lower Strouhal numbers are almost constant and at high frequencies the length scales decay inversely with Strouhal number. Measurements at $9D_j$ compared with that at $5D_j$ suggests that the length scales have increased at low Strouhal numbers, but are nearly unchanged at high Strouhal numbers. These observation are in agreement with measurements made by Harper-Bourne [84]. The ratio of length scales Δ, in the mixed region can therefore be assumed to be equal to 1.0.

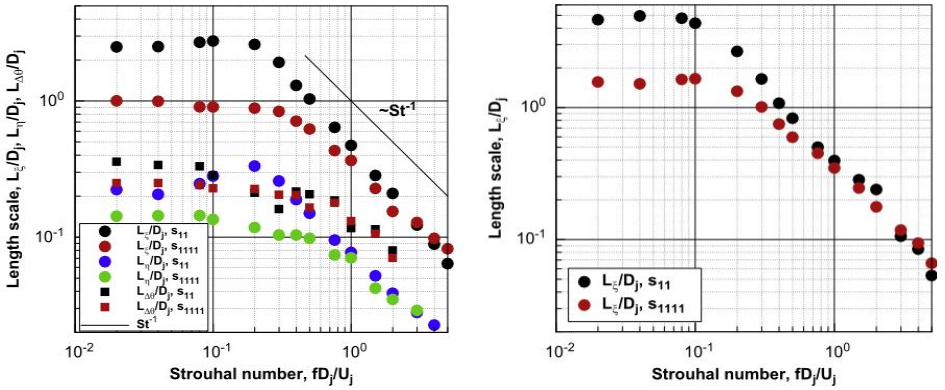

(a) $X/D_j = 5$ (b) $X/D_j = 9$

Figure 4.5 – Variation of axial, radial and azimuthal length scales with Strouhal number. Lipline measurements at two axial locations for a single stream jet [96].

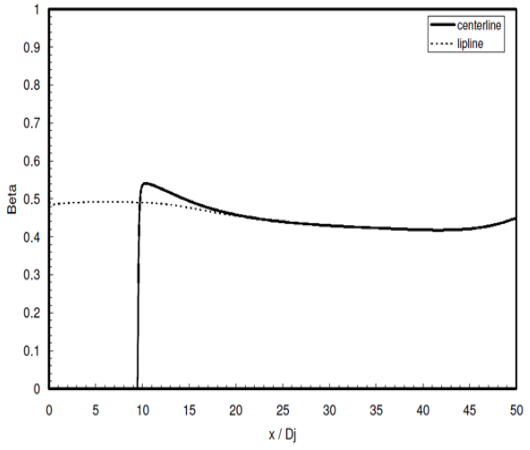

Figure 4.6 – Variation of parameter β computed from Reynolds Stress Modelling for a single stream jet, [53].

Harper-Bourne [116] conducted hot-wire anemometer measurements in a low speed air jet to model jet mixing noise using Lighthill's acoustic analogy evaluated in a fixed frame of reference. The measurements include second and fourth-order two-point space-time correlations for axial velocity, associated cross-spectra and spectral length scales of

the axial and lateral velocity components. The intensity of $\overline{u_t}$ and $\overline{u_t^2}$ were measured at low jet velocities of 30m/s and 61m/s, with the hot-wire probe at the nozzle lip-line at 4 jet diameters in the axial distance were presented as a function of velocity. The ratio of turbulence intensities, $\beta = \overline{u_{t1}^2}/\overline{u_{t1}^2}$ was measured to be about 0.5.

Recently, Almeida et al. [53] has computed the value of β for a single stream jet (Mach number = 0.75), using the Reynolds Stress Modelling method. A constant value of $\beta = 0.5$ at the nozzle lip-line from lip of the nozzle up to 30 axial jet diameters has been computed (see Figure 4.6). We assume β=0.5 in the 3 noise producing regions.

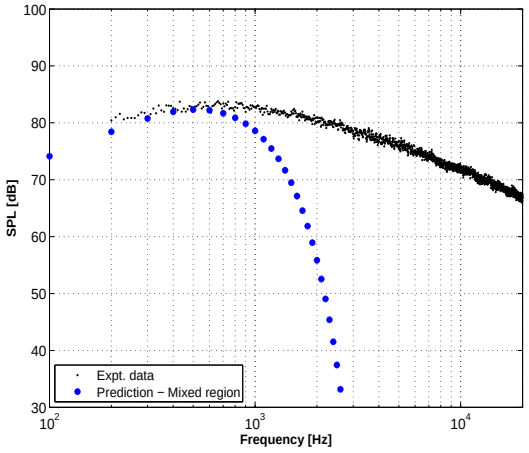

Figure 4.7 – Comparison of experimental data with LRT prediction for the mixed jet for an isothermal single stream jet; [Mach no.= 0.75, D_j=0.1016m, polar angle = 90°].

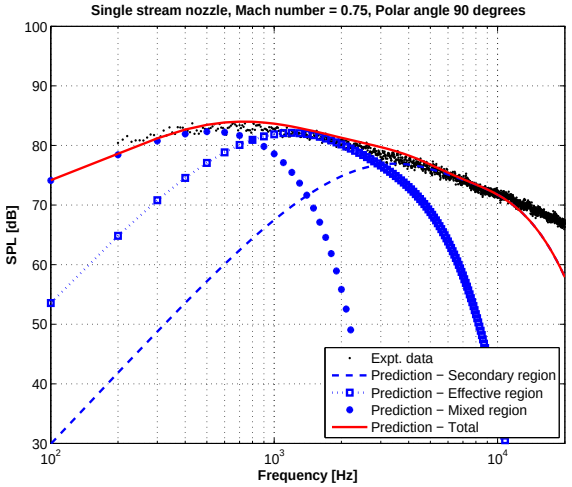

Figure 4.8 – Predicted spectra with individual noise generating regions [D_j = 0.1016m, M = 0.75].

With known estimates of Δ=1.0 and β=0.5, the unknown LRT coefficients C_l and α_T for the mixed jet spectrum are calculated using the LRT method as best-fit to the measured spectrum at the 90° polar observer angle. The comparison of predicted mixed jet spectrum with the measured data at the 90° polar observer angle for an isothermal single stream jet from the SYMPHONY test programme is shown in the Figure (4.7).

The computed LRT coefficients for the mixed jet models the spectral shape and the amplitude of the predicted spectra. These coefficients are kept constant while calculating the secondary and effective jet spectra at the 90° polar angle. The procedure to compute the secondary and effective jet spectra is presented in the next section.

4.5.3 Determining the anisotropy parameters

The assumption of isotropic turbulence in the mixed jet presents a simplified condition to determine C_l and α_T. The turbulence in the secondary region which is near the nozzle exit is anisotropic as the mean velocity gradients are high. This results in the "stretching" of the eddies. Such variations in the eddy aspect ratio are accounted for by the anisotropic parameter Δ. The same is true in the effective region as well.

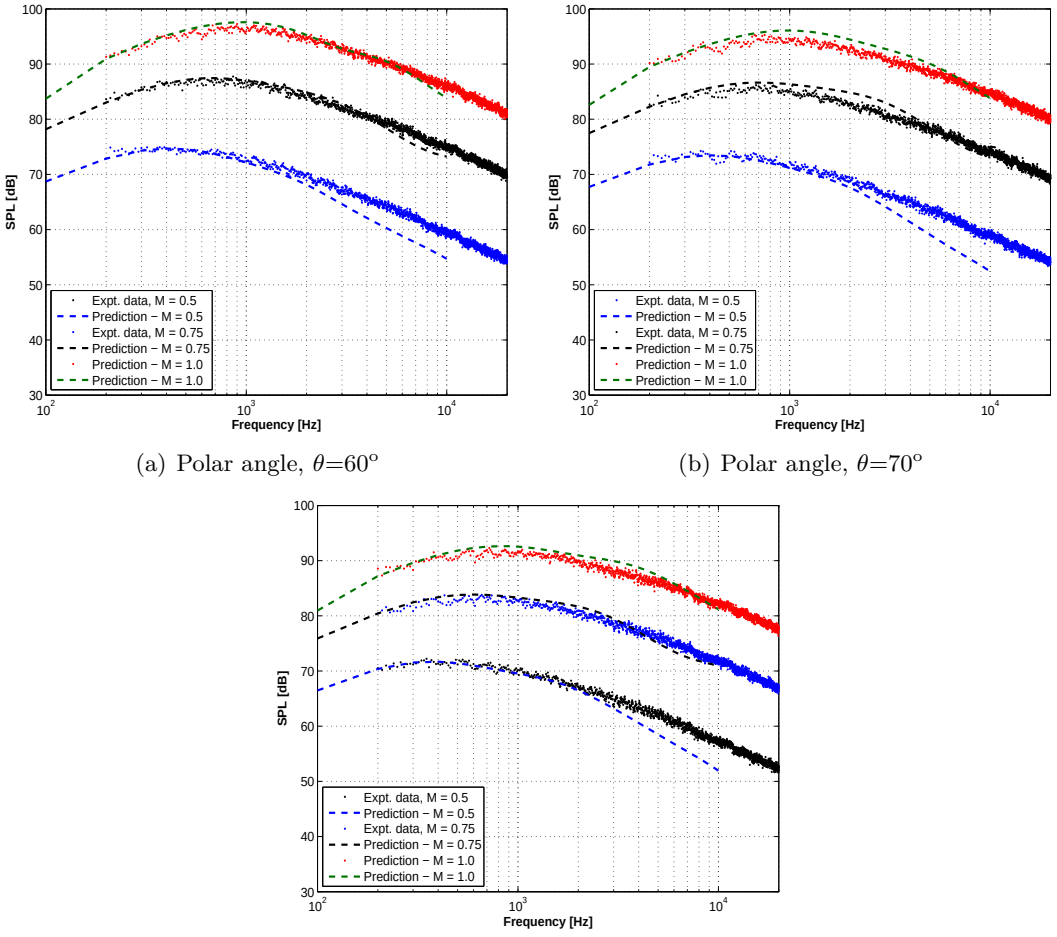

(a) Polar angle, θ=60°

(b) Polar angle, θ=70°

(c) Polar angle, θ=90°

Figure 4.9 – Comparison of LRT predictions with measured data for single stream jets for Mach numbers 0.5, 0.75, 1.0 at polar angle, θ = 60°, 70° and 90°.

For the effective and secondary region, the length scale and time scale coefficients used to compute the mixed jet spectra are used. With β=0.5, values of length-scale ratio, Δ for the secondary and effective region are determined as best-fits to the measured peak and high frequency parts of the spectrum at the 90° polar angle. Spectral predictions from the 3 individual noise producing regions are summed to obtain the total spectrum, as shown

in Figure (4.8). Data shown in Figure (4.8) is for a single stream nozzle (jet diameter, D_j = 0.1016m, acoustic Mach number = 0.75) from the SYMPHONY database.

Figure (4.9) shows predicted spectra at 60°, 70° and 90° polar angles for three Mach numbers, 0.5, 0.75 and 1.0. For polar angles away from the 90° angle, refraction effects have to be considered. For these angles, flow factors calculated from ray tracing has been included. For all these cases, the LRT length scale and time scale coefficients were kept constant at, C_l=0.95, α_T=0.43. This suggests that the LRT coefficients are solely source parameters and are independent of the propagation mechanism.

The application of the improved LRT method shows that a unique set of length-scale and time-scale coefficients can be used to analyse a range of nozzles flow conditions. This also draws us a step closer to our aim to obtain noise predictions with minimal dependence on experimental data.

Justifications for using a constant set LRT length-scale and time-scale coefficients for a range of nozzle flow conditions are as follows:

Constant RANS CFD grid size

For all the single stream jet conditions, the RANS CFD grid generation procedure employed was the same (see Figure (3.18)). The number of grid points were constant for all flow conditions. The LRT acoustic grid used to perform the acoustic computations for each case had the same number of grid points.

CFD procedure

The RANS CFD solution procedure followed using the FLUENT solver to obtain the mean flow for each case is identical. The following solver settings were used:

1. Turbulence model: Standard k-ϵ or SST k-ω,
2. Solver type: Density based, (compressible flow)
3. Turbulence dissipation: based on Power law,
4. No heat transfer between the flow and solid body,
5. Initial turbulence intensity = 1%,
6. Turbulence viscosity ratio = 10,
7. The k-ϵ model coefficients were kept constant: $C_{1\epsilon}$=1.44, $C_{e\epsilon}$=1.92, C_μ=0.09, σ_k=1.0, $\sigma_{k\epsilon}$=1.3.

Identical spectral shape for a family of nozzle flow conditions

1. Here, the term "family of nozzles" is used to define the similarity in the type of nozzle geometry and flow conditions that are considered. For example, all nozzle geometries that are analysed in this thesis were measured at the QinetiQ NTF. Therefore, the rig conditions (e.g. inlet turbulence intensity) and the

experimental set up are known. Therefore, the set of coplanar nozzle geometries with varying flow conditions that were considered for the study were of the same family. But the set of short cowl nozzles that will be analysed later in the thesis will be part of a different family due to the change in the geometry. The presence of a centre-body bullet will influence the noise generation, especially at high frequencies. The LRT coefficients remain constant for a family of nozzles.

2. Once the model coefficients are determined, anomalies associated with RANS derived mean-flow quantities are accounted for. The shape of the spectra for a given nozzle diameter (at the 90^o polar angle) does not change with varying jet velocities. As a result, the LRT time-scale coefficient α_T which is responsible to model the spectral shape at the peak noise level, remains constant for varying jet velocities.
3. As discussed in the literature review, RANS models are known to over-predict the length of the potential core. Such a change in the flow can have an implication in the far-field noise prediction. These changes are also accounted by the LRT model coefficients during the calibration process with measured data. This is consistent with various other RANS based jet noise prediction methods available in the literature [48], [54], [87], [90].

4.5.4 Effect of anisotropy in isothermal single stream jets with varying Mach number

With parameter β fixed at 0.5, the variation of ratio of length-scales with varying Mach number has been investigated. From Figure (4.10), the parameter Δ reduces with increase in Mach number. This is due to increased convection effect associated with increase in Mach number which causes the eddies to stretch in the direction of the jet. Such an effect results in increased turbulence decay resulting in increased noise levels. These trends can be interpolated to obtain an estimate of the value of Δ for jets with other Mach numbers of interest.

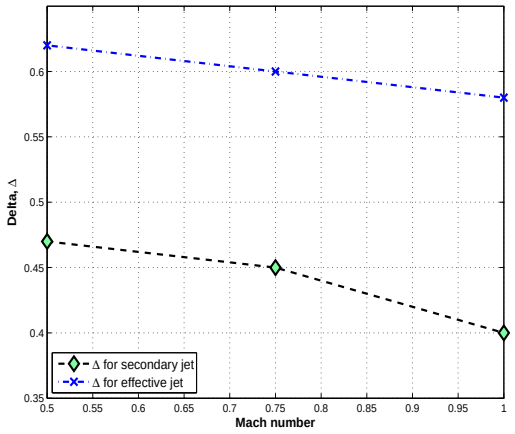

Figure 4.10 – Variation of parameter Δ for single stream jets for varying Mach number

With the help of the parametric study on isothermal single stream jets, an improved procedure to calculate the LRT length-scale and time-scale coefficients, and the anisotropic parameters for varying flow conditions has been presented. In the next section, the parameter study is extended to isothermal coplanar nozzles.

4.6 Application of LRT method to isothermal coplanar nozzles

Along with jet velocity and jet diameter (required for single stream nozzles), parameters such as the velocity ratio (ratio of secondary-to-primary velocity), area ratio and temperature ratio, together with a range of geometric configurations of nozzles will be considered. In this section, the effect of velocity ratio and area ratio on LRT coefficients from static coplanar nozzles are studied. Measured data for these nozzles were obtained from the fundamental coaxial jet noise database from the test programme carried out at the QinetiQ Noise Test Facility (former DRA) [57, 58, 145]. For the coplanar nozzles used, the secondary velocity was fixed at 168m/s and the primary velocity was varied for all area ratio cases. Flow and geometric details are given in Table 4.1.

Spectral predictions for the cases shown in Table (4.1) were obtained by following the procedure described in Section (4.5.1). The vorticity thickness (non-dimensionalised with individual nozzle secondary diameter) for each nozzle case is shown in Figure (4.11). The velocity ratio 1.0 jets has higher vorticity thickness compared to lower velocity ratio nozzle conditions. This means that nozzles with velocity 1.0 spreads more compared to lower velocity ratio nozzles. This implies that the convective effects are high in low velocity ratio nozzles and their noise output will be relatively high. The turbulence mixing region for area ratio 2.0 and 4.0 nozzles with velocity ratio 1.0 is observed at approximately 6.5 jet diameters. For the area ratio 0.87 nozzle (with velocity ratio 1.0), the mixing commences early at 4 jet diameters similar to other velocity ratio and area ratio nozzles.

Area ratio	Primary diameter (m)	Secondary diameter (m)	Primary velocity (m/s)	Secondary velocity (m/s)	Velocity ratio
0.87	0.043	0.058	265 212 168	168	0.63 0.79 1.0
2.0	0.033	0.058	265 212 168	168	0.63 0.79 1.0
4.0	0.033	0.075	265 212 168	168	0.63 0.79 1.0

Table 4.1 – Flow conditions and geometric details of coplanar isothermal nozzles used for the noise calculation; flight stream velocity, $V_f = 0.0$m/s.

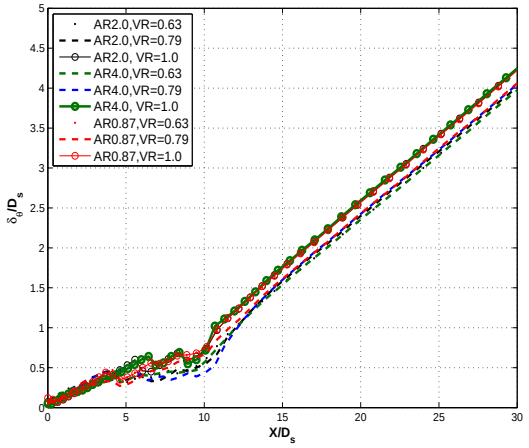

Figure 4.11 – Axial variation of vorticity thickness computed using RANS mean-flow for coplanar nozzles for varying area ratio and velocity ratio.

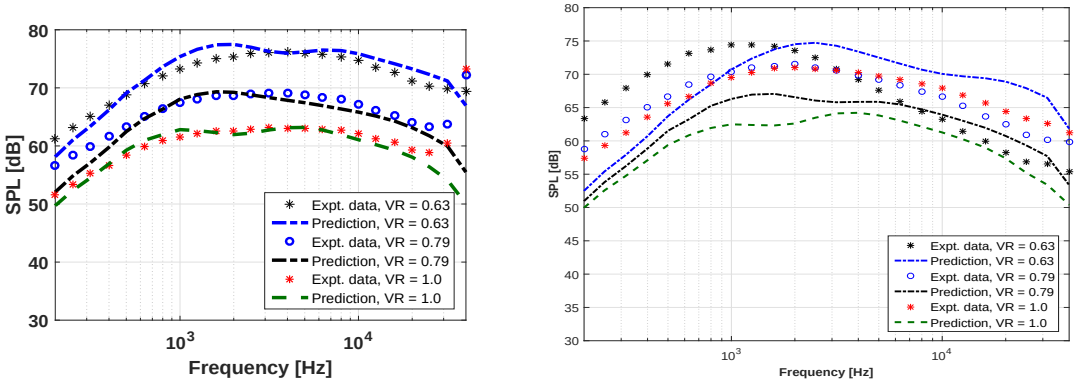

(a) Area ratio 0.87

(b) Area ratio 2.0

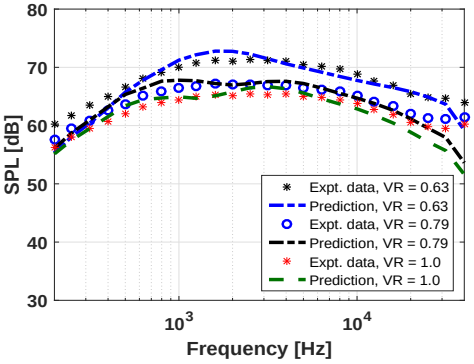

(c) Area ratio 4.0

Figure 4.12 – Effect of area ratio and velocity ratio (VR) on coaxial jet noise spectra for isothermal coplanar nozzles. Comparison of LRT predictions with measured data at the 90° polar angle.

The LRT coefficients and anisotropic parameters were calculated at the 90° polar angle in comparison with the measured spectra. The LRT length-scale coefficient C_L, and time-scale coefficient α_T were 0.40 and 0.29, respectively. These coefficients were kept constant while computing the spectra for other polar angles and also for other coplanar nozzle conditions. Comparison of spectra with measured data at the 90° polar angle is shown in

the Figure (4.12).

Comparisons of 1/3rd-octave band noise spectra between LRT computations and experimental data, for coplanar coaxial nozzles for three velocity ratios and three area ratios are shown in Figure (4.12). It can be observed that, for a given area ratio, SPL increases with increasing velocity ratio. For the AR 4.0 nozzle, the SPLs at the three main noise producing regions are lower compared to the area ratio 0.87 and 2.0 nozzles. Spectral predictions for higher velocity ratios agree well with measured data. But for lower velocity ratios, over-predictions in SPL up to 2.3 dB are observed.

4.7 Effect of eddy length-scale ratio on noise from coplanar nozzles

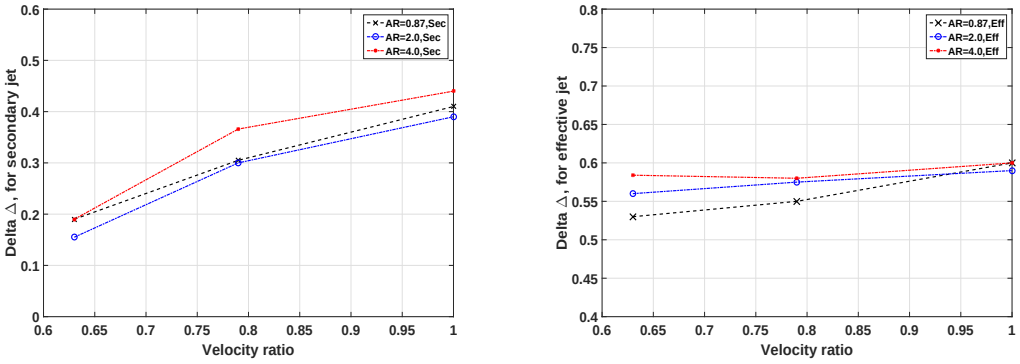

(a) Variation of Δ in secondary jet region

(b) Variation of Δ in effective jet region

Figure 4.13 – Variation of Δ in the secondary and effective region of isothermal coplanar nozzles for varying velocity ratio and area ratios.

The variation of Δ with velocity ratio shows that the length-scale ratio increases with increasing area ratio in both the secondary and effective region. The secondary region closer to the nozzle contains higher turbulence intensities and this causes stretching of eddies thus increasing the length-scale ratio. The stretching effect reduces as an eddy convects downstream from the nozzle which is consistent with the decay/decrease in turbulence.

In the secondary region, the noise is characterised by the secondary velocity and secondary jet diameter. Since the secondary jet velocity for the jets considered in the current study are the same, Δ varies as a function only of secondary diameter. However, for the nozzle with AR 0.87 and VR 0.63, the value of Δ is slightly higher.

In the effective region, the length-scale ratio, Δ, is characterised by the primary velocity and effective diameter, D_e. The effective diameter is a function of primary diameter, D_p, area ratio, AR and velocity ratio, VR. It is defined as, $D_e = D_p\sqrt{(1 + AR \times VR^2)}$ [57, 58]. The variation of Δ in the effective region is similar to the variation of effective diameter for varying velocity ratio and area ratio. For a given area ratio, the effective diameter increases with increasing velocity ratio. But for a given velocity ratio, the variation of effective diameter depends on the primary diameter.

In the next section, the improved procedure to determine the LRT model coefficients

and anisotropy parameters is applied to coplanar nozzles for varying area ratio and velocity ratio. The LRT predictions are further used to assess the effect of mean-flow propagation, effect of velocity ratio and area ratio.

4.8 Application of the LRT method for coplanar nozzles

The LRT method uses a ray tracing method to compute the refraction effects of the sources due to the mean flow. The attenuation or amplification of sources in the far field is quantified in terms of flow factors, or in other words as ΔSPL (see equation (3.69)). Of the three velocity ratios, for practical purposes, velocity ratio 0.79 is significant as most turbofan engine nozzles operates at this velocity ratio. In the next section, the mean flow refraction effects for coplanar nozzles for varying AR and VR are discussed. This is followed by the comparison of spectral and OASPL predictions with experimental data.

4.8.1 Mean-flow refraction effects for coplanar nozzles

In this section, the effect of refraction is analysed in isolation by plotting the flow factors computed using the ray tracing. The flow factor is defined as ratio of the far field intensity to its value without the jet flow with the source strength held constant. The flow factor defined in equation (3.69) shows the amplification or reduction of the SPL due to refraction in the far-field due to a source in the jet plume. Flow factors results in the form of ΔSPL are presented in two forms: (i) by fixing the observer location in the far-field and varying the source location, and (ii) fixing the source position and varying the observer location in the far-field over $0^o < \theta < 180^o$ and $0^o < \varphi < 360^o$ within the jet plume. This enables a better understanding of the three-dimensional nature of the refraction effects for coplanar nozzles for varying area ratios. Figures (4.14), (4.15) and (4.16) shows contour plots of the flow factor, where the negative Flow Factor indicates reduction of SPL due to the flow refraction and positive values show sound amplification.

Flow factors plotted in Figures (4.14), (4.15) and (4.16) shows significant attenuation for all three nozzles for angles 30^o to 50^o measured from the jet axis. This attenuation is due to the cone of silence effect. The cone of silence effect is due to the refraction of rays away from the jet axis due to the flow gradients. As a result, the rays do not propagate at the shallow angles to the jet axis. This creates a shadow zone, causing an attenuation in the sound pressure level. A preliminary method to model the attenuation in the cone of silence is presented in Chapter (6). For angles outside the cone of silence, amplification in the ΔSPL can be observed. However, small amounts of attenuation at these higher angles is observed, but their contribution is not significant towards the far field noise. At the 90^o polar angle no attenuation is observed, as the refraction effect is negligible. ΔSPL in the forward arc angles remains positive for all area ratios. Local amplification zones are also observed caused by sources located off-axis in the shear layer.

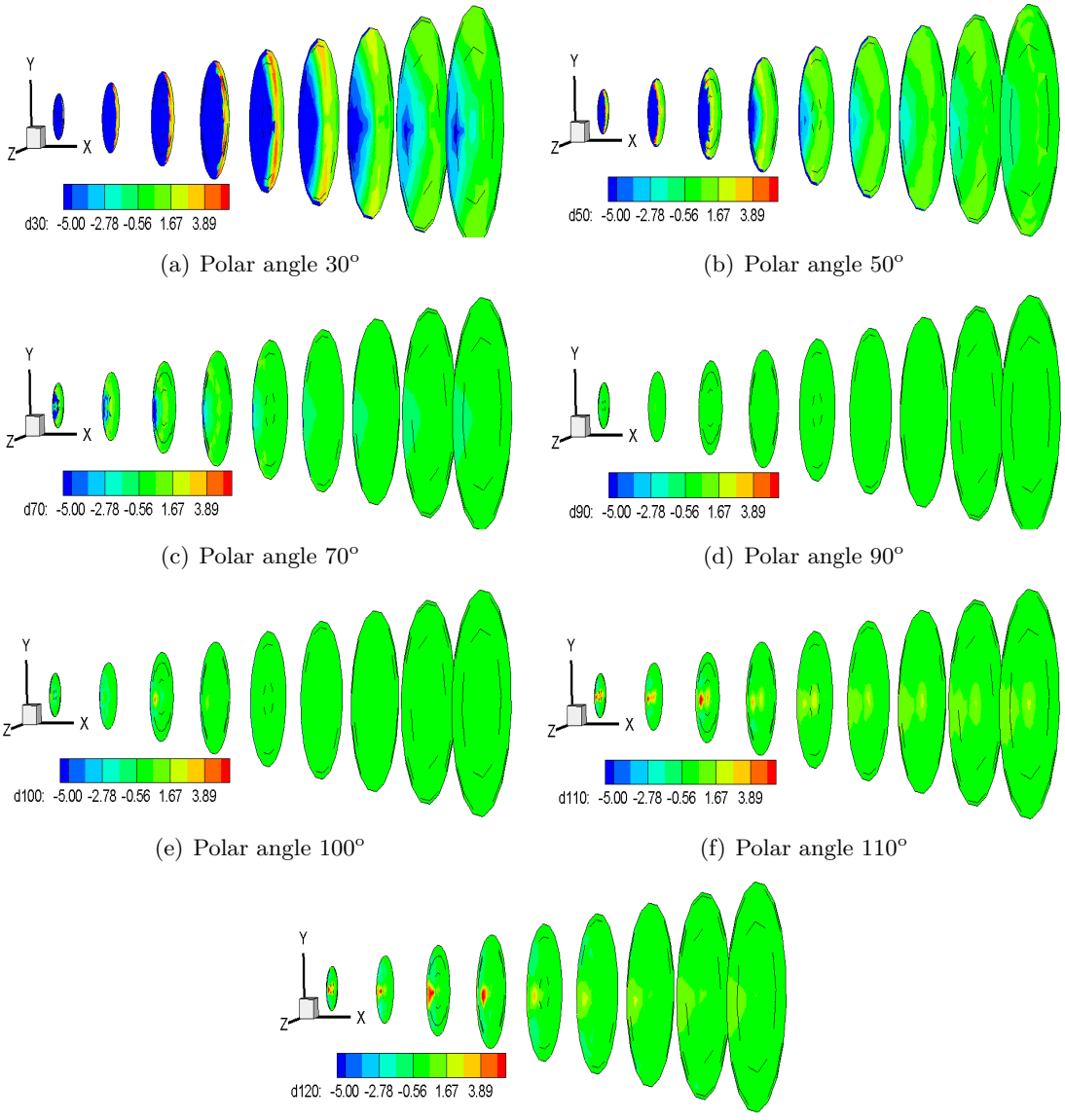

(a) Polar angle 30°

(b) Polar angle 50°

(c) Polar angle 70°

(d) Polar angle 90°

(e) Polar angle 100°

(f) Polar angle 110°

(g) Polar angle 120°

Figure 4.14 – Flow factors for nozzle with area ratio 0.87 and velocity ratio 0.79.

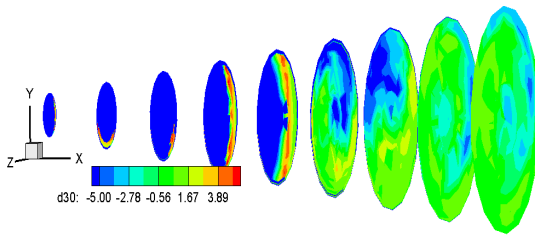

(a) Polar angle 30°

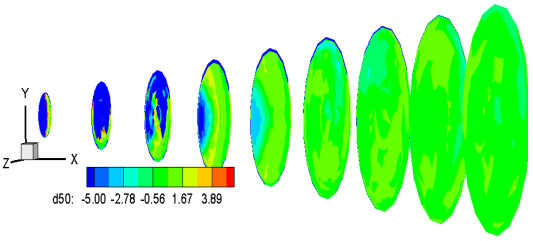

(b) Polar angle 50°

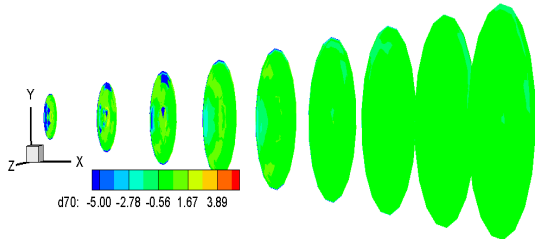

(c) Polar angle 70°

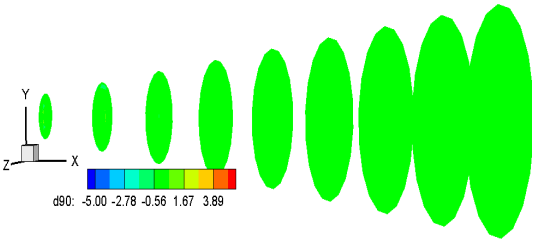

(d) Polar angle 90°

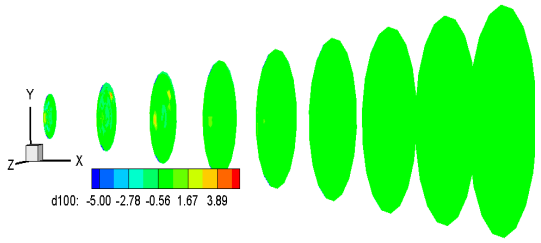

(e) Polar angle 100°

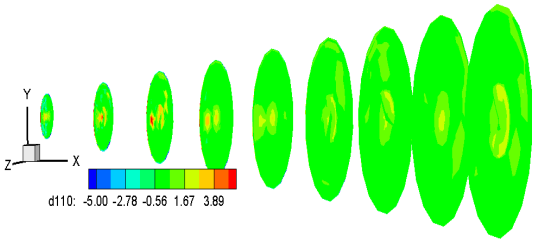

(f) Polar angle 110°

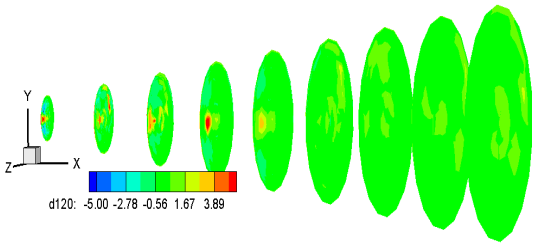

(g) Polar angle 120°

Figure 4.15 – Flow factors for nozzle with area ratio 2.0 and velocity ratio 0.79.

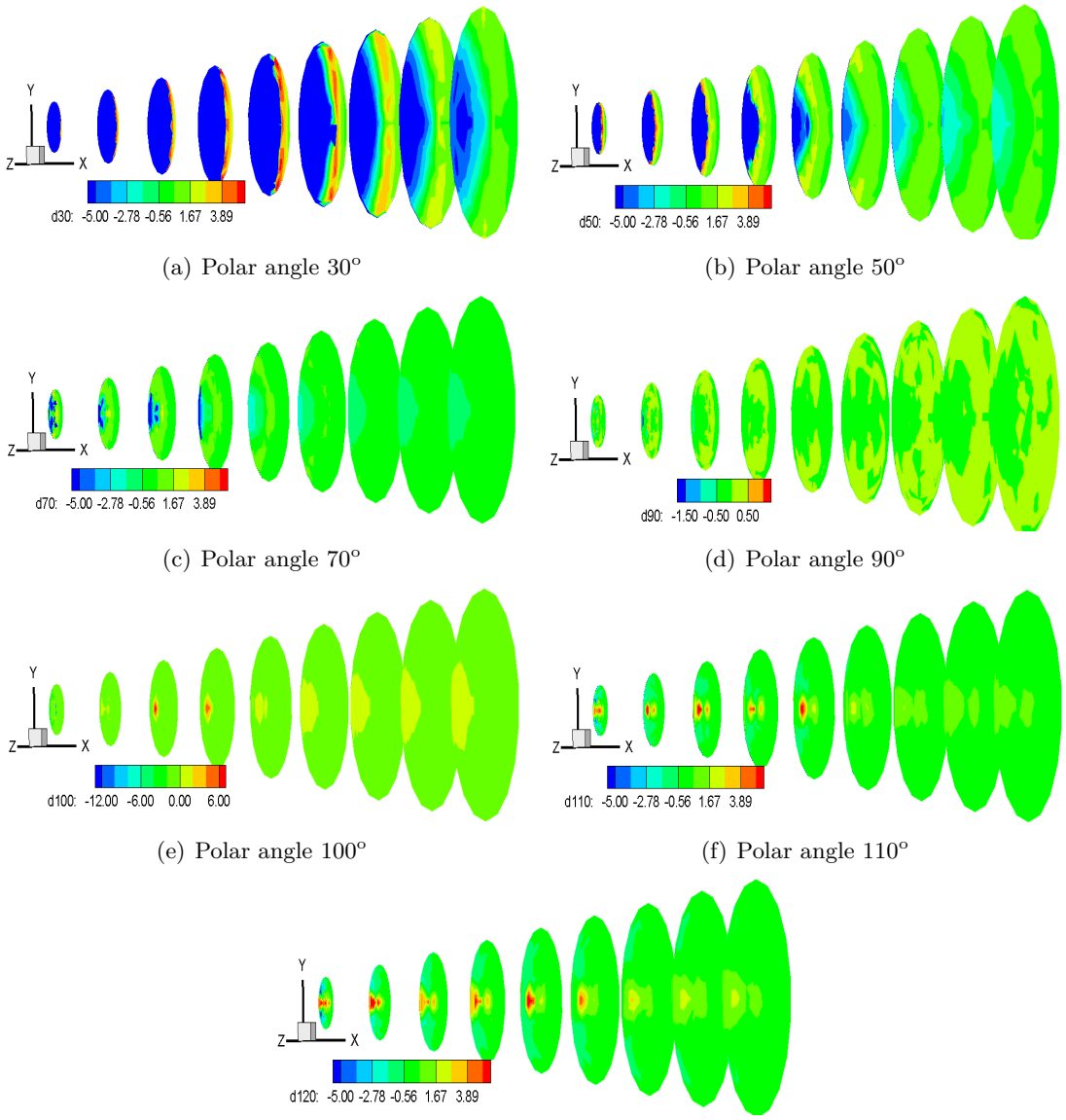

(a) Polar angle 30°

(b) Polar angle 50°

(c) Polar angle 70°

(d) Polar angle 90°

(e) Polar angle 100°

(f) Polar angle 110°

(g) Polar angle 120°

Figure 4.16 – Flow factors for nozzle with area ratio 4.0 and velocity ratio 0.79.

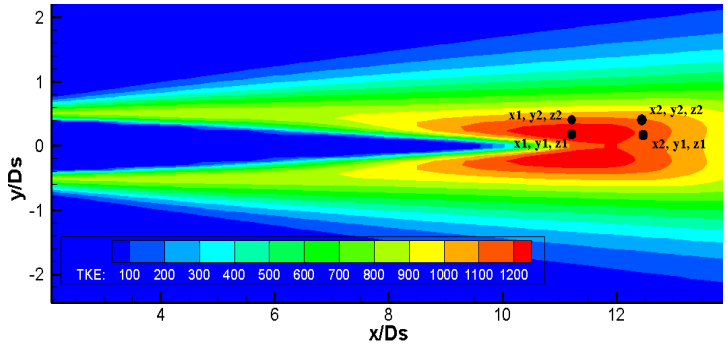

Figure 4.17 – Schematic of source point location used for the flow factor analysis; $x_1 \approx 11.5x/D_s$ and $x_2 \approx 12.5x/D_s$.

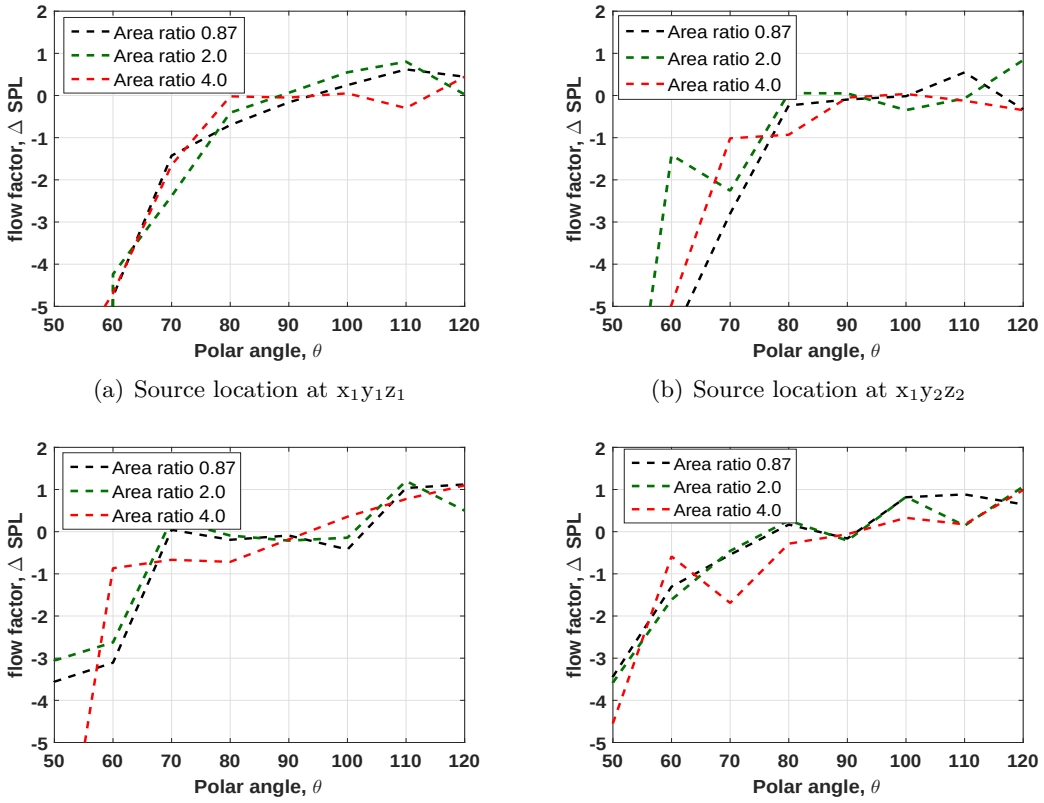

(a) Source location at $x_1y_1z_1$

(b) Source location at $x_1y_2z_2$

(c) Source location at $x_2y_1z_1$

(d) Source location at $x_2y_2z_2$

Figure 4.18 – Effect of area ratio on flow factors for sources located in the mixing layer (velocity ratio 0.79). Source point location as shown in Figure (4.17).

The ΔSPL plots do not provide enough evidence to distinguish the effect of refraction on the area ratio. So a more local investigation of these flow factors has been carried out. Flow factors for sources at two axial locations in the jet shear layer with relatively high turbulence kinetic energy (TKE) are analysed. The location of the sources is shown in Figure (4.17). Magnitude of the TKE for sources located at axial location x_1 are high compared to that located at x_2. From the flow factors plotted in Figure (4.18), it can observed that sources in the area ratio 4.0 nozzle are less noisy compared to area ratio 0.87 and 2.0 for almost all observer angles. This is because the source strength for the area ratio 4.0 nozzle is less due to enhanced mixing in the shear layer.

4.8.2 LRT predictions for coplanar nozzles: Noise spectra

Figures (4.19), (4.20) and (4.21) presents the spectra calculated at various observer angles for nozzles with area ratio 0.87, 2.0 and 4.0, respectively. Except for angles close to the jet axis, predictions agree well with the measured data. However, at the shallow angles, especially at 40° and 50°, which are subjected to the cone of silence affect, it is worth noting that the predictions at the low frequencies agree reasonably well. Most of the low frequency noise is generated from the mixed jet. This shows that the noise in this region is generated by isotropic turbulence. This also suggests that the assumption of isotropic turbulence for the mixed jet is valid.

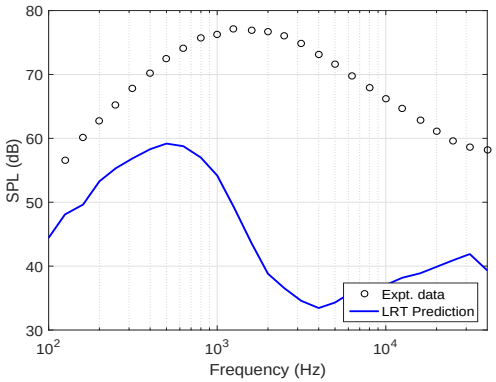

(a) Polar angle 30°

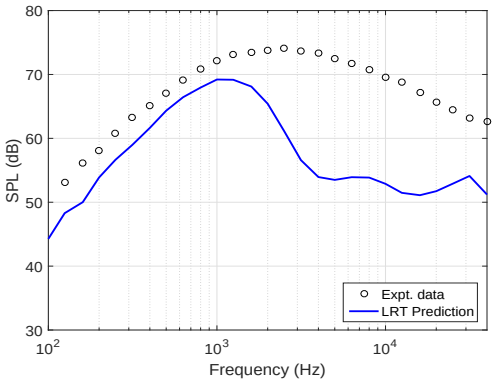

(b) Polar angle 40°

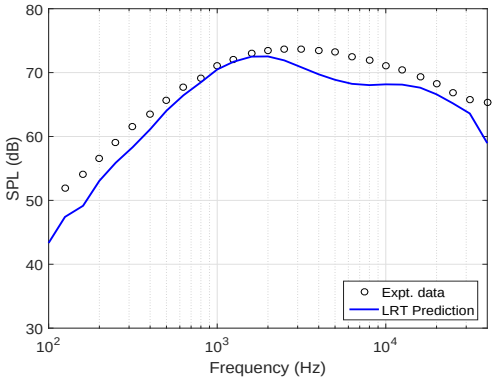

(c) Polar angle 50°

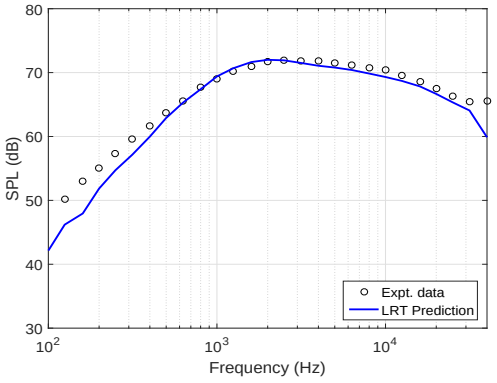

(d) Polar angle 60°

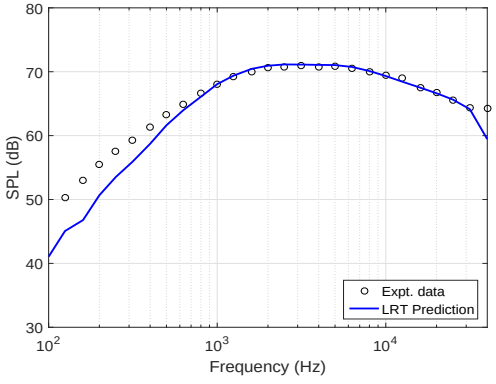

(e) Polar angle 70°

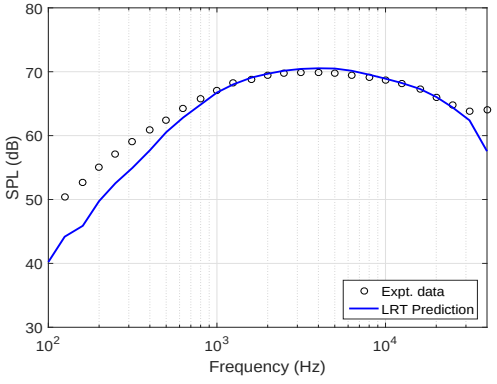

(f) Polar angle 80°

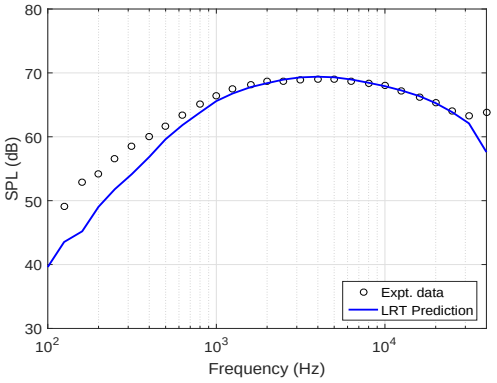

(g) Polar angle 90°

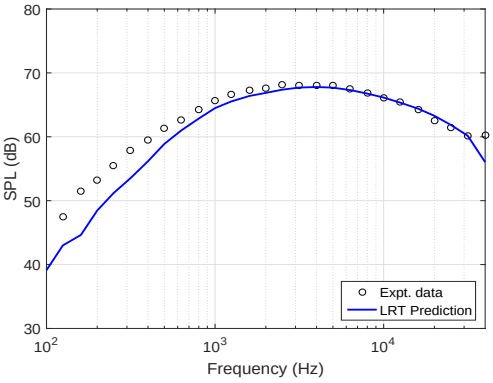

(h) Polar angle 100°

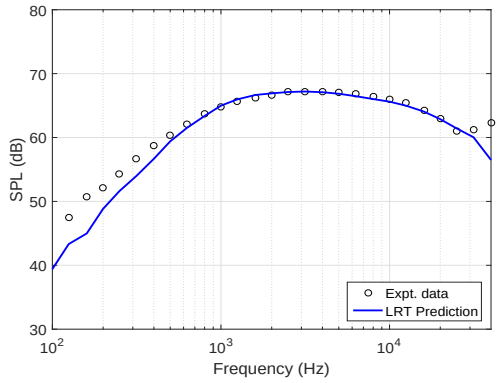

(i) Polar angle 110°

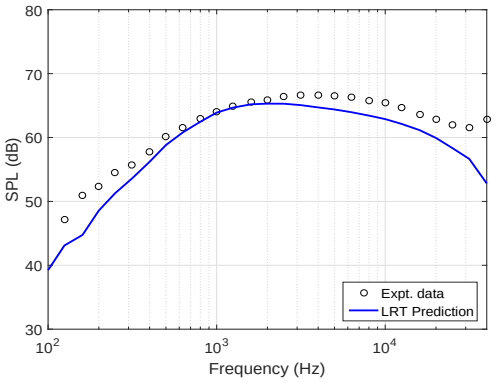

(j) Polar angle 120°

Figure 4.19 – Comparison of LRT predictions of noise spectra with measured data for nozzles with area ratio 0.87 and velocity ratio 0.79.

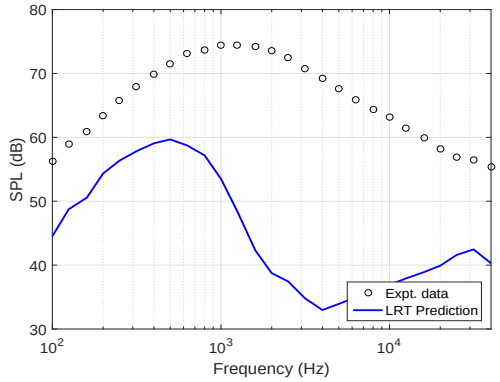

(a) Polar angle 30°

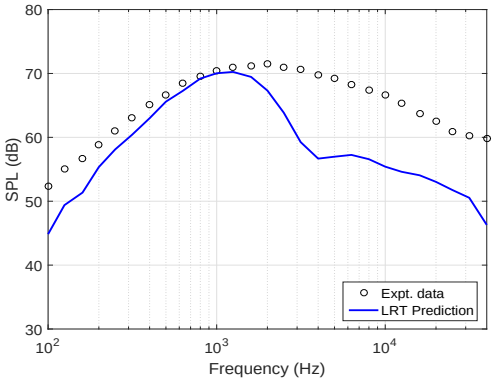

(b) Polar angle 40°

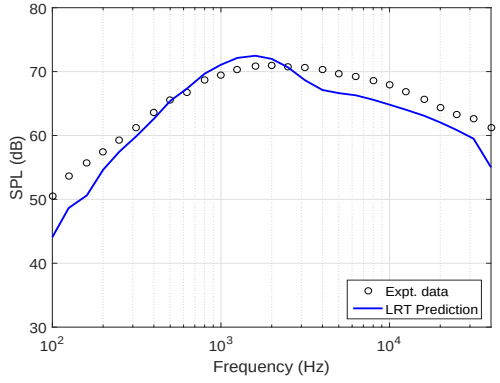

(c) Polar angle 50°

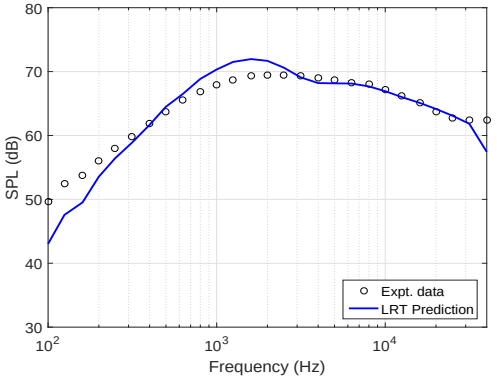

(d) Polar angle 60°

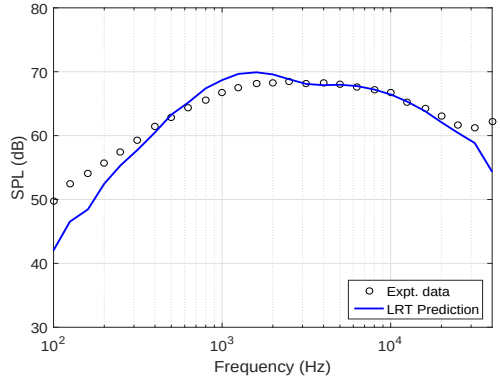

(e) Polar angle 70°

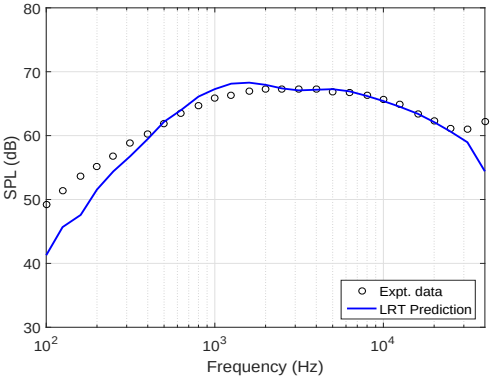

(f) Polar angle 80°

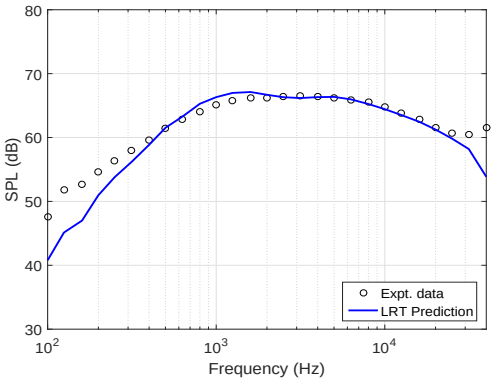

(g) Polar angle 90°

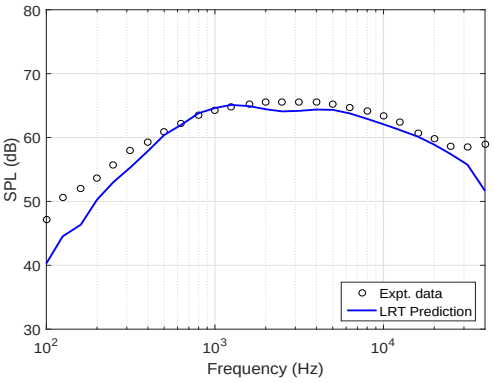

(h) Polar angle 100°

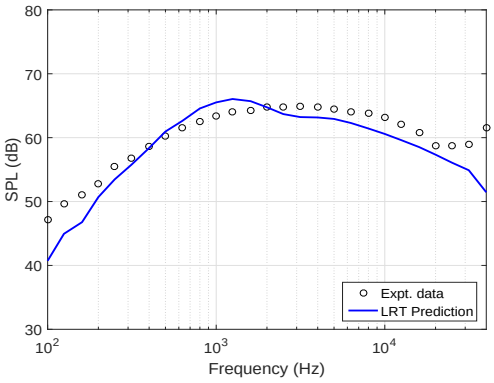

(i) Polar angle 110°

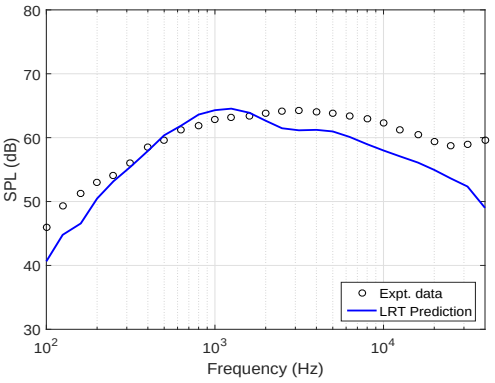

(j) Polar angle 120°

Figure 4.20 – Comparison of LRT predictions of noise spectra with measured data for nozzles with area ratio 2.0 and velocity ratio 0.79.

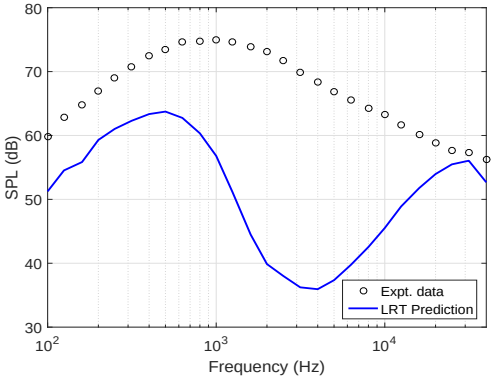

(a) Polar angle 30°

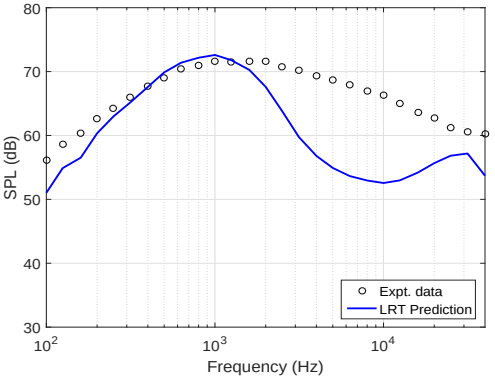

(b) Polar angle 40°

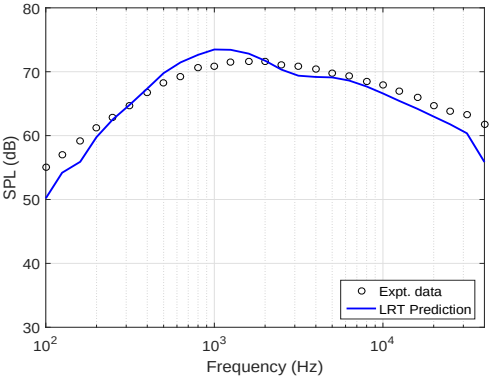

(c) Polar angle 50°

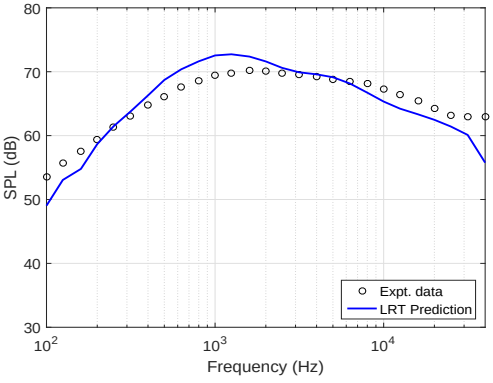

(d) Polar angle 60°

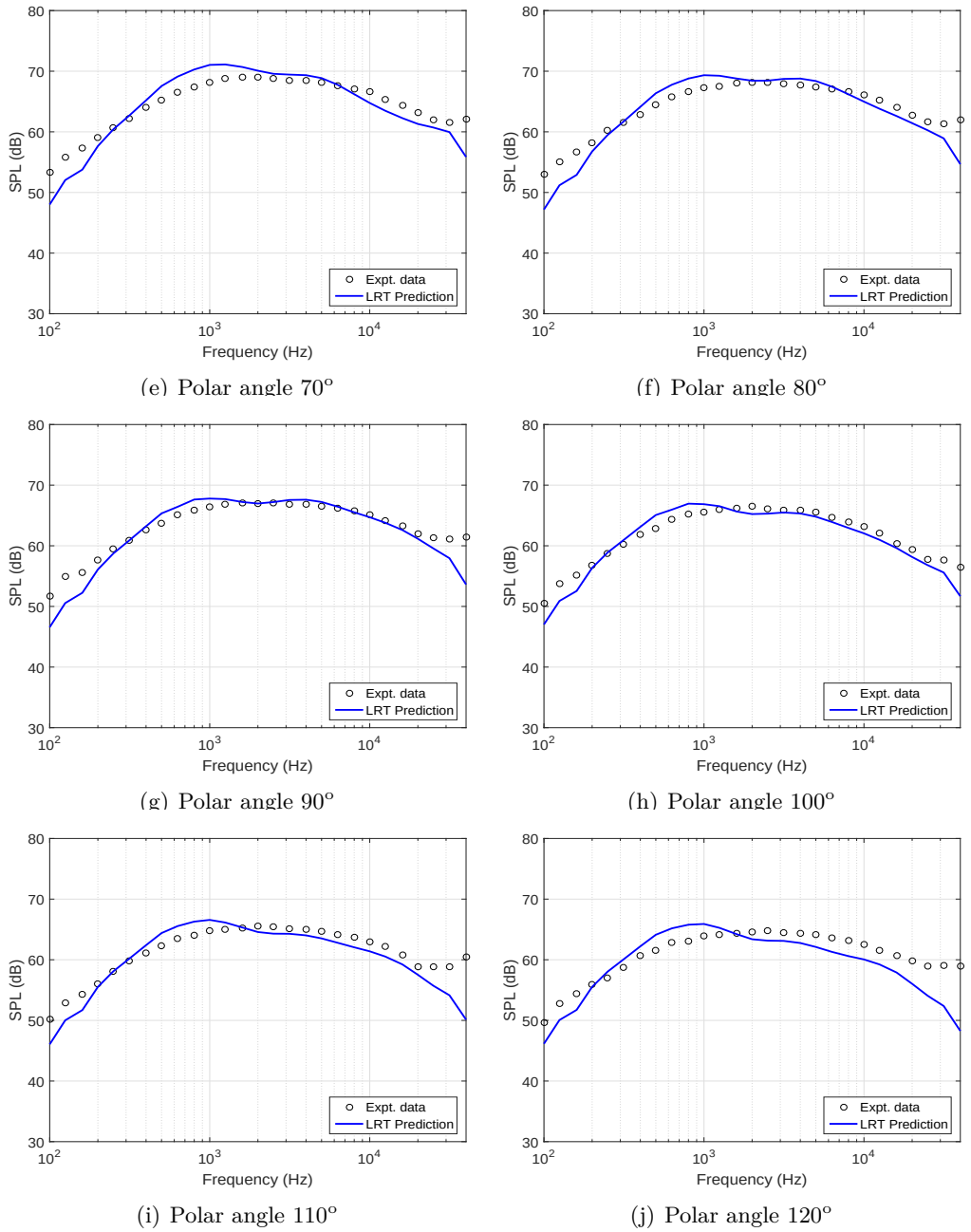

(e) Polar angle 70°

(f) Polar angle 80°

(g) Polar angle 90°

(h) Polar angle 100°

(i) Polar angle 110°

(j) Polar angle 120°

Figure 4.21 – Comparison of LRT prediction of noise spectra with measured data for nozzles with area ratio 4.0 and velocity ratio 0.79.

For the forward arc angles, under-prediction up to 5dB in the high frequencies is obtained. The reasons for the under-predictions at this point is unknown. The dominant noise source in this region is high frequency which is radiated from the secondary region. The flow factor plots suggests that the source propagation in the forward arc angles has an convection amplification effect. Therefore this under-prediction could be due to source definitions in the LRT method.

The new procedure to determine the LRT coefficients was first used on area ratio 4.0 nozzles for varying flow conditions. The predictions agree with measured data at all angles (outside CoS) and frequencies for area ratio 4.0 nozzle. When the same set of coefficients was used on nozzles with lower area ratios 0.87 and 2.0, an under-prediction at low frequencies are obtained. However, the predictions match at peak frequencies (which are most important frequency range, 2000 Hz to 8000 Hz for jet noise) in comparison with measured data. Further, when these model scale nozzles are scaled to full size nozzles based on Strouhal number ($St = fD_j/U_j$), low frequencies become less important compared to peak and high frequencies. Therefore it is important to focus more on peak and high frequencies. From a practical perspective, higher area ratio nozzles offer better noise benefits over lower area nozzles and are therefore most preferred in the industry. From the LRT method viewpoint, it is worth noting that the method captures the trends better for higher area ratio nozzles and care has to be taken which applying the same LRT coefficients for a wide range of nozzle configurations.

4.8.3 LRT predictions for coplanar nozzles: OASPL directivities

For a quadrupole source, directivities are due to the source convection and refraction effects are due to the mean-flow propagation. In the LRT method, source convection effects are included in the source definitions, while the refraction effects are calculated using the ray theory. The directivity plots for the nozzles with area ratio 0.87, 2.0 and 4.0 are shown in Figures (4.22), (4.23) and (4.24), respectively. The overall sound pressure level (OASPL) are higher than sound pressure levels for a given observer angle as it accounts for the intensity of the entire spectrum.

Comparison of OASPL for the three ratio nozzles shows that for a given velocity ratio, the noise directivities reduces with increase in area ratio. The noise level peaks at the 50^o polar angle and it is worth noting that the LRT predictions are within 2dB compared with measured OASPL for angles outside the CoS. For angles inside the CoS ($\theta < 50^o$), significant under-prediction is observed. This is due to the refraction of rays away from the jet axis due to the mean flow. A detailed explanation of noise attenuation in the CoS is presented in Section (6.4).

From the plots it is clear that the LRT significantly under-predicts OASPL directivities at the shallow angles of the jet. The critical CoS angle for area ratio 0.87 nozzle is approximately 60^o and for area ratio 2.0 and 4.0 is approximately 50^o. For a given VR, the rate of mixing of the primary and secondary flows in the shear layer increased with

increasing AR. As a consequence, the flow gradients in the AR 0.87 nozzle is higher compared to AR 2.0 and 4.0 nozzle. Refraction effects are therefore higher in lower AR nozzles which results in large CoS angles (see Figure (4.18)).

From the three area ratio nozzles, it can be observed that noise levels peak at the CoS angles, and that the LRT method is not capable of providing good predictions at the CoS. It is therefore important to develop methods to model the noise in the CoS. In Chapter (6), methods are proposed to model the noise in the CoS.

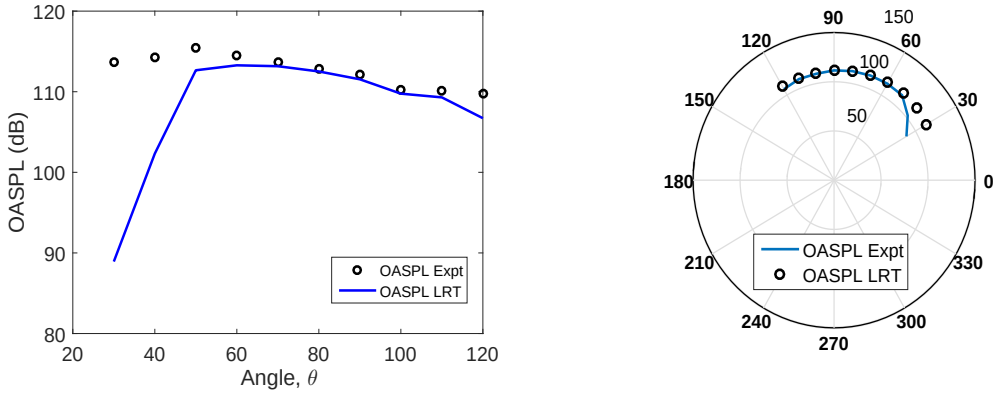

(a) (b)

Figure 4.22 – Comparison of LRT prediction of OASPL with measured data for nozzles with area ratio 0.87 and velocity ratio 0.79.

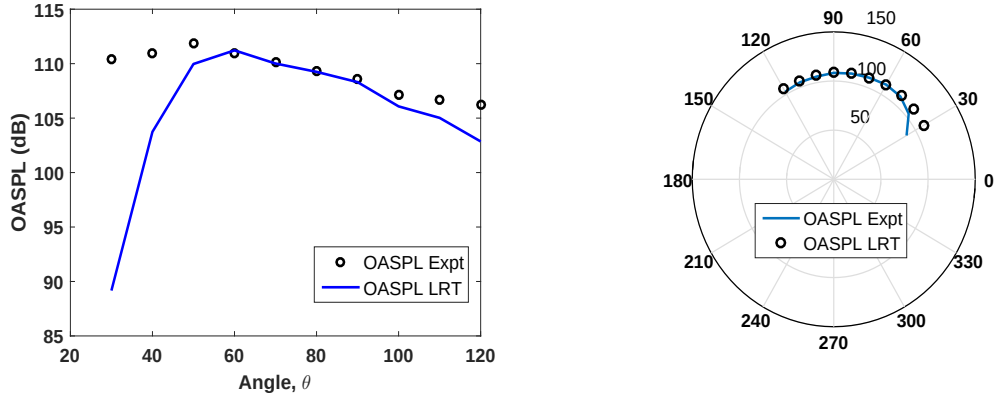

(a) (b)

Figure 4.23 – Comparison of LRT predictions of OASPL with measured data for nozzles with area ratio 2.0 and velocity ratio 0.79.

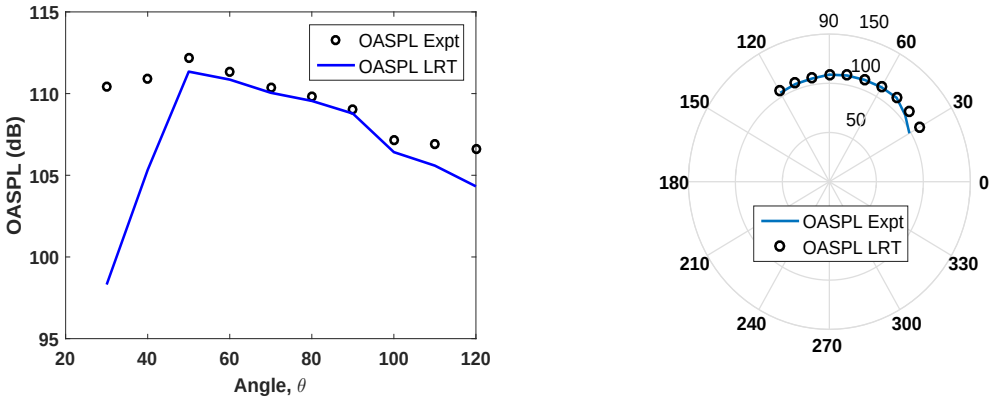

(a) (b)

Figure 4.24 – Comparison of LRT predictions of OASPL with measured data for nozzle with area ratio 4.0 and velocity ratio 0.79.

4.8.4 Effect of velocity ratio/effect of primary nozzle

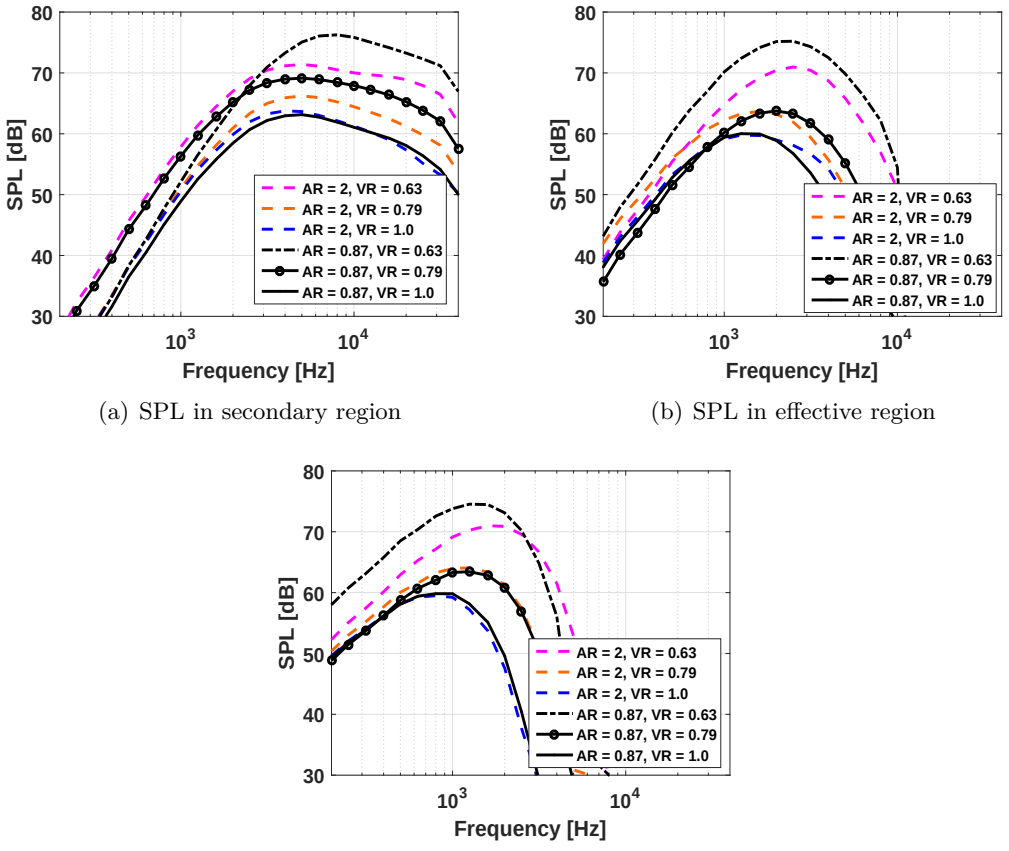

(a) SPL in secondary region

(b) SPL in effective region

(c) SPL in mixed region

Figure 4.25 – LRT predictions showing the effect of velocity and area ratio on the 3 main noise producing regions of the jet at the 90° polar angle.

The coplanar nozzle configurations considered have different primary (core) and secondary diameters, as shown in Table (4.1). To study the effect of primary velocity on the far-field noise for different velocity ratios and area ratios, the noise produced in each noise

producing region of the jet have been analysed. For area ratios 0.87 and 2.0, the secondary diameter is constant but the primary diameters are different. The individual spectra for these nozzle configurations are compared in Figure (4.25).

In the secondary region, noise is characterised by the secondary diameter and secondary velocity. For the area ratio 0.87 nozzle, the bypass area between the primary and secondary nozzles is narrower compared to the area ratio 2.0 nozzle. Therefore, for the area ratio 0.87 nozzle, at velocity ratio 0.63 and 0.79, the primary velocity contributes significantly to the noise generated in the secondary region.

In the effective and mixed jet region, for velocity ratio 0.63, the area ratio 0.87 nozzle is noisier compared to the area ratio 2.0 nozzle. For higher area ratios, the primary nozzle has little effect on noise generation.

In the secondary and effective region, for velocity ratios 0.63 and 0.79, the effect of the primary nozzle on the noise is due to higher velocity gradients in the shear layers. This can also be explained from the variation in the anisotropic parameter Δ in these two regions (see Figure (4.13)).

The plots show that for velocity ratio 1.0, the primary nozzle has a negligible effect on the noise produced from the secondary, effective and mixed jet regions. However, from Figure (4.13(b)), the Δ in the effective jet region tends to be independent of velocity ratio for increasing area ratio. This means that for higher area ratios, the primary nozzle has little effect on the noise generation. At VR=1.0, the ratio of length-scales are the same in the effective jet region which means that the coaxial jet (at VR=1.0) behaves like a single stream jet. Both these effects can also be inferred from Figure (4.25(b)).

4.8.5 Effect of area ratio

Distribution of turbulence kinetic energy is a direct consequence of the mixing process between the core and bypass flows. Comparison of distribution of turbulence kinetic energy for the three area ratios for velocity ratio 0.79 is shown in Figure (4.26). For velocity ratio of 0.79, magnitude of turbulence kinetic energy (TKE) for area ratio 0.87 and 2.0 nozzle are similar levels at $1425\text{m}^2/\text{s}^2$ and $1430\text{m}^2/\text{s}^2$, respectively. In comparison, the TKE for the area ratio 4.0 nozzle is lesser by 10%. The peak TKE level is shifted axially further compared to area ratio 0.87 and 2.0 nozzles. The merging of the primary and secondary shear layers takes place at approximately 12D_s in the area ratio 4.0 nozzle. This enhances the mixing of the jet with the bypass flow, resulting in reduced noise levels. Such improved mixing shifts the peak noise level in the area ratio 4.0 nozzle to low frequencies. For area ratios 0.87 and 2.0, noise levels are higher and their peak noise levels occurs at higher frequencies. Such an effect can be observed for nozzles with velocity ratios 0.63 and 1.0 as well.

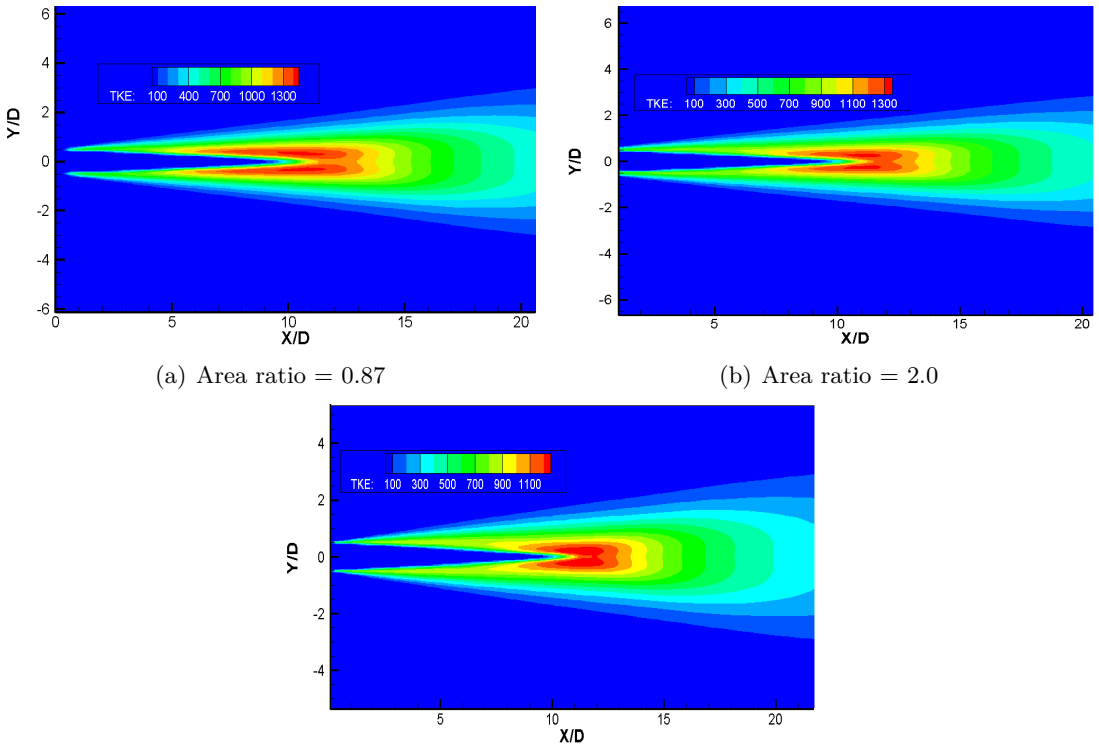

(a) Area ratio = 0.87

(b) Area ratio = 2.0

(c) Area ratio = 4.0

Figure 4.26 – RANS computed peak turbulence kinetic energy (m^2/s^2) location for nozzles with velocity ratio 0.79 for varying AR; axes non-dimensionalised with secondary diameter D_s.

4.9 Chapter summary

In the current chapter, a procedure to determine the model coefficients associated with the RANS solution has been proposed. Such a procedure will eliminate the dependence on experimental data for future nozzle design programmes. Furthermore, amendments to the LRT time-scale has been made to incorporate the local effects of the jet.

The amended LRT time-scale and improved procedure to calculate the LRT coefficients is used to carry out a parametric study on isothermal single stream jets with varying flow conditions and also on isothermal coplanar nozzles with varying area and velocity ratios. It has been observed that, for a family of nozzles, the LRT length-scale and time-scale coefficients do not change due to the constant spectral shape seen in the far-field acoustic data and the RANS modelling procedure followed to obtain the mean flow.

The parametric study of noise from coplanar nozzles for varying area and velocity ratios has been used to validate the noise prediction procedure using the LRT method. This study gives an insight into the eddy aspect ratio and its effect on peak noise levels from the main noise producing regions of isothermal single stream and coaxial jets.

Chapter 5

Characterisation of ultra high bypass ratio nozzles

From the parametric study on coplanar nozzles, it has been shown that an increase in area ratio generates less noise for a given velocity ratio. Noise reductions can also be brought about by increasing the ratio of flow from the secondary nozzle to the flow from the primary nozzle, for a given area ratio. This ratio is called the bypass ratio. With an increase in the bypass ratio, the primary jet velocity is reduced. This, in turn, reduces the noise generation. The high bypass ratio nozzles also produce higher thrust. Thrust requirement has been increasing steadily as larger aircraft and their derivatives have been introduced into service. The need for higher thrust and reduced noise signature has led to the design of higher bypass ratio nozzles. In this chapter, noise from high bypass ratio nozzles will be investigated. A characterisation study is carried out with the help of measured data and semi-empirical prediction methods to infer the effect of flow parameters on the noise generation.

5.1 Ultra High Bypass Ratio (UHBR) nozzles

The advent of high bypass ratio engines have reduced the perceived noise levels of commercial aircraft considerably over last decade. These historical improvements associated with increased bypass ratio (BPR) engines have significantly reduced the jet mixing noise and have also improved the fuel efficiency. However, given the current development for increasing rule stringency and the projected growth in commercial air traffic, it is reasonable to expect further reduction in noise level limits in the next two decades. In the latest FlightPath 2050 noise emission targets, set by the Advisory Council for Aviation Research and innovation in Europe (ACARE), the perceived noise emission of flying aircraft is to be reduced by 65% relative to levels of 2000 by 2050. In technical terms, this target translates into the ACARE goal of reducing perceived noise by 15dB per operation by 2050 [146].

Towards this objective, several noise reduction techniques have been investigated so far. Among these concepts, nozzles with mixing enhancements such as the lobed mixers, chevrons and tabs have proven to be effective. However, these noise reduction features

have associated performance losses. The in-service Rolls-Royce Trent 1000 engine, which powers the Boeing 787 Dreamliner aircraft, has a bypass ratio of approximately 11.0 and incorporates an advanced low noise design. The low noise technology has brought significant noise reductions compared to previous engines of the Trent family. However, more stringent rules to reduce community noise demand further reductions in jet noise, hence, an increase in bypass ratio could be the best alternative.

Besides improved specific fuel efficiency and reduced jet noise levels, high bypass ratio nozzles can potentially improve the propulsive efficiency of the engine. This is because, propulsive efficiency, η_p is linked to the exhaust velocity reduction, $\eta_p = 2/\left(1 + u_e/u_\infty\right)$; where u_e is the exhaust velocity and u_∞ is the speed of the aircraft. However, without a step change in technology, maximising the bypass ratio is constrained by several factors such as, the ground clearance (distance between nacelle lowest point and ground during landing, denoted by the letter 'C' in Figure (5.1)), engine nacelle drag, rotor speed and the length of the fan blades. These design changes will lead to increased close-coupled architectures of the engine with regard to the wing and control surfaces such as flaps. This results in an increase in the noise due to interaction of the jet with the trailing edge of the wing and jet flap interaction. The increased size of the nacelle and other turbomachinery components also increases the weight penalty. Amidst these constraints, the current focus is on developing ultra high bypass ratio (UHBR) engine nozzles (BPR $>$ 12) for the next-generation powerplants. Such technologies could be an alternative solution to move towards the specific fuel consumption (SFC) reduction goals with improved overall powerplant efficiency.

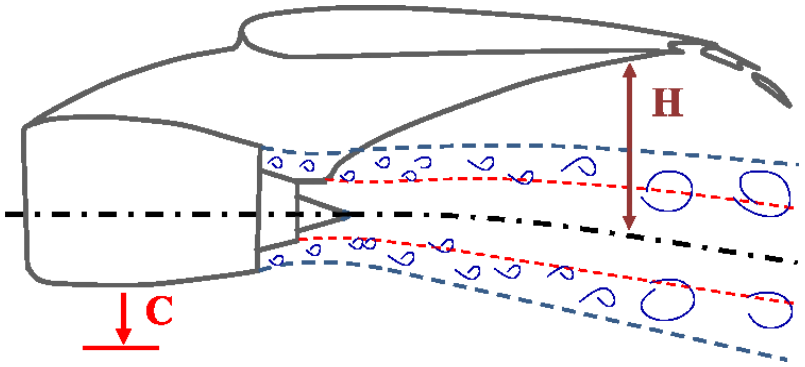

Figure 5.1 – Schematic of a high bypass ratio nozzle with installed wing and deployed flaps; H is the distance from the wing tip to the jet axis, C is the ground clearance.

5.1.1 Description of the JEROMINO project

In the current chapter, far-field noise generated from ultra high bypass ratio (UHBR) nozzles with area ratios up to 8.0 and bypass ratio up to 15.0 are investigated. The UHBR nozzle design work was carried out by Rolls-Royce Deutschland (RRD). The JERONIMO programme is funded by the European commission (7^{th} RTD Framework Programme) and aims to understand and assess the importance of the noise generated by the primary and

secondary shear layers and their principal radiation directions under different operating conditions of ultra high bypass ratio nozzles (i.e. with bypass ratios larger than 12), and the related installed jet-wing interaction noise. The project also aims to minimise the uncertainty in the characterisation of jet noise for novel installation configurations by performing wind tunnel tests and numerical predictions. Ultimately, the aim is to be able to derive design recommendations for future UHBR engine jet noise reductions. In the current chapter, UHBR nozzles will be characterised to study the effect of the following parameters on far-field noise:

1. primary (core) flow

2. velocity ratio

3. bypass ratio

4. flight stream velocity

Measured acoustic data for coaxial nozzles with area ratio (AR) 3.5 and 5.5 from another collaborative noise test program funded by the UK TSB called SILOET (Strategic Investment in Low-Carbon Engine Technology) [147] programme will be made use to study the effect of area ratio.

Along with the LRT method, the semi-empirical ESDU program is also used to obtain predictions. The ESDU program is based on a semi-empirical four–source method developed by Fisher et al. [57, 58], and is also used in the industry. A short description of the ESDU methodology is presented in Appendix (A.3). The ESDU method uses the single stream jet noise database from the Fundamental Coax test campaign at QinetiQ NTF. This method scales the noise from single stream jets to construct sources for coaxial nozzles. Therefore it is capable of providing trends for coaxial nozzles for varying flow configurations. In this chapter, lower area ratio nozzles (area ratio 3.5 and 5.5) are used to compare noise from UHBR nozzles. No measured data is available for all flow configurations (e.g. varying velocity ratio for varying/constant thrust cases) for area ratio 3.5 and 5.5 nozzles. Therefore, ESDU predictions have been used to generate data for comparison purposes to support the UHBR characterisation study. This also gives an opportunity to compare capabilities of the LRT method and also the ESDU program.

With the help of prediction from the LRT and ESDU program, a parametric study is performed to provide recommendations to improve the design of UHBR nozzles at various nozzle operating conditions. In the next section, description of UHBR noise tests conducted at QinetiQ's Noise Test Facility (NTF) at Farnborough, UK is presented. It is followed by a description of the RANS CFD procedure used to obtain the mean-flow quantities for various UHBR nozzle conditions.

5.2 Model-scale test data

All of the data used in this chapter was acquired in the Noise Test Facility (NTF) at QinetiQ, Farnborough. The test campaign was fully funded by Rolls-Royce Deutschland. The Noise Test Facility (NTF) is a large, high-quality anechoic chamber specifically designed for model-scale exhaust noise research. The chamber is approximately 27m long by 26m wide by 17m high, making it suitable for far field noise measurements [147] (Figure 5.2).

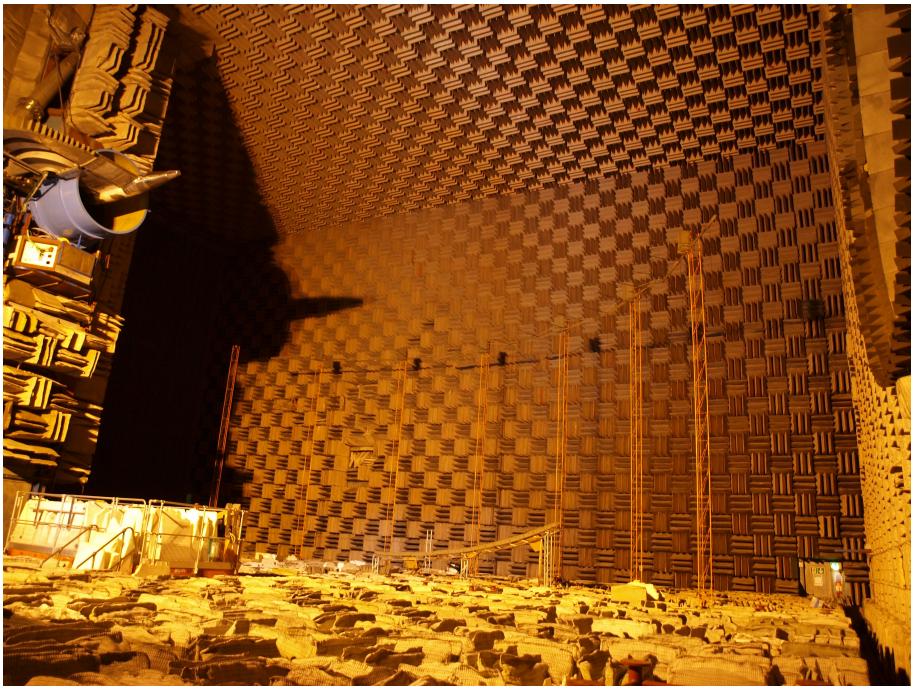

Figure 5.2 – Internal view of the anechoic chamber of the Noise Test Facility at QinetiQ [147].

The chamber is lined with twenty-two thousand non-reflective, acoustic wedges, rendering it anechoic down to frequencies of 90 Hz. The jet flow exhausts from the chamber through a bell-mouth collector of 6m diameter, situated 15m downstream of the nozzle exit plane. The chamber is ventilated with low-velocity ambient air drawn in through acoustically-lined splitters on each side of the rig cubicle by means of large-capacity fans drawing the air from the downstream end of the exhaust collector through tortuous lined passages. Positive ventilation prevents hot-gas recirculation, providing stable noise propagation paths.

5.2.1 NTF acoustic data processing

The NTF acoustic processing system produces data in various formats and standards, including both 1/3-octave and 10 Hz narrow band levels. The 1/3-octave Sound Pressure Levels (SPL) are corrected for system response and with system (electrical) and acoustic background subtracted. The levels are further corrected to a loss-less atmosphere and for spherical spreading to a distance of 1m, and angle and level corrections are applied for propagation through the wind-tunnel shear layer. To obtain levels that would be measured

in the case of an aircraft flying past an observer, a Doppler frequency shift would need to be applied. As it is considered beneficial in the analysis to follow to separate other frequency effects from the Doppler shift, this final step has been neglected here, so we effectively have the case of an observer moving with the aircraft.

The jet rig protrudes into the chamber at a height of 8.73 m. Core and bypass air flows are supplied by a centrifugal compressor, to a maximum combined mass flow of 15kg/s at 3 bar A. Core air is heated to jet exhaust temperatures using an 'Avon' combustion can, specially modified to burn Liquefied Petroleum Gas (LPG), whilst bypass temperatures are controlled by mixing in cooler air from a heat exchanger system. Test models are mounted onto a sting assembly, which is cantilevered into the centre of the 1.8 m diameter open jet used for flight simulation up to Mach 0.33. The air flow for this is supplied by a very large blower (350 kg/s) through an extensive silencing arrangement, such that the noise produced by the flight stream is effectively only due to that of the fundamental jet mixing. Typically, the test model protrudes from the flight-simulation duct by about one duct diameter thereby enabling measurements to be made in the forward arc of the jet. The design of the NTF is discussed in more detail in [148].

A particular feature of the NTF is the boundary-layer suction system, which sucks air from the surfaces of both the sting and the barrel, as shown in Figure (5.3). The boundary layer suction system (BLSS) addresses the boundary layer growth along the axial length of the drum; corner vortices generated at the interface between the drum and aerofoil; and the thickness of the wake from the cantilevered aerofoil section.

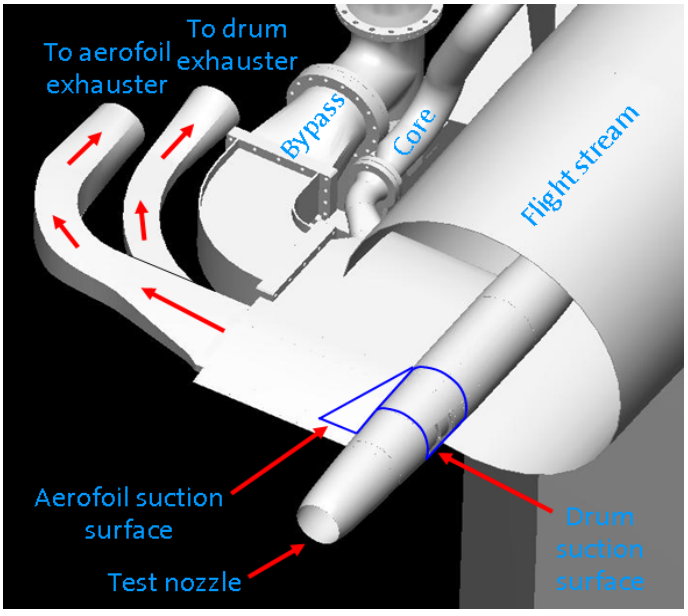

Figure 5.3 – Schematic of the boundary-layer suction system (BLSS) at the NTF [147].

5.3 RANS computations

In this section, RANS CFD procedure employed to obtain the mean-flow quantities for various UHBR nozzle conditions are presented. The UHBR nozzles are 3/4 cowl nozzle geometries with a centre-body bullet protrusion from the primary nozzle. The standard k-ϵ model solves for equations set for regions away from the walls, i.e. in jet regions. RANS solutions for nozzle geometries with a centre-body bullet in this Chapter are obtained using a SST k-ω turbulence model. The SST k-ω model combines the advantages of standard k-ϵ (away from wall boundaries) and standard k-ω models (near wall boundaries) in predicting aerodynamic flows, and in particular in predicting boundary layers under strong adverse pressure gradients and is often preferred by the industry. Dezitter et al. [149] used a SST k-ω turbulence model to compute flows from high bypass nozzles for varying flow conditions. The flow predictions were in good agreement with PIV measurements.

A list of flow conditions for which RANS and LRT simulations were computed are tabulated in Table (5.1). Case 1 is the baseline JERONIMO sideline condition, which will be used to validate the RANS computations. Cases 2, 3 and 4 were chosen to study the effect of velocity ratio at equal thrust and cases 4-6 were chosen to study the effect of flight stream velocity.

The UHBR nozzle was designed by Rolls-Royce Deutschland, and the RANS CFD grid is part of the JERONIMO program. As part of the program, a fine grid with 144 million hexahedral cells and a relatively coarse grid with 15 million hexahedral cells were generated. RANS SST k-ω solutions from ONERA's in-house CFD code 'elsA' [150] were produced for the fine grid. To reduce the computational cost, RANS computations using the coarse grid from ONERA with 14 million grid points, were produced in-house at the ISVR using the FLUENT code. In the next section, validation of the RANS CFD procedure using the elsA and Fluent software for case 1 is presented.

Case No.	Core velocity	Core Temp.(K)	Bypass velocity	Bypass Temp.(K)	Bypass ratio	Flight Vel.	Velocity ratio	Thrust (N)
1.	291	765	230	331	15.3	90	0.79	1561
2.	290	309	193	309	5.0	90	0.67	1370
3.	250	309	200	309	6.3	90	0.80	1372
4.	205	309	205	309	8.1	90	1.00	1358
5.	205	309	205	309	8.1	50	1.00	1358
6.	206	309	206	309	8.0	0	1.00	1358

Table 5.1 – Flow conditions for UHBR nozzles.

5.3.1 RANS data using the elsA code

The elsA multi-application CFD simulation platform deals with internal flows in turbo-machinery and external aerodynamics from the low subsonic to the high supersonic flow regime and relies on the solving of the compressible 3D Navier-Stokes equations. A large

variety of turbulence models from eddy viscosity to full differential Reynolds stress models (DRSM) are implemented in elsA for the Reynolds averaged Navier-Stokes (RANS) equations. Laminar-turbulent transition modelling relies either on criteria, or on solving additional transport equations. Various approaches for Detached Eddy Simulations (DES) and Large Eddy Simulations (LES) are also available [151, 152].

5.3.1.1 Effect of mesh refinement

Most of the noise producing sources is located in the first 25 jet diameters of the jet plume. However, the computational domain was extended up to 40 jet diameters downstream. This allows to avoid static pressure reflections that occur at the boundaries of the grid, fluctuating back towards the nozzle exit. The influence of the refinement of the mesh is the first step of this study. Two different grids with varying grid sizes were investigated: a refined mesh (Mesh 1) and a mesh corresponding to ONERA internal methods (Mesh 2).

The refined grid, Mesh 1, had 144 million grid points with refined external (volume outside the shear layer), primary and secondary shear layers, in order to study the numerical dissipation of turbulence. The coarse grid, mesh 2, had 15 million grid points which had coarsened external volume mesh. Both grids were the same in primary and confluent exhaust planes for the purpose of thrust calculations, and very close to the walls.

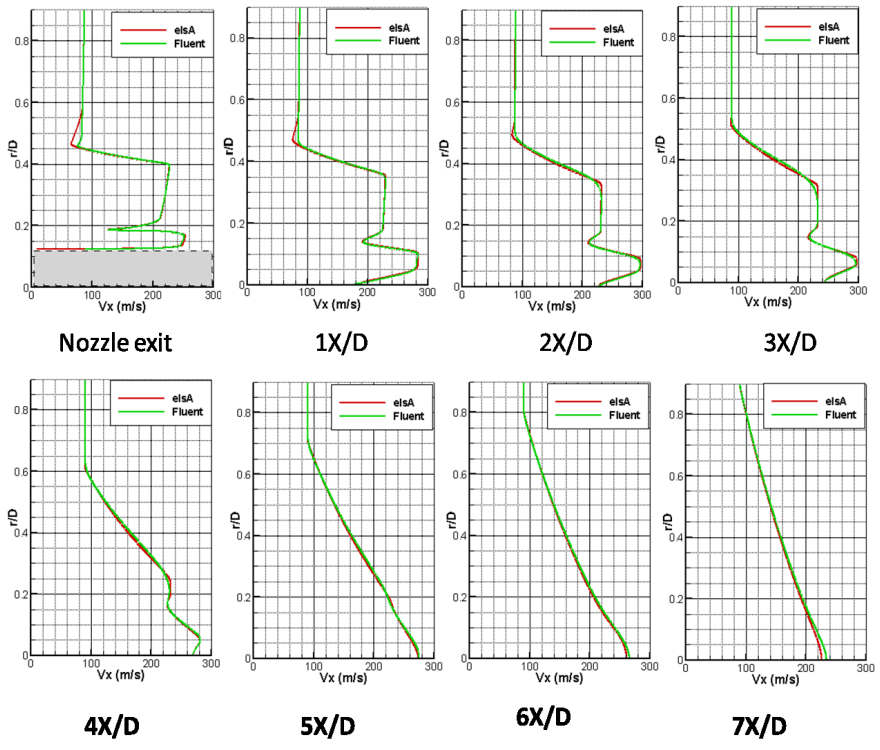

Figure 5.4 – Comparison of mean radial velocity profile at various axial stations obtained using Fluent and elsA.

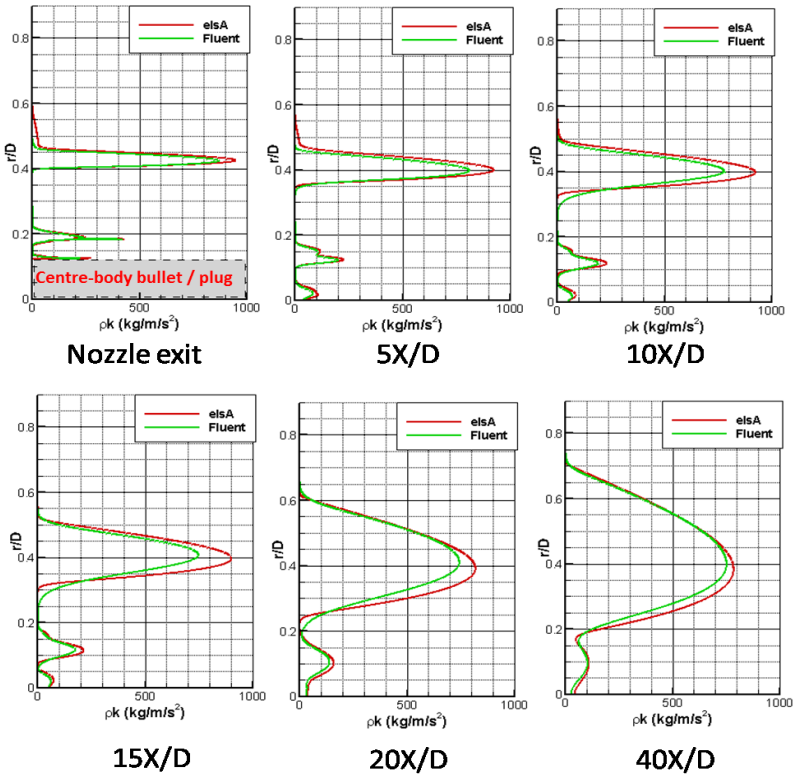

Figure 5.5 – Comparison of mean radial turbulent kinetic energy density profile, ρk, at various axial stations obtained using Fluent and elsA.

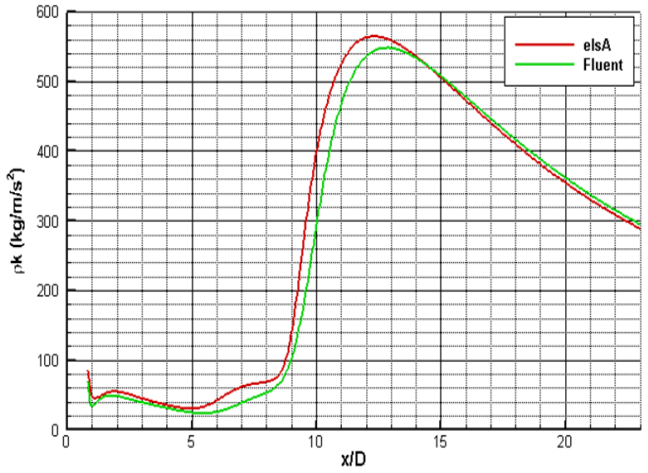

Figure 5.6 – Comparison of mean axial turbulent kinetic energy density profile, ρk, at the nozzle lip-line obtained using Fluent and elsA.

Steady RANS calculations for case 1 in Table 5.1 using mesh 1 was carried out using the elsA code by Onera using a SST k-ω turbulence model. RANS computations using mesh 2 were carried out using the FLUENT code at the ISVR. Details of the simulation using FLUENT is presented in the next section. The RANS FLUENT calculation for case 1 conditions using mesh 2 is benchmarked against aerodynamic results obtained from the elsA code using mesh 1. A comparison of mean velocity and turbulent kinetic energy

density values from the two RANS solvers are shown in Figures (5.4) to (5.7). The mean velocity and turbulent kinetic energy density data obtained using FLUENT agrees well with predictions from elsA code. This also shows that mesh 2 can be used to perform RANS computations for other flow conditions and can save significant amount of computation time. However, small discrepancies are noticeable in the secondary/external flow shear layer near the nozzle exhaust, where the refinement between both meshes is the most different, but they are negligible and do not affect the flow calculations further downstream.

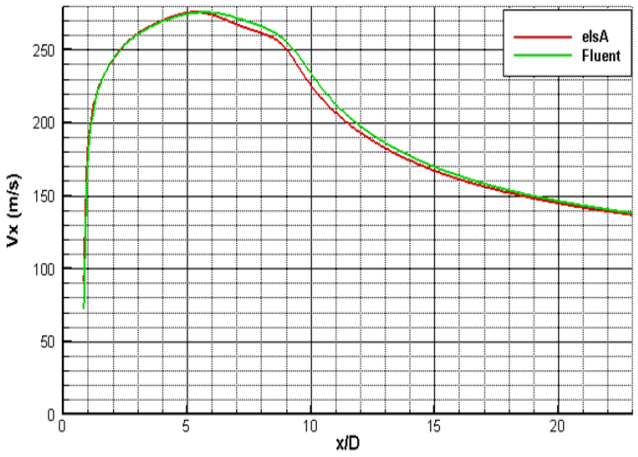

Figure 5.7 – Comparison of velocity at the nozzle lip-line obtained using Fluent and elsA.

5.4 RANS Simulations using FLUENT (ISVR)

The in-house RANS computations were performed using the 3D FLUENT solver. The FLUENT solutions were validated against the elsA solver for the baseline case, using the using a SST k-ω turbulence model for consistency.

5.4.1 RANS boundary conditions and solver settings

The boundary conditions applied on the model using FLUENT is tabulated in Table (B.2). For the UHBR cases, convergence was not achieved with a pressure inlet boundary condition using the SST k-ω model, therefore a mass flow inlet boundary condition was used. Mass flow data was available from experiment data.

Boundary Conditions	k-ω model	Input Data
Inlet free-field	Mass flow	Mass flow rate and temperature
Inlet Core	Mass flow	Mass flow rate and temperature
Inlet bypass	Mass flow	Mass flow rate and temperature
Far-field	Pressure far-field	Pressure and temperature
Exit	Pressure outlet	Pressure and temperature
Symmetry	Symmetry	Symmetry plane
Nozzle/plug/struts	Wall	No slip, Stationary wall

Table 5.2 – Boundary conditions using SST k-ω turbulence model in the FLUENT solver

The key solver settings used in FLUENT are listed below:

- Solver: Steady-state density-based coupled solver
- Viscous model: Standard k-ω, with Standard Wall function
- Formulation: Implicit
- Flux Type: Roe-FDS
- Gradient: Green-Gauss Cell method
- Flow: Second-Order Upwind scheme
- Turbulent Kinetic Energy: Second-Order Upwind scheme
- Turbulent Dissipation Rate: Power Law

5.4.2 Inlet conditions and flow initialisation

The effect of initial conditions on the evolution of the flow and noise generation mechanism in jets has been studied extensively. The inlet conditions affect the spreading rate of the jet and in turn the length of the potential core in the single stream jets, and the reattachment point of the two streams in coaxial jets. For example, as the initial turbulence intensity increases, the shear layers develop more slowly with much lower root-mean-square (r.m.s.) fluctuating velocities, and the jet potential cores are longer. Some of the experimental work in investigating the initial conditions was carried out by Ko and Kwan [153], Hill et al. [154], Bogusławski et al. [155], Husain and Hussain [156], Zaman et al. [157], Warda et al. [158, 159] and Antonia [160]. Hill et al. [154] investigated the effect of nozzle boundary layers on jet mixing rates in single stream nozzles with varying inlet velocities. When the boundary layer was turbulent the results for both the centerline velocity decay and the variation in turbulence intensity downstream of the nozzle lip were found to be independent of velocity. In contrast, when the initial boundary layer was laminar, the centreline velocity decay and turbulence intensity downstream of the nozzle lip for found to vary with the jet velocity [154].

Bogey et al. in a series of LES work attempted to compute the effect of initial turbulence on far-field noise in subsonic jets. In one such work, the aim was to study the influence of the initial turbulence on far-field noise in subsonic jets at identical Mach (M = 0.9)and Reynolds numbers ($\mathrm{Re_D}$= 10^5), characterized by similar mean velocity profiles but peak turbulence intensities u'_e/u_j ranging from 0 to 12% at the nozzle exit [161]. The reduction of the noise levels was observed to be sharp for low u'_e/u_j, but smoother for higher u'_e/u_j. At the radiation angle of $\theta = 90^o$, for example, they differ by 7.6 dB between 0% and 3% u'_e/u_j, 2.5 dB between 3% and 6% u'_e/u_j, 1.9 dB between 6% and 9% u'_e/u_j, and only 0.7 dB between 9% and 12% u'_e/u_j. The numerical results reported by Bogey et al. illustrate the great importance of taking into account the issue of inflow conditions to accurately predict noise generation in subsonic jets. In simulations, it is thus necessary to specify initial conditions as close as possible to the corresponding experimental conditions, when the latter are known.

For the nozzles analysed in the current thesis, flow and acoustics data were measured at the QinetiQ Noise Test Facility. Flow measurements included inlet pressure, mass flow and turbulence at the inlet. Harper-Bourne and Pinker [148, 162] presented Kulite measurements of turbulence intensity of about 1% over the main flow areas, i.e., including the nozzle and the flight stream. This was used as the CFD boundary condition for the Inlet core, Inlet bypass and at the Inlet free-field boundary.

- Momentum settings
  - Reference frame: Absolutes,
  - Mass Flow Specification Method: Mass flow rate (kg/s),
  - Mass flow rate (kg/s): Measured mass flow data at the inlet (core/bypass/flight stream)
- Turbulence
  - Specification Method: Intensity and Viscosity ratio,
  - Turbulent Intensity (%): 1,
  - Turbulent Viscosity Ratio: 10
- Thermal: Temperature at the inlet to the core/bypass/flight stream (K)

CFD iterations were initialised through the Inlet free-field boundary using the Standard Initialisation option available in FLUENT. While simulating cases with zero flight velocity (static condition), a non-zero value of velocity (approx. Mach number = 0.05) was used.

5.5 LRT predictions

After obtaining the RANS mean flow for the conditions in Table (5.1), the LRT method was used to calculate the spectra at the 90^o polar angle. The schematic of the LRT computational domain is shown in Figure (5.8). The LRT computational domain starts from the edge of the secondary nozzle and extends up to 30 secondary nozzle diameters axially and up to 3 secondary nozzle diameters in both the radial and azimuthal directions. As discussed in Section (4.5.1), all RANS-based jet noise prediction methods involve determining a set of coefficients to obtain a good fit to the experiment data at the 90^o polar angle. This practice arises due to the use of RANS data which do not account for flow unsteadiness, flow anisotropy, temperature effects and also the effect of large-scale structures.

The LRT method has two model coefficients associated with the turbulence length-scale (C_l) and time-scale (α_T), and two set of anisotropy parameters, Δ and β, respectively. Using the concept of the four-source method, the turbulence length-scales in the mixed jet region is assumed to be isotropic, which allows us to set the anisotropy parameters Δ and β as 1 and 0, respectively. The LRT coefficients C_l and α_T were then calculated at the 90^o polar angle in comparison with the measured spectra. The LRT length-scale C_l, and

time-scale coefficient α_T, was 1.1 and 0.5, respectively. For the effective and secondary jet region, value of β=0.5, and Δ was determined at best fits to the measured spectrum at the 90^o polar angle. The final spectrum is the summation of the 3 individual spectrum.

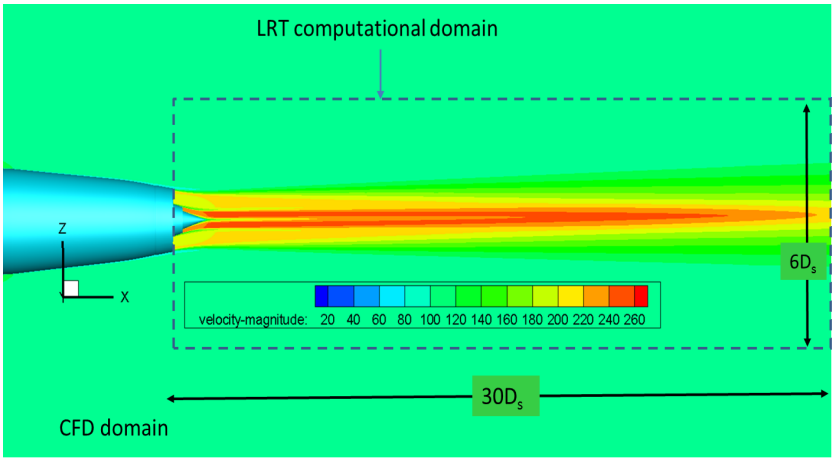

Figure 5.8 – Schematic showing the CFD and LRT computational domain; velocity magnitude (m/s), D_s (m).

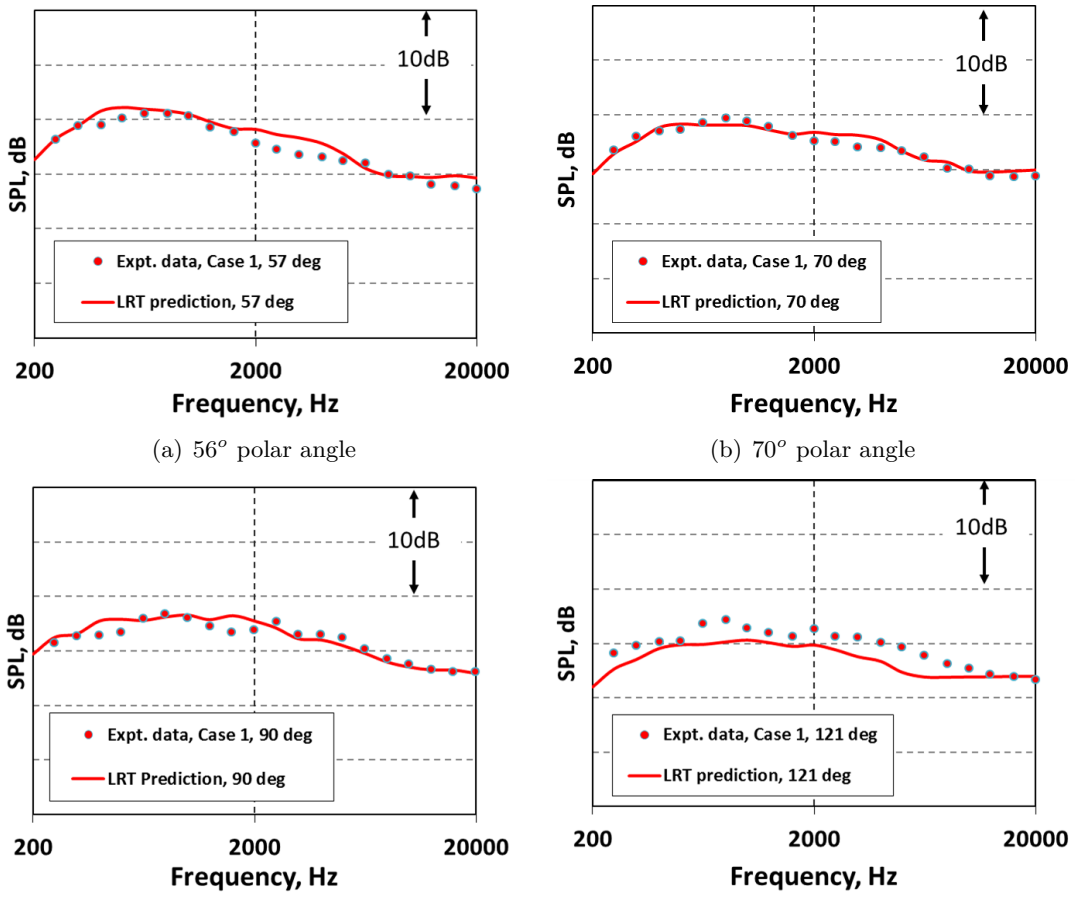

(a) 56^o polar angle

(b) 70^o polar angle

(c) 90^o polar angle

(d) 120^o polar angle

Figure 5.9 – Comparison of LRT predictions with UHBR data for Case 1 at various polar angles.

Figure (5.9) shows the comparison of LRT predictions for the baseline case 1 with

measured data at various polar angles. The predictions for both cases are within 1.5 dB of the data across the entire frequency range. The LRT model coefficients C_l and α_T were kept constant while computing the spectra for other polar angles and also for other UHBR nozzle conditions.

5.6 Validation of ESDU predictions

The noise from single stream jets can be predicted using simple scaling laws derived from experimental databases. This is due to the small number of flow parameters involved in calculating the far-field noise. For coaxial jets, there are clearly parameters involved. However, the number of parameters can be reduced by relating the noise from a coaxial jet to three equivalent fully-mixed jets, i.e.

$$SPL_{coax} = SPL_{mix} + f\left(VR, \theta, \phi\right) \tag{5.1}$$

where SPL_{mix} is the sound pressure level produced by a single stream jet with the same mass flow and mass-averaged temperature as the combined core and bypass streams of the coaxial jet and where, $f\left(VR, \theta, \phi\right)$ is a function of velocity ratio VR and observer angle only. This implies that a coaxial jet noise spectrum can be 'constructed' by scaling the noise from three equivalent single stream jets.

The ESDU semi-empirical, four-source method works using this equivalent single stream jet concept. Additional ESDU programs are also available to estimate static-to-flight effects on noise from single stream and coaxial stream nozzles. These programs are simple and are computationally fast (i.e. few seconds). In this report, the ESDU program is used to estimate noise from coaxial stream nozzles for both static and flight conditions. These programs are faster than the LRT method, which also requires CFD data as a prerequisite.

To perform the characterisation study for noise from UHBR coaxial nozzles, a large number of geometry and flow parameters are involved. For example, in the current study approximately 10 flow parameters are involved and also involves the effect of combination of some of these parameters. To compute noise from UHBR nozzles using the LRT method to perform a characterisation study, it can be challenging considering the huge amount of CFD and LRT data that will be involved. Further, with no experimental data for UHBR nozzles, depending on large LRT and CFD database can be expensive. Therefore, the use of the relatively simple and computationally fast ESDU programs were found to be appropriate.

The four-source ESDU method was originally developed using flow measurements and acoustic data for coplanar nozzles with area ratio of up to two. It was further amended to predict noise from nozzles with a area ratio up to four. It is also worth noting that the ESDU program includes an amendment to extend static single stream and coaxial stream jet noise predictions to flight. In the current report, the ESDU program will be used to estimate noise from nozzles with area ratios greater than four, both under static and flight

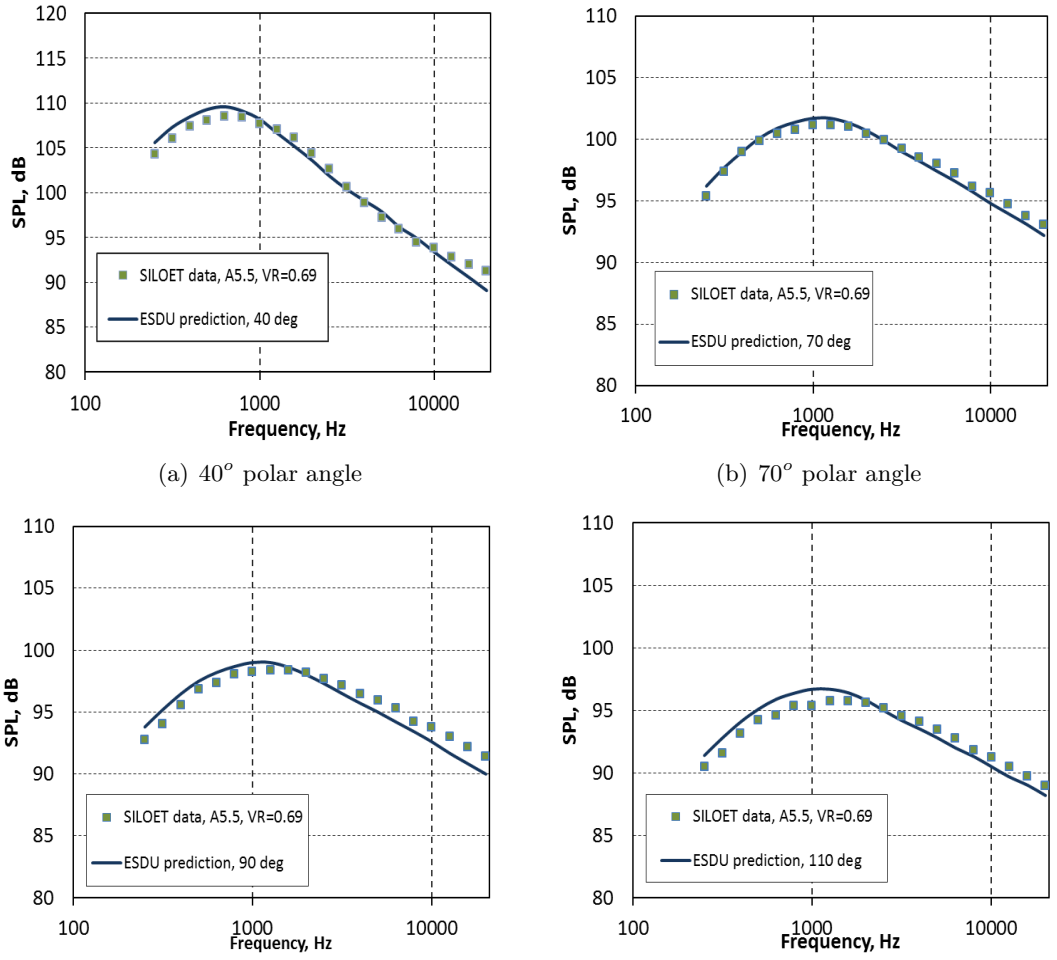

(a) 40^o polar angle

(b) 70^o polar angle

(c) 90^o polar angle

(d) 110^o polar angle

Figure 5.10 – $1/3^{\text{rd}}$ octave band spectral comparison of ESDU predictions with SILOET experimental data; [AR = 5.5, VR = 0.69, TR = 1.0 and V_f=0m/s]

conditions.

Before applying the ESDU programs to make predictions for UHBR conditions, it is possible to validate the method for nozzles with area ratio less than eight, and at both static and flight conditions. In the next section, noise predictions from two coaxial nozzles from the SILOET database with a area ratio equal to 3.5 and 5.5 under static conditions will be presented [147]. These will be followed by predictions for flight velocities equal to 50m/s and 90m/s, respectively. The predictions will all be compared with measured acoustic data at different polar observer angles.

5.6.1 Noise prediction at static conditions

The noise prediction program ESDU98019 has been used to estimate noise from coaxial nozzles under static and in-flight ambient flow conditions. The method splits the coaxial mixing noise into three single-stream jet noise sources which are modified appropriately and then summed.

Predictions for the SILOET coaxial nozzle area ratio 5.5 with a centre-body bullet are shown in Figure (5.10). The velocity ratio is 0.69, and temperature ratio is 1.0. ESDU predictions for the static case ($V_f = 0$m/s) are within 1.5dB at 20kHz of the experimental data. As described in Section (A.3), the ESDU/four-source method has been developed to predict noise from coaxial nozzles with area ratios up to 4.0. However, the predictions for an area ratio 5.5 nozzle under static conditions are reasonably good with an acceptable tolerance.

5.6.2 Noise prediction at flight conditions

The ESDU 14014 program provides a computerised method for estimating static-to-flight effects on coaxial jet noise. The method splits the coaxial mixing noise into three single-stream jet noise sources which are modified appropriately and then summed. To each of the three equivalent single stream jet sources calculated using ESDU98019, a static-to-flight appropriately is added. The procedure for this is described below.

There are three basic changes in a jet noise spectrum due to a flight stream. The first is the spectral shape change arising from changes in jet refraction due to the additional flight shear layer. The second and third changes are the shifts in amplitude and frequency arising from the effects of motion on the sources. The approach used in the ESDU14014 method considers the change in jet refraction via an angle transposition and uses empirical correlations of experimental data to predict amplitude and frequency changes [163].

5.6.2.1 Spectral shape changes

The ESDU14014 method assumes that the changes in spectral shape in going from static to flight conditions may be attributed solely to changes in jet refraction. This leads to a

simple angle transposition such that a static jet noise spectrum at an emission angle, θ_j , will have the same spectral shape as a flight spectrum at another emission angle, θ_e.

The flight emission angle θ_e, corresponding to a given static angle can be obtained explicitly from the relationship

$$\cos\theta_e = \frac{\cos\theta_j}{1 - 0.65M\cos\theta_j}. \tag{5.2}$$

The SPLs are then reduced in flight by an amount given by

$$\Delta SPL = 10\log_{10}\left(\frac{V_j}{V_j - V_f}\right)^m. \tag{5.3}$$

The velocity exponent m is given by the following empirically-derived expression,

$$\begin{aligned} m = 5.4 - \tau + 4.2\left(1 - 0.5\frac{V_f}{V_j}\right)\left(\frac{V_j}{c_o}\cos\theta_e\right) & \\ + \left(\frac{V_j}{c_o}\right)^{1.3}(0.5\cos\theta_e - 1)\sin 2\theta_e & \\ + \tau\left(\frac{V_j}{c_o}\right)\left[1 - 2\left(\frac{V_j}{c_o}\right)\cos^2\theta_e\right]\cos\theta e, & \end{aligned}$$

where the temperature function, τ, is given by,

$$\tau = \frac{1.2TR\,(TR-1)}{TR\,(TR-1)} - 0.3\left(\frac{V_j}{c_o}\right)^{1.7} \tag{5.4}$$

and TR is the ratio of the jet static to ambient temperature,

$$TR = \frac{T_{js}}{T_0}. \tag{5.5}$$

Finally, the frequencies are adjusted according to the following expression

$$\frac{f_F}{f_s} = \left(1 - \frac{V_f}{V_j}\right)\left[1 + 1.2\tau\left(\frac{V_f}{V_j}\right)\sin\theta_e\right]\left(1 + 0.2\sin^2 2\theta_e\cos^2\theta_e - 0.08\tau\right). \tag{5.6}$$

5.6.3 Predictions

By using the equations in the previous subsection, predictions were made for the SILOET AR 5.5 coaxial nozzle with velocity ratio = 0.69 and flight stream velocity of 50m/s. Spectra at four polar angles are compared with measured data in Figure (5.11). The predictions seems to agree reasonably well with the measured data at the 70^o and 90^o polar angles, but not so well further into the rear arc and into the forward arc. This is illustrated more clearly by the 'deltas' shown in Figure (5.12), where ΔSPL = $\mathrm{SPL_{data}}$ - $\mathrm{SPL_{prediction}}$. For the rear-arc angle (i.e, 40^o polar angle), the ESDU method appears to under-predict both at the peak and at very high-frequency, but over-predicts heavily at low frequencies in the forward-arc (i.e at 110^o).

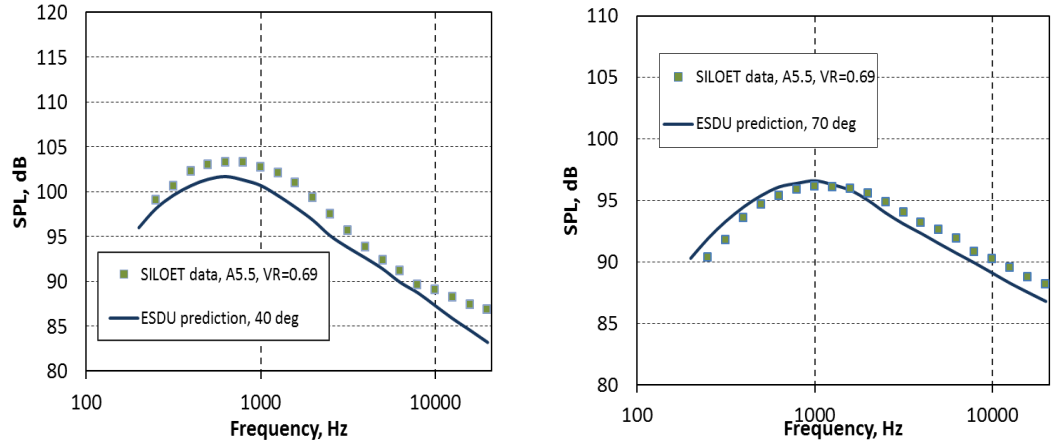

(a) 40^o polar angle (b) 70^o polar angle

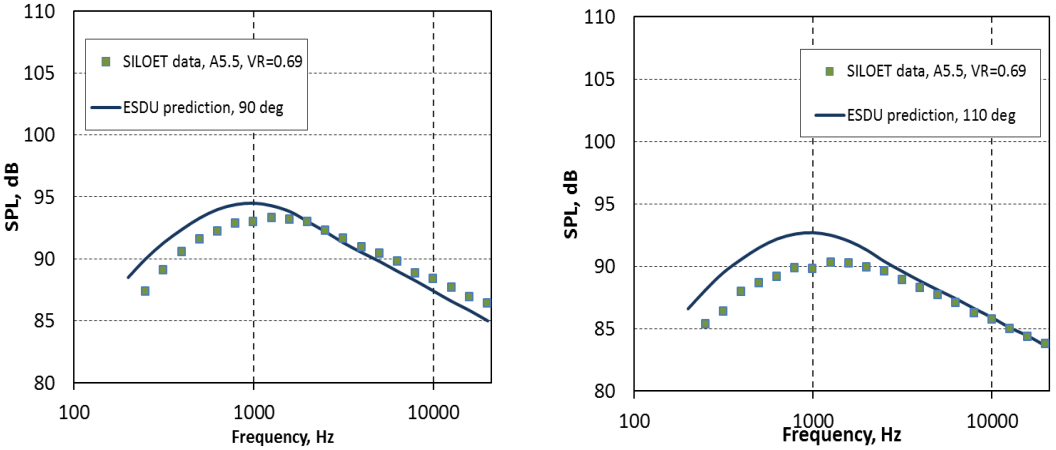

(c) 90^o polar angle (d) 110^o polar angle

Figure 5.11 – $1/3^{rd}$ octave band spectral comparison of ESDU predictions with SILOET experimental data; [AR = 5.5, VR = 0.69, TR = 1.0 and V_f=50m/s]

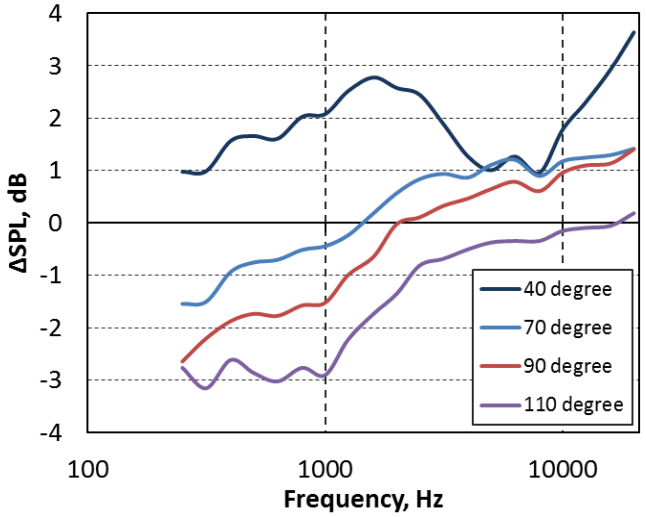

Figure 5.12 – ΔdB plot between ESDU predictions and S33A55 data for V_f=50m/s.

Predictions for the SILOET AR = 5.5 nozzle with flight stream velocity equal to 90m/s

are compared with measured data in Figure (5.13). The predictions clearly compare worse at higher flight stream velocities at all polar angles. The difference between the predictions and measured data approaches 4 dB at low-frequencies and 5 dB at high-frequencies (see Figure (5.14)). This shows that the ESDU program fails to predict the noise from coaxial nozzles with higher area ratios in flight.

5.6.4 Accuracy of the ESDU program

The model used in the ESDU program has been developed for coplanar nozzles with area ratios up to 4. The accuracy of the coaxial stream predictions therefore, depends on the accuracy of the single stream data embedded within the ESDU program. The single stream data set is reported to suffer from errors in the high octave frequency bands (a consequence of poor performance of the 1/3-octave analyser then in use). These errors can result in erroneous predictions at the high-frequencies above 8kHz.

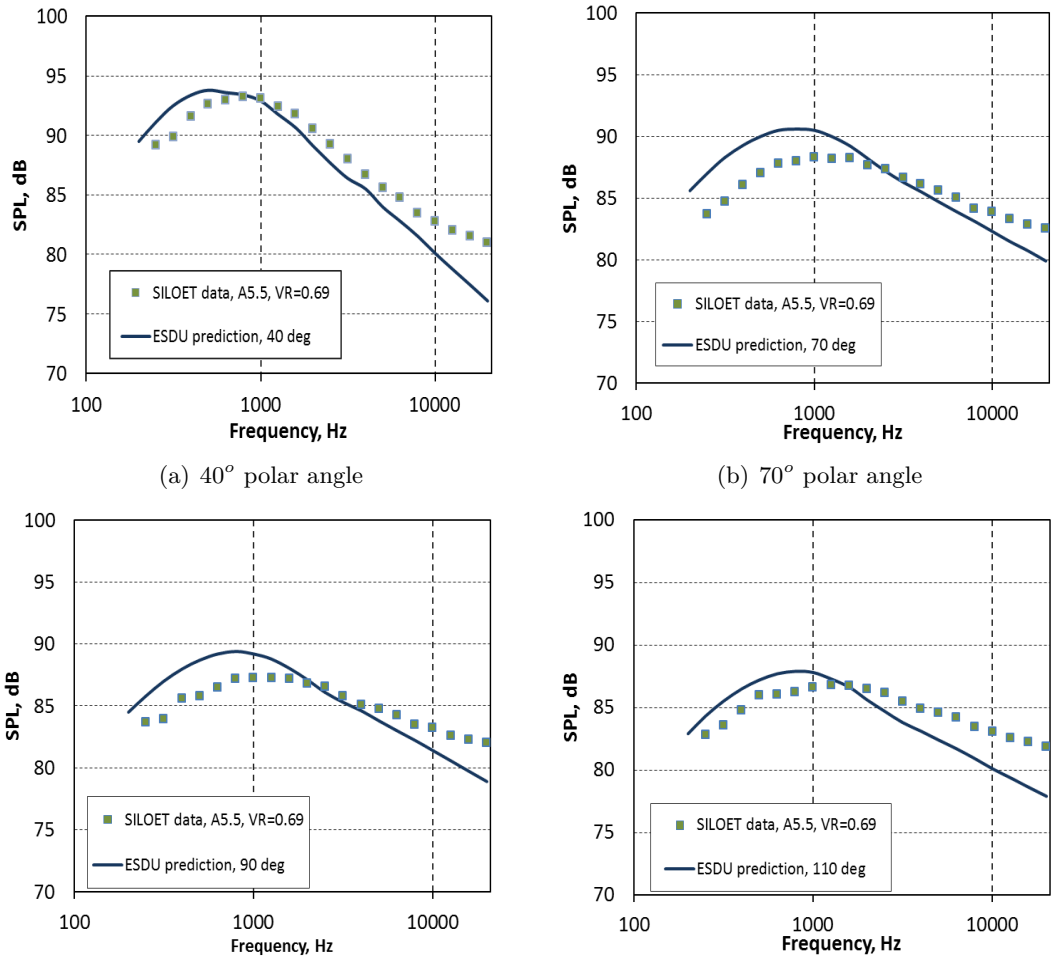

(a) 40^o polar angle

(b) 70^o polar angle

(c) 90^o polar angle

(d) 110^o polar angle

Figure 5.13 – Comparison of ESDU predictions with SILOET data; [AR = 5.5, VR = 0.69, TR = 1.0 and V_f=90m/s]

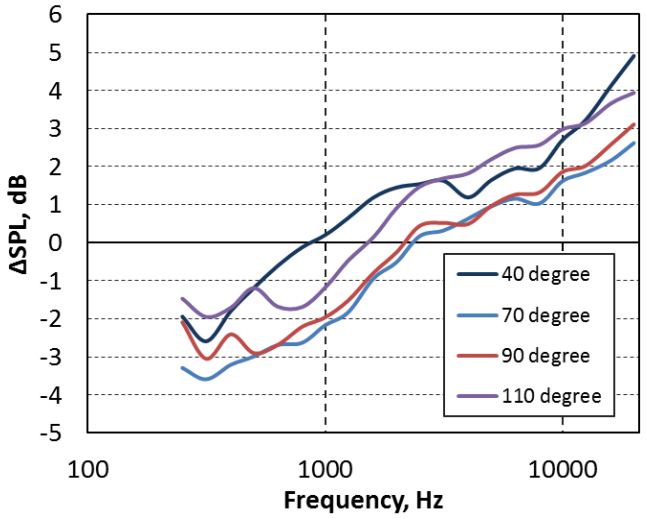

Figure 5.14 – ΔdB plot between ESDU predictions and S33A55 data for V_f=90m/s.

5.6.5 Comparison of ESDU predictions with UHBR data

The ESDU program 14014v10 was used to predict the noise for the UHBR baseline conditions at the 90° polar angle. Predictions are compared with measured data from the UHBR database along with LRT predictions in Figure (5.15). The ΔdB plot in Figure (5.16) shows that the LRT predictions are within 1.5 dB in comparison with the measured data and the ESDU predictions are out by about 3 dB, both at the low and high-frequencies. It is also worth noting that the 'deltas' for the ESDU predictions are lower for the UHBR nozzle (area ratio 8.1) when compared with predictions for area ratio 5.5.

From the assessments carried out so far, it can be concluded that the LRT predictions compares better than the ESDU program for in-flight UHBR nozzles. The ESDU program predicts the far-field noise well for higher area ratio nozzles (up to area ratio 5.5) at static conditions, but performs poorly in-flight.

5.7 Results

5.7.1 Effect of velocity ratio

Noise from coaxial stream nozzles generate considerably less noise compared to single stream conical nozzles. The mixing of flows from the secondary (bypass) and the primary (core) nozzles reduces the turbulence intensity and thus the noise. The velocity ratio of the primary to secondary stream is the main variable which determines the spectral shape of the mixing region [164]. The study of far-field noise due to varying velocity ratio can determine whether noise is attenuated or amplified as a result of core and bypass flow variations. The study of effect of velocity ratio in UHBR nozzles is important to understand the effect of the core with respect to the bypass flow on noise generation.

A number of studies have been carried out to investigate the noise differences between

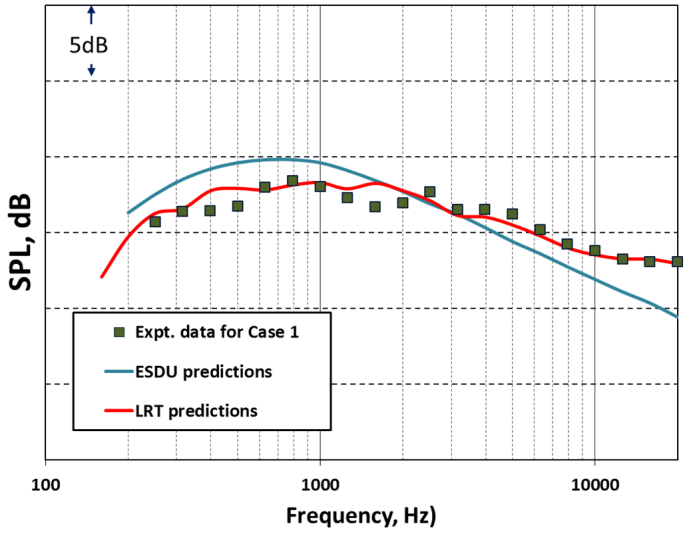

Figure 5.15 – Comparison of ESDU predictions with UHBR data for Case 1 at the 90^o polar angle.

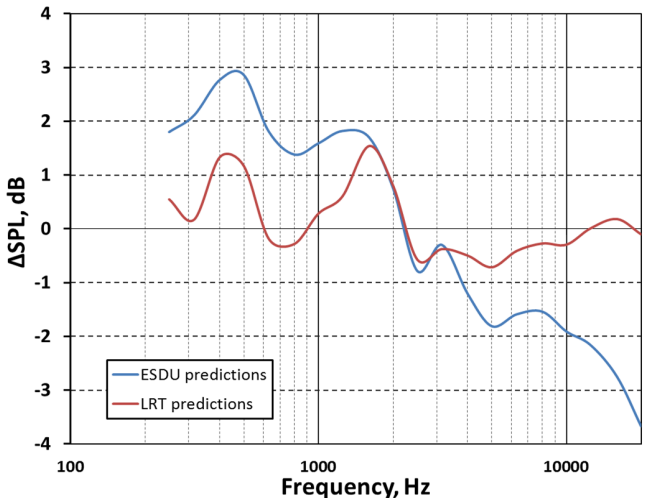

Figure 5.16 – ΔdB plot between ESDU and LRT predictions with UHBR data for Case 1 at the 90^o polar angle.

a coaxial jet and a single stream jet [164, 165, 166]. In most of these studies, comparisons were made between subsonic coaxial nozzles and single equivalent jets (SEJ) with the same thrust, mass flow rate and exit area. Perhaps, it is difficult to realise a uniformly mixed SEJ. And in practice, the exhaust flow is seldom uniform. The velocity ratio is an important parameter which influences the mixing characteristics of a coaxial nozzle. In the current section, the effect of varying velocity ratios and flight velocity on far-field noise from UHBR nozzles are investigated.

5.7.2 Description of cases considered for the study

The noise from a coaxial nozzle is dependent on a host of thermodynamic (eg. velocity ratio, temperature ratio etc) and geometric parameters (such as area ratio), which define the noise sources. Conceptually, one could visualise three distinct noise sources: the inner

shear layer between the primary and secondary streams, the outer shear layer between the secondary and ambient streams, and the fully merged jet farther downstream, with characteristic length and velocity scales being different for each source [167]. From the concept of the four-source method, it is known that the shear layer between the secondary and ambient streams region is characterised by the secondary jet velocity, temperature and nozzle diameter. This region mainly comprises of small-scale turbulence and contributes towards the high frequency part of the spectrum. The fully merged jet mainly comprises of large-scale turbulence and contributes towards the low frequency part of the spectrum. The effective jet which comprises of the inner shear layer between the primary and the secondary streams contributes towards the peak noise levels. As part of the VR study, the secondary and primary velocities are varied in such a way that the noise from the individual noise producing source regions can be investigated.

In the current study, the VR is varied in two ways. In the first set of the study, the secondary velocity is kept constant while the primary velocity is allowed to vary. This will allow to study the effect of VR on the noise generated in the peak and the low frequency part of the noise spectrum. This combination produces an increase in thrust for decreasing values of VR. In the second part of the study, both the secondary and the primary velocities are varied so as to obtain constant mixed velocities. This combination produces a constant thrust for varying VR. For UHBR nozzles it is not practical to have VR greater than one, where the secondary velocity is more than the primary velocity. In the next section, ESDU prediction for UHBR nozzles under static conditions are obtained to investigate the effect of VR for varying thrust.

5.7.3 Effect of velocity ratio for varying thrust

For the varying thrust study, changes to the velocity ratio are obtained by varying the primary velocity and by keeping the secondary velocity constant. Cases for varying thrust and varying VR for UHBR nozzle with AR = 8.1 and $V_{\mathrm{f}} = 0$m/s are listed in Table (5.3). Thrust from a coaxial nozzles depends upon the jet temperature, velocity ratio and the area ratio. For the current study, we have assumed cold jet conditions with temperature ratio equal to 1.0 and area ratio is equal to 8.1.

Core velocity (m/s)	Bypass velocity (m/s)	Bypass ratio	Velocity ratio	Mixed velocity (m/s)	Thrust (N)
200	200	8.1	1.00	200.0	1290
220		7.4	0.91	202.4	1320
250		6.5	0.80	206.7	1370
280		5.8	0.71	211.8	1428
310		5.2	0.65	217.7	1490

Table 5.3 – Flow conditions for UHBR nozzles for varying VR and varying thrust.

The ESDU predictions of SPL spectra and OASPL directivity for the cases listed

in Table 5.3 are presented in Figures (5.17) and (5.18), respectively. From the four-source method, we know the noise from the mixed jet dominates the low-frequencies and the secondary jet dominates at high-frequencies. The noise spectra presented in Figure (5.17) shows that for all VRs except VR=0.65, the high-frequency noise is independent of primary velocity. This is because the secondary velocity of all these conditions (i.e. VR > 0.65) is the same, U_s = 200m/s. For VR=0.65, the shear layer between the primary and secondary flow generates an extra noise source that generates excess high-frequency noise when compared with higher VRs. The source strength due to the interaction of these two shear layers will be a function of the relative jet velocity (U_p - U_s) [57]. The increase in noise due to varying VRs relative to VR=1 is presented in Figure (5.19). With increase in primary velocity, the effective velocity and the mixed velocity is increased. This increases the peak and the low frequency noise at all angles. For angles closer to the jet axis, the increase in low-frequency noise is relatively high due to the large-scale structures. The large-scale structures are efficient radiators of noise at the shallow angles to the jet axis. At low-frequencies, noise is amplified due to the mean flow acoustic interaction effects. These amplification effects are consequences of mean acoustic interactions acting on the sources [80].

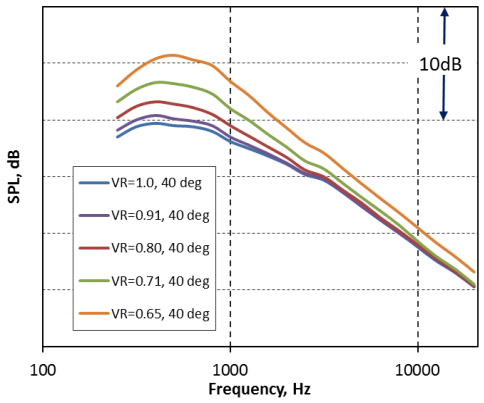

(a) 40^o polar angle

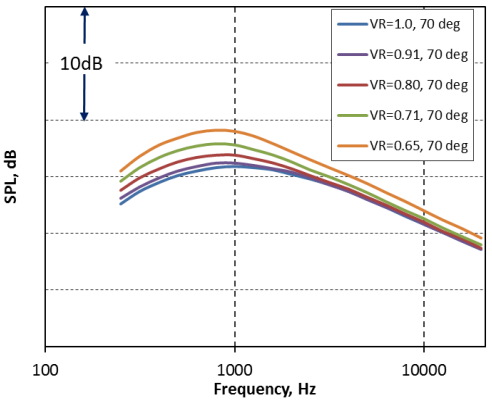

(b) 70^o polar angle

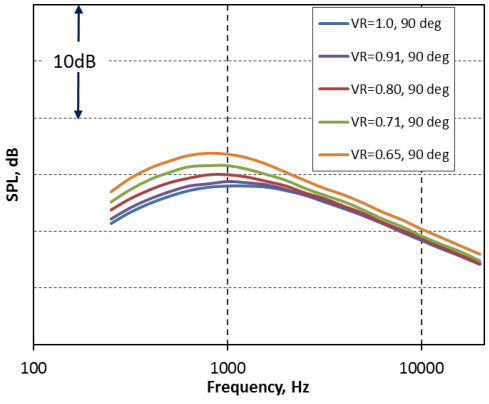

(c) 90^o polar angle

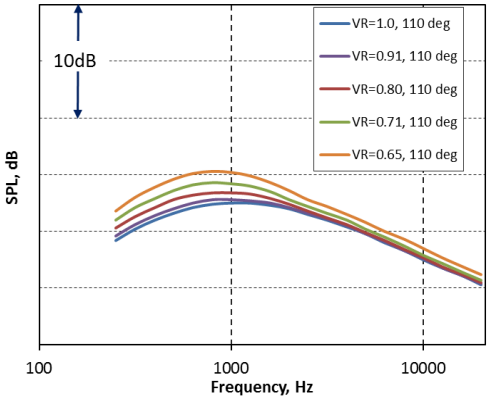

(d) 110^o polar angle

Figure 5.17 – ESDU predictions of spectra for nozzle with AR 8.1 for varying VR; [U_s=200m/s, varying U_p, TR = 1.0, V_f = 0m/s].

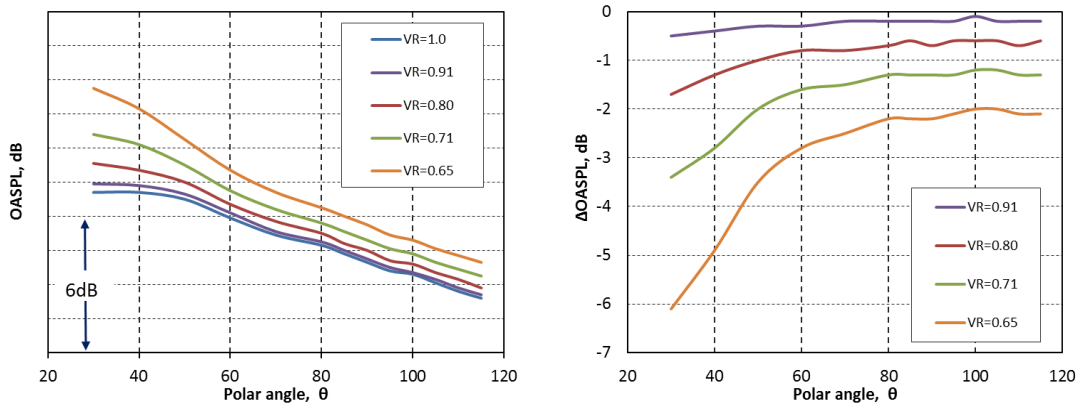

(a) ESDU predictions of OASPL (b) ΔOASPL relative to VR=1.0

Figure 5.18 – ESDU prediction of OASPL and ΔOASPL's plot varying VR with respect to the VR=1.0 for nozzle with AR 8.1 for varying VR (varying thrust); [U_s=200m/s, varying U_p, TR=1.0, V_f=0m/s].

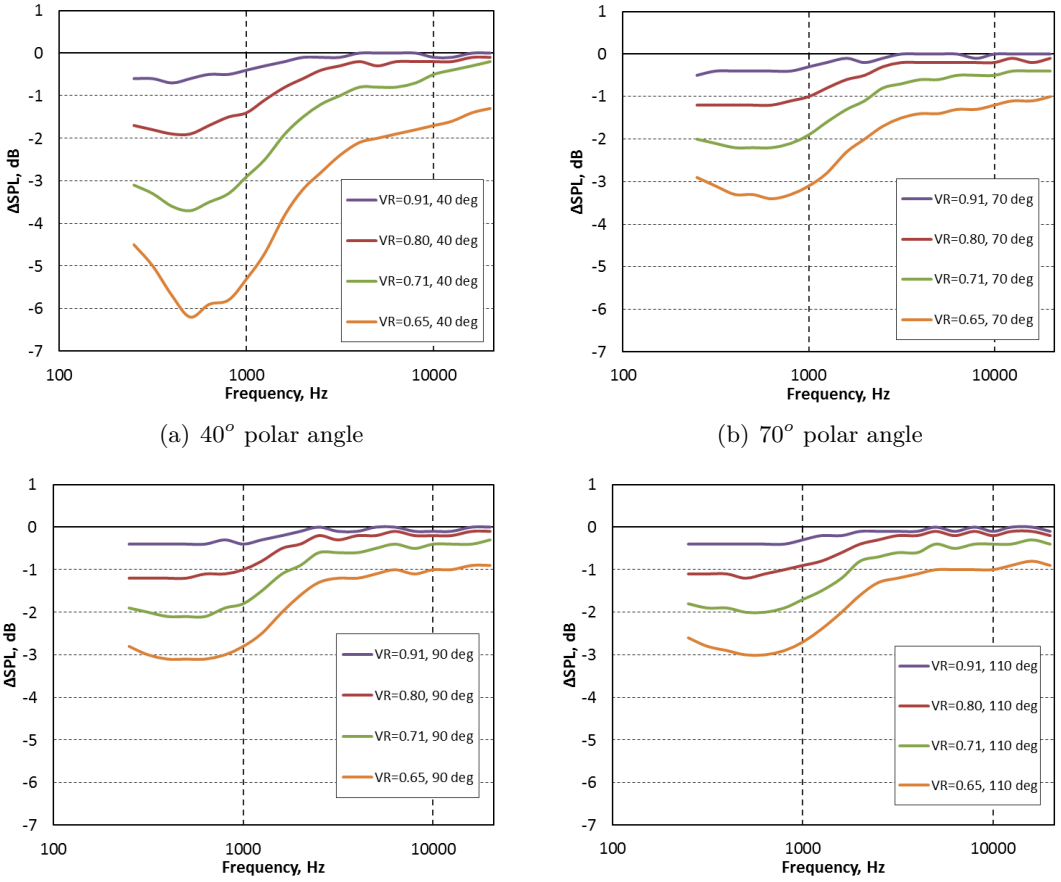

(a) 40^o polar angle (b) 70^o polar angle

(c) 90^o polar angle (d) 110^o polar angle

Figure 5.19 – ΔSPL plot varying VR with respect to VR=1.0 case for nozzle with AR=8.1 for varying VR (varying thrust); U_s=200m/s, varying U_p, TR=1.0, V_f=0m/s.

Before we discuss the effect of VR for nozzles with constant thrust, it is important to understand that the constant thrust concept allows one to make comparisons with a SEJ. In the next section, the SEJ concept is discussed.

5.7.4 Single equivalent jet (SEJ)

The flow due to the combined primary and secondary jet could be realised by a portion of the flow from a single-nozzle jet which has an equivalent nozzle diameter, velocity and temperature. Such a single stream jet is termed as an "single equivalent jet" (SEJ). The thrust of the SEJ must equal the thrust of the actual coaxial jet:

$$F_{SEJ} = \rho_{SEJ} U_{SEJ}^2 D_{SEJ}^2 = \rho_p U_p^2 D_p^2 + \rho_s U_s^2 \left(D_s^2 - D_p^2 \right), \tag{5.7}$$

where the subscripts p and s denote primary and secondary nozzle quantities, respectively. For an isothermal (or constant density) jet, which will be considered here, the above equation simplifies to,

$$U_{SEJ}^2 D_{SEJ}^2 = U_p^2 D_p^2 + U_s^2 \left(D_s^2 - D_p^2 \right). \tag{5.8}$$

In the current study, since we are characterising noise due to varying VR on a constant thrust basis, it is essential to compare the noise with that from a SEJ. The SEJ has a jet diameter of 0.1813m, jet velocity of 202m/s and static temperature of 287K.

5.7.5 Effect of velocity ratio for constant thrust

In this section, both the secondary and the primary velocities are varied so as to obtain constant mixed velocities. ESDU predictions for flow conditions shown in Table (5.4) are presented (AR=8.1, TR = 1.0 and V_{f} = 0m/s).

Core velocity (m/s)	Bypass velocity (m/s)	Bypass ratio	Velocity ratio (m/s)	Mixed velocity (m/s)	Thrust (N)
205	205	8.1	1.00	205.0	1360
220	203	7.5	0.92	205.0	1356
250	200	6.5	0.80	206.7	1372
290	193	5.4	0.67	208.2	1369

Table 5.4 – Flow conditions for UHBR nozzles for varying VR and constant thrust.

The ESDU predictions of spectra and OASPL for these cases are presented in Figures (5.20) and (5.22), respectively. For these cases, the secondary velocity and mixed velocities are similar. Therefore, the noise output is within a maximum of ± 2dB throughout the spectrum at all VRs except VR=0.67 as shown in the ΔdB plots in Figure (5.21).

The ΔdB's are taken relative to the SEJ. From the spectral predictions, it can be observed that the noise generated at low frequencies is a function of the mixed velocity and at high frequencies, it is mainly a function of the secondary velocity. Except at angles closer to the jet axis (i.e. up to 50$^{\mathrm{o}}$ polar angle), the maximum difference in SPL relative to a SEJ is ±1.5 dB. For VR=0.67, relatively higher the mixed velocities adds another 1dB to the low frequencies, especially at the shallow angles. From this it can be concluded that the noise from UHBR nozzles with constant thrust can be modelled using a SEJ.

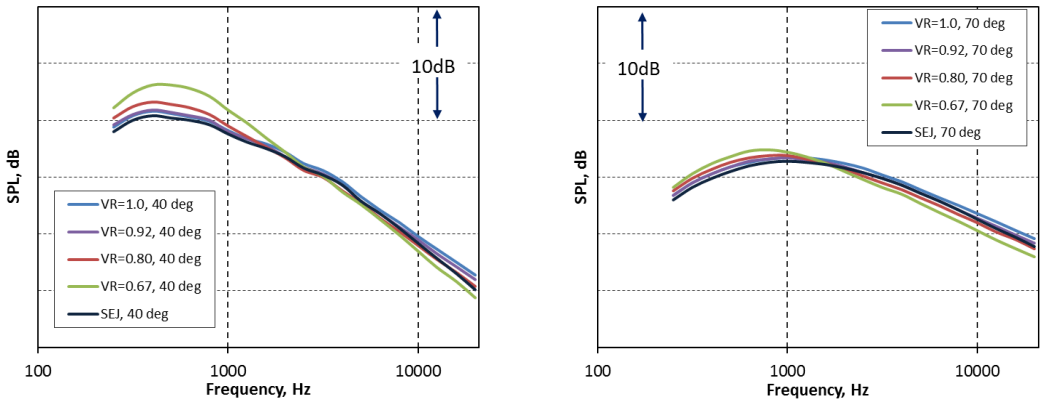

(a) 40^o polar angle

(b) 70^o polar angle

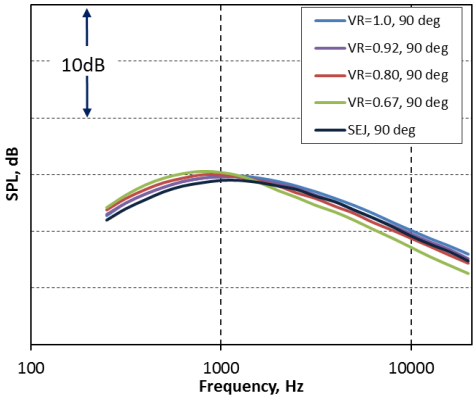

(c) 90^o polar angle

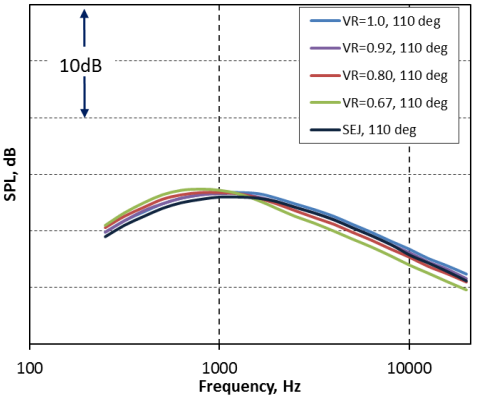

(d) 110^o polar angle

Figure 5.20 – ESDU predictions of SPL spectra for nozzle with AR 8.1 for varying velocity ratio; [Varying U_p and U_s, TR=1.0, V_f=0m/s].

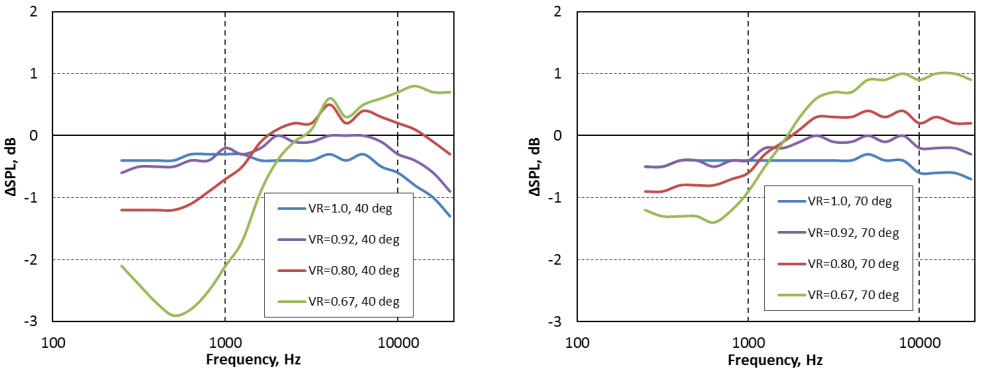

(a) 40^o polar angle

(b) 70^o polar angle

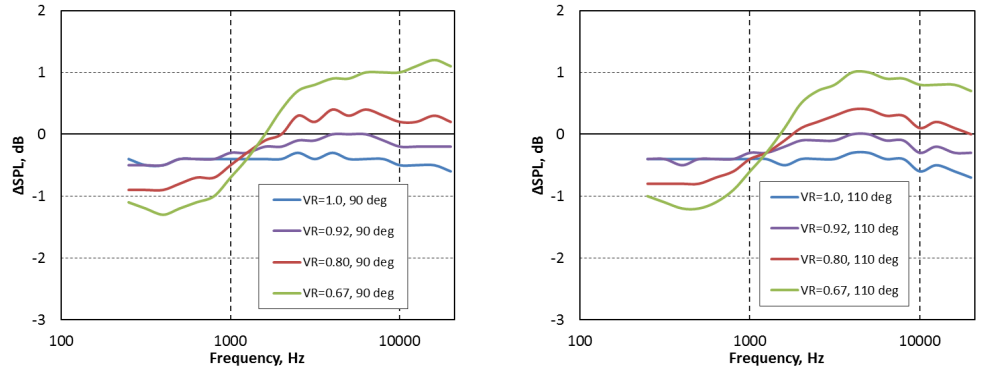

(c) 90^o polar angle

(d) 110^o polar angle

Figure 5.21 – ΔSPL plot for varying VR with respect to a SEJ for nozzle with AR 8.1 for varying VR (constant thrust); [Varying U_s and U_p, TR=1.0, V_f=0m/s].

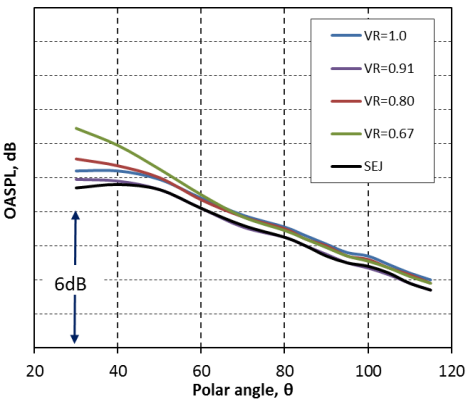

(a) ESDU predictions of OASPL

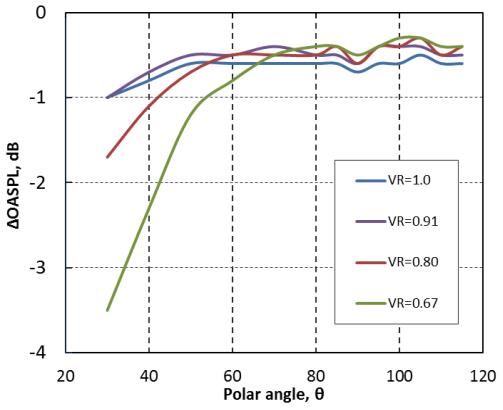

(b) ΔOASPL relative to SEJ

Figure 5.22 – ESDU prediction of OASPL and ΔOASPL's for varying VR with respect to SEJ for UHBR nozzle for varying VR (constant thrust); [Varying U_s and U_p, TR=1.0, V_f=0m/s].

5.7.6 Effect of Area Ratio (AR)

From the previous section, it has been shown that a SEJ can be used to model the noise from UHBR nozzles. In this section, the effect of VR on lower area ratios viz., AR = 3.5 and 5.5 are investigated along with the UHBR nozzle. ESDU predictions for AR = 3.5 and 5.5 nozzles for varying and constant thrust conditions under static conditions and

TR=1.0 are used for the characterisation study. The flow conditions for AR = 3.5 and 5.5 nozzles are shown in Tables (5.5) to (5.8) for constant thrust and varying thrust cases, respectively.

For varying thrust, the secondary velocity was fixed and the primary velocity was varied. For constant thrust cases, both the primary and secondary velocities were varied. The predictions for these cases are shown in Figures (5.23) to (5.26) for nozzles with area ratio 3.5 and 5.5 for varying thrust and constant thrust conditions, respectively.

Core velocity (m/s)	Bypass velocity (m/s)	Bypass ratio	Velocity ratio (m/s)	Mixed velocity (m/s)	Thrust (N)
224	224	3.2	1.00	224	935
262	214	2.6	0.82	227	956
295	206	2.2	0.70	233	989
305	200	2.1	0.66	234	980

Table 5.5 – Flow conditions for AR = 3.5 nozzle for varying VR and constant thrust.

Core velocity (m/s)	Bypass velocity (m/s)	Bypass ratio	Velocity ratio	Mixed velocity (m/s)	Thrust (N)
224	224	3.2	1.00	224	937
250	224	2.9	0.90	231	992
280	224	2.6	0.80	240	1062
319	220	2.2	0.69	251	1141
339	224	2.1	0.66	261	1225

Table 5.6 – Flow conditions for AR=3.5 nozzle for varying VR and varying thrust.

For cases with constant thrust, SPL spectra are compared with their equivalent single stream jet as well. In coaxial nozzles with varying area ratios, the noise produced for a given velocity ratio depends on the merging of the jet and secondary streams. For nozzles with relatively lower AR (smaller bypass area), the two streams before the end of the potential core of the primary stream, where the velocity starts to decrease due to the increased rate of mixing between the two streams. This results in a new shear layer with a much larger velocity gradient across it and this, in turn will lead to an increase in the peak turbulence intensities. However, for nozzles with larger AR (high bypass area), the primary flow mixes out before it merges with the bypass flow. This results in little or no increase in peak turbulence intensities and in turn the far-field noise [168].

For cases with constant thrust, it can be shown that noise from higher area ratios are comparable to the noise from their SEJ. To elaborate this, the SPL from the ARs 3.5, 5.5 and 8.1 nozzles (with constant thrust case) at the 90^o polar angle was collapsed on their mixed jet characteristics (V_{mix}) as shown in the Figure (5.27). This amplifies the differences in the peak and high-frequencies. To estimate the difference with respect to the SEJ, ΔSPLs are shown separately in the Figure (5.28) for AR's 3.5, 5.5 and 8.1.

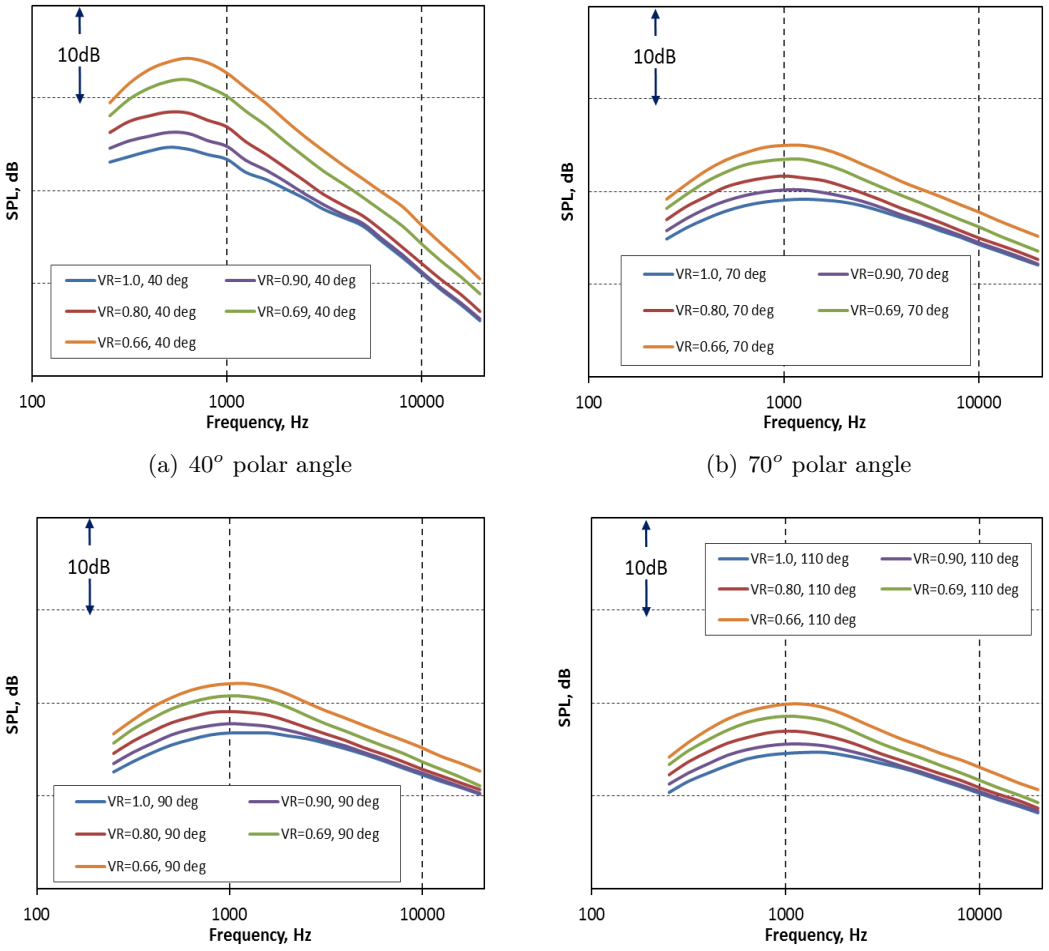

(a) 40^o polar angle

(b) 70^o polar angle

(c) 90^o polar angle

(d) 110^o polar angle

Figure 5.23 – ESDU predictions of SPL spectra for nozzle with AR 3.5 for varying VR (varying thrust); [U_s=224m/s, varying U_p, TR = 1.0, V_f=0m/s].

The maximum difference relative to the SEJ for the AR = 3.5 nozzle is about 3.5 dB, 3 dB for AR = 5.5 and 2 dB for AR = 8.1 nozzle at the lower VR. This further suggests that higher area ratio nozzles behave similarly to a single stream jet. Or in other words, noise from UHBR nozzles can be constructed using a SEJ.

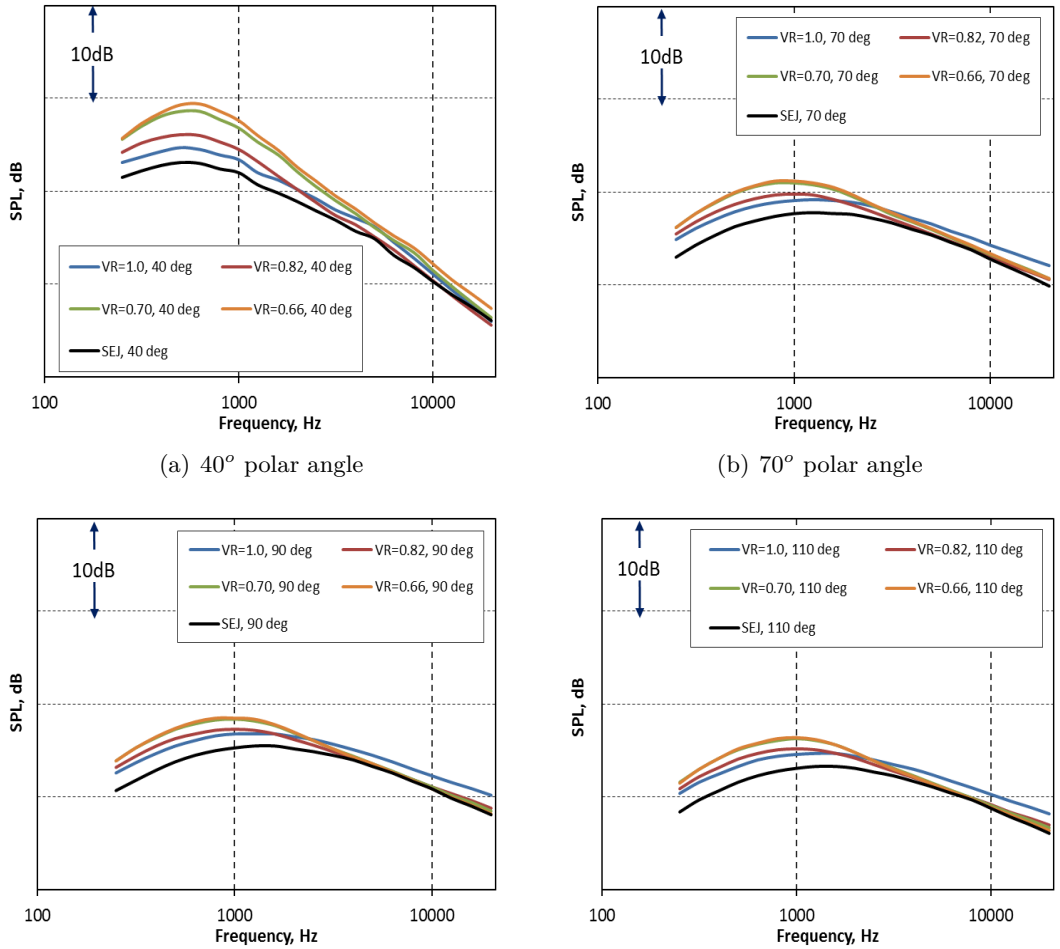

(a) 40^o polar angle

(b) 70^o polar angle

(c) 90^o polar angle

(d) 110^o polar angle

Figure 5.24 – ESDU predictions of SPL spectra for nozzle with AR 3.5 for varying VR (constant thrust); [varying U_p and U_s, TR=1.0, V_f=0m/s].

Core velocity (m/s)	Bypass velocity (m/s)	Bypass ratio	Velocity ratio (m/s)	Mixed velocity (m/s)	Thrust (N)
224	224	4.9	1.00	224	835
265	216	4.0	0.82	226	842
296	208	3.5	0.70	228	844
310	205	3.5	0.66	230	851

Table 5.7 – Flow conditions for AR = 5.5 nozzle for varying VR and constant thrust.

Core velocity (m/s)	Bypass velocity (m/s)	Bypass ratio	Velocity ratio	Mixed velocity (m/s)	Thrust (N)
224	224	4.9	1.00	224	835
250		4.4	0.90	228	870
280		4.0	0.80	235	915
325		3.4	0.69	247	992
339		3.3	0.66	251	1017

Table 5.8 – Flow conditions for AR=5.5 nozzle for varying VR and varying thrust.

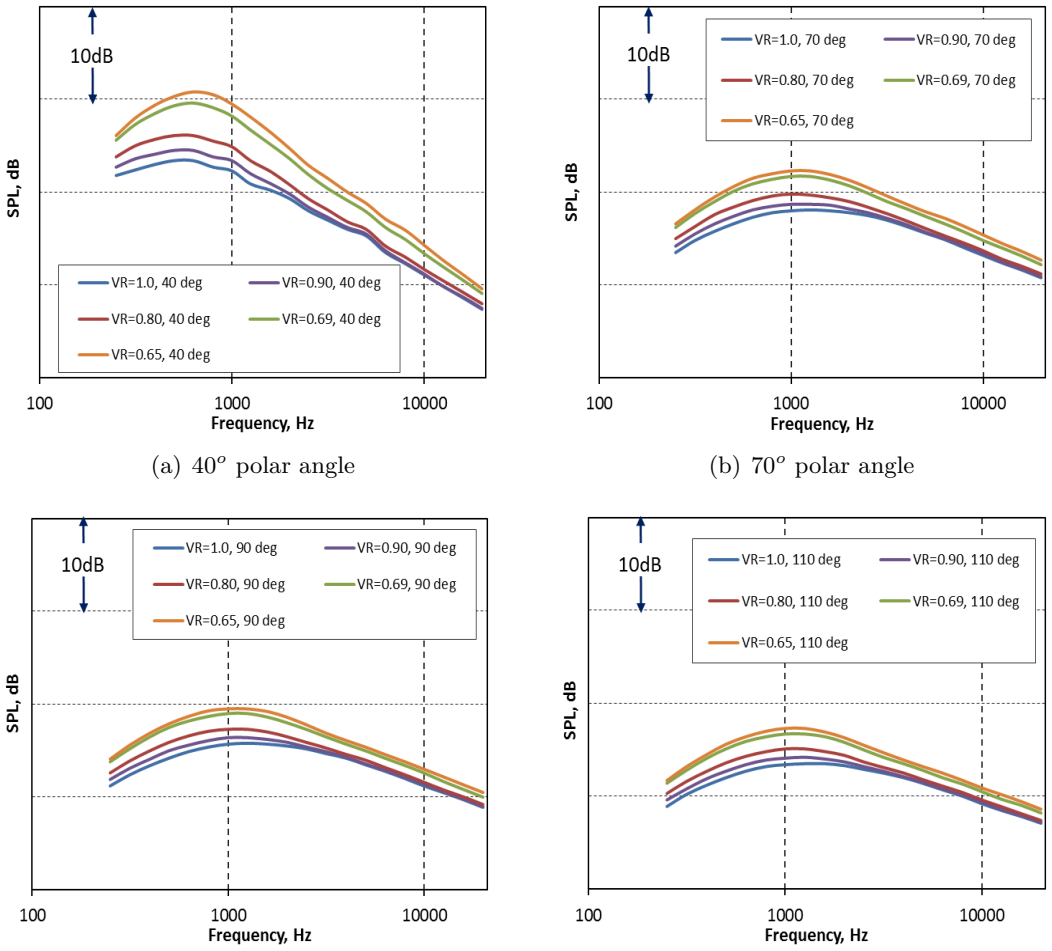

(a) 40^o polar angle

(b) 70^o polar angle

(c) 90^o polar angle

(d) 110^o polar angle

Figure 5.25 – ESDU predictions of SPL spectra for nozzle with AR 5.5 for varying VR (varying thrust); [U_s=224m/s, varying U_p, TR=1.0, V_f=0m/s].

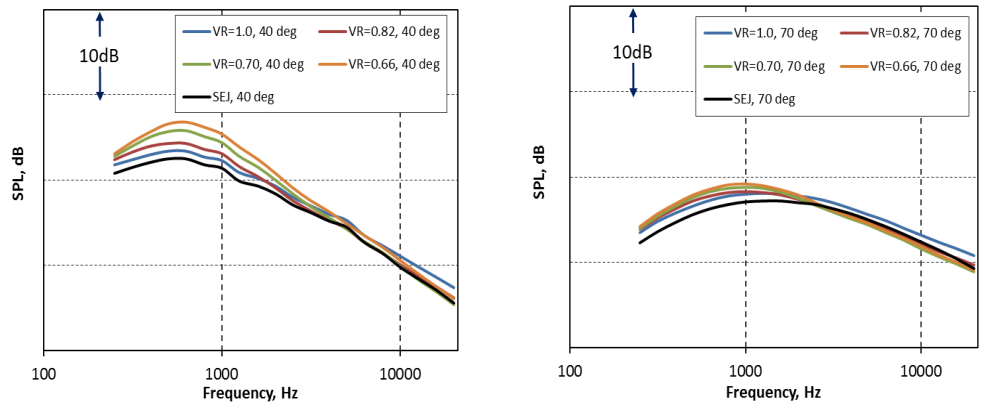

(a) 40^o polar angle (b) 70^o polar angle

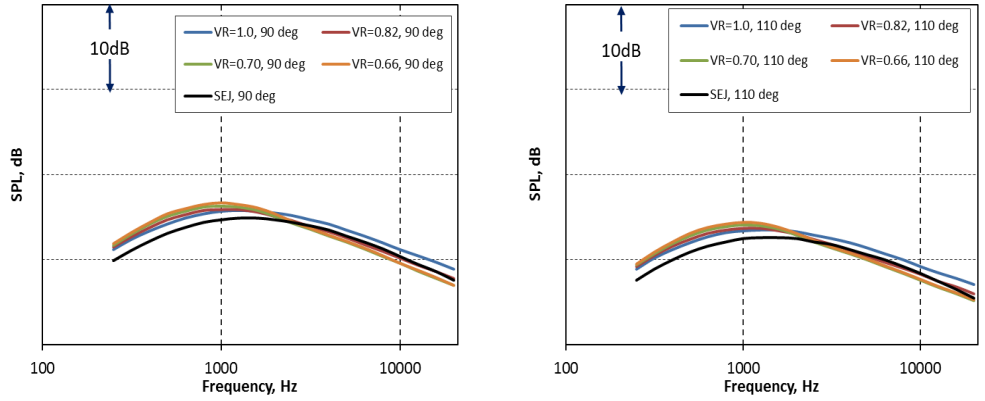

(c) 90^o polar angle (d) 110^o polar angle

Figure 5.26 – Spectral prediction for nozzle with AR 5.5 for varying velocity ratio (constant thrust); [varying U_p and U_s, TR=1.0, V_f=0m/s].

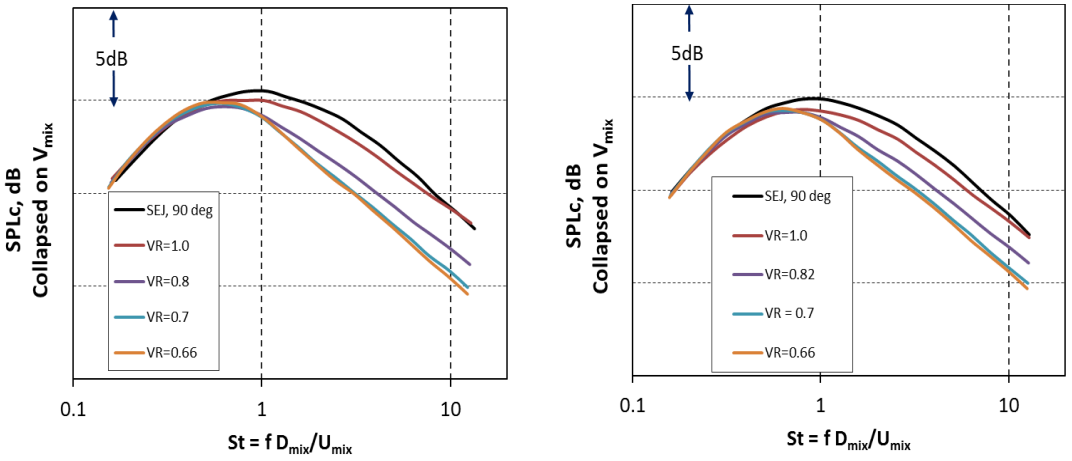

(a) AR = 3.5 (b) AR = 5.5

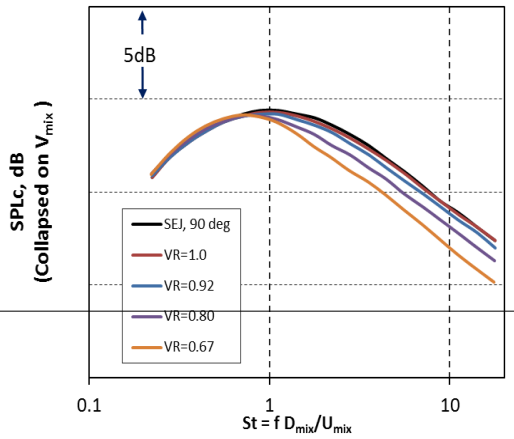

(c) AR = 8.1

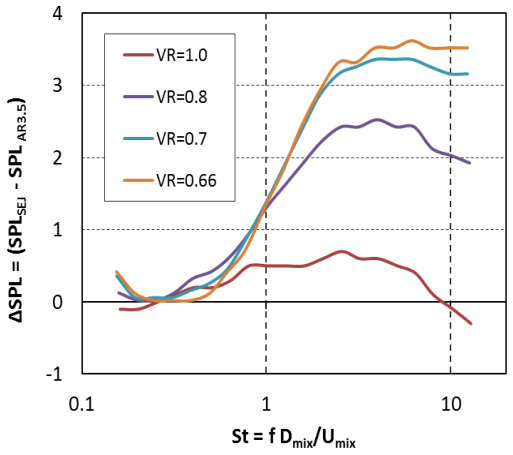

(a) AR = 3.5

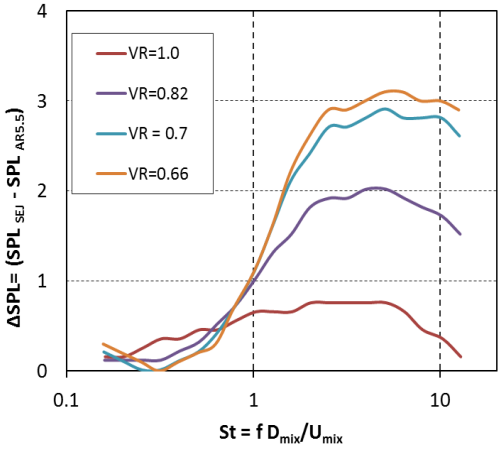

(b) AR = 5.5

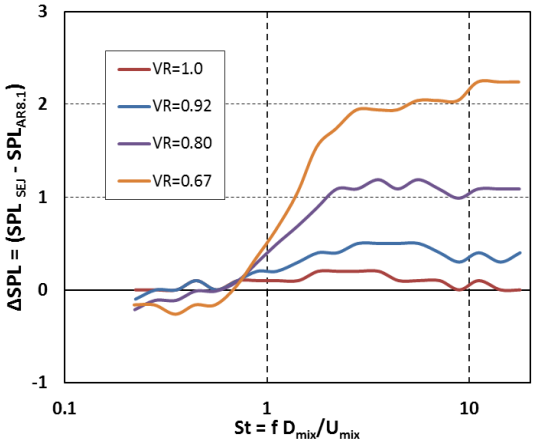

(c) AR = 8.1

Figure 5.28 – ΔSPLs for nozzles with varying AR with respect to their SEJ at the 90° polar angle.

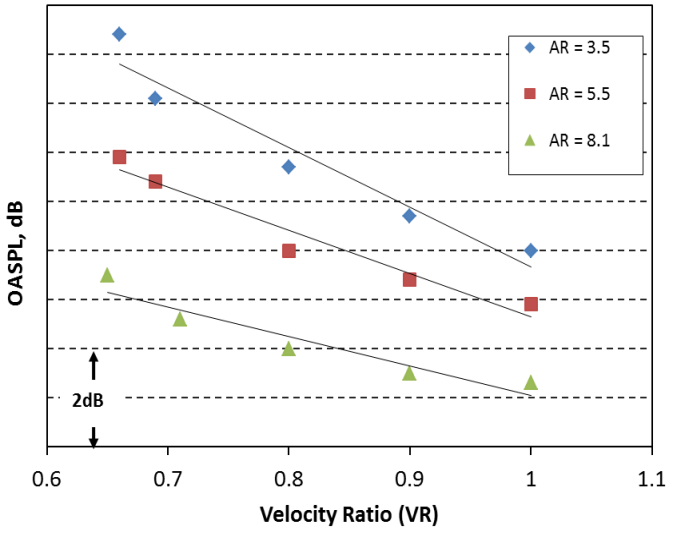

Figure 5.29 – ESDU predictions of OASPL for nozzles with varying AR and VR (varying thrust) at the 90° polar angle. Black lines are the least-squared fits.

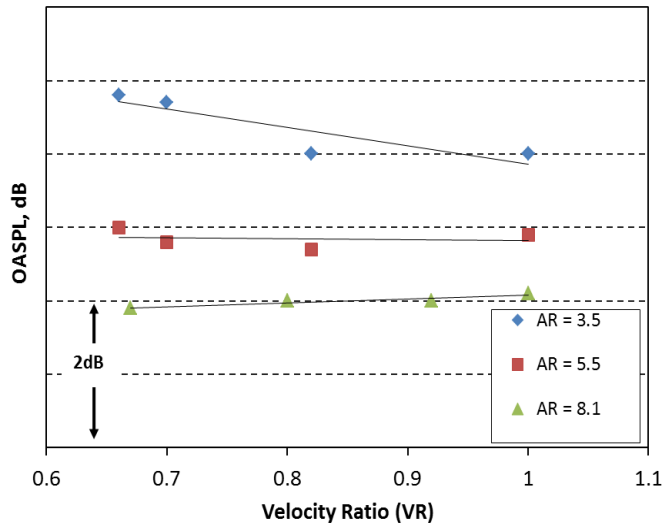

Figure 5.30 – ESDU predictions of OASPL for nozzles with varying AR and VR (constant thrust) at the 90° polar angle. Black lines are the least-squared fits.

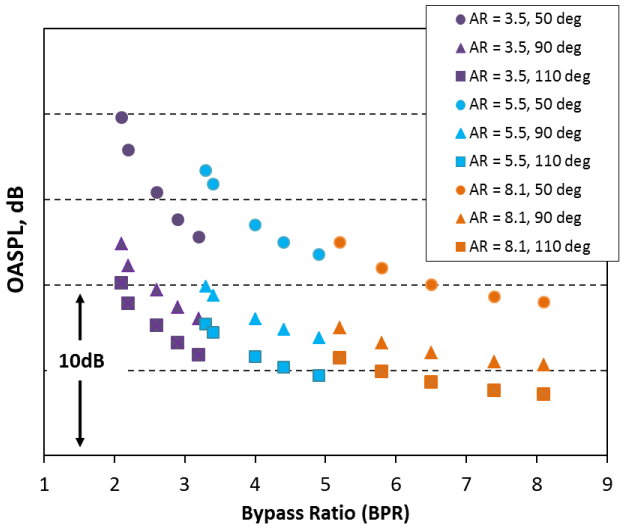

Figure 5.31 – ESDU predictions of OASPL for nozzles with varying AR and BPR (varying thrust).

The OASPL for varying AR and VR for cases with varying thrust and constant thrust are shown in Figures (5.29) and (5.30), respectively. For both cases, it can be concluded that as AR increases, noise from coaxial nozzles tends to be similar to a single stream jet. For cases with constant thrust, the noise is independent of VR. With increase in area ratio, the difference in noise between the highest and the lowest VR tends to zero.

The other parameter which is a function of area ratio and velocity ratio is the bypass ratio. In Figure (5.31), the variation of all three parameter, (i.e., AR, VR and BPR) are presented. From this plot, the noise benefits offered by UHBR nozzles are evident. Also shown are the effect of directivities on bypass ratio. The noise at angles closer to the jet axis are dominated by large-scale energy bearing eddies. The pattern in the noise generated at shallow angles are similar in all the three area ratios considered. That is,

no noise benefit is evident due to the various turbulence scales of aerodynamic noise in UHBR nozzles.

5.7.7 Effect of flight stream velocity

The effect of flight stream on jet mixing noise has been discussed briefly in Section (5.6.2). In this section, the flight effects for a UHBR nozzle are presented. For this study, cases 4, 5 and 6 from the Table (5.1) are considered. The cases with two non-zero flight streams (cases 4 and 5) are compared with the static case. RANS SST k-ω data were obtained for these cases using the procedure described in the previous section. ESDU predictions are also computed for comparison.

The presence of a flight stream over a jet forms an additional shear layer where a low velocity stream of air interacts with the secondary jet (close to the nozzle), the transition jet (near the end of the jet potential core) and the fully mixed jet (downstream of the potential core). This additional shear layer essentially stretches and dilutes the noise sources in the jet and reduces the amount of noise radiated throughout the entire spectrum. In coaxial jets, the spreading of the shear layer depends on the velocity ratio and on the flight stream velocity, which in turn effects the mixing characteristics of the jet. The width of the shear layer can also be related to the local vorticity thickness, δ_θ. The vorticity thickness is defined as,

$$\delta_\theta = \frac{\Delta U}{|\partial U/\partial r|_{max}}, \tag{5.9}$$

where the difference in mean velocity, $\Delta U = r_{5\%}$ - $r_{95\%}$, where $r_{5\%}$ and $r_{95\%}$ are the radial distances at which the mean velocity has fallen by 5% and 95% respectively.

The variation of vorticity thickness for UHBR nozzle (cases 4, 5 and 6) with varying flight stream velocities is shown in Figure (5.32). From the figure, two aspects are clearly evident, the decrease in the width of the shear layer with an increase in flight velocity and, the increase in the length of the potential core with an increase in flight velocity.

From the variation in the vorticity thickness, a significant reduction in noise can be expected. Using the RANS data, LRT predictions were obtained for the three cases at the 90^o polar angle. The predictions were validated against experimental data from the UHBR database. Predictions from the ESDU program were performed and used for the assessment.

The comparison of LRT and ESDU predictions are presented in Figures (5.33) and (5.35). The spectral predictions from both methods agree well at the 90^o polar angle for the three flight conditions. It can be seen that the noise reduction due to flight is uniform across the spectrum. This is illustrated more clearly by the ΔdBs shown in Figure (5.34) where, ΔSPL = $SPL_s - SPL_f$. The reduction in SPL due to flight velocity of 50m/s is about 7 dB, and it is up to 15 dB for V_f = 90m/s.

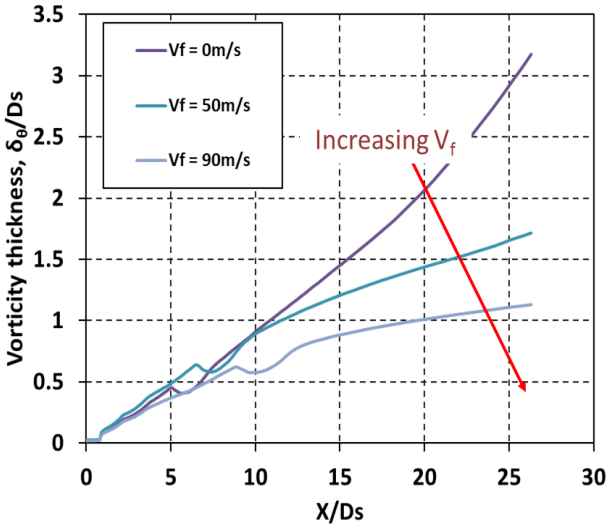

Figure 5.32 – Axial variation of vorticity thickness for UHBR nozzles for varying V_f.

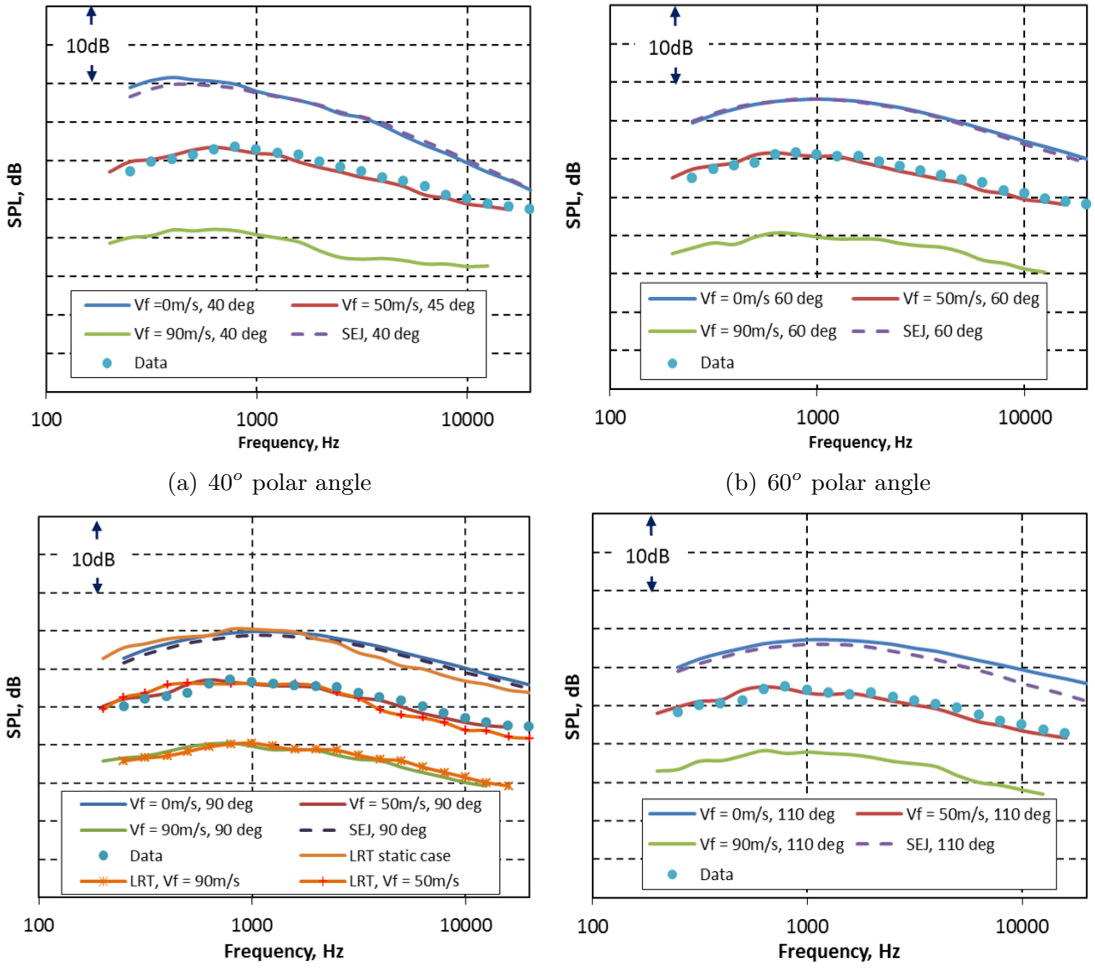

(a) 40^o polar angle

(b) 60^o polar angle

(c) 90^o polar angle

(d) 110^o polar angle

Figure 5.33 – Spectral predictions from the LRT method and ESDU program for varying V_f.

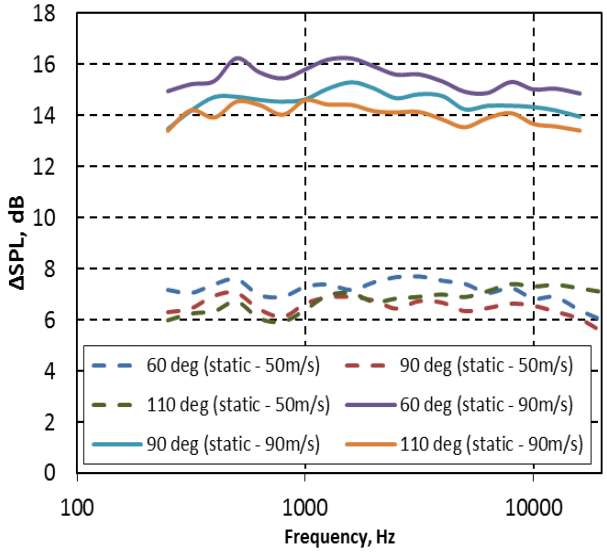

Figure 5.34 – Changes to SPL due to flight, UHBR nozzle.

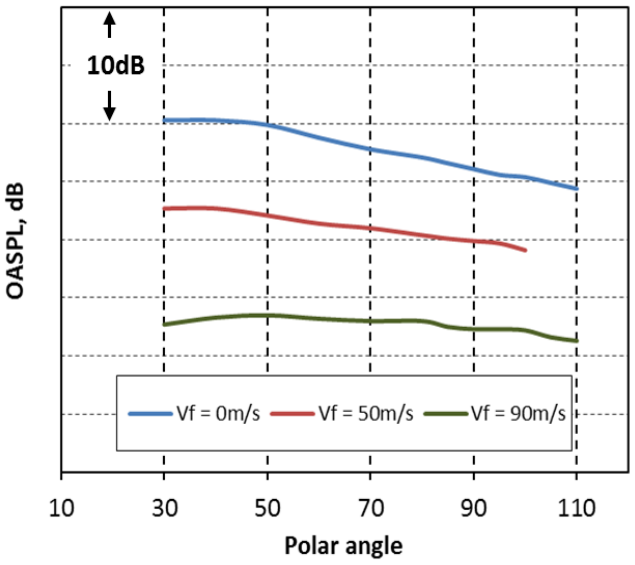

Figure 5.35 – OASPL predictions from the LRT method and ESDU program for varying V_f.

5.8 Effect of eddy length-scale ratio on noise from coaxial nozzles

Using the LRT method, the variation of the eddy length-scale ratio, Δ in the secondary and effective region for cases 1 to 4 listed in Table are determined. The variation of Δ is shown in Figure (5.37). The eddies in the secondary shear layer are subjected to a stretching effect in the stream-wise direction due to the higher rate of shear close to the nozzle exit. This results in finer length-scale ratio of approximately 0.3 for varying VR. In the effective jet region, the secondary and core flows are mixed which reduces the strength in the shear layer. The eddies therefore larger in size in the effective region due to the reduced stretching effect. Figure (5.37), suggests that Δ, in both, secondary and effective

region is independent of velocity ratio.

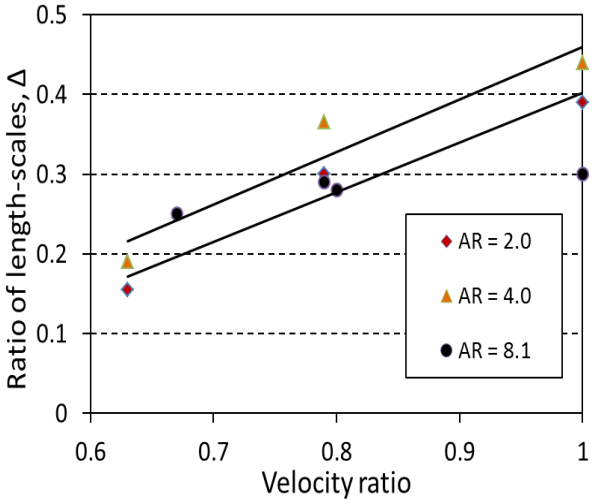

(a) Variation of Δ in secondary jet region

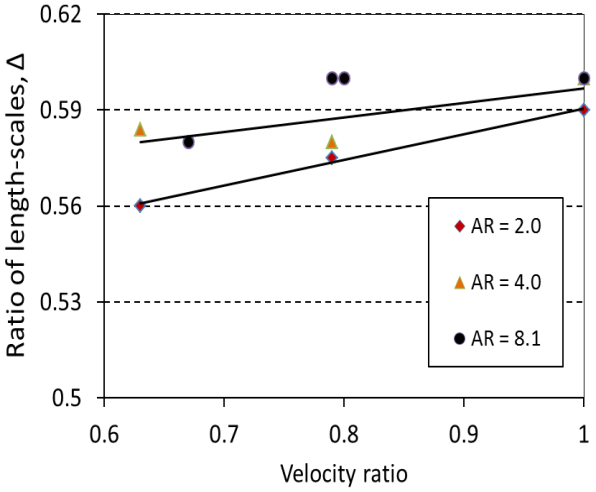

(b) Variation of Δ in effective jet region

Figure 5.36 – Variation of Δ in the secondary & effective jet region for varying AR and VR. Black lines are the least-squared fits.

At this point, the length-scale ratios calculated for the coplanar nozzles with varying AR and VR can be compared with the UHBR nozzle. In Figure (5.36), Δ in the secondary and effective region for area ratios 2.0, 4.0 and 8.1 and varying velocity ratios are presented. In both, secondary and effective regions, the length-scale ratios show an increasing trend with an increase in VR for all AR. It also suggests that range of variation of Δ for area ratios between 2.0 and 8.1 is narrow in both the secondary and effective jet region. These statistics can be used as an input for the noise prediction from nozzles with varying area ratio, both coplanar and nozzle with a centre-body bullet for varying VR.

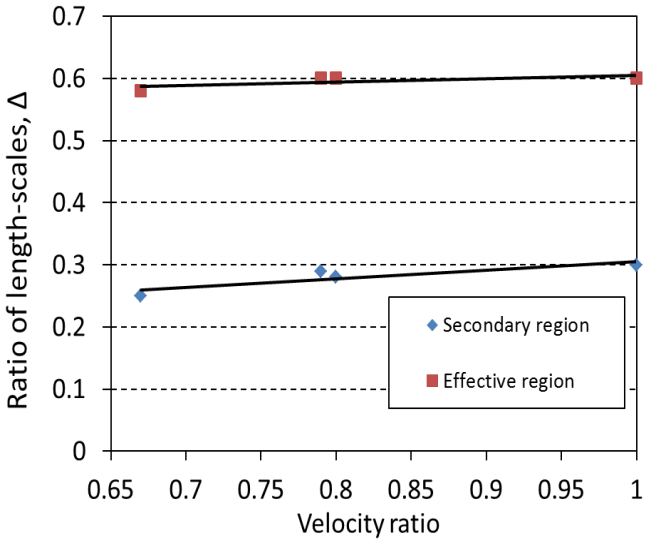

Figure 5.37 – Variation of eddy length-scale ratio, Δ, in UHBR nozzles for varying VR.

5.9 Chapter summary

In this Chapter, a far-field noise characterisation study of UHBR nozzles for varying velocity ratio, flight velocity and bypass ratio using the LRT method and the semi-empirical four-source method are presented. The effect of area ratio on far-field noise is also investigated by comparing different area ratios and flow conditions. From the results obtained from the two prediction methods, the following conclusions have been drawn.

Methods such as the ESDU, does not provide insight into the physics involved in the noise generation. Therefore physics-based methods such as the LRT method is essential to understand the jet mixing noise generation mechanism. LRT results are used to assess the change in length scale ratio which informs about the noise source in the important noise producing regions in UHBR nozzles. Such data can be further extended to investigate jet wing installation effects, cabin noise etc. The LRT data (e.g. calibration coefficients) can be further used to predict noise from UBHR nozzles for other flow conditions and if there are potential nozzle design modifications, for which no test data is available and can therefore be cost effective.

There is a working hypothesis that with increase in BPR, nozzles tend to behave more like a single stream jet. In this chapter, it has been proven that noise from UHBR nozzles can be predicted using an equivalent single stream nozzle. This has been achieved by comparing noise from lower BPR/area ratio nozzles at numerous flow conditions. This simplifies and reduces the computational effort required in predicting noise from UHBR nozzles.

Effect of velocity ratio

To infer the effect of velocity ratio, UHBR nozzle conditions with varying VR were created on the basis of varying thrust and constant thrust. For the varying thrust case (i.e. a fixed secondary velocity and varying primary velocity), from the ESDU predictions, a difference of up to 3dB difference in SPL between lower VR relative to VR1.0 case was seen at low and peak frequencies at all angles except in the forward arc. In the forward arc, the ΔSPL was nearly 6dB, which is due to higher mixed velocities. The change in high frequency noise remains constant at 1dB at all angles. For varying thrust cases, the OASPL reduces with increasing VR at all observer angles. For constant thrust cases, both the primary and secondary velocities were varied. The noise thus generated was independent of VR.

Effect of area ratio

ESDU predictions were obtained for area ratios 3.5, 5.5 and 8.1 for varying velocity ratios, both for varying thrust and constant thrust. For cases with varying thrust, the OASPL reduces linearly with an increase in AR which is due to the global reduction in shear. With increase in AR, the difference in noise between the highest and the lowest VR tends to zero because the nozzles are tending towards a single stream jet. The noise benefits from a UHBR nozzle were also compared for varying bypass ratios. For varying thrust cases, the OASPL reduces with increasing AR band BPR at all observer angles. For constant thrust cases, with increasing BPR and AR, the OASPL tends to become independent of VR at all observer angles. The study showed that noise from nozzles with higher area ratios can be modelled using a single equivalent jet.

Effect of flight velocity

ESDU and LRT predictions for cases with varying flight velocities ($V_f = 50$m/s and 90m/s) have been obtained. These predictions have been compared with measured UHBR data. For the UHBR nozzles, flight effect is independent of frequency (approximately ±1dB) across the entire frequency range. The reduction in SPL due to flight velocity of 50m/s is about 7dB, and it is up to 15dB for $V_f = 90$m/s at all polar angles.

Chapter 6

Cone of silence prediction

In Section (3.5), the advantages offered by ray theory to calculate the propagation effects in jets have been described. However, some of the shortcomings of ray theory, especially the cone of silence has been presented. In this chapter, the CoS problem will be investigated and methods to model the propagation in the CoS are developed.

6.1 Introduction

This chapter concerns the development of methods to model propagation effects when using geometric acoustics or ray theory to calculate the flow-interaction effects arising from jet flows. In the previous chapter, the use of ray theory to calculate propagation effects in jets were described. It was also pointed out that the real ray tracing method used was not generalised enough to compute the field in the Cone of Silence (CoS). In the current chapter, the flexibility within the LRT method to decouple the source and the propagation model is exploited to investigate the propagation model independently to provide an engineering estimate of the CoS acoustic field. This is carried out by developing methods to model the attenuation within the CoS without explicitly resorting to complex ray tracing computations. Two methods are proposed in the current work: the first method is based on modelling the exponential decay using an approximate WKB solution developed by Mani et al. [44] (MGB method) in their analysis of the Lilley equation for a parallel shear flow; the second exploits the canonical nature of the CoS boundary to continue solutions inside the CoS via a complex ray embedded inside the Airy function and its derivative. In case of the latter, the predictions are benchmarked against Lilley's Green's function solution for a parallel shear flow using a variety of parametric studies. The MGB solution is applied to an isothermal single stream jet and the noise predictions at the CoS angles are compared with experimental data.

6.2 Is the Cone of Silence important?

As per the aircraft noise certification standards (eg. the ICAO [7]), the noise measured at the sideline and the flyover certification points are the reference points at take-off (see

Figure 6.1(a)). From Figure 6.1(b), it is evident that jet noise is one of the dominant sources of noise at take-off.

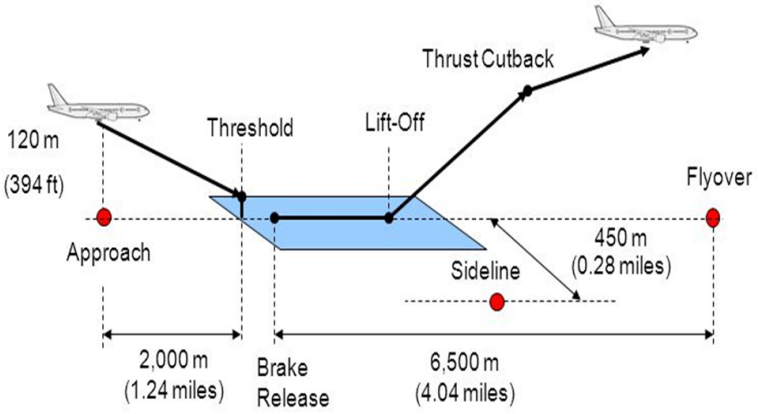

(a) Aircraft certification route showing positions of approach, lateral and flyover microphones.

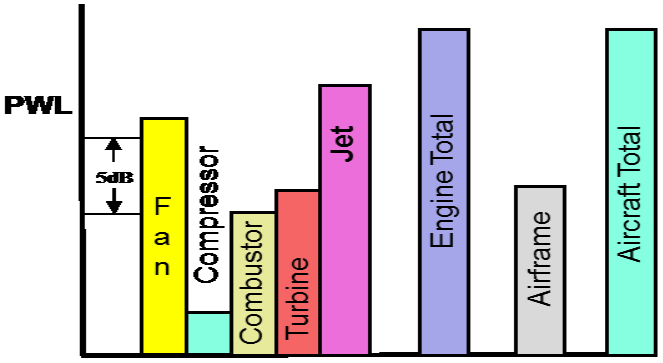

(b) Noise contribution from various sources at the take-off certification point

Figure 6.1 – Schematic showing the aircraft noise certification points and the sound power level (PWL) at the take-off condition [1].

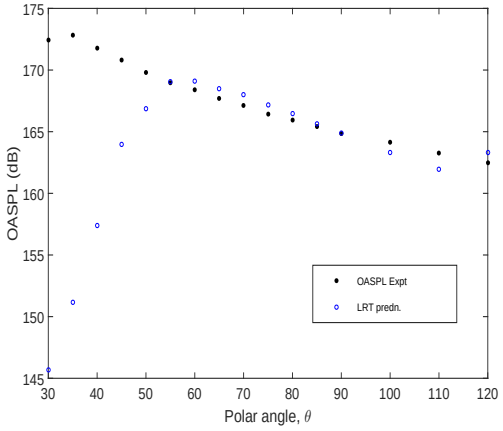

Figure 6.2 – OASPL plot for an isothermal single stream jet [M = 0.75, D_j=0.1016m]

In Figure (6.2), the OASPL computed using the LRT method is compared against measured OASPL for an isolated single stream jet. The plot clearly shows that jet noise

peaks at angles closer to the jet axis. The peak noise levels arise from the beaming jet noise sources from the shallow angles to the jet. Since the flyover and the sideline reference microphones are subjected to a high jet exposure time suggests that the noise from the CoS can be a potential contributor to the Effective Perceived Noise Levels (EPNL) calculations.

Analytical models such as the one proposed by Wundrow and Khavaran [26], suggest that there exists a non-trivial complex field in the CoS, and that the rays suffer exponential decay due to the flow-acoustics interaction, causing the ray trajectories and their amplitudes to migrate to the complex plane. The ray tracing routine in the LRT method is not capable of tracing rays in the complex plane. Therefore, it is important to infer the complex contribution from the ray tracing routine which uses only real rays to calculate the mean-flow propagation/refraction effects.

Before focussing on the contribution from complex rays, it is important to understand the effect of refraction that can be computed using the LRT method. In the next section, the effect of refraction is analysed by only considering the results computed using the propagation model (i.e. without using the source definitions) by using the mean-flow computed using RANS CFD for an isothermal single stream jet with Mach number 0.75.

6.3 Mean-flow propagation effects from a RANS CFD jet

In this section, propagation effects in the far-field from an isothermal CFD jet with Mach number 0.75 is analysed by plotting the flow factor (as ΔSPLs) computed using the ray tracing ('real' rays) at various source locations as shown in Figure (6.3). Flow factors are defined as ratio of the far field intensity to its value without the jet flow with the source strength held constant. The flow factor indicate the amplification or reduction of the SPL due to mean-flow refraction effects in the far-field due to a noise source in the jet plume.

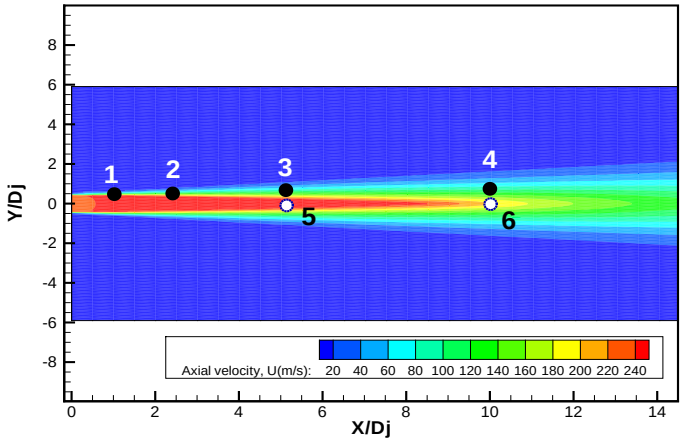

Figure 6.3 – Axial velocity computed using RANS for an isothermal single stream jet (M = 0.75). Source point location in the nozzle lip line (source points 1 to 4) and in the centreline (source points 5 & 6) to study refraction effects.

In this section, the flow factors in terms of a ΔSPL, (see equation (3.69)) are presented

in two forms: (i) by fixing the observer location in the far-field and varying the source location, and (ii) fixing the source position and varying the observer location in the far-field over $0^o < \theta < 180^o$ and $0^o < \varphi < 360^o$ within the jet plume. Although the nozzle considered here is axisymmetric, the fields generated by the ray trajectories are three-dimensional in nature.

The effect of refraction is investigated at two regions in the jet plume, in the jet shear layer and in the potential core. First, sources located along the jet shear layer ($Y/D_j = 0.5$) at different axial positions as shown in Figure (6.3) are considered. The jet shear layer is where the turbulent kinetic energy (k) peaks, and from the relation $I_{1111}(\Omega) \propto k^{7/2}$, given in equation (3.35), can be considered as the most important noise generation region. Figure (6.4) shows the contour plots of the flow factor, where the negative values of ΔSPL indicates an attenuation, and positive values show sound amplification in the far-field. The white space at polar angles closer to the jet represents the cone of silence region. In the CoS region, no real rays are collected. Flow factors are shown for source points 1 to 4 which are placed in the nozzle lip line at varying axially downstream of the jet as a function of polar and azimuthal angles.

For the off-axis source located at $X/D_j = 1$ and $Y/D_j = 0.5$, the blank space up to $\theta = 45^o$ (marked by the dashed line) defines the CoS boundary. The cone of silence is symmetrical and variable in shape along the azimuthal axis, see Figure (6.4(a)). The high intensity region from $\varphi = 90^o$ to 270^o, marked as region B, is due to the concentration of the ray field causing a divergence in the ray amplitude. This phenomena where an envelope of rays tangent, indicates a caustic where the ray amplitude is also singular. Such an accumulation of rays at caustic points is due to the mean-flow refraction effect. At caustics, rays are clearly not valid. This kind of caustic generated at the CoS boundary is the simplest form of caustics and is called a smooth caustic or a fold caustic [133]. Further, another interesting cusp-like structure can be observed at φ=180^o, marked as region C in Figure (6.4(a)). These structures are the second in the hierarchy of caustics, called as Cusp caustics. Caustics are described in more detail in section (6.9).

For a source located further downstream at $X/D_j = 2.5$ and $Y/D_j = 0.5$, the flow factors are shown in Figure (6.4(b)). It can be observed that the structure of the caustics shrink in size with a reduction in the magnitude of the flow factors. Similar kind of a trend can be observed for a source located further downstream at $X/D_j = 5$ and $Y/D_j = 0.5$, see Figure (6.4(d)). As the source moves axially downstream of the nozzle, the flow gradients gets weaker with the spreading of the jet shear layer. This allows more rays to convect through the flow causing a reduction in the amplitude at the caustics. However, no significant change in the CoS boundary is observed for sources located up to $X/D_j = 5$, suggesting that sources in these parts of the shear layer are subjected to the CoS effect.

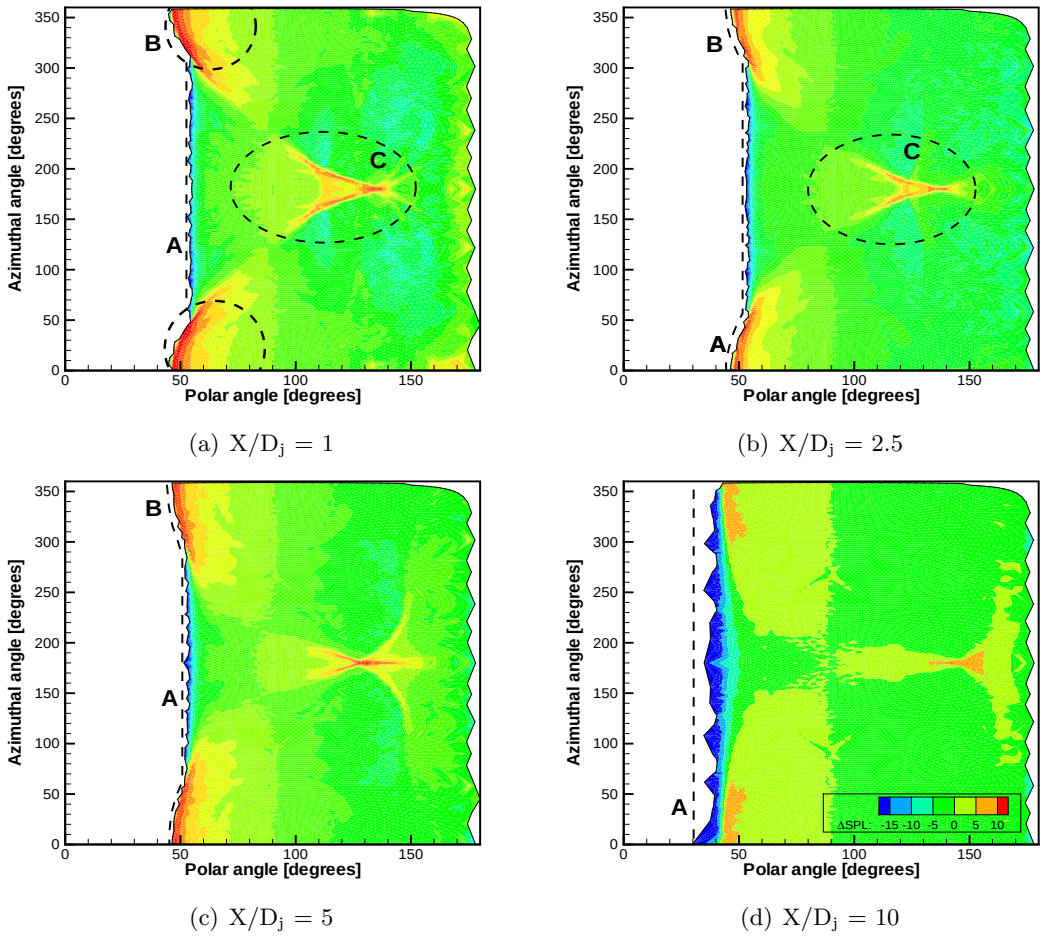

(a) $X/D_j = 1$ (b) $X/D_j = 2.5$

(c) $X/D_j = 5$ (d) $X/D_j = 10$

Figure 6.4 – Flow factor for sources on the lip line of an isothermal jet with M = 0.75. Sources are placed at varying axial positions; azimuthal angle, $\varphi = 90^o$. The blank space at lower polar angles is the cone of silence. The dashed line marks the CoS boundary.

Flow factor results for a source located at the end of the potential core ($X/D_j = 10$ and $Y/D_j = 0.5$) shows considerable changes in the shape, and a reduction in the CoS boundary to $\approx 30^o$. This is due to the weakening of the velocity gradients in the shear layer. The caustic structures in this case are almost absent and the amplitude in the vicinity of the caustic regions are further reduced. From this study, it can be concluded that sources in the jet shear layer up to the end of the potential core are significant contributors towards the CoS and have to be considered to model the exponential decay in the CoS region.

So far, the point sources that have been located in the nozzle lip line were considered. Although the sources located in the lip line are significant noise generators in a jet, it would be interesting to observe the flow factors for point sources located in the jet centreline. Point sources 5 and 6 located along the jet centreline ($Y/D_j = 0$) at different axial positions are shown in Figure (6.3). Flow factors for on-axis point sources located at $X/D_j = 5$ and $X/D_j = 10$ are shown in Figure (6.5). For both these sources, flow factors are symmetrical along the azimuthal axis without caustics or any locally amplified regions. The CoS boundary for the source located at $X/D_j = 5$ is $\approx 50^o$, whereas for the source at $X/D_j = 10$ is $\approx 35^o$. For the source located closer to the nozzle exit, the rays have to propagate through a much denser shear layer compared to the source located further downstream of

the nozzle where the shear layer is relatively weak resulting in reduced refraction effects. Structurally, these flow factors look similar to the flow factors for a point source shown in Figure (6.4(d)).

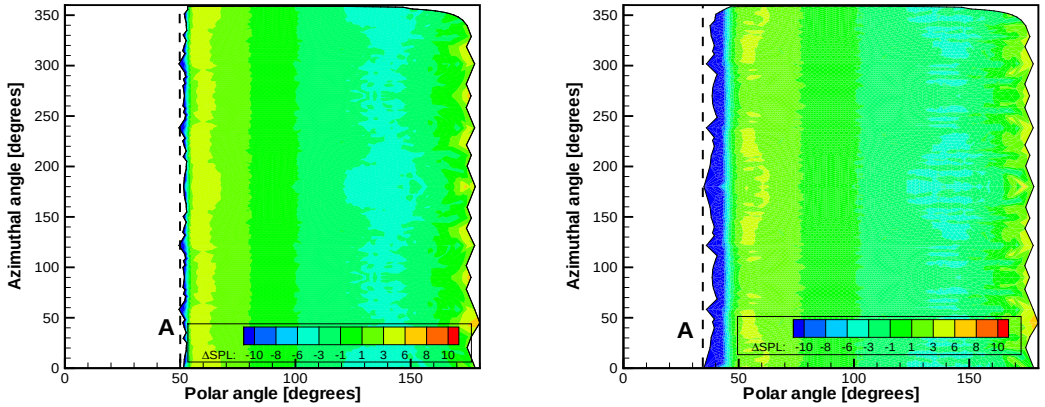

(a) $X/D_j = 5$, $Y/D_j = 0$ (b) $X/D_j = 10$, $Y/D_j = 0$

Figure 6.5 – Flow factor for sources on the centreline of an isothermal jet with M = 0.75. Sources are placed at varying axial positions; azimuthal angle, $\varphi = 90^o$.

From the flow factor results analysed so far, the shortcoming of ray theory in the CoS has been realised. It has been identified that the fold caustic delimits the CoS boundary. Therefore, identifying the location of fold caustics are essential to be able to compute the complex field on the other side of the caustic surface. In this chapter, two methods to calculate the exponential decay in the CoS is presented. Before getting into the details of these methods, an understanding of the ray propagation within the CoS is necessary. In the next section, a pedagogical example is used to show how the CoS works using a stratified fluid layer (Slab problem). This is a simple analogy to understand the complex rays in the CoS. It is followed by the theory to model the exponential decay in the CoS.

6.4 Background theory

The acoustic-mean flow interaction within the cone of silence can be explained considering simple acoustic systems in the context of layered media. Let us consider a stratified fluid layer of thickness 'L' as depicted in Figure 6.6, with density, ρ_1, sound speed, c_1, surrounded by fluid with a lower sound speed, c_o. If an incident wave, 'I' arriving at an angle, θ, satisfies the condition $c_o/\sin\theta < c_1$, produces evanescent waves within the fluid barrier. The magnitude of these waves decays exponentially, but if the barrier is not too thick a weaker disturbance, in the form of a transmitted wave 'T', can propagate further.

A cone of silence exists if the axial phase speed, $c_p = u_s + c_s > c_o$, where, u_s and c_s are the velocity and sound speed in the source region, respectively. A wave field, propagation in a moving flow field, having certain frequency, ω, and axial wavenumber, k_x, will only propagate (i.e., have a real transverse wave-number) provided its axial phase speed $c_p = \omega/k_x$ is supersonic relative to the fluid flow. In the limiting case where, c_p

$=(c_p)_{min}$, the wave will emerge out of the cone of silence.

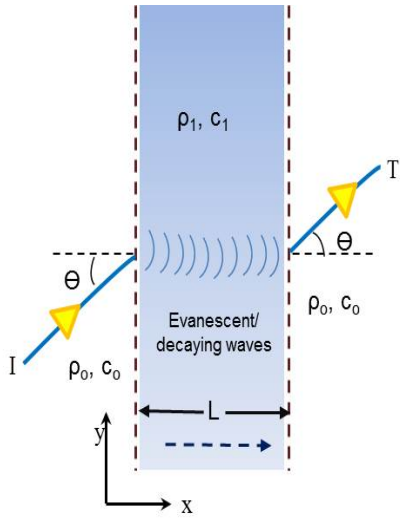

Figure 6.6 – A schematic showing the generation of exponentially decaying waves when a ray passes through a fluid barrier.

If the axial phase speed c_p is less than $u_y + c_y$ between the source location y_s (also referred to as 'turning point'), but becomes supersonic relative to the fluid beyond $y = y_t$, the disturbance will have a transverse wavenumber which is imaginary for $y_s < y < y_t$, and real for $y > y_t$. Thus, propagating waves can enter the cone of silence, but only having crossed the fluid barrier from point y_s to y_t as 'evanescent' or non-propagating disturbances as shown in Figure (6.6). This means that the ray trajectories and their amplitudes migrates to the complex plane.

These 'non-propagating' disturbances (evanescent waves) are valid only in the high-frequency limit. To identify these non-propagating disturbances, a local radial wavenumber is used. Throughout the present study of acoustic-mean flow interaction, the high-frequency limit is being used, therefore the local wavenumber concept is described in the next section.

The example described above was for a stationary medium with two turning points. In the next section, a mathematical model to calculate the exponential decay is derived for a parallel shear flow is presented.

6.5 Method 1 - Patch method

It has been shown that the ray theory works well outside the CoS, and that we need to develop solutions inside the CoS. The field near the CoS boundary can be considered as a two-point boundary value problem, where the solution varies rapidly on one side (outside the CoS), and varies slowly on the other side (inside the CoS). So, there is a thin transition layers where the solutions can jump abruptly, while away from the layers the solution behaves regularly and vary slowly. Such a problem can be solved by calculating

the asymptotic approximation to the solutions of the field both inside and outer the CoS. These solutions are then 'patched' (or combined) to obtain a uniformly valid solution across the field. In the current method, ray solutions outside the CoS are patched with the exponential decay calculated inside the CoS.

6.5.1 Flow-acoustics interaction

So far, attempts have been made to obtain analytical solutions within the CoS by Wundrow and Khavaran [26], Morfey & Sczewczyk [169] and up to some extent by Tester & Morfey [125]. The standard method of finding solutions within this shadow region have been to take the high frequency limit and then find asymptotic solutions to the Lilley's Green's function. The closest solution was provided by Wundrow and Khavaran [26], who applied the WKB technique to demonstrate the determination of amplitudes from complex rays. The solution procedure proposed are computationally difficult to be adopted into the LRT method. Therefore, the main objective of the current work is to find a solution inside the CoS for a nozzle flow, which could be adaptable within the existing LRT method.

Consider a point source embedded in a two dimensional representation of a shear layer located at a certain axial location downstream of the jet exit plane as shown in Figure (6.7). Here, since the source is embedded in the shear layer, the problem reduces to a single turning point problem. The mean flow Mach number profile is defined as $M_j \operatorname{sech}^2(2y)$, where $M_j = u(y)/c(y)$. Here, on the scale of the acoustic wavelength the relative changes in the flow parameters are assumed small, due to the geometric acoustic (GA) limit.

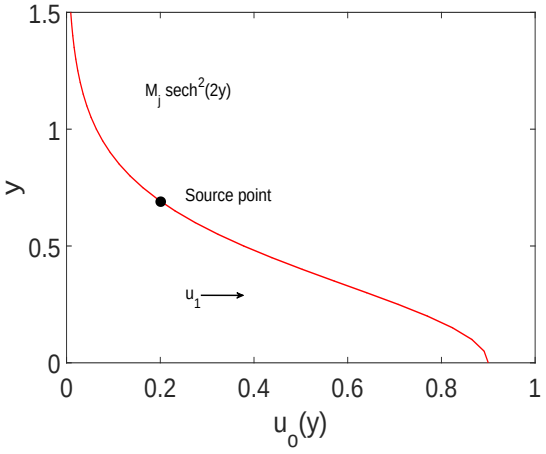

Figure 6.7 – Velocity profile; cross-section of $M_j \operatorname{sech}^2(2y)$.

The mean flow profile is assumed to hold at all axial stations upstream and downstream; thus $u = u(y)$ and $c = c(y)$. Following Morfey and Szewczyk [169], who use the WKB method, the local pressure field may be written as,

$$P^2(x,y,t) = \left\{\rho c^2 / k_y(y)\right\}^{0.5} . A(y) \exp\left(i \int_{y_s}^{y_t} k_y(y)\, \mathrm{d}y\right) \exp\left(i k_1 x - i\omega t\right), \tag{6.1}$$

where the transverse wavenumber k_y is given by

$$k_y^2 = \left[\{\omega - k_1 u(y)\} / c(y)\right]^2 - k_1^2, \tag{6.2}$$

and $c(y)$ and $u(y)$ are the local speed of sound and flow velocity respectively, ω is the radian frequency in a fixed reference frame and k_1 is the axial wavenumber, is constant in the radial direction due to the assumed parallel shear flow.

Since the flow is not uniform, the amplitude $A(y)$ will vary with y, but because of the imposed GA limitation the variation is small on a scale of the wavelength. Equation (6.1) then represents a propagating wave-field. Likewise, the radial wavenumber k_y will vary slowly in the radial direction and by inspection, equation (6.2) can be either real, imaginary or equal to zero.

If the radial wavenumber is real then equation (6.1) represents a locally propagating wave-field. If it is imaginary no propagation will occur and the amplitude of the pressure wave-field will decay according to,

$$A(y) \exp\left(-\int_{y_s}^{y_t} |k_y|\, \mathrm{d}y\right). \tag{6.3}$$

Suppose k_y starts off imaginary at the source radial position, y_s, then since k_y varies with y a radial location may occur such that k_y becomes real. This radial location is known as the "turning point" y_t and defines the location where the source is cut-on or cut-off.

An expression for k_y at the source location may be obtained in terms of the radiation angle θ_o as follows. From equation (6.2),

$$k_y^2 = \left[\{\omega - k_1\, u(y)\} / c_s\right]^2 - k_1^2, \tag{6.4}$$

where u_s and c_s are the flow parameters at the source position. Since $k_1 = (\omega/c_o)\cos\theta_o$, where θ_o is the polar radiation angle in the far field relative to the jet axis, equation (6.4) can be written as,

$$k_y^2 = (\omega/c_o)^2 \left\{\left[1 - (u(y)/c(y))\cos\theta_o\right]^2 (c(y)/c_o)^{-2} - \cos^2\theta_o\right\}. \tag{6.5}$$

For an isothermal jet, $c(y)/c_o \approx 1$ and the overall wavenumber, k_o can be written in

terms of ω and c_o as $k_o = (\omega/c_o)$. Incorporating this condition in equation (6.3), gives

$$A(y)\exp\left(-\int_{y_s}^{y_t}|k_y|\,\mathrm{d}y\right) = A(y)\exp\left(-k_o\int_{y_s}^{y_t}\sqrt{\left|[1-(u(y)/c(y))\cos\theta_o]^2-\cos^2\theta_o\right|}\mathrm{d}y\right), \tag{6.6}$$

where, $\mathrm{u(y)/c(y)} = M_j\,\mathrm{sech}^2(2y)$.

Equation (6.6) is an important relation which can be used to determine the amplitude decay due to the CoS affect. This method of modelling the exponential decay using an approximate WKB solution has been developed by Mani, Gliebe and Balsa [44] in their analysis of the Lilley's equation for a parallel shear flow. This method will be used to patch together with the solutions outside the CoS. In the next section, the Patch method is applied to an isothermal single stream jet and the predictions are validated against experimental data.

6.6 Validation of the Patch method for a single stream jet

In this section, the Patch method is applied to an isothermal (temperature ratio, TR= 1.0) single stream jet (Mach no. = 0.75, $\mathrm{D_j}$ = 0.1016m) from the SYMPHONY database, to demonstrate the capability of the method to recover the 'lost' energy by accounting for the exponential decay due to the fluid shielding in the CoS. Results are compared against experimental data and previous LRT predictions (i.e., with no CoS modelling involved).

6.6.1 Assumptions for the Patch method

The method is based on certain assumptions and are as listed below:

- Equation (6.6) [44] is used to compute the shielding effects of the jet and is based on the assumption of parallel flow jets, wherein the velocity and temperature profiles are functions of the radial variable only.
- For the isothermal jet considered, a single turning point has been assumed, where the modes are initially cut-off and gets cut-on at the turning point location in the flow [44].
- The modal summation of the damped sources are carried out only for the zeroth order azimuthal mode.
- The calculation procedure is applied to sources which lie within eight jet diameter along the jet axis only. This is because the cone of silence mainly affects the high frequency sources, which usually lie within the axial length of the potential core.

6.6.2 Identifying the sources subjected to the CoS effect

Firstly, the LRT method has been used to generate virtual sources points (source co-ordinates) based on the local Mach number informed by the input CFD data. A total of

1404 source points were generated.

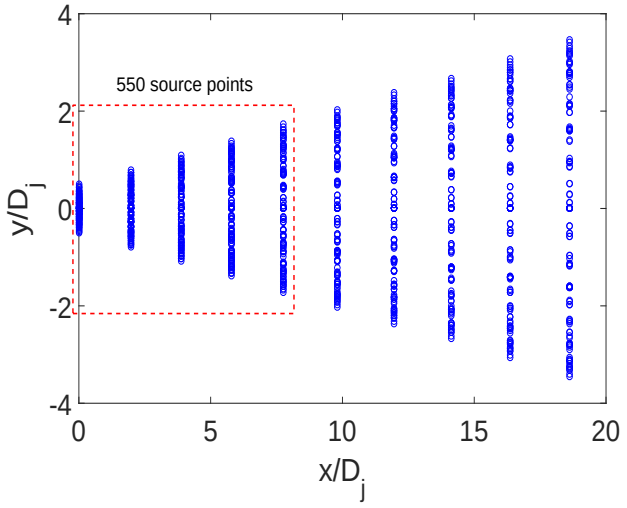

Figure 6.8 – Sources points within a single stream jet generated using the LRT method that are considered for the calculation using the Patch method.

The mean flow propagation effects of these sources were calculated using the ray tracing routine which is part of the LRT method. Approximately 655,000 rays were launched from each source to calculate the attenuation and amplification from each point source in terms of flow factors. Rays propagating towards the shallow angles to the jet are usually refracted due to the mean flow gradients, resulting in an attenuation in the far field. Most rays at these regions suffer total internal reflection (TIR) and do not propagate outside the jet as they get 'trapped'. Rays propagating from sources at shallow angles ranging from 30^o to 50^o polar angles, that are affected by the cone-of-silence, experience a Total Internal Reflection (TIR). Such rays do not propagate outside the jet but are instead 'trapped' within the jet. The output from such trapped rays are fixed at a default value of -200 dB (as ΔSPL). From the ray tracing results, sources that are attenuated (mainly due to TIR effect) in the far field are chosen for the CoS calculation, and are as shown in Figure 6.8. Sources in the current context refers to the location in the flow where the fluid shielding is dominant and inhibit the propagation of rays to the desired observer location in the far field.

6.6.3 Calculation of turning points and exponential decay factors

In the present work, shielding function defined in the MGB method, equation (6.7) is used. The derivation of the shielding function (see equation (A.2)) is given in the Appendix section (A). Equation (6.7) is generalisation of equation (6.6) to include a Doppler function.

$$g^2(r,\theta) = \frac{(1 - M_s \cos\theta)^2 (c_s/c_o)^2 - \cos^2\theta}{(1 - M_c \cos\theta)^2} \tag{6.7}$$

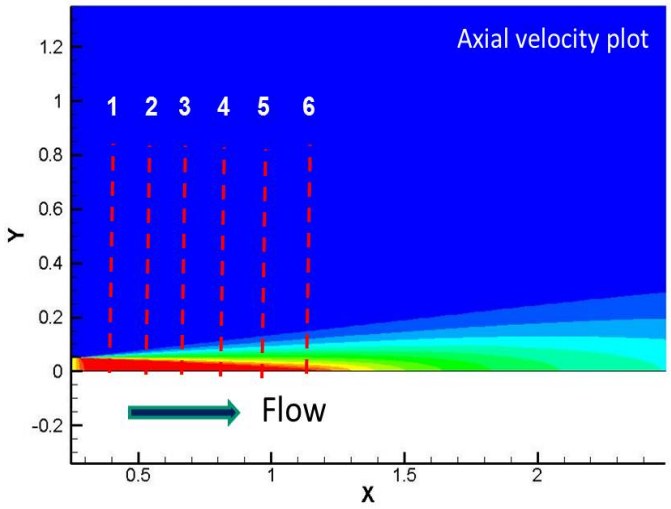

Figure 6.9 – Axial velocity contour of an isothermal single stream computed using RANS. The flow domain is split up into segments to calculate turning points for sources within each flow segment.

where, $M_s = U(r)/c_o$; $c_o = 340m/s$, $M_c = 0.25 \times M_s + 0.55 \times M_J = 0.25 \times \frac{U(r)}{c_o} + 0.55 \times U_j/c_o$.

The shielding function in equation (6.7) is defined as a g^2 to differentiate between the one defined in equation (6.6). Since we are using a 3D CFD jet, the radial coordinate is defined as r. The values of velocity $U(r)$ and speed of sound profiles c_o are obtained from the CFD data.

Apart from the parallel shear flow assumption, most of the previous work in the literature on determining turning points have used radial velocity and temperature curve fits of the jet data. For example, Tester and Morfey [125] and Suzuki & Lele [71] used a finite thickness cylindrical shear layer, Mani et al. [44] and Balsa [73] have used parallel shear flow to define turning points. In the present work, we use an axi-symmetric spreading jet flow data as a realistic approach to calculate turning points and in turn to determine the attenuation within the CoS.

The jet is divided into 6 flow segments along the axial length of the potential core (∼8 times diameter) as shown in Figure (6.9), based on the co-ordinates of the first 6 slices of sources that are generated. Out of all the source points generated, 550 source points within the potential core are distributed in the six segments with approximately 90 source points in each segment. For each flow segment, the location in the shear layer where the function $g^2(r, \theta)$ changes sign is the turning point, r_σ. In each flow segment the turning point locations were determined for observer angles 30°, 40° and 50°. The turning point for each observer angle marks the radial location in the flow where the shielding exists for sources in that particular radial location of the jet. Hence the sources will have a common turning point for a particular observer angle. The axial and azimuthal variations will remain constant as the transition of the source in x and φ direction will be too small

for compared to the entire jet in the far field. Therefore, the azimuthal coordinate of the turning point is assumed to be equal to that of the radial coordinate. Figure (6.10) shows the location of turning points for each flow segment for the 30^o polar angle.

The decay experienced by each source depends on the radial location of the source in the jet, r_s, frequency, jet velocity, jet temperature and far-field radiation angle. The deeper the source is embedded in the jet, higher is its frequency, smaller will be its pressure amplification in the far-field which is a direct consequence of the acoustic shielding. The exponential damping (or attenuation) of the propagation is proportional to $k_o L = \omega L/c_0$, where L is the effective distance between the source, r_s, and the turning point, r_σ in a given flow segment and angle θ. Therefore, for every source in each of the flow segment, the effective distance, L was calculated along with the value of the shielding function $g^2\,(r, \theta)$ at the turning point. Although the exponential decay is a strong function of frequency, at this stage the value of frequency is taken as 1.0, as the frequency parameter will be accounted in the LRT calculation when the sources are assigned with its inherent source strength and directivities. For a single turning point problem, where the radial wave number starts off being imaginary from the source location r_s and becomes real at the turning point r_σ, the exponential decay is given as,

$$A_{decay} = \exp\{-\,k_o \int_{r_s}^{r_\sigma} \sqrt{|g^2(r,\theta)|}\,\mathrm{d}r\} \tag{6.8}$$

where, r_s is the source location and r_σ is the turning point location in the radial flow coordinate.

6.6.4 Calculation of source strength

In this step, the inherent source strength and source directivities of the jet was calculated using the LRT source model (see Section 3.3). The source strength was calculated for a range of frequencies (200Hz to 10000Hz) for 30^o, 40^o and 50^o polar angles, at 0^o azimuthal angle.

6.6.5 Associating the decay factors with the flow factors

The decay factors calculated in the last section are associated with the flow factors (ΔSPL) of each source considered for the preliminary CoS calculation. The resulting term ξ_s, which represents the amount of decay the source suffers as function of frequency, is defined as:

$$\xi_s(X, Y, Z, \theta) = A_{decay} \times \Delta SPL. \tag{6.9}$$

The source strength for each source in the jet are then combined with ξ as a function of polar angle θ and frequency.

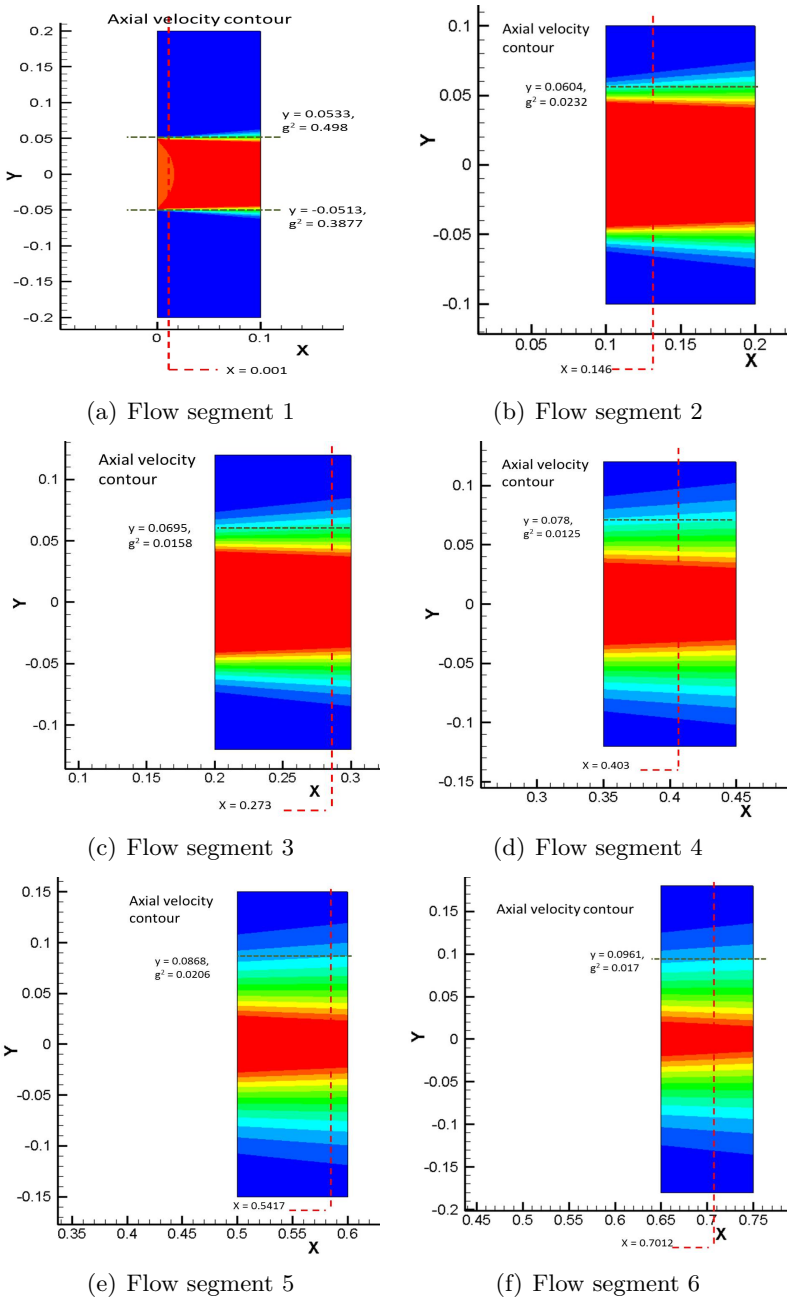

(a) Flow segment 1 (b) Flow segment 2

(c) Flow segment 3 (d) Flow segment 4

(e) Flow segment 5 (f) Flow segment 6

Figure 6.10 – Schematic representation of location of turning points Y, for each flow segment at 30° polar angle. Dashed line represents the axial location (x) of source points within each segment, g^2 is the value of $g^2(r,\theta)$ function at the turning point.

6.7 Results

The comparison of predicted spectra using the Patch method against experimental data at 30°, 40° and 50° polar angles for an isothermal single stream jet are as shown in Figure (6.11). Also included in the plots are real ray tracing results. From the plots it can be inferred that the Patch method is able to model the *lost* energy within the CoS when compared with ray theory solutions. Significant improvements throughout the spectrum at 30° and 40° polar angles are obtained. As a result, improvements in the OASPL directivities up to 18dB and 12db at the 30° and 40° polar angle, respectively are obtained using the Patch method in comparison with the ray theory solutions (see Figure (6.12)). Clearly, the agreement of predictions from the Patch method with the measured data improves with increase in frequency. This is expected as the method is based on a high-frequency approximation solution.

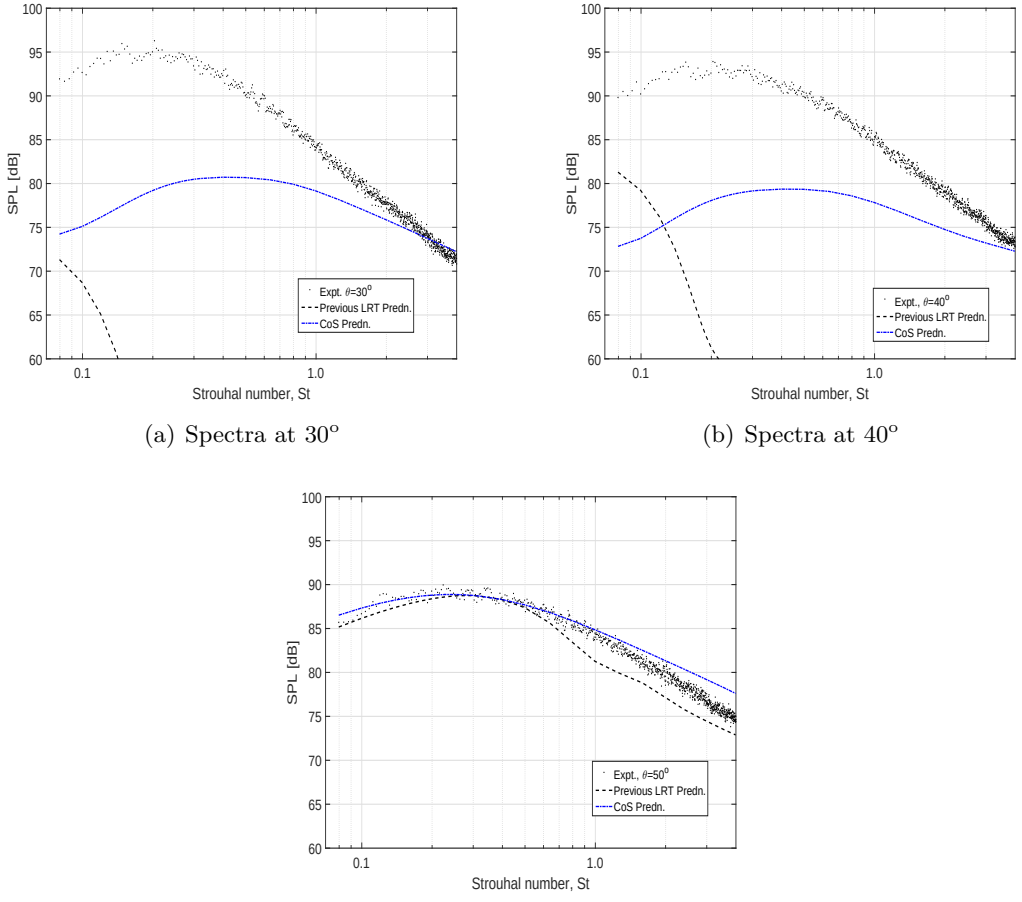

(a) Spectra at 30°

(b) Spectra at 40°

(c) Spectra at 50°

Figure 6.11 – Comparison of spectra calculated using the Patch method with previous LRT predictions (ray theory solutions) and measured data at 30°, 40° and 50° polar angles.

The 50° polar angle, can be called the critical CoS angle, θ_c. At this angular location, which is the CoS boundary, refraction effects are not as severe compared to angles much closer to the jet axis. Most of the rays manage to propagate to the far-field. This can be observed from the previous LRT calculations shown in Figure (6.11(c)). This also implies

that the exponential decay has been double accounted at this angular position by the Patch method which results in a over-prediction of up to 2.5dB at Strouhal number = 4.0, at the 50^o polar angle.

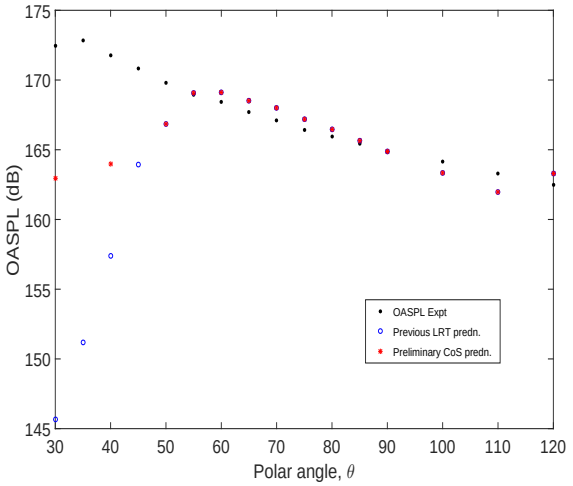

Figure 6.12 – Comparison of OASPL calculated using the Patch method with previous LRT predictions (ray theory solutions) and measured data (Mach no.=0.75, TR=1.0, D_j=0.1016m).

In comparison with the measured data, the Patch method under-predicts the SPL by up to 15dB at low frequencies (Strouhal number = 0.1) at the 30^o and 40^o polar angles. This is expected as the solution procedure employed is based on an high frequency approximation, and hence the decay from low-frequency sources were not accounted, and this can result in an under-prediction.

6.8 Limitations of the Patch method

The main limitations of the Patch method lies in the underlying assumptions. Some of the reasons for the under-predictions are listed below.

- Firstly, the method is based on the assumption of a parallel shear flow. Since the method was applied to a spreading jet, it is a deviation from the model assumption which induces errors in the predictions.
- The method is a 1D approximation and therefore does not account for the field variation in the azimuthal direction. Stone et al. [138] shows that the exponential decay varies significantly with azimuthal variation.
- It has been shown that the field within the CoS is dominated by complex rays. The Patch method does not address the problems such as multiplicity of rays and is a very simplified method to precisely calculate the contribution from complex rays.
- Accounting for the fluid shielding is another aspect which determines the accuracy of the method. Important factors which determines the amount of shielding are the

precise location of turning points, effective wave-number–frequency decomposition and turbulence scattering. The sharp jumps in the velocity and speed of sound gradients in the CFD mean-flow data can cause discrepancies in the calculation of turning points. In the calculation of decay factors, only the zeroth order azimuthal mode was considered. But inside the cone of silence, the lower order modes dominate and can influence the decay of the source [169].

- Besides the factors related to mean-flow propagation, the noise in the CoS depends on the source strength. At shallow angles to the jet axis, it has been shown that large-scale structures (LSS) are the dominant noise generating sources [41, 99, 106, 107]. Since the complex rays in the CoS are exponentially small, the calculation of noise can lead to errors when coupled with incorrect source definitions. The LRT method does not include a large-scale structure source. This is another potential reason for the under-predictions by the Patch method.

The above limitations suggests a need for another method which is capable of addressing the limitations of the Patch method. The good place to start looking for the improvements are at correcting for the ray deficiencies.

From the flow factor results presented in Section (6.3), it has been shown that the occurrence of caustics delimits the high frequency field near the CoS. Caustics are one of the deficiencies of ray theory. Recent developments by Stone et al. [138] have seen these deficiencies accounted for, creating a complex ray tracing (CRT) routine. In Section (6.10), approximations to the method proposed by Stone et al. [138] are introduced for the calculation of complex rays. This will allow the demonstration of Method 2, which focuses on the calculation of the dominant complex rays within the cone of silence (CoS) without recourse to complex ray tracing. Before getting into the details of the method, an understanding of the formation of caustics is necessary. In the next section, a brief description of caustics is presented.

6.9 Caustics

Caustics occur when a two or three or more ray paths tangent in space. The envelope of these tangencies generate a caustic surface. At caustics, the rays predict erroneously singular amplitudes. The blow-up of amplitudes due to caustics are one of the deficiencies of ray theory and these needs to be corrected.

Figure (6.13) shows the formation of caustics due to refraction by the water waves distorting the stream bed producing bright lines. Caustics also denote sharp spatial discontinuities in ray behaviour; the patterns of rays are different on each side of a caustic. Variation of the intensity, P due to such spatial discontinuities due to a field is shown in the Figure (6.14). On either of the caustic boundary, two distinct regions exist. On the illuminated region, the intensity is non-zero (oscillating) and on the other side of the caustic, intensity decreasing rapidly to zero creating a shadow region.

Figure 6.13 – Photograph showing the formation of caustics (localised bright spots) due to the refraction of light rays on the water surface and the river bed [B J Venkatesh, January 2013].

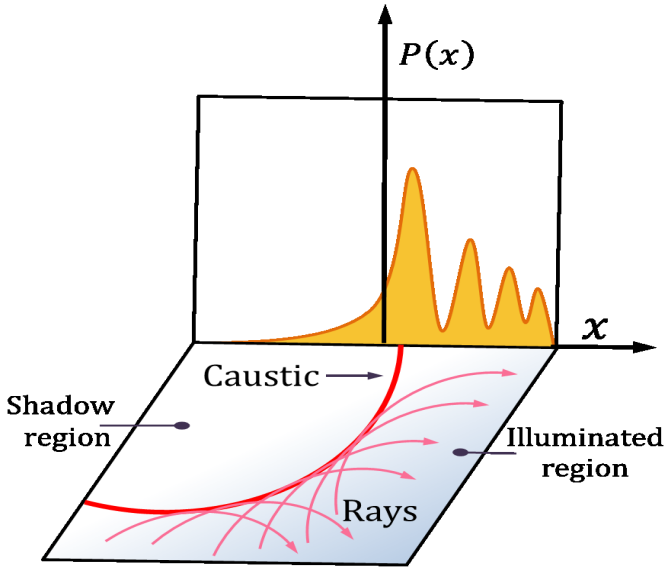

Figure 6.14 – Distribution of the field intensity, P near a caustic [170].

The caustic patterns can be simple or complicated. The classification of these different types of caustics are described by "catastrophe theory", in the terminology of René Thom [171, 172]. This term was adopted because when the locus of singularities corresponding to a given system is crossed the state of the system undergoes an abrupt and qualitative change: a "catastrophe". Catastrophe theory provides the correct uniform solution to replace the caustic rays in a generic flow.

The commonest type is a smoothly curved surface generated by two rays is called a fold catastrophe. In section (6.3), it has been shown that the fold caustic delimits the high intensity point at the CoS boundary (see Figure 6.15). Therefore, identifying the location of fold caustics in the given field is essential to be able to compute the complex field on the other side of the fold caustic. In the current thesis, we only focus on the fold caustic.

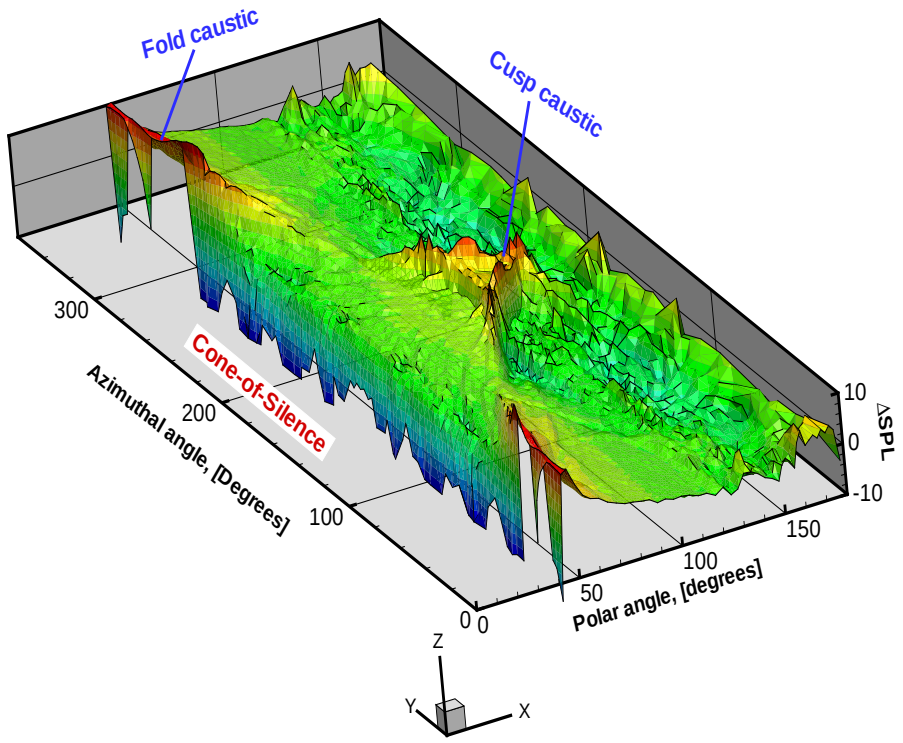

Figure 6.15 – 3D flow factor plot obtained using the LRT method for a source on the lipline (azimuthal angle, $\varphi = 90^{o}$) & X/D_j=1 for an isothermal jet with M = 0.75. The plot highlights the fold & cusp caustic and also the CoS region.

6.9.1 Fold caustics

In terms of geometrical acoustics, caustics surfaces are formed by the locus of points where the ray-tube area vanishes and where the geometrical approximation breaks down (see Figure (6.16)). This abrupt change in state at the caustic surface is seen as a change in the number of rays which arrive at a given point in space, resulting in a CoS on the other side of the caustic.

The type of caustic shown in Figure (6.16) is called a fold or smooth caustic. The fold caustic is the simplest type of structurally stable caustics described by the Catastrophe theory. A fold caustic can be generated using only 2 rays, as shown schematically in Figure (6.17). At points in space where the two rays tangent gives rise to increased ray intensities (see Figure (6.14)). Since the Jacobian (see equation (3.68)) is equal to the area of the cross-sectional surface element of the elementary ray tube, it is clear that at the caustic point the rays forming the tube cross each other so that the tube shrinks to zero. As the ray crosses a caustic, the Jacobian changes its sign and the phase suffers a negative shift of $-\pi/2$ for a fold caustic [137, 173]. This aspect of phase shift will be made use while computing the field in the vicinity of the fold caustic in Method 2.

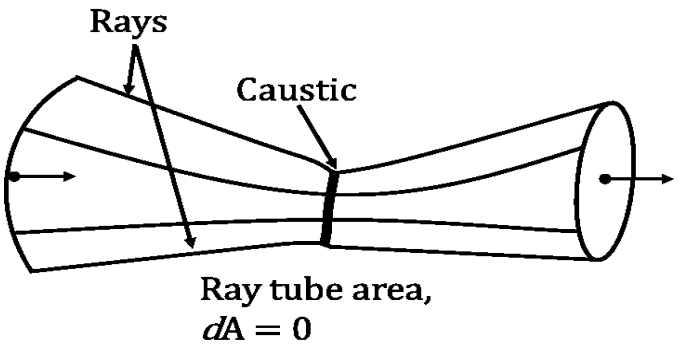

Figure 6.16 – A schematic showing the ray paths at caustic points, where the elemental area of the ray tube, $dA = 0$ [137].

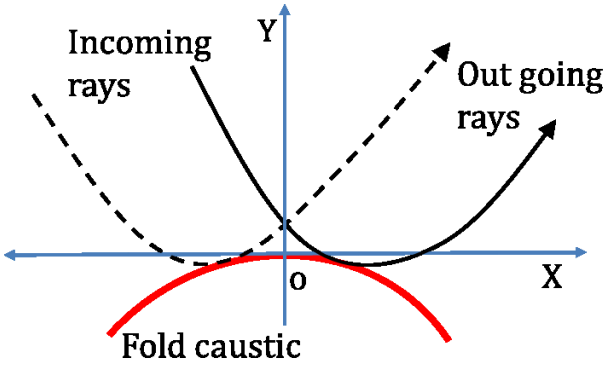

Figure 6.17 – A schematic showing the geometry of a fold (in red) caustic caused due to the tangency of two incoming rays [174].

In the simplest case of a fold caustic, the generic solution for the pressure field is represented by the linear combination of the Airy function and its derivative [172, 173]. In the Figure (6.18(a)), the flow factor plot for an isothermal jet with a source at X/D_j=1 and Y/D_j=0.5 (nozzle lipline). The field across the constant azimuthal line AA, can be described using an Airy function. The Airy function can be used to represent the ray field near and away from the fold caustic through its oscillating behaviour in the interference region in the vicinity of the caustic and the exponential decay in the CoS region (see Figure 6.18(b)). The oscillating patterns is due to the diffracted rays which are generally produced by the incident rays which hit edges, corners or vertices of boundary surfaces, or which graze such surfaces [175]. The interference pattern on either side of the fold caustic surface is highlighted in Figure (6.18(a)). This region is characterised by reducing ray intensity away from the caustic surface. The exponential decay on the other side of the caustic is due to the contribution from the complex rays. The flow factor plot shown in the Figure (6.18(a)) were computed using real rays and does not account for the contribution from the complex rays which are critical for the CoS.

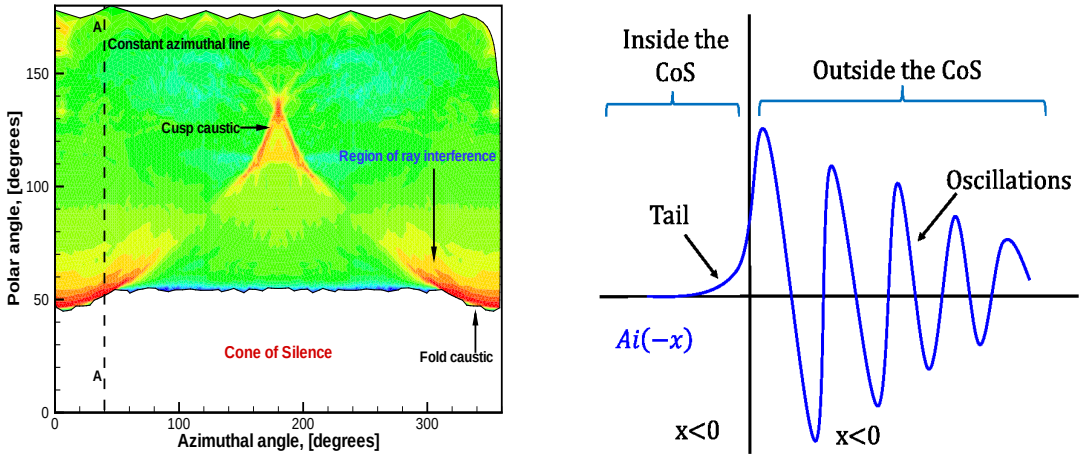

(a) ΔSPL plot for a source at the nozzle lipline of an isothermal jet

(b) The Airy function, Ai(-x)

Figure 6.18 – Realisation of the analogy between the ray solution at constant φ for a source in a jet with the Airy function solution.

Tracing rays in the complex plane is more computationally expensive than standard ray procedures (i.e. using real rays). For a given source point, the number of equations involved in complex ray tracing is 3 times more than system of equations required in real ray tracing. The system of equations that are solved for real rays are described in Section (3.5.3). As seen before, the average number of source points required to discritize a single stream jet flow to calculate flow factors is about 2000 sources (see Section (3.6.2)). The number of rays traced through the mean flow from each source is about 655,000 in 3D. Tracing real rays from such flow domain requires about 3 days to compute flow factors on a desktop computer with 12Gb RAM. To trace a couple of complex rays from a single source point in an isothermal parallel shear flow, it takes about 2 hours on a desktop computer. To trace large number of complex rays for a realistic jet flow with numerous source points will increase computational costs. Further, the complexity increases when complex rays are to be traced from a 3D grid with mean flow data associated with it. Therefore it is expedient to look for approximate methods to bypass explicit complex ray tracing computations. These are based upon two properties of the CoS, or particularly the boundary of the cone of silence as seen from the flow factor plots. Firstly, the cone of silence boundary is formed by partly a fold caustic and that this is true for a wide number of jets. Secondly, the modelling of the CoS need only to consider the field near the fold caustic as this is the dominant region, and that this can be achieved by using symmetry properties of the uniform solution at this caustic using only real ray calculations. This allows some flexibility on how the global field is then calculated as the approximate method, Method 2, can be used with other ray methods such as that in [90].

In the next section, a brief requisite theory for making computations alongside an argument for the complex ray tracing approximations is presented, followed by the out-

line of the algorithm used to carry out the computations. The proposed Method 2 is demonstrated using a parametric study of a parallel shear flow problem.

6.10 Method 2: Theory and CoS approximations

Contributions to the development and application of asymptotic methods to describe the field in the vicinity of different types of caustics can be found in the works of Ludwig [173], Berry [172], Kravtos & Orlov [133] etc. It has been indicated that the calculation of the field in the vicinity of the fold caustic is the a prerequisite to compute the field inside the CoS. It has also been discussed that the uniform Airy function and its derivatives can be used to model fold caustics. In this work, the generalised Airy function solutions proposed by Ludwig [173] is used to replace the fold caustic. To compute the field outside the caustic, the amplitude and phase information from ray tracing is provided as an input to the Airy function solution. The complex field inside the CoS is computed using the complex ray naturally embedded in the Airy function and its derivatives.

The numerical method to continue the solution from outside the caustic into the complex region has been carried out as a boundary value problem [138]. This procedure is applied to a parallel shear flow problem and a parametric study is carried out for varying flow parameters. Predictions are benchmarked against solutions to Lilley's equation.

Before looking at the uniform solutions and the application of it, some theory regarding complex ray approximations is presented in the next section.

6.10.1 Theory

In this section, the bare essentials pertaining to ray deficiencies are presented. For a given flow field rays are fired off from point sources to the far-field which is set as an initial value problem (IVP) as given by equations (3.58) and (3.59). This allows the ray position $\boldsymbol{x_p}(t)$ to propagate away from the source $\boldsymbol{x}_s$ after an integration time t given the initial ray direction of $(\boldsymbol{\mu}, \boldsymbol{\lambda})$. The ray propagates information pertaining to ray amplitude P and phase τ, so that a ray has the value $P\mathrm{e}^{\mathrm{i}k_0\tau}$, where k_0 is the characteristic wavenumber of the problem. Notably, the ray field approximation is valid in the high-frequency limit, i.e., $k_0 \to \infty$, and k_0's explicit representation in ray problems leads to ray computations being independent of k_0.

As discussed earlier, in free space jet flows there are three common ray deficiencies: multiplicity, caustics, and complex rays. These are addressed by Stone et al. [138], and the method used to tackle these aspects will be made use as the current approximation relies upon the theory governing their solution.

Multiplicity is encountered when more than one ray arrives at a given observer position. This is due to the nonlinear eikonal equation (3.48) that governs rays at leading order (Hanyga [176]). The IVP of equations (3.58) and (3.59) is not in a form convenient for determining all rays that arrive at a desired receiver point $\boldsymbol{x}_R$. The most straightforward

way of overcoming this is by posing an optimal function, $\boldsymbol{F}$, which relates the ray position parameters, $\boldsymbol{x_p}(t)$ and $\boldsymbol{\mu}, \lambda$ to the receiver point $\boldsymbol{x}_R$,

$$\boldsymbol{F} \equiv \boldsymbol{x_p}(t, (\boldsymbol{\mu}, \lambda)) - \boldsymbol{x}_R. \tag{6.10}$$

Solutions to $\boldsymbol{F} = \boldsymbol{0}$ are the required multiplicities for $\boldsymbol{x}_R$ and can be found using techniques detailed in [138, 176]. This ensures that all the rays fired from the source point $\boldsymbol{x}_s$ reaches the far-field, $\boldsymbol{x}_R$. The ray solutions can then be combined coherently in a sum for the field p, for example for two rays,

$$p \sim P^{(1)} \mathrm{e}^{\mathrm{i}k_0\tau^{(1)}} + P^{(2)} \mathrm{e}^{\mathrm{i}k_0\tau^{(2)}}. \tag{6.11}$$

The second deficiency pertains to the singular behaviour that occurs when rays encounter caustics. These singularities can be corrected using the uniform solutions proposed by Ludwig [173]. In the case of a two ray system, or fold caustic, the uniform solution is given by the Airy function and its derivative, i.e.,

$$p \sim k_0^{1/6} \left(-2\pi\mathrm{i}\right)^{1/2} \mathrm{e}^{\mathrm{i}k_0 A_{CE}} \left(c_0 - \mathrm{i}k_0^{-1/3} c_1 \frac{\partial}{\partial\tilde{\xi}}\right) \mathrm{Ai}(\tilde{\xi}). \tag{6.12}$$

In equation (6.12), the term which involves the derivative of the Airy function is relatively small near the caustic, but prominent away from the caustic. In analogy with the ray field, computation of equation (6.12) requires the amplitude coefficients c_0 and c_1, and the phase/control terms A_{CE} and $\tilde{\xi}$. The problem is now to determine $c_{0,1}$, A_{CE} and $\tilde{\xi}$. Fortunately, these variables can be determined in closed form as a function of the phases and amplitudes of the two rays that blow up at the caustic, [177] (see Figure (6.14)). First, though, we express $\tilde{\xi}$ as $\tilde{\xi} = k_0^{2/3}\xi$, so that mappings are independent of k_0. The variables are then determined to be:

$$\xi = -\Gamma_p = -\left(3(\tau^{(1)} - \tau^{(2)})/4\right)^{2/3}, \quad A_{CE} = \frac{1}{2}\left(S^{(1)} + S^{(2)}\right), \tag{6.13}$$

and,

$$c_0 = 2^{-1/2}\Gamma_p^{1/4}\left(P^{(1)} + \mathrm{i}P^{(2)}\right), \quad c_1 = 2^{-1/2}\Gamma_p^{-1/4}\left(P^{(1)} - \mathrm{i}P^{(2)}\right). \tag{6.14}$$

In the case of a fold caustic, one amplitude, $P^{(2)}$ is imaginary, so that $P^{(2)} = -\mathrm{i}|P^{(2)}|$ leads to $c_0, c_1 \in \mathbb{R}$.

The third deficiency pertains to the calculation of complex rays. In this work, the aim is to bypass the explicit calculation of complex rays in the case of two-ray or fold caustics. This is due to two reasons: firstly, complex rays are more expensive to compute than real rays; secondly, industrial jet profiles are not always amenable to being analytically continued into complex space - a procedure that is required in some form or another.

6.10.2 CoS approximations.

From the procedure described so far, the pressure field outside the caustic can be computed. Next, the aim is to calculate the field on the caustic and then continue the solution into the complex space, where the approximate solution will be used.

The way the complex ray computation is bypassed is by considering the complex ray naturally embedded in the uniform solution, or more particularly the Airy function and its derivative. It is essential to note that at a caustic, the phase parameter, $\tilde{\xi} = \Gamma_p = 0$, however, moving away from the caustic $\tilde{\xi}$ increases in size, i.e., $|\tilde{\xi}| \gg 1$. In this scenario, the asymptotic approximations of the Airy function and derivative can be used to get back to the ray field [173]. For the Airy function term in equation (6.12) this leads to,

$$p \sim \begin{cases} 2^{1/2} c_0 \Gamma_p^{-1/4} \mathrm{e}^{-\mathrm{i}\pi/4} \mathrm{e}^{\mathrm{i}k_0 A_{CE}} \cos\left(\frac{2}{3} k_0 \Gamma_p^{3/2} - \pi/4\right), & \Gamma_p > 0, \\ 2^{-1/2} c_0 (-\Gamma_p)^{-1/4} \mathrm{e}^{-\mathrm{i}\pi/4} \mathrm{e}^{\mathrm{i}k_0 A_{CE}} \mathrm{e}^{-2k_0(-\Gamma_p)^{3/2}/3}, & \Gamma_p < 0, \end{cases} \tag{6.15}$$

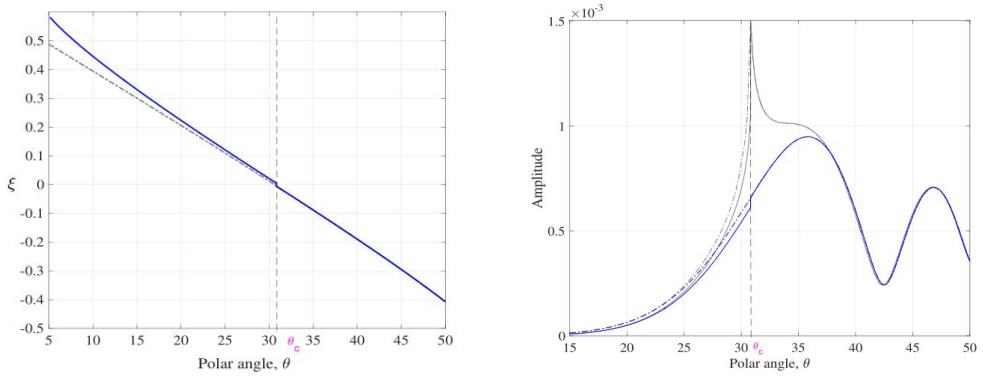

(a) ξ benchmark (b) Amplitude benchmark

Figure 6.19 – Benchmarks for symmetry method. (a) ξ benchmark: blue line, symmetry method, dashed, exact. (b) amplitude benchmark: blue line, uniform; grey line, ray; solid line, symmetry method; dot-dash line, exact. Angle in degrees.

Next, to compute the solutions for the complex ray embedded in the Airy function, the amplitude coefficients c_0 and c_1, and the phase/control terms A_{CE} and $\tilde{\xi}$ in the complex plane has to be determined. These coefficients can then be substituted in equation (6.12).

This may seem unnecessary given that the ray field was computed originally: however, there is a symmetry that can be exploited so that the exponentially small CoS rays can be determined from $\Gamma_p > 0$. This is best illustrated in Figure (6.19(a)), where the calculation of $\Gamma_p > 0$ is rotated in phase by π to approximate $\Gamma_p < 0$. In a vicinity close to the caustic Γ_p behaves linearly, however with increasing distance Γ_p deviates from this. Importantly, it is the linear behaviour near-caustic that allows for the most significant region of the CoS to be modelled most accurately. This is shown in Figure 6.19(b), where both ray and uniform symmetry approximations are in good agreement with the exact complex ray solution in the CoS, i.e., $\theta < \theta_c$. The approximation does show a slight jump as it passes through θ_c: this is to be expected as ξ also shows this jump due to the symmetry rotation

coupled with the fact that ξ may not exactly pass through zero at θ_c.

The linear behaviour that allows for this symmetry argument is derived from catastrophe theory (see for e.g., Poston & Stewart [178]). In essence, caustics are mapping to a canonical form (fold): as the caustic is approached from either side the caustic begins to mirror the symmetric canonical form more and more: linearity reflects this. The approximation of the CoS is complete by rotating the A_{CE} and c_0, c_1 values about the caustic. There is no need to change the sign/phase of these values. It can be shown that these quantities behave similarly to that of ξ in Figure (6.19(a)). This symmetry argument is a novel addition to the work presented by Stone et al. [138], to compute the solutions for the complex ray embedded in the Airy function, the amplitude coefficients c_0 and c_1, and the phase/control terms A_{CE} and $\tilde{\xi}$ in the complex plane.

6.11 Algorithm

In this section, the algorithm to numerical compute the procedure of Section (6.10) is presented. The following algorithm uses a mixture of IVP and BVP ray tracing to achieve results.

1. Ray tracing: A distribution of rays are fired off from a point source in the shear layer, $\boldsymbol{x}_s$ according to IVP with an interrupt criterion $\sqrt{\boldsymbol{x_p}(t) \cdot \boldsymbol{x_p}(t)} = R$ when sphere (far-field) (i.e., Σ_R) is intersected. Illustration shown in Figure (6.20(a)).

2. Record endpoint (EP) of ray as it hits Σ_R (see Figure (6.20(a)) & (6.20(b))) in θ, φ coordinates. Determine boundary of data to find the CoS boundary, B, as shown by the red line in Figure (6.20(b)).

3. Determine caustic rays along B (e.g., Figure (6.20(b)), p_1 and cusp caustic rays, p_3) in the forward arc (thus eliminating high angle caustic points, e.g., p_4) to get fold caustic delimiting the CoS. Use amplitude (via a tolerance, $|\text{Jacobian}| = \mathcal{O}(1/R)$) as criterion for choosing the caustic points, as shown by red EPs in Figure (6.20(b)).

4. Determine multiplicity region, delimited in θ by θ_d, using endpoints of caustic (e.g., shown by p_2 in Figure (6.20(b))). So the region between θ_d and the caustic points (e.g. points p_1 and p_2) is the multiplicity region. See also [138] for understanding of multiplicity zone.

5. Working in constant φ, apply the 2-point boundary value problem (BVP) ray tracing to the multiplicity region and continue up to B. To get both fold rays, start by locating first branch of solution with approximation $(\boldsymbol{\mu}, \boldsymbol{\lambda}) = \{\theta, \varphi\}$ iterate along this branch up to caustic.

6. Compute uniform solutions for real rays in multiplicity region.

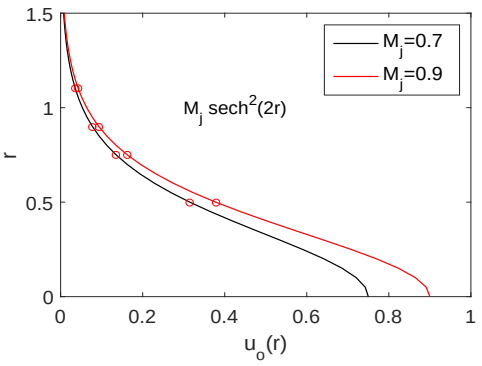

Figure 6.21 – Parallel shear flow profiles with source locations

Table 6.1 – Test matrix

Mach no	0.7		0.9	
Source Pos.	0.5	0.75	0.9	1.1

7. Continue into the CoS using symmetry methods as discussed in Section (6.10.2).

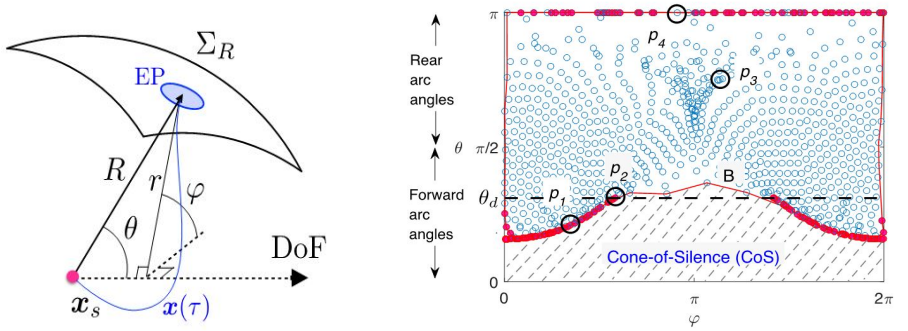

(a) IVP (blue line, ray) and spherical polar coord. system, $\{R, \theta, \varphi\}$; Direction of Flow (DoF); End-Point (EP).

(b) Collection of EPs on Σ_R. Blue EP, regular. Red EP, caustic. Red line, boundary of data. p_i's, key points. Hatched region, CoS. Forward arc $\theta = \pi/2$. Dashed line, θ_d.

Figure 6.20 – (a) Illustration of IVP realisation. (b) EP collection in θ, φ coords.

6.12 Parallel shear flow and results

In this section, the theory and algorithm of Sections (6.10) and (6.11) to provide high-frequency solutions to an isothermal parallel shear flow governed by Lilley's equation [16] are presented. The benchmark of CRT is shown in [138], which is coupled with the symmetry argument described in Section (6.10). Using this procedure, a parametric study to model the CoS for two Mach numbers and four source positions is carried out.

For this study we will use the velocity profile $M(r) = M_j \text{sech}^2(2r)$, where M_j is the Mach number. The profiles, source positions (z_s) and Mach numbers used to compute the results are shown in Figure (6.21) and Table (6.1), respectively.

In Figure (6.22), the first stages (steps 1 to 4) of the algorithm using the parameters in Table (6.1). These clearly illustrate the variability of the CoS, particularly as r_s is altered. Notably, the CoS increases in size with decreasing r_s dominating the forward arc, increasing the necessity for the computation of the complex there. The CoS also varies in φ much more with increasing source radius, r_s, as this leads to larger asymmetry in the

ray field, this also means that more rays (from the same distribution of $(\boldsymbol{\mu}, \lambda)$) end up as fold caustic rays rather than ending up in the rear arc.

Although these plots depict an intermediary step of the algorithm, they are significant themselves. It is known that caustics indicate high noise content due to the intensity increases in their vicinity. These plots also indicate noise content in point source solutions for this very reason. Not only are caustics located, but the ray numbers/densities are indicative of how the acoustic field behaves: low densities lead to low noise content; high densities the converse.

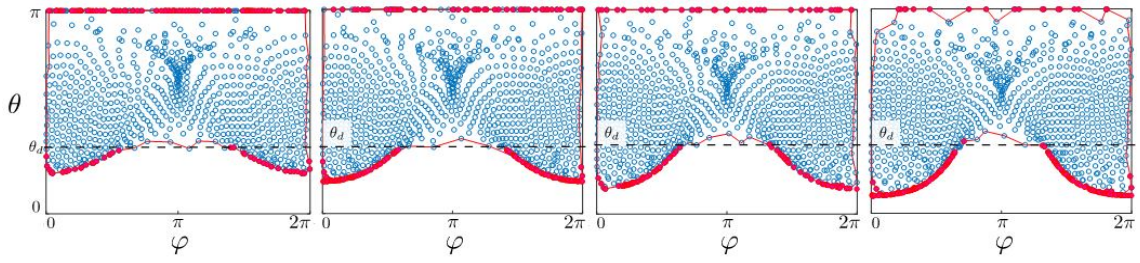

(a) $z_s = 0.5$ (b) $z_s = 0.75$ (c) $z_s = 0.9$ (d) $z_s = 1.1$

(a) $M_j = 0.7$

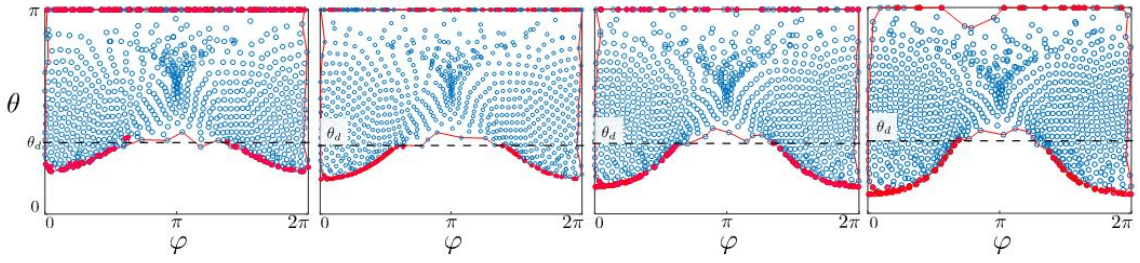

(a) $z_s = 0.5$ (b) $z_s = 0.75$ (c) $z_s = 0.9$ (d) $z_s = 1.1$

(b) $M_j = 0.9$

Figure 6.22 – Ray IVP intersection plots with caustics overlaid for the parameters in table 1.

We can now compute a constant φ cross section of the field. This is shown in figure 6.23 for various wavenumbers. The key point here is that once the essential elements of the field are calculated, e.g., phase and amplitude, the field for a particular wavenumber can be computed instantaneously using (6.11). Additionally, these solutions show how the field depends on frequency. Alongside the typical increase of oscillations accompanying an increase in wavenumber, one also sees that the shift in the CoS angle with k_0 and azimuthal angle φ.

The effect of changing φ upon the field are shown in Figure (6.24). Each of the figures here show the self similar behaviour that one would except of the fold caustic. A solution spanning a larger multiplicity zone can be mapped to one with a smaller multiplicity zone but higher wavenumber. It can also be seen that as φ increases the multiplicity zone and its subsequent oscillations also reduce. This is in-keeping with the CoS boundary being formed by both a caustic - giving intensity rises and oscillation - and a regular boundary without oscillation.

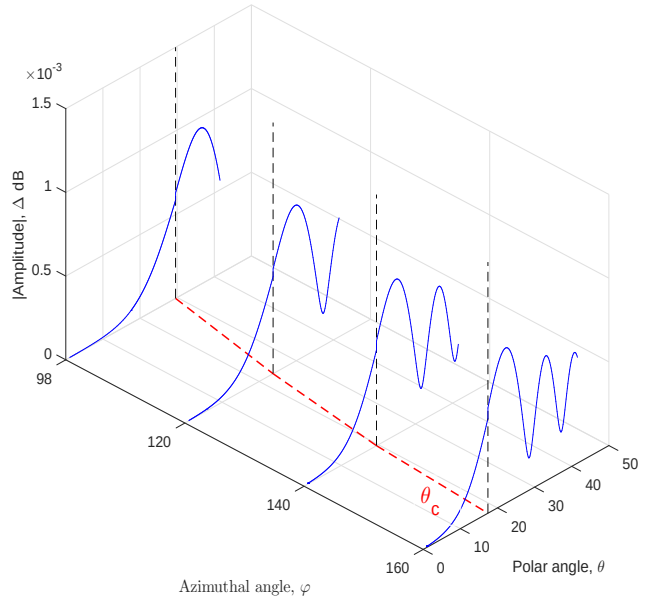

Figure 6.23 – Constant φ cross section for several wavenumbers, for a source located at $z_s = 1.1$, Mach number = 0.9. CoS angle, θ_c. Angle in degrees.

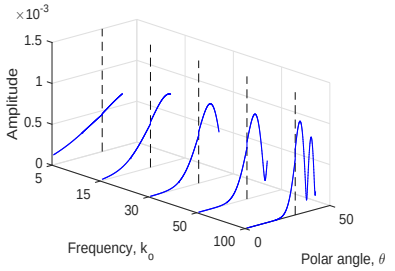

(a) $\varphi = 98°$

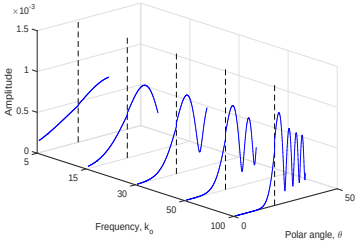

(b) $\varphi = 120°$

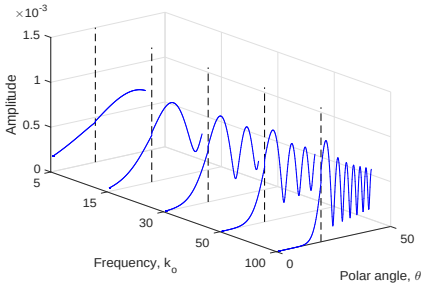

(c) $\varphi = 140°$

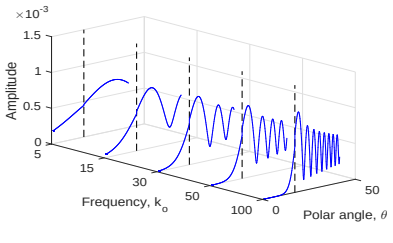

(d) $\varphi = 160$

Figure 6.24 – Uniform amplitude using symmetry method at various φ cross sections for wavenumbers $k_0 = \{5, 15, 30, 50, 100\}$, Mach number = 0.9.

6.13 Chapter summary

In this chapter, some of the deficiencies of ray theory has been addressed. The cone of silence is not a fault in the ray theory but is only a limitation. It has been highlighted that the noise from the CoS is a significant contributor towards the EPNL calculations. The acoustic field within the CoS is dominated by evanescent waves and the calculation of complex rays are typically not accounted for in generic ray programmes. Complex ray tracing methods are computationally expensive and adapting these methods to realistic jets can be computationally tedious.

In this chapter, two methods to model the exponential decay in the CoS region are proposed. The first method is called the Patch method. It uses an approximate WKB solution developed by Mani et al. [44] (MGB method) to model the attenuation in the CoS and contribution from the real rays outside the coS. The Patch method is applied to an isothermal single stream jet and the LRT predictions are validated with the experimental data. Good improvement at high frequencies at polar angles 30, 40 and 50 degrees are obtained compared to the contribution only from real rays. The patch method does not predict the low-frequency noise well as the method is based on high-frequency approximation.

In the second part, a new method of modelling the field within the CoS, without recourse to complex ray tracing is proposed. The method exploits the symmetry feature of the uniform solution given by the Airy function and its derivatives to continue the field computations into the complex space. In the current work, uniform solutions and ray solutions are calculated for an isothermal parallel shear flow governed by Lilley's equation. Good agreement in the results have been obtained when compared with exact complex ray solutions of Lilley's point source. Using this method, the CoS boundary along with the caustic locations can be determined which are indicative of the noise intensities for a given flow condition. The procedure is capable of computing both near-field and far-field solutions. From the parametric study it can be shown that the method can be applied to more generic flows.

Chapter 7

Conclusions

7.1 Research outcomes

The study presented in this thesis is an outcome of an active collaboration with the project sponsor Rolls-Royce plc. The prime aim of this thesis was to improve a computationally fast engineering jet noise prediction tool to predict jet noise with acceptable agreement compared with experimental data, from realistic nozzle geometries. Improvements to the in-house RANS-based prediction method, the LRT, have been proposed to enable the method to support the low-noise nozzle design activities for future aircraft.

7.1.1 Improvements and application of the LRT method

In this thesis, improvements in three areas have been proposed. The first research problem was to develop a method to reduce the dependency of the LRT method on experimental data to calculate the far-field noise. For that purpose, a simple procedure to determine the LRT model coefficients has been proposed. The procedure not only reduces the dependencies on experimental data but also addresses the anisotropic aspects in the flow and their effect on the far-field noise. An extensive parametric study has been performed by applying the improved procedure to coplanar nozzles with varying area ratio (AR) and velocity ratio (VR). The LRT predictions for all the nozzles conditions analysed were within ± 2 dB in comparison with the experimental data for angles outside the cone of silence. The implementation of anisotropy in the LRT method improves the prediction in the low-frequency part of the spectrum at the shallow angles to the jet axis. This is an improvement when compared with predictions which does not account for the anisotropy aspect in the jet.

For the parametric study, coplanar nozzles with three different area ratios and velocity ratios have been analysed in Chapter (4). The effect of the primary nozzle on far-field noise reduces with an increase in the area ratio. From the study, the effect of different noise producing regions in the jet and their contribution towards far-field noise has been investigated. For a given area ratio, an increase in velocity ratio increases the noise in the entire spectrum. For a velocity ratio 1.0, the amplitude of the noise produced in the three

main noise producing regions, the secondary, the effective and in the mixed jet region are the same. This suggests that the noise can be modelled using a single stream jet.

From the parametric study, it has been shown that the LRT model coefficients can be fixed while calculating noise from a family of nozzles. Therefore, as an outcome from Chapter (4), it has been shown that far-field noise predictions can be obtained using the LRT method for a family of nozzle operating conditions with reduced dependency of experimental data.

7.1.2 Characterisation of ultra high bypass ratio nozzles

A far-field noise characterisation study of UHBR nozzles for varying velocity ratio, flight velocity and bypass ratio using the LRT method and the semi-empirical ESDU method have been presented. The effect of area ratio on far-field noise has also been investigated by comparing different area ratios and flow conditions. From the results obtained from the two prediction methods, the following conclusions have been drawn.

Effect of velocity ratio

To infer the effect of velocity ratio, UHBR nozzle conditions with varying VR were created on the basis of varying thrust and constant thrust. For the varying thrust case (i.e. a fixed secondary velocity and varying primary velocity), from the ESDU predictions, a difference of up to 3 dB difference in SPL between lower VR relative to VR1.0 case was seen at low and peak frequencies at all angles except in the forward arc. In the forward arc, the ΔSPL was nearly 6dB, which is due to higher mixed velocities. The change in high frequency noise remains constant at 1dB at all angles. For varying thrust cases, the OASPL reduces with increasing VR at all observer angles. For constant thrust cases, both the primary and secondary velocities were varied. The noise thus generated was independent of VR.

Effect of area ratio

ESDU predictions were obtained for area ratios 3.5, 5.5 and 8.1 for varying velocity ratios, both for varying thrust and constant thrust. For cases with varying thrust, the overall sound pressure level (OASPL) reduces linearly with an increase in AR which is due to the global reduction in shear. With increase in area ratio (AR), the difference in noise between the highest and the lowest VR tends to zero because the nozzles are tending towards a single stream jet. The noise benefits from a UHBR nozzle were also compared for varying bypass ratios. For varying thrust cases, the OASPL reduces with increasing AR band BPR at all observer angles. For constant thrust cases, with increasing BPR and AR, the OASPL tends to become independent of VR at all observer angles. The study showed that noise from nozzles with higher area ratios can be modelled using a single equivalent jet.

Effect of flight velocity

ESDU and LRT predictions for cases with varying flight velocities ($V_f = 50$m/s and 90m/s) have been obtained. These predictions have been compared with scaled data from the SILOET database. For the UHBR nozzles, flight effect is independent of frequency (approximately $\pm$1dB) across the entire frequency range. The reduction in SPL due to flight velocity of 50m/s is about 7 dB, and it is up to 15 dB for $V_f = 90$m/s at all polar angles.

Effect of anisotropy

For single stream jets, the effect of variation of eddy aspect ratio (Δ) for varying jet velocities has been studied. For a value of β=0.5 (for axisymmetric turbulence), the parameter Δ in the secondary and effective region has been shown to be a consequence of the jet Mach number.

Another outcome of the extensive parametric study performed on varying nozzle geometry, area ratio and velocity ratio has been the assessment of the variation the eddy length-scale ratio, Δ, in the secondary and the effective jet region. Variation of Δ for area ratios 2.0, 4.0 and 8.1 and varying velocity ratios have been investigated. For the coaxial nozzles analysed, Δ in the effective jet region, tends to be independent of velocity ratio with increasing area ratio. This means that for higher area ratios, the primary nozzle has little effect on the noise generation. In both, secondary and effective regions, the length-scale ratios show an increasing trend with an increase in VR for all AR. It also suggests that range of variation of Δ for area ratios between 2.0 and 8.1 is narrow in both the secondary and effective jet region. These statistics can be used as an input for the noise prediction from nozzles with varying area ratio, both coplanar and nozzle with a centre-body bullet for varying VR.

7.1.3 Cone-of-Silence Solution

The need for jet noise predictions to predict noise in the cone of silence has been highlighted. In this regard, two set of methods to model the exponential decay in the CoS region have been proposed. The first method is called the Patch method. It uses an approximate WKB solution developed by Mani et al. (MGB method) to model the attenuation in the CoS and contribution from the real rays outside the CoS. The Patch method has been applied to an isothermal single stream jet and the LRT predictions have been validated with the experimental data. Good improvement at high frequencies at polar angles 30, 40 and 50 degrees have been obtained compared to the contribution only from real rays. However, the patch method does not predict the low-frequency noise well as the method is based on high-frequency approximation.

In the second part, a new method of modelling the field within the CoS, without recourse to complex ray tracing has been proposed. The method exploits the symmetry feature of the uniform solution given by the Airy function and its derivatives to continue

the field computations into the complex space. Uniform solutions and ray solutions have been calculated for an isothermal parallel shear flow governed by Lilley's equation. Good agreement in the results have been obtained when compared with exact complex ray solutions of Lilley's point source. Using this method, the CoS boundary along with the caustic locations can be determined, and are indicative of the noise intensities for a given flow condition. The procedure is capable of computing both near-field and far-field solutions. From the parametric study it can be shown that the method can be applied to more generic flows. The new method is computationally less expensive compared to the complex ray tracing method and could be extended to compute the field within the CoS for realistic jets (e.g., mean flows derived from CFD computations).

The improvements proposed in this thesis addresses the practical needs of an engineering jet noise prediction tool. The implementation of the methods proposed can potentially improve and assist engine manufacturers in the design of low-noise nozzles for future aircraft with reduced design lead times.

7.2 Future work

The research carried throughout this PhD is amenable to further research. Some areas for future work are suggested below.

- The LRT does not include a model to model the noise from heated jets. Addition of a hot source is essential as the flow from the engine core is hot.
- In this thesis, the procedure proposed to determine the LRT coefficients were considering axisymmetric nozzles. Future nozzles flow fields are asymmetric (e.g. chevron nozzles). Therefore, there is need for a method to relate the length-scale and time-scale coefficients with the local variation of the flow parameters in the shear layer.
- The Patch method proposed in the current work needs to be improvements at the low-frequencies at the cone of silence angles. A low frequency solution proposed by Lilley can be included to the current method to improve predictions at the low frequencies.
- The uniform asymptotic method using Airy function and its derivatives can be applied to CFD jet flows. Complex continuation methods or jump conditions proposed by Henderson and Keller [179] can be adopted when using CFD flow fields.
- The parametric study carried out in this thesis was focused on isothermal jets only. The study can be extended to investigate the effect of temperature ratio with other flow parameters on far-field noise.
- To improve the noise predictions for UHBR nozzles using the ESDU program, good quality single stream data has to be updated to include temperature effects.

Chapter A

Appendix A

A.1 Generalised high frequency shielding theory

The purpose of this section is to determine the fluid shielding integrals which could be used to locate turning points of the pressure fields of high frequency sources immersed in parallel jet-like sheared flows. Fluid shielding depends on the location of the source and the incidence angle of incident wave. Although Lighthill's classical theory of jet noise describes the prominent source of noise as the double divergence of the turbulence stress tensor, the theory fails to account for fluid shielding effect as it does not take acoustic mean flow interactions into account explicitly. Hence the starting point of the discuss is Lilley's equation for transverse sheared mean flow as shown in equation (A.1),

$$L\Pi = \frac{\mathrm{D}}{\mathrm{D}t}\left(\frac{\mathrm{D}^2}{\mathrm{D}t^2} - \nabla.c_o^2\nabla\right)\Pi + 2c_o^2\nabla.\frac{\mathrm{d}U}{\mathrm{d}r_o}\frac{\partial^2}{\partial y_1 \partial r_o} = \Gamma \tag{A.0}$$

where Π denotes the acoustic pressure fluctuation,

$$\frac{\mathrm{D}}{\mathrm{D}t} = \frac{\partial}{\partial \tau} + U\frac{\partial}{\partial y_1}$$

is the convective derivative relative to the mean flow. The term Γ represents the acoustic source distribution for a circular jet with velocity profiles approximated by an inviscid, transverse sheared flow and is given by,

$$\Gamma = \frac{\mathrm{D}}{\mathrm{D}t}\frac{\partial^2 u_i u_j}{\partial y_i \partial y_j} - 2\frac{\mathrm{d}U}{\mathrm{d}r_o}\nabla r_o.\frac{\partial^2 u_i u_j}{\partial y_1 \partial y_i} \tag{A.-1}$$

where, $r_o = \sqrt{y_2^2 + y_3^2}$ is the radial coordinate in a standard cylindrical coordinate system with polar axis in the y_1 direction for radial velocity profile.

The Green's function in the integral form and let $g_l(X,t|Y,t)$ denote an outgoing wave (in the variables X,t) solutions to the inhomogeneous equations

$$L_x g_l = C_\infty^2 \delta(X-Y)(t-\tau) \tag{A.-1}$$

where C_∞ is the ambient speed of sound, and

$$L_x = \frac{\mathrm{D}}{\mathrm{D}t}\left(\frac{\mathrm{D}^2}{\mathrm{D}t^2} - \frac{\partial}{\partial x_i}c_o^2\frac{\partial}{\partial x_i}\right) + 2c_o^2\frac{\mathrm{d}U}{\mathrm{d}r}\frac{\partial^2}{\partial x_1 \partial r}. \tag{A.-1}$$

Since the source term,$\Gamma = \frac{\mathrm{D}}{\mathrm{D}t}\Pi$, inserting the outgoing wave solutions for the propagation and source terms separately,

$$\Pi(X,t) = -\frac{2}{c_\infty^2}\int_{-T}^{T}\int g_l \frac{\partial v_j}{\partial y_i}\frac{\partial v_k}{\partial y_j}\frac{\partial v_i}{\partial y_k}\mathrm{d}Y\mathrm{d}\tau \tag{A.-1}$$

$$\Pi(X,t) = \frac{1}{c_\infty^2}\int_{-T}^{T}\int g_l\left(\frac{\mathrm{D}}{\mathrm{D}t}\frac{\partial^2 u_i u_j}{\partial y_i \partial y_j} - 2\frac{\mathrm{d}U}{\mathrm{d}r_o}\nabla r_o.\frac{\partial^2 u_i u_j}{\partial y_1 \partial y_i}\right)\mathrm{d}Y\mathrm{d}\tau \tag{A.-1}$$

When the observation point X is outside the jet the mean velocity U is zero. It is assumed that the first term on the right side of equation A.1 can provide a good approximation to the source term. Equation A.1 can then be integrated by parts to obtain

$$\Pi(X,t) = \frac{1}{c_\infty^2}\int_{-T}^{T}\int \frac{\partial^2 g_L}{\partial y_i \partial y_j}u_i u_j \mathrm{d}Y\mathrm{d}\tau \tag{A.-1}$$

where it follows from equation A.1 that

$$g_L \equiv -\frac{\mathrm{D}}{\mathrm{D}\tau}g_l$$

must satisfy the equation

$$L_x g_L = -c_\infty^2\frac{\mathrm{D}}{\mathrm{D}t}\delta(X-Y)(t-\tau) = c_\infty^2\frac{\mathrm{D}}{\mathrm{D}t}\delta(X-Y)(t-\tau). \tag{A.-2}$$

The Fourier transforms of equation A.1 are,

$$P(X) = \frac{1}{c_\infty^2}\int \frac{\partial^2 G_\omega(X\backslash Y)}{\partial y_i \partial y_j}\left(u_i u_j\right)^t \mathrm{d}Y \tag{A.-2}$$

where the superscript t is used to denote the Fourier transforms of the source terms while

$$P = \frac{1}{2\pi}\int_{-\infty}^{-\infty} e^{i\omega t}\Pi(X,t)\mathrm{d}t$$

is the Fourier transform of the pressure variable,

$$G_\omega(X\backslash Y) = \int_{-\infty}^{\infty} e^{i\omega(t-\tau)}g_L \mathrm{d}t$$

are the Fourier transforms of the Green's functions – referred to as the *reduced* Green's functions for a source located at Y.

When the mean flow depends only on the radial coordinate $r = \sqrt{(x_2^2 + x_3^2)}$, a formal solution for the sound field can be obtained by reducing equation by finding the Fourier

transform G_ω of the solutions given in equation A.1 must be of the form

$$G_\omega(X\backslash Y) = \frac{1}{(2\pi)^2}\sum_{n=-\infty}^{\infty} e^{in\Delta\varphi}\int_{-\infty}^{\infty} G_n(r\backslash r_o;\omega,k_1)e^{-ik_1(x_1-y1)}\mathrm{d}k_1 \qquad \text{(A.-4)}$$

where $\Delta\varphi \equiv \tan^{-1}(x_3/x_2) - \tan^{-1}(y_3/y_2)$ is the difference in azimuthal angles of the observation point and source point coordinates. The Fourier coefficients G_n are determined by the ordinary differential equation:

$$a^2\frac{\phi^2}{r}\left\{\frac{\mathrm{d}}{\mathrm{d}r}\left(\frac{r}{\phi^2}\frac{\mathrm{d}G_n}{\mathrm{d}r}\right) + \left[k_o^2\left(1-\frac{k^2}{\phi^2}\right)r - \frac{n^2}{r\phi^2}\right]G_n\right\} = -\frac{\delta(r-r_o)}{r} \qquad \text{(A.-4)}$$

where, $\phi = 1 + kM(r)/a(r)$, $k \equiv k_1/k_o$ is the wave number ratio, $a(r) \equiv c_o(r)/c_\infty$ is the speed of sound normalised by the ambient speed of sound c_∞, and $M(r) = U(r)/c_\infty$ is the local Mach number based on the ambient sound speed.

We are only interested in the region $r > r_J > r_o$ where the observer is outside the jet and the source point is inside. Which means equation A.1 must be solved to the conditions that G_n remains bounded at $r = 0$ and behaves like at outgoing wave at $r \to \infty$. The solutions satisfying these conditions can be expressed in terms of two linearly independent homogeneous solutions to equation A.1, say $w_1(r)$ and $w_2(r)$, by using the relation:

$$G_n(r\backslash r_o) = \frac{\mathrm{w}_1(r)\mathrm{w}_2(r_o)}{a^2(r_o)W(r_o)} \qquad \text{(A.-4)}$$

where $W(r) = \mathrm{w}_1(r)\mathrm{w}_2'(r) - \mathrm{w}_2(r) - \mathrm{w}_1'(r)$ (equation A.1) is the *Wronskain* and the prime denote differentiation with respect to r and the w_j have been chosen such that

$$\mathrm{w}_1 \to \text{constant} \times r^{-1/2}e^{ik_o}\sqrt{1-k^2r} \quad \text{as} \quad r \to \infty,$$
$$\mathrm{w}_1 \to \text{constant} \times r^n \quad \text{as} \quad r \to \infty$$

Only the $r > r_s$ form of G_n is given since primary interest is in the behaviour of the solution in the far field. Equation A.1 can be solved either numerically or by obtaining separated solutions for the interior and exterior regions of an assumed velocity and sound speed profiles and to match the results using appropriate jump conditions across the velocity discontinuity at the edge of the jet in general. However, when the limiting case of high frequency is considered, the equations become simple enough to be solved analytically.

A.2 High-frequency solution, far field approximation

The high-frequency or geometric acoustics (GA) limit describes the situation where the wavelength of the acoustic field, $1/k_o = c_\infty$, is much shorter than the characteristic length scale of the mean flow, viz. the jet radius or the width of the jet shear layer

$$r_j = \frac{1}{M_J}\int_0^\infty \frac{u(r)}{c(r)}\mathrm{d}r = \frac{1}{M_J}\int_0^\infty \frac{M(r)}{a(r)}\mathrm{d}r$$

where M_J is the jet Mach number which is considered to be the ratio of the axial velocity to the local speed of sound at the jet centre line. The stream wise wavelength $1/k_1$ scales like $1/k_o$ in the present analysis and the high-frequency limit can be expressed as

$$\frac{\omega}{c_\infty} = k_o \to \infty \quad with \quad \frac{k_1}{k_o} = k = O(1)$$

where the mean flow quantities are all assumed to be of order one.

The asymptotic approximation for G_ω is obtained by determining the high-frequency behaviour of w_1 and w_2. To facilitate this, new dependent variables ν_1 and ν_2 are introduced:

$$\mathrm{w}_r(r) = \frac{\phi(r)}{\sqrt{r}}\nu_j(r) \quad for \;\; j = 1, 2$$

where $\phi(1-Mcos\theta)/a$. Substituting into equations A.1 and A.1 shows that ν_j must satisfy,

$$\nu^{''} + [k_o^2\, q_n(r) + s(r)]\nu = 0 \tag{A.-7}$$

where,

$$q_n \equiv \phi^2 + k^2 - \left(\frac{n}{k_o r}\right)^2 \tag{A.-7}$$

and

$$s(r) \equiv \frac{\phi^{''}}{\phi} + \frac{\phi^{'}}{\phi_r} - 2\left(\frac{\phi^{'}}{\phi}\right)^2 + \left(\frac{1}{2r}\right)^2 \tag{A.-7}$$

The parameters q_n and s are arbitrary functions of r.

From equation A.2, the turning point in the flow where q_n changes its sign and is important to determine where the modes cuts-on (real and propagating) or cuts-off (imaginary and non-propagating). When the acoustic Mach number exceeds unity or when the jet velocity and temperature profiles are non-monotonic, there may be none, one or two turning points. However, for a subsonic isothermal jet profile occurrence of only one turning point are been reported [44, 169]. In this condition, the source is embedded within the shear layer where the source is acoustically shielded, i.e., negative region of shielding exhibited by the parameter q_n. In the present work, the sources are assumed to be in the region of negative shielding and the turning point where the source starts to propagate will be determined. Similar expression as in equation A.2 was obtained by Tester and Morfey, and by Mani, Gliebe and Balsa's MGB theory. Tester and Morfey defines [125] the parameter q_n as a modified radial wave number q, given by the expression A.2 for a parallel shear flow as radiation into the cone of silence at high frequencies, for a source located in a region where q is imaginary

$$q^2 = k^2 - k_\varphi^2 \tag{A.-7}$$

where,

$$q^2 = k^2 - (n^2 - 0.25)/R^2; \tag{A.-7}$$

and,

$$k^2 = (c_o/c)^2\{1 - (U/c_o)\}^2 - cos^2\theta_o, \quad U = U(R), \; c = c(R). \tag{A.-7}$$

$R = k_o r$ are normalised radial coordinates, $k_o = \omega/c_o$ the acoustic wave number and r the radial co-ordinate. The MGB method defines the shielding function, equation A.2, which can be obtained by simplifying equation A.1.

$$g^2(r) = \frac{(1 - M_s \cos\theta)^2 (c_s/c_o)^2 - \cos^2\theta}{(1 - M_c \cos\theta)^2} \tag{A.-7}$$

The behaviour of the acoustic pressure P depends on the algebraic sign of g^2. P is oscillatory for $g^2 > 0$, and exponential for $g^2 < 0$. The location in the shear layer where g^2 changes sign is known as the 'turning point', r_σ. According to these shielding functions, the locations of the sources are arbitrary. For a given observer angle and flow profile, the profile $g^2(r)$ indicates the positive and negative zones. But in the current work, the turning points for fixed source location in a given flow profile has been determined. Hence the position of the source r_s from the turning point can be accounted by calculating the exponential decay when $r < r_\sigma$ due to the factor defined by Goldstein and in the MGB method,

$$A_{decay} = exp\{-k_o(L)\}$$

The geometric interpretation of the argument of the above exponential is given by,

$$A_{decay} = exp(-2k_o \int_{r_s}^{r_\sigma} |g^2| \mathrm{d}r) \tag{A.-8}$$

The exponential damping (or attenuation) of the propagation is proportional to $k_o L = \omega L/c_\infty$, where L is the effective distance of the fluid surrounding the source. Thus, deeper the source is embedded in the jet, higher is its frequency, smaller will be its pressure amplification in the far-field which is a direct consequence of the acoustic shielding.

A.3 The four-source method and the ESDU program

The four-source prediction method [180] was initiated by DERA Pyestock and developed by the Institute of Sound and Vibration Research (ISVR), at the University of Southampton. The prediction model is based on the concept of the 4-source method proposed by Fisher et al. [57, 58].

The four-source method assumes that coaxial jet noise can be defined by the sum of three single stream jets - the secondary jet, the mixed jet and the effective jet. The prediction derives the velocity, temperature, diameter, area and the cut-off frequency for each jet based on the co-axial jet parameters. The noise spectrum for each jet is predicted using a single stream prediction procedure. In this case, the Engineering Science Data Unit (ESDU) single-stream prediction program, A9819V10 [181], is used to obtain the contribution of the equivalent single-stream jets. The three spectra are then summed to produce

the spectrum for the complete coaxial jet. The flow conditions and geometric dimensions of the coaxial configuration are required to enable the conditions and dimensions of the three single stream jets to be calculated. A fourth stream for the primary-secondary jet interaction layer has also been added to the program. This is not part of the original method, but has been included because this source can become significant when using low area ratio engines or high velocity ratios. The schematic of the concept is shown in Figure (A.1).

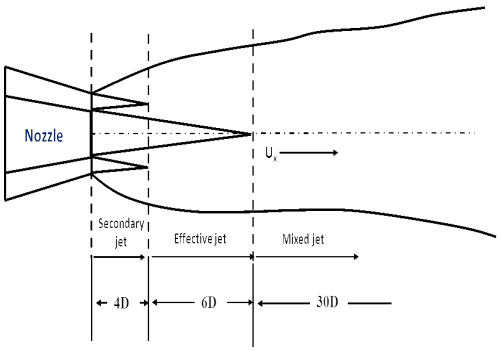

Figure A.1 – Main noise producing regions for a coaxial jet

Each of the 3 main noise producing regions are described as follows:

Secondary region:
This region comprises of potential cores of both primary and secondary jets and axially extends up to the end of the potential core of the secondary jet, i.e., equivalent of a single stream jet. This region is characterised by the secondary jet velocity, temperature and nozzle diameter. This region mainly comprises of small-scale turbulence and contributes towards the high frequency part of the spectrum.

Effective region:
In this region the shear layers of both the primary and secondary merge giving rise to peak turbulence levels up to 10% of the primary velocity for a coaxial jet (up to 15% for a single stream isolated, isothermal jet). The velocity in this region is characterised by primary velocity and by effective diameter, D_e defined as,

$$D_e = D_p \sqrt{(1 + AR \times VR^2)}, \tag{A.-8}$$

where, area ratio, AR is the ratio of area of secondary diameter to primary/core diameter ($\mathrm{AR} = \mathrm{A_s}/\mathrm{A_p}$), and velocity ratio, VR is the ratio of secondary/bypass velocity to primary/core velocity, ($\mathrm{VR} = \mathrm{V_s}/\mathrm{V_p}$).

Mixed region:
Far downstream of the jet, noise is characterised by mixed-flow jet velocity (primary, secondary and ambient flow), mixed diameter, and temperature. This region mainly comprises of large-scale turbulence and contributes towards the low frequency part of the

spectrum. Expressions for mixed velocity V_m, and mixed diameter, D_m is defined as,

$$V_m = V_p \frac{(1 + AR \times VR^2)}{(1 + AR \times VR)}, \qquad \text{and} \qquad D_m = D_p \frac{(1 + AR \times VR)^2}{\sqrt{(1 + AR \times VR^2)}} \tag{A.-8}$$

A.3.1 Description of ESDU A98019V10

The ESDU single-stream prediction program predicts noise levels by using a series of interpolations/extrapolations on a jet noise database using normalised jet velocity and temperature ratio as the independent variables. The process is performed through the normalised frequency (Strouhal) range of interest at chosen radiation angles to the jet axis. The ESDU database is valid for radiation angles in the range 30^o to 120^o polar angle to the jet axis, θ.

A.3.2 ESDU Program architecture

The ESDU program has been coded using Fortran. The program is structured in three main parts: the input program, the ESDU A9819v10 Single-Stream Prediction Program, and the output program.

1. The input program reads the individual jet parameters and performs the calculations required for input into ESDU A9819V10. It also performs general calculations to split the coaxial jet into three/four separate single-stream jets. Data files are written in ESDU input format ready to be run in the single-stream program.

2. The ESDU A9819v10 Single-Stream Prediction Program performs the predictions for the three or four separate single-stream jets, using the jet parameters calculated by the input program.

3. The output program performs calculations on the predicted single-stream data and writes the output files. The SPLs for the individual jet predictions are combined to give the 'Total' spectrum.

The ESDU code has been validated against various experimental databases available at the QinetiQ test facility [180].

Chapter B

Appendix B

B.1 RANS CFD procedure

In the current Appendix, various steps involved in computing RANS flow field from jet nozzles are presented. This includes the preprocessing stage, construction of the CFD domain around the nozzle and methods to generate good quality grids. The boundary conditions and solver settings described in this Appendix are mainly focussed on k-ϵ models with a FLUENT solver. At end of the chapter, validation of the CFD procedure using predictions from a 3D centre-body nozzle with PIV data has been presented.

B.1.1 CFD domain

The grid generation process is the most important step in any type of CFD simulation. The grid depends on the type of analysis, complexity of the geometry, availability of computational resource and accuracy. Grid generation begins with the right kind of domain around the nozzle geometry. Following are the steps used for building the CFD domain around the nozzle.

- For axisymmetric nozzle geometries, both single stream and coplanar, the problem can be considered as 2D-axisymmetric.
- Figure (B.1) shows the extent of a 2D-axisymmetric CFD domain to capture the flow from a single stream nozzle. The domain size is generally kept sufficiently large to let the mean flow variables settle to freestream conditions. Figure (B.2) shows a structured quadrilateral mesh of a 2D-axisymmetric CFD domain.
- For nozzle geometries with 3D features such as the centre-body bullet, pylon and struts (supporting structure to hold the bullet upright), a 180^o sector model is recommended (see Figure (B.3)). Such an approach is capable of accounting the effect of slid structures on the flow and in turn noise and can significantly reduce the grid size when compared to a full 360^o model.
- For 180^o sector models, the symmetry plane can be modelled with a symmetry boundary condition which indirectly accounts for the other half of the model.

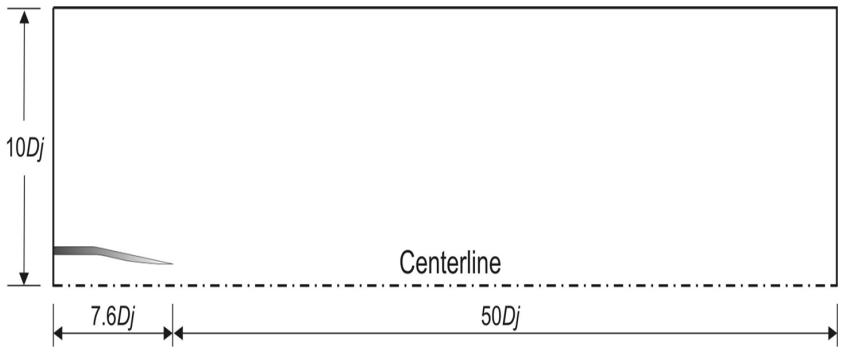

Figure B.1 – Schematic of a 2D CFD flow domain for a single stream nozzle [139].

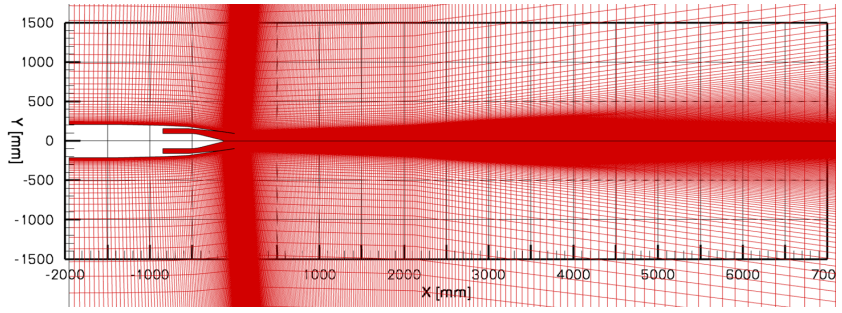

Figure B.2 – Schematic of a 2D RANS CFD mesh with approximately 60,000 cells for a single stream nozzle. Mesh generated at the Institute of Acoustics (IoA), Warsaw, contracted through Rolls-Royce plc.

B.1.2 Grid generation

Good quality mesh is critical to the quality and convergence of the flow simulations. For jet noise applications structured multi-block hexahedral meshes are preferable. Structured meshes offer higher numerical accuracy, less cell count than the unstructured meshes and also present relatively easier implementation of higher order numerical schemes. In most solvers a structured grid requires less memory, provides good accuracy and allows a better boundary-layer resolution than an unstructured grid. The mesh size and the resolution depends on the type of turbulence model that will be used.

For jet noise applications the k-ϵ turbulence model is the most widely used. In the literature for jet noise simulation, the k-ω Menter SST has also been used. However in this report, most of the procedures discussed are for a standard k-ϵ simulation. The k-ϵ turbulence model is a high Reynolds number model and relies on wall models to predict the production and dissipation of turbulence at the boundary. Given below are some guidelines for generating a mesh which is suitable for a RANS simulation using a standard k-ϵ turbulence model.

- Having a well resolved grid in the jet shear layers is of utmost importance. The mesh points are to be concentrated in the shear layers clustered in the nozzle wall.

- Near the nozzle walls the grid refinement is determined by the 'y$^+$' value. y$^+$ is the height of the CFD cell adjacent to the boundary non-dimensionalised by the friction velocity and kinematic viscosity of the fluid. A wall-function simulation normally requires that y$^+$ of the first cell outside the walls is in the log-layer, which starts at about y$^+$ 30 and, depending on the Reynolds number, extends up to y$^+$ 150. In the log layer, there is equilibrium between production and dissipation of the turbulent kinetic energy, therefore it decreases the turbulent instability in near-wall simulations. High Reynolds number turbulence models such as the k-ϵ require $30 <$ y$^+$ < 150. It is recommended to have at least 40 to 50 points in attached boundary layers, with y$^+$ $= 1$ at the walls.

- Figure B.2 shows refined shear layer mesh points for a single stream nozzle. Similarly, figures (B.3) and (B.4) shows the girds for a coaxial stream nozzle with a pylon.

- Typically the cell size should not change with more than a factor of 1.25 between neighbouring cells. For a well resolved boundary layer mesh, the radial stretch factor is best kept at less than 2% between jet and exchange surfaces for acoustic simulation.

- In order to ensure that the generated grid has the optimum number of grid points to provide desired solution accuracy, a grid independence study is recommended. For this study, at least 3 grids are required: a coarse grid, fine grid and a medium sized grid. Flow parameters such are turbulent kinetic energy and velocity from the coarse grid and fine grid are to be compared with measured data, if available. If measured data is not available, coarse gird solutions can be compared with fine grid solutions. Based on the percentage error between measured (or fine grid solution if measured data is not available), the size of the medium grid can be determined. The size of the medium grid can be obtained by either refining or coarsening the grid outside the jet region.

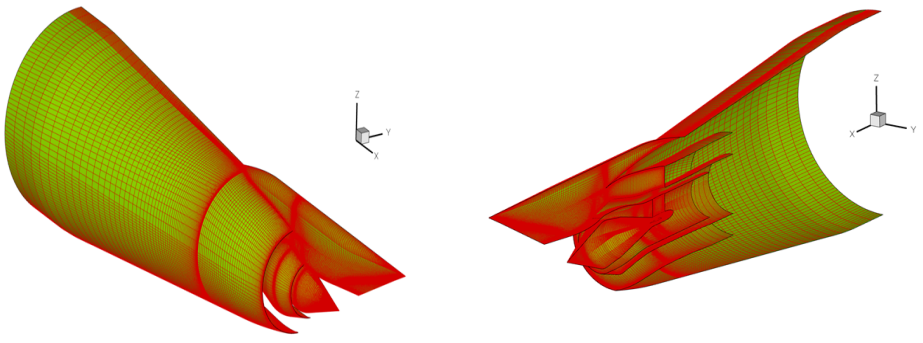

(a) (b)

Figure B.3 – RANS mesh for a coaxial nozzle with a pylon Mesh generated at the Institute of Acoustics (IoA), Warsaw, contracted through Rolls-Royce plc.

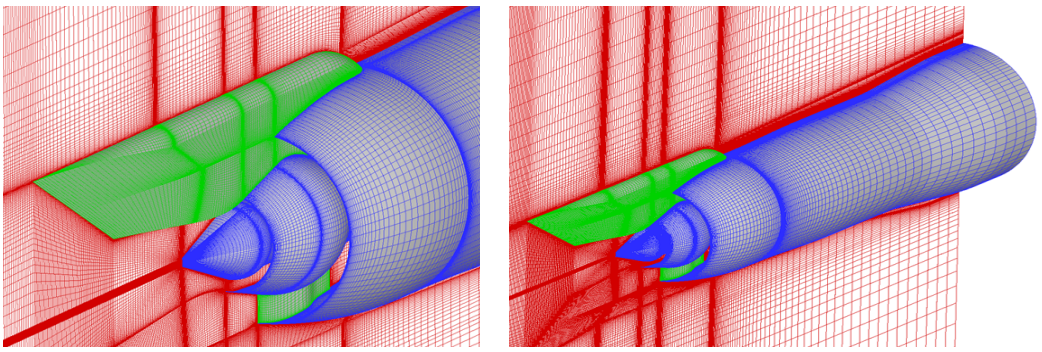

(a) (b)

Figure B.4 – Surface and symmetry plane grid lines for a coaxial nozzle showing the grid density in the shear layers; fully hexahedral grid with approximately 8 million elements.

B.2 RANS Solver Settings

B.2.1 Turbulence model

Within the class of RANS methods, there are two-equation turbulence models and the one equation model. The one equation model is the Spalart-Allmaras model which solves a transport equation to output only the turbulent kinetic energy. The two-equation turbulence models have been used most frequently for jet aeroacoustics analyses because of their capability to provide mean flow and turbulent kinetic energy fields necessary for subsequent acoustic analysis. The standard k-ϵ and the SST (Shear Stress Transport) k-ω model are the most popularly used turbulence model for jet flow calculations. The SST k-ω model is a union of the two models, k-ϵ away from the walls and the k-ω in the wall region.

B.3 Boundary conditions

Typical boundary conditions for 2D and 3D are schematically shown in the Figure (B.5). The boundary conditions vary for k-ϵ and k-ω turbulence model. Tables (B.1) and (B.2) describes the boundary conditions for k-ϵ and k-ω turbulence model using the FLUENT solver. These boundary conditions are pertaining to a 180^o sector model of a coaxial nozzle with a centre-body bullet as shown in Figure (B.3(a)).

While using these turbulence models, a good practice would be to use the computed flow at the nozzle exit plane as the inflow conditions for the computation of the exhaust planes.

Note:

- For nozzles with semi-installed features such as the pylon, should be modelled as a ‘no slip’, stationary wall.

- While simulating cases with zero flight velocity (static condition), a non-zero value of velocity (approx. Mach number = 0.05) has to be inputted.

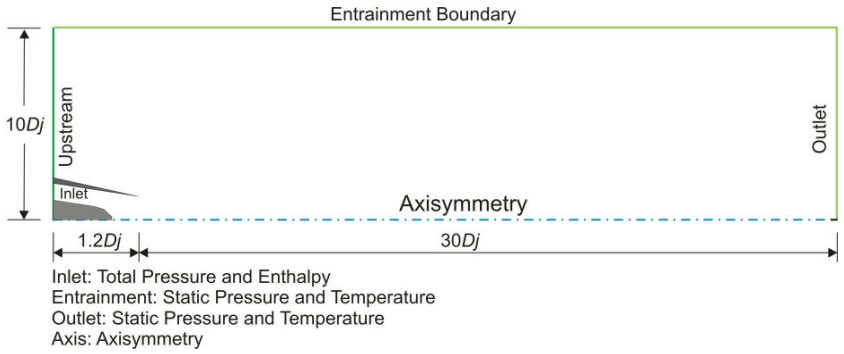

(a) 2D domain - single stream jet

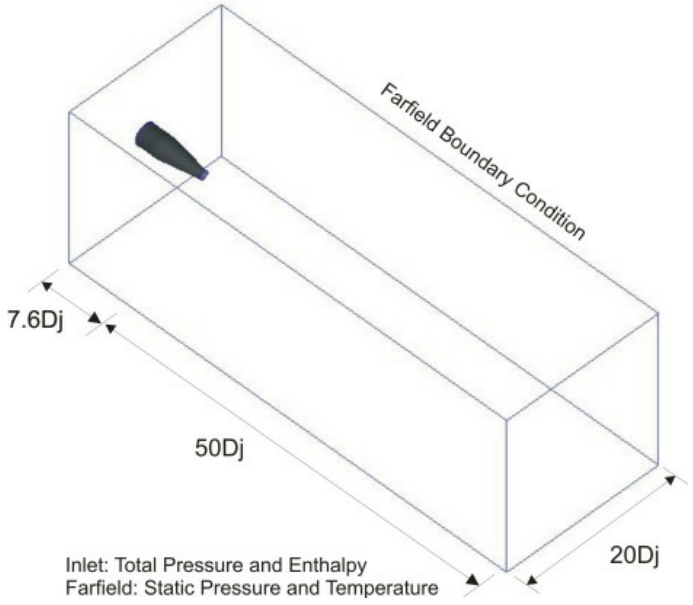

(b) 3D domain - coaxial stream nozzle

Figure B.5 – Computational domain and boundary conditions for a coplanar nozzle [139]

Boundary Conditions	k-ϵ model	Input Data
Inlet free-field	Pressure inlet	Pressure and temperature
Inlet Core	Pressure inlet	Total pressure and temperature
Inlet bypass	Pressure inlet	Total pressure and temperature
Far-field	Pressure far-field	Pressure and temperature
Exit	Pressure outlet	Pressure and temperature
Symmetry	Symmetry	NA
Nozzle/plug/struts	Wall	No slip, Stationary wall

Table B.1 – Boundary conditions using k-ϵ turbulence model in FLUENT solver

Boundary Conditions	k-ω model	Input Data
Inlet free-field	Mass flow	Mass flow rate and temperature
Inlet Core	Mass flow	Mass flow rate and temperature
Inlet bypass	Mass flow	Mass flow rate and temperature
Far-field	Pressure far-field	Pressure and temperature
Exit	Pressure outlet	Pressure and temperature
Symmetry	Symmetry	NA
Nozzle/plug/struts	Wall	No slip, Stationary wall

Table B.2 – Boundary conditions using k-ω turbulence model in FLUENT solver

B.3.1 Solver settings

There are two kinds of solvers available in FLUENT, Pressure-based solver and Density-based coupled solver. The pressure-based solvers take momentum and pressure (or pressure correction) as the primary variables. Pressure-velocity coupling algorithms are derived by reformatting the continuity equation. Density-Based Coupled Solver solves equations for continuity, momentum, energy, and turbulence equations. Pressure is obtained through the equation of state. Additional scalar equations are solved in a segregated fashion. The density-based solver can use either an implicit or explicit solution approach. The implicit solution uses a point-implicit Gauss Seidel / symmetric block Gauss-Seidel method to solve for variables. This method was originally designed for solving compressible flow problems. It solves the equations in a fully coupled manner, which requires significantly greater computer memory and usually more computation (CPU) time if implicit discretisation is used. The Implicit solution approach is generally preferred to the explicit approach, which has a very strict limit on time step size. For jet flow simulation density-based solver is recommended over pressure-based solver because the pressure-based algorithm gives higher dispersion and dissipation error in comparison with density-based solution method. Therefore a steady-state density-based coupled solver is recommended. Guidelines for further model settings are listed below:

- Switch on the calculation of the energy equation
- Viscous model: Standard k-ϵ, with Standard Wall function,
- Formulation: Implicit,
- Flux Type: Roe-FDS,

Following are the guidelines for setting the gradients of solution variables:

- Gradient: Green-Gauss Cell method,
- Flow: Second-Order Upwind scheme,
- Turbulent Kinetic Energy: Second-Order Upwind scheme,
- Turbulent Dissipation Rate: Power Law

B.3.2 Initialisation and Convergence

Iterative procedure requires that all solution variables be initialised before calculating a solution. The type of solution initialisation can influence the solution convergence and the final result. A realistic initial guess improves solution stability and accelerates convergence. As discussed in Section (5.4.2), solution can be initialised at the Inlet free-field boundary or at the core or bypass nozzle boundary.

Flows modelled using k-ϵ option can be initialised at the inlet of the core and bypass nozzle using a pressure inlet boundary conditions. The solution has to be initialised in the entire flow field (in all cells). Given below are the initialisation settings:

- Momentum settings
  - Reference frame: Absolute ,
  - Gauge Total pressure (Pascal): Ratio of Total pressure to static pressure at the core and bypass nozzle,
  - Initial Gauge pressure (Pascal): Chamber pressure.
- Turbulence
  - Specification Method: Intensity and Viscosity ratio,
  - Turbulent Intensity (%): 1,
  - Turbulent Viscosity Ratio: 10.
- Thermal: Chamber temperature (K)

B.3.3 Convergence criteria

For most jet flow calculations, convergence of the solution can be estimated by looking at the residual plot. Residual plots show the residual values of continuity, momentum, energy and turbulent equations against the specified tolerance. Residual tolerance of at least 10^{-4} for all equations is recommended.

At times, due to various reasons achieving the required convergence can be difficult. It could be due to numerical instabilities arising with an incorrect boundary conditions, poor quality mesh, and/or inappropriate solver settings. Such cases result in non-converging or diverging residual plot. In such circumstances, the following troubleshooting steps can be employed:

- Ensure that the problem is well-posed,
- Compute an initial solution using a first-order discretisation scheme,
- Decrease the Courant number (for density-based solver)

The Courant number is a transient term included in the density-based solver even for steady state problems. The Courant number defines the time step size. It is given as,

$$\Delta t = \frac{(CFL)\,\Delta x}{U} \tag{B.0}$$

where CFL stands for Courant-Friedrichs-Lewy-number, U is the appropriate velocity scale, and Δx is grid spacing.

The default value of Courant number for density-based solver is 5. For density-based implicit solver, the Courant number is not limited by stability constraints unlike explicity solver. The Courant number can be reduced when having difficulty with convergence.

B.4 Benchmarking the CFD results

Using the CFD procedures described above, benchmarking of flow calculations from a coaxial stream nozzle with PIV data (Particle Image Velocimetry) has been described. The RANS and PIV tests were conducted as part of the VITAL (EnVIronmenTALly Friendly Aero Engine) test campaign which was a European research project (under FP6). Extensive aeroacoustic wind tunnel tests were conducted in the ONERA CEPRA19 facility, with the aim of characterising installation effects of typical very high bypass ratio engines. The RANS grid and flow computations using the FLUENT solver were run at the Institute of Aviation (IoA), Warsaw on behalf of the project partner, Rolls-Royce plc. The RANS data from this project are presented in this section are stored in the ISVR database.

B.4.1 Comparison of PIV data with RANS predictions

The configuration described here is a coaxial stream nozzle, with a pylon and the lower bifurcation. The mesh used is a three dimensional multi-block structured mesh, which has about 8 million nodes. The CFD mesh of the nozzle is as shown in Figure (B.3) and (B.4). Computations were carried out by IoA, contracted by Rolls-Royce plc, using the FLUENT multi-block structured solver and using the Standard k-ϵ turbulence model.

The simulation was run for nozzle operating condition of velocity ratio 0.83, temperature ratio 2.4 and flight velocity of 30m/s. A 3D, steady-state, density-based coupled solver was employed. The governing equations were solved with a second order accuracy and the Standard k-ϵ turbulence model was used. The boundary conditions imposed on the model were similar to the ones tabulated in Table (B.1). The solver settings were as listed in Section (B.3.1). The problem was initialised with a Pressure Inlet boundary condition with inlet pressure values at the core nozzle, bypass nozzle and at the inlet free-field. To improve the convergence a CFL value of 3 was used.

Figure (B.6) and Figure (B.7) present the mean velocity and TKE fields and profiles in the symmetry plane for both the experimental and CFD results. Figures (B.8) and (B.10(c)) show the comparison of PIV data and CFD predictions of TKE and axial velocity at planes close to the nozzle (X=2.4D). From Figure B.10(b) it can be seen that the

experimental jet is not fully aligned with the symmetric plane y=0, but the CFD simulation predicts the symmetry behaviour as expected. Figure (B.9) shows the comparison of the TKE field in the mixing region (X=7.2D). Despite a general underestimation of the TKE level in the mixing region, the comparison shows a good prediction by CFD of the free-stream velocity effect. Part of the discrepancy in the central part of the jet were reported due to the setting of the turbulent variables at the bypass and core in-flow boundaries [149].

CFD analyses were also performed with corrections for compressibility and density gradients within the elsA multi-block structured solver for the SST k-ω turbulence model. In addition, a higher order discretisation scheme was evaluated and Richardson and Hessian error estimation techniques were applied. Further, these CFD computations were successfully used as an input for noise sources generation and propagation using numerical acoustic tools. These numerical analyses are reported to have showed good agreement with experimental acoustic measurements as well [149].

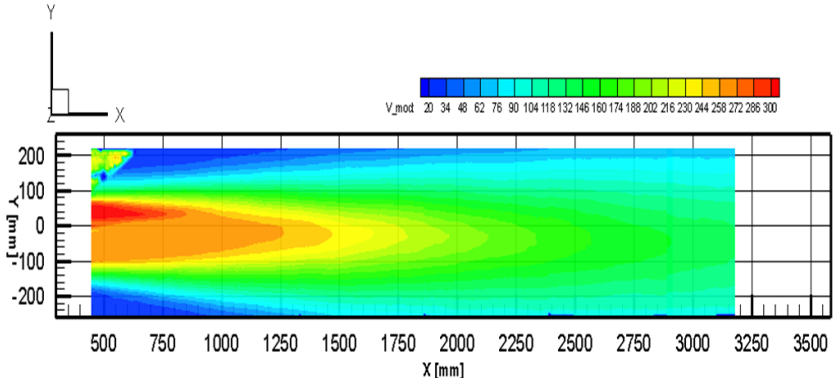

(a) PIV data of axial velocity

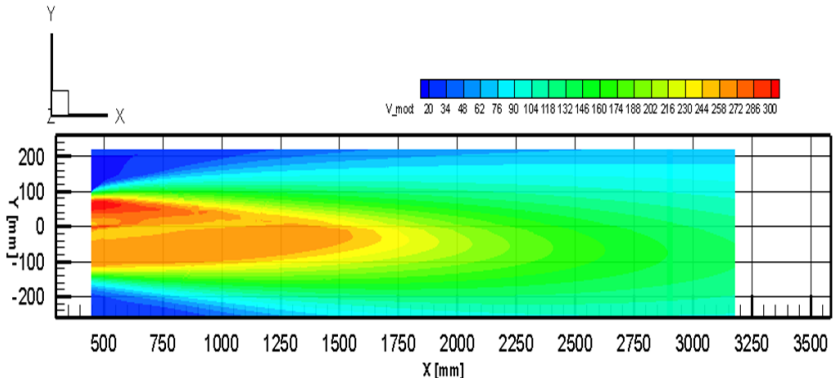

(b) CFD prediction of axial velocity

Figure B.6 – Axial velocity Fields in the symmetric plane

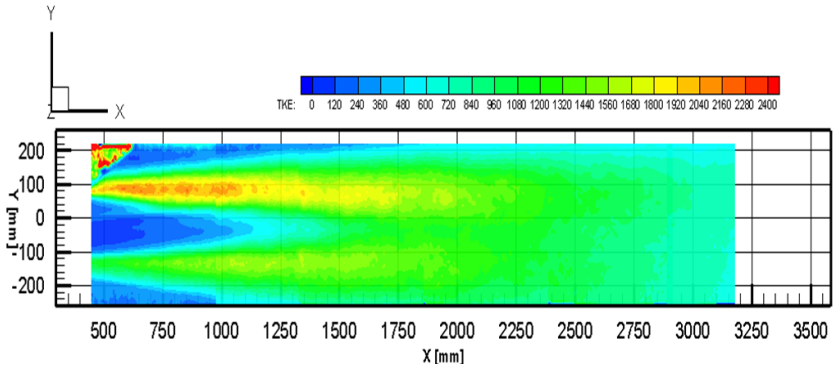

(a) PIV data of TKE

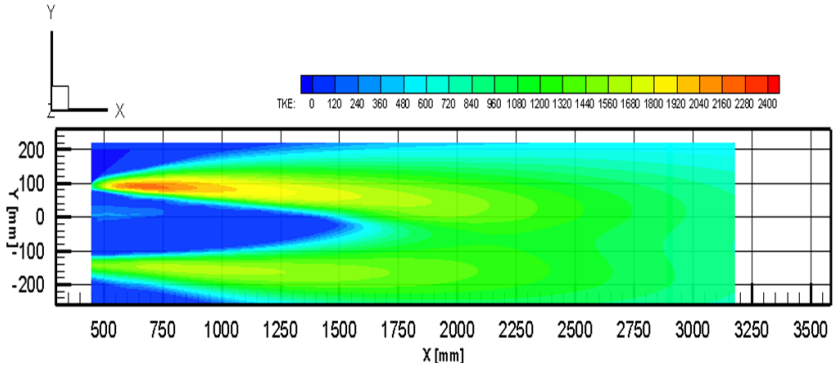

(b) CFD prediction of TKE

Figure B.7 – TKE field in the symmetry plane

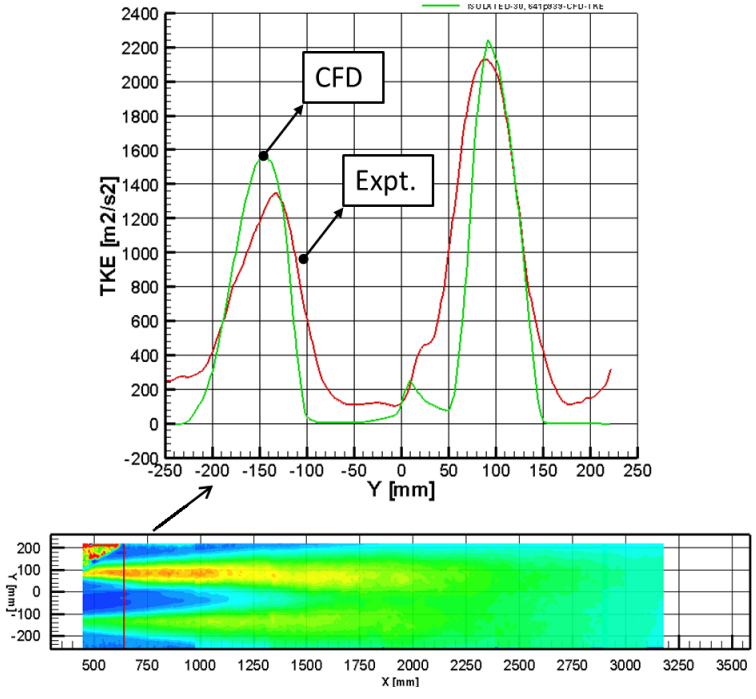

Figure B.8 – Comparison of TKE between PIV data and CFD predictions at X=2.4D

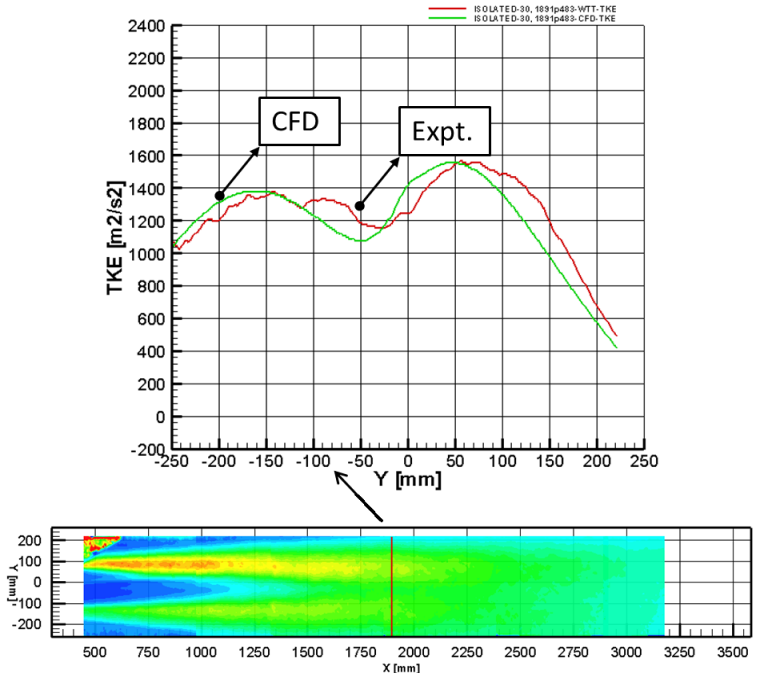

Figure B.9 – Comparison of TKE between PIV and CFD predictions at X=7.2D

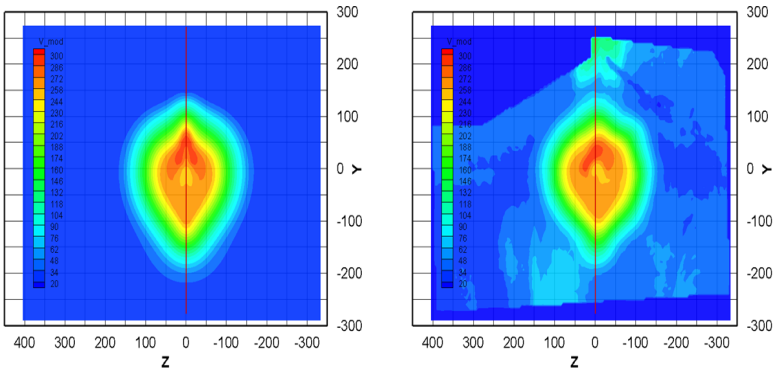

(a) PIV data (b) CFD prediction

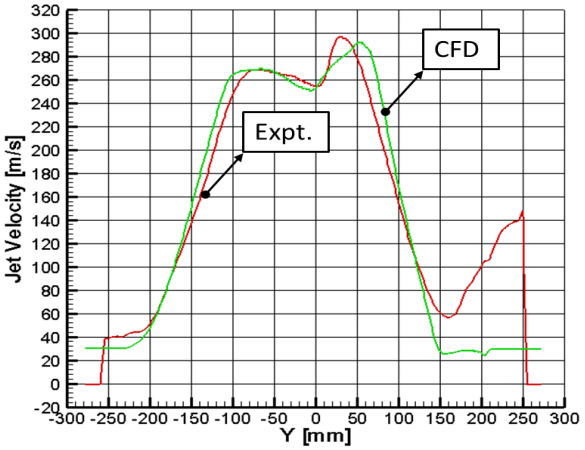

(c) Comparison of expt. vs CFD data

Figure B.10 – Axial velocity field in the cross-stream planes, X=2.4D

References

[1] RJ Astley, A Agarwal, KR Holland, PF Joseph, RH Self, MG Smith, R Sugimoto, and BJ Tester. Predicting and reducing aircraft noise. In *Proceedings of ICSV14*, 2007.

[2] POAL Davies, MJ Fisher, and MJ Barratt. The characteristics of the turbulence in the mixing region of a round jet. *Journal of Fluid Mechanics*, 15(03):337–367, 1963.

[3] J Bridges and C A Brown. Parametric testing of chevrons on single flow hot jets. In *AIAA Paper 2004-2824*, 2004.

[4] R. Rylander and M. Bjorkman. Annoyance by aircraft noise around small airports. *Journal of Sound and Vibration*, 205(4):533 – 537, 1997.

[5] R. Rylander. Physiological aspects of noise-induced stress and annoyance. *Journal of Sound and Vibration*, 277(3):471–478, 2004.

[6] U. S. Department of Transportation. Noise standards: Aircraft type and airworthiness certification, FAA report, chapter 14 CFR, part 36. Technical report, Federal Aviation Administration (FAA), Office of Environment and Energy, 2012.

[7] International Civil Aviation Organisation. Annex 16, to the convention on international civil aviation, environmental protection,. vol. 1: Aircraft noise, chapter 14,. Technical report, International Civil Aviation Organisation, 2014.

[8] U.S. Department of Transportation. Faa aerospace forecast: Fiscal years 2009-2025. Technical report, Federal Aviation Administration Aviation Policy and Plans, 2009.

[9] HK Tanna. An experimental study of jet noise part ii: shock associated noise. *Journal of Sound and Vibration*, 50(3):429–444, 1977.

[10] K Viswanathan, MB Alkislar, and MJ Czech. Characteristics of the shock noise component of jet noise. *AIAA Journal*, 48(1):25–46, 2010.

[11] K Viswanathan. Scaling laws and a method for identifying components of jet noise. *AIAA Journal*, 44(10):2274–2285, 2006.

[12] FB Greatrex. Engine noise. *Journal of Royal Aeronautical Society*, 58:223–231, 1954.

[13] A Powell. A survey of experiments on jet noise: A study of the mechanism of noise production of jet engines, with brief notes on its reduction. *Aircraft Engineering and Aerospace Technology*, 26(1):2–8, 1954.

[14] M J Lighthill. On sound generated aerodynamically. i. general theory. *Proceedings of the Royal Society of London. Series A. Mathematical and Physical Sciences*, 211 (1107):564–587, 1952.

[15] M J Lighthill. On sound generated aerodynamically. ii. turbulence as a source of sound. *Proceedings of the Royal Society of London. Series A. Mathematical and Physical Sciences*, 222(1148):1–32, 1954.

[16] M E Goldstein. *Aeroacoustics*, volume 1. New York, McGraw-Hill International Book Co., 1976.

[17] Jonathan B Freund. Noise sources in a low-reynolds-number turbulent jet at mach 0.9. *Journal of Fluid Mechanics*, 438:277–305, 2001.

[18] JE Ffowcs Williams. The noise from turbulence convected at high speed. *Philosophical Transactions for the Royal Society of London. Series A, Mathematical and Physical Sciences*, pages 469–503, 1963.

[19] GM Lilley. Jet noise classical theory and experiments. In *Aeroacoustics of flight vehicles: theory and practice*, 1, ed. H.H. Hubbard:pp. 211–289, 1991.

[20] PA Lush. Measurements of subsonic jet noise and comparison with theory. *Journal of Fluid Mechanics*, 46(03):477–500, 1971.

[21] OM Phillips. On the generation of sound by supersonic turbulent shear layers. *Journal of Fluid Mechanics*, 9(01):1–28, 1960.

[22] GM Lilley. The generation and radiation of supersonic jet noise. iv. theory of turbulence generated jet noise, noise radiation from upstream sources and combustion noise. *United States Air Force Aero Propulsion Laboratory TR-72-53*, 1972.

[23] ME Goldstein. A unified approach to some recent developments in jet noise theory. *International Journal of Aeroacoustics*, 1(1):1–16, 2002.

[24] GM Lilley. The radiated noise from isotropic turbulence with applications to the theory of jet noise. *Journal of Sound and Vibration*, 190(3):463–476, 1996.

[25] ME Goldstein. Relation between the generalized acoustic analogy and lilley's contributions to aeroacoustics. *International Journal of Aeroacoustics*, 9(4):401–418, 2010.

[26] D W Wundrow and A Khavaran. On the applicability of high-frequency approximations to lilley's equation. *Journal of Sound and Vibration*, 272(3):793–830, 2004.

[27] ME Goldstein. A generalized acoustic analogy. *Journal of Fluid Mechanics*, 488: 315–333, 2003.

[28] H Xia, P G Tucker, and S Eastwood. Large-eddy simulations of chevron jet flows with noise predictions. *International Journal of Heat and Fluid Flow*, 30(6):1067–1079, 2009.

[29] V F Dippold, L E Foster, and M R Wiese. Computational analyses of offset-stream nozzles for noise reduction. *Journal of Propulsion and Power*, 25(1):204–217, 2009.

[30] K Viswanathan. Nozzle shaping for reduction of jet noise from single jets. *AIAA Journal*, 43(5):1008–1022, 2005.

[31] K Viswanathan, M Shur, PR Spalart, and M Strelets. Flow and noise predictions for single and dual-stream beveled nozzles. *AIAA Journal*, 46(3):601–626, 2008.

[32] D Papamoschou. New method for jet noise reduction in turbofan engines. *AIAA Journal*, 42(11):2245–2253, 2004.

[33] D Papamoschou and M Debiasi. Conceptual development of quiet turbofan engines for supersonic aircraft. *Journal of propulsion and power*, 19(2):161–169, 2003.

[34] A Witkowska, D Juvé, and JG Brasseur. Numerical study of noise from isotropic turbulence. *Journal of Computational Acoustics*, 5(03):317–336, 1997.

[35] T Colonius, SK Lele, and P Moin. Sound generation in a mixing layer. *Journal of Fluid Mechanics*, 330:375–409, 1997.

[36] JB Freund, SK Lele, and P Moin. Numerical simulation of a mach 1.92 turbulent jet and its sound field. *AIAA Journal*, 38(11):2023–2031, 2000.

[37] C Bogey, C Bailly, and D Juvé. Noise investigation of a high subsonic, moderate reynolds number jet using a compressible large eddy simulation. *Theoretical and Computational Fluid Dynamics*, 16(4):273–297, 2003.

[38] DJ Bodony and SK Lele. On using large-eddy simulation for the prediction of noise from cold and heated turbulent jets. *Physics of Fluids*, 17(8):085103, 2005.

[39] C Bogey and C Bailly. Computation of a high reynolds number jet and its radiated noise using large eddy simulation based on explicit filtering. *Computers & fluids*, 35 (10):1344–1358, 2006.

[40] A Uzun, AS Lyrintzis, and GA Blaisdell. Coupling of integral acoustics methods with les for jet noise prediction. *International Journal of Aeroacoustics*, 3(4):297–346, 2004.

[41] SA Karabasov, MZ Afsar, TP Hynes, AP Dowling, WA McMullan, CD Pokora, GJ Page, and JJ McGuirk. Jet noise: acoustic analogy informed by large eddy simulation. *AIAA Journal*, 48(7):1312–1325, 2010.

[42] DJ Bodony and SK Lele. Review of the current status of jet noise predictions using large-eddy simulation. *AIAA paper*, 468:2006, 2006.

[43] HS Ribner. Quadrupole correlations governing the pattern of jet noise. *Journal of Fluid Mechanics*, 38(01):1–24, 1969.

[44] T F Balsa, P R Gliebe, R A Kantola, J C F Wang, and R Mani. High velocity jet noise source location and reduction: Task 2 - theoretical development and basic experiment. Technical report, Washington-DC: Federal Aviation Administration Report, FAA-RD-76-79- II, 1978.

[45] W Béchara, P Lafon, C Bailly, and SM Candel. Application of a κ-ε turbulence model to the prediction of noise for simple and coaxial free jets. *The Journal of the Acoustical Society of America*, 97(6):3518–3531, 1995.

[46] C Bailly, S Candel, and P Lafon. Prediction of supersonic jet noise from a statistical acoustic model and a compressible turbulence closure. *Journal of Sound and Vibration*, 194(2):219–242, 1996.

[47] C Bailly, P Lafon, and S Candel. Subsonic and supersonic jet noise predictions from statistical source models. *AIAA Journal*, 35(11):1688–1696, 1997.

[48] A Khavaran, EA Krejsa, and CM Kim. Computation of supersonic jet mixing noise for an axisymmetric convergent-divergent nozzle. *Journal of Aircraft*, 31(3):603–609, 1994.

[49] A Khavaran and E Krejsa. Role of anisotropy in turbulent mixing noise. In *AIAA paper 98-2289*, 1998.

[50] A Khavaran. Role of anisotropy in turbulent mixing noise. *AIAA Journal*, 37(7): 832–841, 1999.

[51] A Khavaran and J Bridges. Modelling of fine-scale turbulence mixing noise. *Journal of Sound and Vibration*, 279(3):1131–1154, 2005.

[52] Abdelkader Frendi, Wade D Dorland, Thein Maung, Tom Nesman, and Ten-See Wang. A jet engine noise measurement and prediction tool. *The Journal of the Acoustical Society of America*, 112(5):2036–2042, 2002.

[53] O Almeida, M Azarpeyvand, and RH Self. Revisiting the role of anisotropy for jet noise modeling. In *AIAA 2003-3319*, 2003.

[54] CKW Tam and L Auriault. Jet mixing noise from fine-scale turbulence. *AIAA Journal*, 37(2):145–153, 1999.

[55] N K Depuru Mohan, A P Dowling, S A Karabasov, H Xia, O Graham, T P Hynes, and P G Tucker. Acoustic sources and far-field noise of chevron and round jets. *AIAA Journal*, 53(9):2421–2436, 2015.

[56] J. T. Stone, R. H. Self, and C. J. Howls. Cones of silence, complex rays and catastrophes: high-frequency flowŰacoustic interaction effects. *Journal of Fluid Mechanics*, 853:37Ű71, 2018.

[57] MJ Fisher, GA Preston, and WD Bryce. A modelling of the noise from simple coaxial jets, part i: with unheated primary flow. *Journal of Sound and Vibration*, 209(3):385–403, 1998.

[58] MJ Fisher, GA Preston, and CJ Mead. A modelling of the noise from simple coaxial jets, part ii: with heated primary flow. *Journal of Sound and Vibration*, 209(3): 405–417, 1998.

[59] NWM Ko and ASH Kwan. The initial region of subsonic coaxial jets. *Journal of Fluid Mechanics*, 73(02):305–332, 1976.

[60] SF Birch, DA Lyubimov, VP Maslov, AN Secundov, and K Ya Yakubovsky. A rans based jet noise prediction procedure. In *AIAA 2007-3727*, 2007.

[61] AT Thies and CKW Tam. Computation of turbulent axisymmetric and non-axisymmetric jet flows using the k-epsilon model. *AIAA Journal*, 34(2):309–316, 1996.

[62] L Koch, James Bridges, and Abbas Khavaran. Flow field comparisons from three navier-stokes solvers for an axisymmetric separate flow jet. In *40th AIAA Aerospace Sciences Meeting & Exhibit*, page 672, 2002.

[63] Nicholas J Georgiadis, Dennis A Yoder, and William B Engblom. Evaluation of modified two-equation turbulence models for jet flow predictions. *AIAA journal*, 44 (12):3107–3114, 2006.

[64] DC Kenzakowski. Turbulence modeling improvements for jet noise prediction using piv datasets. In *AIAA 2004-2978*, 2004.

[65] SB Pope. An explanation of the turbulent round-jet/plane-jet anomaly. *AIAA Journal*, 16(3):279–281, 1978.

[66] CKW Tam, M Golebiowski, and JM Seiner. On the two components of turbulent mixing noise from supersonic jets. In *AIAA Paper 96-1716*, 1996.

[67] K Viswanathan. Analysis of the two similarity components of turbulent mixing noise. *AIAA Journal*, 40(9):1735–1744, 2002.

[68] TF Balsa and PR Gliebe. Aerodynamics and noise of coaxial jets. *AIAA Journal*, 15(11):1550–1558, 1977.

[69] TF Balsa. The acoustic field of sources in shear flow with application to jet noise: convective amplification. *Journal of Fluid Mechanics*, 79(01):33–47, 1977.

[70] M Azarpeyvand. *Some aspects of RANS based jet noise prediction*. PhD thesis, University of Southampton, 2008.

[71] T Suzuki and SK Lele. Refracted arrival waves in a zone of silence from a finite thickness mixing layer. *The Journal of the Acoustical Society of America*, 111(2): 716–728, 2002.

[72] WA Engblom, A Khavaran, and J Bridges. Numerical prediction of chevron nozzle noise reduction using WIND-MGBK methodology. In *AIAA paper 2004-2979*, 2004.

[73] TF Balsa. Refraction and shielding of sound from a source in a jet. *Journal of Fluid Mechanics*, 76(03):443–456, 1976.

[74] A Khavaran and N J Georgiadis. Aeroacoustics of supersonic elliptic jets. In *AIAA Paper 1996-0641*, 1996.

[75] A Hamed, A Khavaran, and S Lee. The flow and acoustic predictions for a high by-pass ratio exhaust nozzle. In *AIAA paper 98-3257*, 1998.

[76] A Frendi, T Nesman, and T-S Wang. On the effect of time scaling on the noise radiated by an engine plume. *Journal of Sound and Vibration*, 256(5):969–979, 2002.

[77] A Khavaran and E A Krejsa. Propagating of high-frequency jet noise using geometric acoustics. In *AIAA Paper 93-0147*, 1993.

[78] A Khavaran and E A Krejsa. Refraction of high-frequency jet noise in an arbitrary jet flow. In *AIAA Paper 94-0139*, 1994.

[79] P J Morris and F Farassat. Acoustic analogy and alternative theories for jet noise prediction. *AIAA Journal*, 40(4):671–680, 2002.

[80] PJ Morris and S Boluriaan. The prediction of jet noise from CFD data, 10^{th} aiaa. In *CEAS Aeroacoustics Conference*, pages 2009–2019, 2004.

[81] Nishant Raizada and Philip Morris. Prediction of noise from high speed subsonic jets using an acoustic analogy. In *12^{th} AIAA/CEAS Aeroacoustics Conference (27^{th} AIAA Aeroacoustics Conference)*, page 2596, 2006.

[82] Preetham Rao and Philip Morris. Some finite element applications in frequency domain aeroacoustics. In *10^{th} AIAA/CEAS Aeroacoustics Conference*, page 2962, 2004.

[83] RH Self. Jet noise prediction using the lighthill acoustic analogy. *Journal of Sound and Vibration*, 275(3):757–768, 2004.

[84] M Harper-Bourne. Jet near-field noise prediction. In *AIAA Paper 99–1838*, 1999.

[85] R H Self and A Bassetti. A rans based jet noise prediction scheme. In *AIAA Paper 2003-3325*, 2003.

[86] G J Page, J J McGuirk, M Hossain, R H Self, and A Bassetti. A CFD-coupled acoustics approach for coaxial jet noise. In *AIAA paper 2003-3286*, 2003.

[87] M Azarpeyvand and RH Self. Improved jet noise modeling using a new time-scale. *The Journal of the Acoustical Society of America*, 126(3):1015–1025, 2009.

[88] R H Self and M Azarpeyvand. Utilization of turbulent energy transfer rate time-scale in aeroacoustics with application to heated jets. *International Journal of Aeroacoustics*, 7(2):83–102, 2008.

[89] C R Ilário da Silva. *Development of a novel RANS-based method for the computational aeroacoustics of high speed jets*. PhD thesis, Universidade de São Paulo Escola Politécnica, 2011.

[90] Carlos RS Ilário, Mahdi Azarpeyvand, Victor Rosa, Rod H Self, and Júlio R Meneghini. Prediction of jet mixing noise with Lighthill's Acoustic Analogy and geometrical acoustics. *The Journal of the Acoustical Society of America*, 141(2):1203–1213, 2017.

[91] Herbert S Ribner. On the strength distribution of noise sources along a jet. *The Journal of the Acoustical Society of America*, 30(7):676–676, 1958.

[92] M Goldstein and B Rosenbaum. Effect of anisotropic turbulence on aerodynamic noise. *The Journal of the Acoustical Society of America*, 54(3):630–645, 1973.

[93] GM Lilley. On the noise from jets. *Agard cp-131*, 13:12, 1974.

[94] A A Townsend. *The Structure of Turbulent Shear Flow*. Cambridge university press, 1956.

[95] P Jordan and Y Gervais. Modelling self-and shear-noise mechanisms in inhomogeneous, anisotropic turbulence. *Journal of Sound and Vibration*, 279(3):529–555, 2005.

[96] PJ Morris and KBMQ Zaman. Velocity measurements in jets with application to noise source modeling. *Journal of Sound and Vibration*, 329(4):394–414, 2010.

[97] I Proudman. The generation of noise by isotropic turbulence. In *Proceedings of the Royal Society of London A: Mathematical, Physical and Engineering Sciences*, volume 214, pages 119–132. The Royal Society, 1952.

[98] Garry L Brown and Anatol Roshko. On density effects and large structure in turbulent mixing layers. *Journal of Fluid Mechanics*, 64(04):775–816, 1974.

[99] Christopher K. W. Tam, K. Viswanathan, K. K. Ahuja, and J. Panda. The sources of jet noise: experimental evidence. *Journal of Fluid Mechanics*, 615:253–292, 2008.

[100] William C Meecham and GW Ford. Acoustic radiation from isotropic turbulence. *The Journal of the Acoustical Society of America*, 30(4):318–322, 1958.

[101] Robert Rubinstein and Ye Zhou. Time correlations and the frequency spectrum of sound radiated by turbulent flows. Technical report, ICASE report, NASA-CR-201648, NAS 1.26:201648, 1997.

[102] Brian Thurow, Mo Samimy, and Walter Lempert. Compressibility effects on turbulence structures of axisymmetric mixing layers. *Physics of Fluids*, 15(6):1755–1765, 2003.

[103] S CJ Crow and FH Champagne. Orderly structure in jet turbulence. *Journal of Fluid Mechanics*, 48(3):547–591, 1971.

[104] Christopher KW Tam and Laurent Auriault. Mean flow refraction effects on sound radiated from localized sources in a jet. *Journal of Fluid Mechanics*, 370:149–174, 1998.

[105] J Atvars, LK Schubert, and HS Ribner. Refraction of sound from a point source placed in an air jet. *The Journal of the Acoustical Society of America*, 37(1):168–170, 1965.

[106] Jayanta Panda and Richard G Seasholtz. Experimental investigation of density fluctuations in high-speed jets and correlation with generated noise. *Journal of Fluid Mechanics*, 450:97–130, 2002.

[107] Jayanta Panda, Richard G Seasholtz, and Kristie A Elam. Investigation of noise sources in high-speed jets via correlation measurements. *Journal of Fluid Mechanics*, 537:349–385, 2005.

[108] Patrick M Hurdle, WC Meecham, and Brent K Hodder. Investigation of the aerodynamic noise generating region of a jet engine by means of the simple source fluid dilatation model. *The Journal of the Acoustical Society of America*, 56(6):1708–1721, 1974.

[109] M Schaffar. Direct measurements of the correlation between axial in-jet velocity fluctuations and far field noise near the axis of a cold jet. *Journal of Sound and Vibration*, 64(1):73–83, 1979.

[110] Christophe Bogey and Christophe Bailly. Investigation of sound sources in subsonic jets using causality methods on les data. In *AIAA paper 2005-2885*, 2005.

[111] J M Seiner, L Ukeiley, and M K Ponton. Jet noise source measurements using piv. In *AIAA paper 99-1896*, 1999.

[112] JB Freund. Noise-source turbulence statistics and the noise from a mach 0.9 jet. *Physics of Fluids (1994-present)*, 15(6):1788–1799, 2003.

[113] George Keith Batchelor. *The theory of homogeneous turbulence*. Cambridge university press, 1953.

[114] S Chandrasekhar. The theory of axisymmetric turbulence. *Philosophical Transactions of the Royal Society of London. Series A, Mathematical and Physical Sciences*, 242(855):557–577, 1950.

[115] A Khavaran, J Bridges, and J B Freund. A parametric study of fine-scale turbulence mixing noise. In *AIAA Paper 2002-2419*, 2002.

[116] M Harper-Bourne. Jet noise turbulence measurements. In *AIAA Paper 2003-3214*, 2003.

[117] M Billson. *Computational techniques for jet noise predictions*. PhD thesis, Department of Thermo and Fluid Dynamics, Chalmers University of Technology, Gothenburg, Sweden, 2002.

[118] J Bridges and M P Wernet. Turbulence measurements of separate flow nozzles with mixing enhancement features. In *AIAA Paper 2002-2484*, 2002.

[119] A Khavaran. Refraction and shielding of noise in non-axisymmetric jets. In *AIAA Paper 1996-1780*, 1996.

[120] Stewart Cant. *SB Pope, Turbulent Flows, Cambridge University Press, Cambridge, UK, 2000, 771 pp.* Elsevier, 2003.

[121] GT Csanady. The effect of mean velocity variations on jet noise. *Journal of Fluid Mechanics*, 26(01):183–197, 1966.

[122] G Lilley, P Morris, and B Tester. On the theory of jet noise and its applications. In *Aeroacoustics Conference*, page 987, 1973.

[123] R Mani. The influence of jet flow on jet noise. part 1. the noise of unheated jets. *Journal of Fluid Mechanics*, 73(04):753–778, 1976.

[124] R Mani. The influence of jet flow on jet noise. part 2. the noise of heated jets. *Journal of Fluid Mechanics*, 73(04):779–793, 1976.

[125] BJ Tester and CL Morfey. Developments in jet noise modelling – theoretical predictions and comparisons with measured data. *Journal of Sound and Vibration*, 46(1): 79–103, 1976.

[126] J W S Rayleigh. *Theory of Sound*, volume 2. Dover Publications Inc., 1945.

[127] D Blokhintzev. The propagation of sound in an inhomogeneous and moving medium i. *The Journal of the Acoustical Society of America*, 18(2):322–328, 1946.

[128] Wallace D Hayes. Energy invariant for geometric acoustics in a moving medium. *Physics of Fluids*, 11:1654–1656, 1968.

[129] Bernard D Seckler and Joseph B Keller. Geometrical theory of diffraction in inhomogeneous media. *The Journal of the Acoustical Society of America*, 31(2):192–205, 1959.

[130] Bernard D Seckler and Joseph B Keller. Asymptotic theory of diffraction in inhomogeneous media. *The Journal of the Acoustical Society of America*, 31(2):206–216, 1959.

[131] D Papamoschou. Zones of influence in the compressible shear layer. *Fluid Dynamics Research*, 11(05):217–228, 1993.

[132] A D Pierce. *Acoustics: an introduction to its physical principles and applications*. McGraw-Hill New York, 1981.

[133] Yu A Kravtsov and Yu I Orlov. Caustics, catastrophes, and wave fields. *Soviet Physics Uspekhi*, 26(12):1038, 1983.

[134] JB Freund and TG Fleischman. Ray traces through unsteady jet turbulence. *International Journal of Aeroacoustics*, 1(1):83–96, 2002.

[135] P McLaughlin. *A Contribution to Jet Noise Installation Problem*. PhD thesis, University of Southampton, 2011.

[136] Philip Mc Laughlin, RH Self, PJR Strange, and AD Moore. A 3-dimensional installation effects prediction method for a distributed jet source. In *13^{th} AIAA/CEAS Aeroacoustics Conference(28^{th} AIAA Aeroacoustics Conference)*, 2007.

[137] Vlastislav Cerveny. *Seismic ray theory*. Cambridge university press, 2005.

[138] Jonathan T Stone, RH Self, and Chris J Howls. A complex ray-tracing tool for high-frequency mean field flow-interaction effects in jets. In *Proc. 20th AIAA/CEAS Aeroacoustics Conference*, 2014.

[139] Odenir de Almeida. *Aeroacoustics of dual-stream jets with application to turbofan engines*. PhD thesis, São José dos Campos - SP, Brazil, 2009.

[140] BJ Venkatesh and RH Self. Assessment of current semi-empirical jet mixing model against SILOET & SYMPHONY databases. HARMONY programme, Deliverable 3.1.2, Institute of Sound and Vibration Research, University of Southampton, December, 2013.

[141] James Bridges. Effect of heat on space-time correlations in jets. *AIAA paper*, 2534: 2006, 2006.

[142] F Kerhervé, J Fitzpatrick, and P Jordan. The frequency dependence of jet turbulence for noise source modelling. *Journal of Sound and Vibration*, 296(1):209–225, 2006.

[143] O Power, F Kerhervé, J Fitzpatrick, and P Jordan. Measurements of turbulence statistics in high subsonic jets. In *AIAA Paper 2004-3021*, 2004.

[144] V Fleury, C Bailly, E Jondeau, M Michard, and D Juvé. Space-time correlations in two subsonic jets using dual particle image velocimetry measurements. *AIAA Journal*, 46(10):2498–2509, 2008.

[145] Craig J Mead. Further model-scale data acquired at higher area and temperature ratio for the study of coaxial jet noise. Technical Report Noise Note 126/93, Defence Research Agency, Pystock, Farnborough, UK, June 1993.

[146] ACARE Flightpath. 2050-europe's vision for aviation. *Advisory Council for Aeronautics Research in Europe*, 2011.

[147] S Nauri. Test conduct report for siloet 3.2 phase 4+: Acoustic tests version 1.0, QINETIQ/13/01799/1. Technical report, QinetiQ Ltd, Farnborough, UK, 2013.

[148] Richard Pinker. The enhancement of the QinetiQ noise test facility for larger-scale exhaust systems. In *10th AIAA/CEAS Aeroacoustics Conference*, 2004.

[149] F Dezitter, H Bezard, X de Saint Victor, K Zeggai, K Britchford, G Joubert, and G Puigt. Installation effects characterization of vhbr engines part iii: CFD assessment for jet mixing. In *15th AIAA/CEAS Aeroacoustics Conference*, page 3370, 2009.

[150] Laurent Cambier, Sébastien Heib, and Sylvie Plot. The Onera elsA CFD software: input from research and feedback from industry. *Mechanics & Industry*, 14(3):159–174, 2013.

[151] Alexandre Vuillemin, Pierre Loheac, Gilles Rahier, François Vuillot, and Nicolas Lupoglazoff. Aeroacoustic numerical method assessment for a double stream nozzle. In *11th AIAA/CEAS Aeroacoustics Conference*, page 3043, 2005.

[152] Laurent Cambier and Jean-Pierre Veuillot. Status of the elsA software for flow simulation and multi-disciplinary applications. In *46th AIAA Aerospace Sciences meeting and exhibit*, page 664, 2008.

[153] NWM Ko and ASH Kwan. The initial region of subsonic coaxial jets. *Journal of Fluid Mechanics*, 73(2):305–332, 1976.

[154] William G Hill Jr, Richard C Jenkins, and Barry L Gilbert. Effects of the initial boundary-layer state on turbulent jet mixing. *AIAA journal*, 14(11):1513–1514, 1976.

[155] L Bogusławski and Cz O Popiel. Flow structure of the free round turbulent jet in the initial region. *Journal of Fluid Mechanics*, 90(3):531–539, 1979.

[156] ZD Husain and AKMF Hussain. Axisymmetric mixing layer: influence of the initial and boundary conditions. *AIAA Journal*, 17(1):48–55, 1979.

[157] KBMQ Zaman. Effect of initial condition on subsonic jet noise. *AIAA journal*, 23 (9):1370–1373, 1985.

[158] HA Warda, SZ Kassab, KA Elshorbagy, and EA Elsaadawy. An experimental investigation of the near-field region of free turbulent round central and annular jets. *Flow Measurement and Instrumentation*, 10(1):1–14, 1999.

[159] HA Warda, SZ Kassab, KA Elshorbagy, and EA Elsaadawy. An experimental investigation of the near-field region of a free turbulent coaxial jet using lda. *Flow Measurement and Instrumentation*, 10(1):15–26, 1999.

[160] RA Antonia and Q Zhao. Effect of initial conditions on a circular jet. *Experiments in fluids*, 31(3):319–323, 2001.

[161] Christophe Bogey, Olivier Marsden, and Christophe Bailly. Influence of initial turbulence level on the flow and sound fields of a subsonic jet at a diameter-based reynolds number of 10 5. *Journal of Fluid Mechanics*, 701:352–385, 2012.

[162] Marcus Harper-Bourne. Commissioning and validation of a new jet rig for the qinetiq noise test facility. In *14^{th} AIAA/CEAS Aeroacoustics Conference*, 2008.

[163] W Bryce. The prediction of static-to-flight changes in jet noise. In *AIAA Paper 1984-2358*, 1984.

[164] Dimitri Papamoschou and Sara Rostamimonjezi. Effect of velocity ratio on noise source distribution of coaxial jets. *AIAA Journal*, 48(7):1504–1512, 2010.

[165] W Olsen and R Friedman. Jet noise from coaxial nozzles over a wide range of geometric and flow parameters. In *12^{th} Aerospace Sciences Meeting*, page 43, 1974.

[166] TJ Williams, MRMH Ali, and JS Anderson. Noise and flow characteristics of coaxial jets. *Journal of Mechanical Engineering Science*, 11(2):133–142, 1969.

[167] K Viswanathan. Parametric study of noise from dual-stream nozzles. *Journal of Fluid Mechanics*, 521:35–68, 2004.

[168] Stanley Birch, D Lyubimov, P Buchshtab, A Secundov, and K Yakubovsky. Jet-pylon interaction effects. In *11th AIAA/CEAS Aeroacoustics Conference*, page 3082, 2005.

[169] CL Morfey and V Szewczyk. Jet noise modelling by geometric acoustics. part ii: Theory and prediction inside the cone of silence. Technical report, ISVR Technical Report No. 92, University of Southampton, 1977.

[170] Yu A Kravtsov and Yu I Orlov. *Caustics, catastrophes and wave fields*, volume 15. Springer Science & Business Media, 2012.

[171] Tim Poston and Ian Stewart. *Catastrophe theory and its applications*. Courier Corporation, 2014.

[172] Michael V Berry. Waves and thom's theorem. *Advances in Physics*, 25(1):1–26, 1976.

[173] Donald Ludwig. Uniform asymptotic expansions at a caustic. *Communications on Pure and Applied Mathematics*, 19(2):215–250, 1966.

[174] Régis Marchiano, François Coulouvrat, and Richard Grenon. Numerical simulation of shock wave focusing at fold caustics, with application to sonic boom. *The Journal of the Acoustical Society of America*, 114(4):1758–1771, 2003.

[175] Joseph B Keller. Geometrical theory of diffraction. *JOSA*, 52(2):116–130, 1962.

[176] Andrzej Hanyga. Point-to-curve ray tracing. *pure and applied geophysics*, 148(3-4): 387–420, 1996.

[177] M. V. Berry and C. J. Howls. Integrals with coalescing saddles. http://dlmf.nist.gov/36, Release 1.0.10 of 2015-08-07, 2006.

[178] Tim Poston and Ian Stewart. *Catastrophe theory and its applications*. Courier Corporation, 2014.

[179] ME Henderson and HB Keller. Complex bifurcation from real paths. *SIAM Journal on Applied Mathematics*, 50(2):460–482, 1990.

[180] RS Murchie. Prediction program for co-axial jet noise, using a single-stream database. Technical report, DERA Pyestock, UK, September, 2000.

[181] ESDU International. Computer-based estimation procedure for single-stream jet noise. Technical report, ESDU98019, November, 1998.